## *Constraining anomalous couplings in the gauge-Higgs sector at high-energy colliders*

OCHOA-VALERIANO, OSCAR

# Constraining anomalous couplings in the gauge-Higgs sector at high-energy colliders

Oscar Ochoa Valeriano

A Thesis presented for the degree of
Doctor of Philosophy


Institute for Particle Physics Phenomenology
Department of Physics
Durham University
United Kingdom

May 2022

*Dedicated to*

Los Toya, Exiliados y deportados

*and*

Pato[†]

# Constraining anomalous couplings in the gauge-Higgs sector at high-energy colliders

Oscar Ochoa Valeriano

Submitted for the degree of Doctor of Philosophy, May 2022

**Abstract**

Several physical phenomena suggest that the Standard Model is not the ultimate theory possible for describing Nature, and looking for deviations from the theory prediction might be a hint for physics beyond the Standard Model. Nevertheless, the lack of tantalising evidence for new resonant physics, along with our ignorance of the energy scale at which such physics should arise, require us to improve current precision measurements to further test the Standard Model.

It is possible to treat the Standard Model as an Effective Field Theory, valid up to a high cut-off energy scale above the electroweak scale, equipped with a new set of Lorentz structures, the so-called *anomalous couplings*, that extend and parametrise with modified couplings the vertices allowed by the Standard Model. The interactions between the Higgs and the gauge bosons are thought to be a promising avenue to scrutinise the Standard Model for any new physics effects.

In this Thesis we explore the gauge-Higgs sector to segregate the anomalous couplings that arise in viewing the Standard Model as an Effective Field Theory. In doing so, we investigate the capability of current and future experiments at constraining said anomalous couplings through standard processes involving gauge-Higgs interactions that might shed light on what potentially lies beyond the Standard Model.

We study the so-called *golden channel* in the environment of the High-Luminosity Large Hadron Collider, as well as the *Higgs-strahlung* and *Z-boson fusion* processes at the high-energy stages of both the International Linear Collider and the Compact Linear Collider. These channels allow us to project stringent bounds on anomalous couplings in the gauge-Higgs sector that can be probed at high-energy colliders.

# Declaration

The work in this Thesis is based on research carried out at the Institute for Particle Physics Phenomenology, Department of Physics, University of Durham, England, United Kingdom. No part of this Thesis has been submitted elsewhere for any other degree or qualification and it is all my own work unless referenced to the contrary in the text. The chapters listed below are based on joint research:

- Chapter 4 contains results which have been published in: S. Banerjee, R. S. Gupta, **O. Ochoa-Valeriano**, M. Spannowsky and E. Venturini, *A fully differential SMEFT analysis of the golden channel using the method of moments*, *JHEP* **06** (2021) 031 [arXiv:2012.11631] [INSPIRE]. I generated the Monte Carlo samples, as well as implemented and optimised the collider analysis.

- Chapter 5 contains results which have been published in: S. Banerjee, R. S. Gupta, **O. Ochoa-Valeriano** and M. Spannowsky, *High energy lepton colliders as the ultimate Higgs microscopes*, *JHEP* **02** (2022) 176 [arXiv:2109.14634] [INSPIRE]. I generated the Monte Carlo samples, as well as implemented and optimised the collider analyses.

# Acknowledgements

Hace algunos cuantos años escuché del escritor argentino Andrés Oppenheimer la siguiente frase: *toda gran innovación es el último eslabón de una larga cadena de fracasos*. Me parece más atractivo el caso general: *todo gran logro...* He aquí, pues, mi gran logro: el compendio de once años de trabajo, desde la licenciatura hasta el doctorado, que no se podrían entender sin el apoyo incondicional de mi familia. A ustedes, mis grandes pilares, les dedico cada una de las letras que hay en estas páginas, pues difícilmente encontraré otra manera de escribir en unas cuantas líneas lo que significó para mí aprender a la distancia que siempre encontraré en ustedes una gran fuente de fortaleza, sin importar lo sinuoso del camino.

After nearly sixty months of ups and downs learning what doing research in particle physics is like, this Thesis illustrates the outcome of such an experience at the Institute for Particle Physics Phenomenology. Throughout the years I have met extraordinary people that pushed me, one way or another, several times to keep going. I am most thankful to my supervisor, Michael Spannowsky, who gave me the possibility to work with him and write this work under his mentorship. *Danke schön*, Michael, not only for giving me the chance to learn a bit from a top physicist like you, but for the patience and guidance during all those chats that lasted more than ten minutes against your will, too.

As a PhD student I worked on several research projects that involved absorbing knowledge from heavyweights in their fields. To Céline Bœhm, Christoph Englert, Chris Hays, Roman Kogler, and Frank Krauss, my sincere gratitude for sharing your expertise and having me on board, mostly since I know that I was a particularly annoying student when I could not figure things out by myself.

Frustration kicked in several times throughout this journey, which made it difficult for me to be as productive and independent as I would have wanted. However, Shankha Banerjee, Raquel Gómez Ambrosio, Rick Sandeepan Gupta, and Elena Venturini, took me under their wings and did their best to guide me when I needed it the most. I am having a really hard time trying to put into words everything I would like to say to you all, but perhaps a huge thank you might do for now.

On a daily basis I had the chance to walk through the same front doors as several caring people that, one way or another, quickly became a support network for me. Asli, Andrew, Joey, Matthew, Phil, Robin, Ryan, Tommaso, Wendy: this experience would have been way more complicated without you around, and am grateful for having had the chance to meet you all. Kudos to Adam, Joanne(s), Linda, Paul, and Trudy, for being the best support staff one could ask for.

I am grateful to Jessica, Joey, Matthew, Parisa, Phil, Raquel, Rick, Ryan, and Shankha, who kindly agreed to proofread parts of this Thesis, and would like to apologise in case their eyes ended up bleeding. Further, my warmest thanks to David J. Miller and Frank Krauss for acting as examiners.

Estar lejos de México ha sido complicado, pero afortunadamente encontré en Durham gente que me hizo sentir como en casa, y espero con ansias el día en el que nuestros caminos se encuentren nuevamente. Abraham, Andrea, Balder, David, Diego, Diana, Ishiba, Karen, Marcos, así como mis chavos del *Dominó ahora por whats*, han jugado un papel importante en mi desarrollo personal durante los últimos años, y eso nunca lo olvidaré. Agradecimientos especiales para Alexis, Carlos, Μαριάννα, y Maura, por tantas veces en las que convivir con ustedes eran pequeños momentos que me mantenían a flote un día a la vez.

Aunque este capítulo de mi vida lo he escrito en el extranjero, difícilmente lo habría podido lograr sin el continuo aliento de todas aquellas personas que han sido partícipes de ello, de una u otra manera, desde muchos mensajes de texto contestados semanas después de haberlos leído. *Amor Ibero*, *IFOS uia*, Agustín, Claudia, Erick, Héctor, Hugo, Laura, Maca, Manuel, Mariana, Mario, Michael, Mónica, Pancho,

Paola, Pepe, Ricardo, Sara: gracias por su paciencia y soporte, pues sé que un simple mensaje siempre es suficiente para que estén junto a mí al pie del cañón. Asimismo, agradezco al Consejo Nacional de Ciencia y Tecnología (CONACYT) por financiar mis estudios de posgrado.

Mi interés en las turbias aguas de la física fue un despertar involuntario en un inicio, y en un acto de justicia debo agradecer a José Zahoul y Jesús Flores Téllez por empujarme en esta dirección y compartir sus experiencias conmigo. Una vez sumergido, la participación de Alfredo$^{\dagger}$, Fabiola, Felipe, James, Nacho, y Salvador$^{\dagger}$, fue crucial para tomar las decisiones adecuadas en momentos llenos de dudas. Y esas resoluciones me llevaron a aprender y ver hacia arriba a Cristy, mi gurú particulera, a quien le debo más de lo que puedo escribir en unas líneas— gran parte de lo que he aprendido ha sido gracias a que sigues guiándome, y este alumnito siempre estará agradecido de haber tenido una miss como tú. A todos, ¡gracias!

Last but not least, quiero dedicar estas últimas líneas desde el fondo de mi corazón a Atenea, quien me ha acompañado tanto a la distancia como en persona desde hace varios años. El gran apoyo incondicional que me has brindado continuamente, muchas veces soportando y tolerando varios episodios de desesperación, es algo que atesoro con especial cariño. Tu gran fortaleza, entre otras cualidades de las cuales aprendo continuamente, me ha enseñado que siempre es posible hacer que los demonios más asesinos beban agua de nuestras manos. Gracias ¡totales!

**For I wouldn't have made it this far without any of you.**

*Physics is like sex: sure, it may give some practical results, but that's not why we do it.*

— R. P. Feynman

# Contents

# List of Figures

# List of Tables

# Chapter 1

# Introduction

The late 19th and early 20th centuries correspond to a period of rapid evolution of scientific ideas[1] concerned with the description of physical phenomena that were beyond what 'common sense' dictates; since the discovery of the electron in 1897 by J. J. Thomson, the understanding of Nature's building blocks, *a.k.a. elementary particles*, has been one of the main tasks of modern physics over time.

From Max Planck and his postulate on quantisation of the electromagnetic energy, giving birth to Quantum Mechanics, to Emmy Noether's discovery of the interplay between symmetry and conservation laws, passing through Albert Einstein's theory of Relativity and Paul Dirac's attempts to construct a relativistic framework of Quantum Mechanics, physicists were able to group together the mathematical foundations of quantum systems and field theory at high energies and accommodate them into arguably the most successful description of Nature to date, called *Quantum Field Theory* [1, 2].

The current and best understanding of the particle world we have is called the *Standard Model of Particle Physics*, which encompasses a set of quantum field theories that allow us to study, describe, and predict the interaction between elementary particles [3–5] at length scales of $\mathcal{O}\left(10^{-18}\,\mathrm{m}\right)$ to a high precision. Despite its success

[1] One could refer to Thomas Kuhn's or Karl Popper's treatises on scientific discovery for an in-depth philosophical discussion, although this is beyond the scope of this work.

the Standard Model fails to account for several physical phenomena, as we will see later, which suggests that it is not the ultimate theory available for the description of Nature. However, if one wants to construct a more robust description of the quantum fields that compose our Universe, inevitably one has to begin by taking the Standard Model, due to its well-tested agreement with many observations, and extend it to the physical scale of interest in some way. In other words, the ultimate theory (if any exists) of Nature at even smaller lengths (or, equivalently, higher energies), should reproduce or resemble the Standard Model in its low-energy limit.

Although the Standard Model is known to agree well with a plethora of measurements, there is still room for an improvement of the precision studies carried out by the experiments. Any deviation from the theory prediction might be a hint for new physics beyond the Standard Model that might help explain the shortcomings of our current theory related to unexplained phenomena observed in Nature. It is therefore of great importance to set tighter bounds on areas of the Standard Model that are more loosely constrained than others to determine whether experiments can find discrepancies between theory and data.

Measuring the properties of the particles described by the theory will help to set constraints on new physics scenarios from experimental observations, such as the mass, couplings, decay width, and cross-sections of the recently discovered Higgs boson. Because of their large masses, the interactions between the Higgs and the gauge bosons (*gauge-Higgs sector*) are thought to be an avenue to scrutinise the Standard Model for any new physics effects, regardless of the energy scale (unknown to date) at which these become evident and relevant. In performing such studies, it is possible to extend the Standard Model by parametrising its allowed interactions with modified couplings and a new set of Lorentz structures, the so-called *anomalous couplings*. These arise from viewing the Standard Model as an *effective theory* valid up to a high cut-off energy scale which is expected to lie well above the electroweak scale, *i.e.*, the low-energy approximation of a more complete, robust theory.

In this Thesis we explore the gauge-Higgs sector to segregate the anomalous coup-

lings that arise in the perturbative expansion of the Standard Model viewed as an Effective Field Theory at current and future colliders. In doing so, it is possible to set constraints on processes that might shed light on what potentially lies beyond the Standard Model. This Thesis is structured as follows: the remainder of Chapter 1 is aimed at introducing the Standard Model, along with some of its features, shortcomings, and possible ways in which physicists intend to extend it. In Chapter 2 we introduce the basic ideas of Effective Field Theory, and discuss the interplay between effective theories and measurements at colliders in Chapter 3, which is the core idea behind constraining Standard Model expectations to look for discrepancies with data. In Chapters 4 and 5 we consider the application of using differential distributions to constrain Wilson coefficients at colliders. Finally, we conclude and summarise the Thesis in Chapter 6.

## 1.1 The Standard Model of Particle Physics

Nature's elementary particles are described by one of the most successful physical theories to date, known as the Standard Model of Particle Physics (SM). Being a Quantum Field Theory (QFT) it encompasses a set of operator-valued quantum fields invariant under the Poincaré group[2], with their excitations understood as fundamental particles, and interactions encapsulated in a Lagrangian formulation necessary to predict and interpret the experimental data delivered by high-energy colliders. It is a non-Abelian gauge field theory[3] which combines the theory of Quantum Chromodynamics (QCD), weak interactions, and Quantum Electrodynamics (QED).

The interactions between bosons (integer spin; Bose-Einstein statistics) and fermions (half-integer spin; Fermi-Dirac statistics) are described by the concept of symmetry. Bosons are responsible for the interactions we commonly know as *forces*, while fermions constitute the building blocks of *matter* in the Universe; mass terms in the

[2]The group of space-time symmetries, a combination of both Lorentz boosts and translations.

[3]QFT in which the Lagrangian density remains invariant under local transformations of the operator-valued fields.

Lagrangian are generated by the so-called *Higgs mechanism*. Together (gauge bosons + fermions + Higgs boson) these construct the Lagrangian defining the theory.

The gauge symmetry of the SM corresponds to the gauge group,

$$G_{\text{SM}} = SU(3)_C \times SU(2)_L \times U(1)_Y, \tag{1.1.1}$$

formed by the non-Abelian $SU(N)$ ($N = 3, 2$) and the Abelian $U(1)$ groups, each describing a fundamental force in Nature: strong, weak, and electromagnetic, respectively[4].

The $SU(3)$ non-Abelian gauge group corresponds to the strong interaction between colour charges, mediated by *gluons* ($g$), and described by QCD [6–8]. Yang and Mills [9] explained the weak interactions, responsible for radioactive decays and coupled to the left-handed weak isospin, with a non-Abelian gauge theory based on the $SU(2)$ symmetry group. Finally, the Abelian $U(1)$ symmetry group corresponds to hypercharge interactions. The electro-weak unification by Glashow [10] concluded that the weak and hypercharge interactions are, similar to electricity and magnetism, two sides of the same coin, giving rise to the theory of electroweak (EW) interactions [11, 12] described by the $SU(2)_L \times U(1)_Y$ gauge group.

The theory predicts the gauge bosons to be massless. However, experimental evidence for the short-range action of weak interactions imply that these mediators are massive. Introducing by hand in the Lagrangian mass terms for the weak bosons breaks gauge invariance, needed for the theory to be renormalisable [13, 14], and violates unitarity in $W_L W_L$ scattering, where $L$ stands for the longitudinal polarisation. *What to do?*

Adding a complex scalar field with non-zero vacuum expectation value (vev) in the Lagrangian, charged under the gauge group, generates mass terms for the particle content of the underlying theory, preserving gauge invariance, and keeping it unitary and renormalisable. This mechanism, owed (independently) to Brout and Englert [15], Higgs [16], and Guralnik, Hagen and Kibble [17], is called *spontaneous symmetry*

[4] The remaining known fundamental force, gravity, is best described by Einstein's Theory of General Relativity, and it is beyond the scope of the SM (see Sec. 1.3).

*breaking* (SSB), or "Higgs mechanism" for short. After SSB, which gives mass to the weak $W^+, W^-$, and $Z$-bosons, the EW gauge group is broken down to the $U(1)_Q$ symmetry group as,

$$SU(2)_L \times U(1)_Y \to U(1)_Q, \tag{1.1.2}$$

corresponding to interactions between electrically charged particles, mediated by (massless) photons ($\gamma$), and described by QED [18].

We now turn our attention to describing the terms constructing the Lagrangian of the theory, which consists of gauge-invariant terms as follows:

$$\mathcal{L}_{\text{SM}} = \mathcal{L}_{\text{Gauge}} + \mathcal{L}_{\text{Fermion}} + \mathcal{L}_{\text{Higgs}}. \tag{1.1.3}$$

Here, the kinetic terms for the gauge and matter fields, as well as their interactions, are encapsulated in the first two pieces. The Higgs term contains the gauge-Higgs, matter-Higgs interactions, and the potential for the additional complex scalar field.

### 1.1.1 Gauge sector

Gauge bosons, obeying Bose-Einstein statistics, are the mediators of interactions between elementary particles. These are spin-1 particles which correspond to the excitation of gauge fields arising from the gauge-invariant requirement of the SM Lagrangian, belonging to the adjoint representation of the gauge group as,

$$SU(3)_C : G^a_\mu \in (\mathbf{8}, \mathbf{1}, 0), \;\; SU(2)_L : W^i_\mu \in (\mathbf{1}, \mathbf{3}, 0), \;\; U(1)_Y : B_\mu \in (\mathbf{1}, \mathbf{1}, 0), \tag{1.1.4}$$

where the first and second entries in the parentheses correspond to the representation under $SU(3)_C$ and $SU(2)_L$, respectively, and the third one gives the hypercharge. The spin-1 property of these gauge bosons associate them to a vector field represented by four-vector potentials condensed in the field-strength tensors,

$$\begin{aligned} G^a_{\mu\nu} &= \partial_\mu G^a_\nu - \partial_\nu G^a_\mu + g_S f^{abc} G^b_\mu G^c_\nu, \\ W^i_{\mu\nu} &= \partial_\mu W^i_\nu - \partial_\nu W^i_\mu + g\epsilon^{ijk} W^j_\mu W^k_\nu, \\ B_{\mu\nu} &= \partial_\mu B_\nu - \partial_\nu B_\mu, \end{aligned} \tag{1.1.5}$$

where $g_S$ and $g$ are the coupling strengths of their respective groups. The index $a \in [1, 8]$ is a colour index in the adjoint representation of $SU(3)_C$, and the index $i \in [1, 3]$ stands for each $SU(2)_L$ $W^i_\mu$ field in the adjoint representation of the gauge group. Further, the structure constants for $SU(3)_C$ and $SU(2)_L$ are denoted by $f^{abc}$ and the Levi-Civita tensor $\epsilon^{ijk}$, respectively.

The structure constants $K^{mnp}$ of the associated $SU(N)$ gauge group[5] are part of the commutation relations satisfied by the generators $T^m$ of the group,

$$[T^m, T^n] = iK^{mnp}T^p, \tag{1.1.6}$$

with the indices $m$, $n$, and $p$ running from 1 to $N^2 - 1$ for each $SU(N)$ symmetry group. The generators $T^m$ are traceless Hermitian matrices with a representation-dependent dimension: $N \times N$ matrices in the fundamental representation, and $\left(N^2 - 1\right) \times \left(N^2 - 1\right)$ in the adjoint representation[6]. It is important to mention that in Eq. (1.1.5) the gauge group $U(1)_Y$ also has a coupling strength denoted by $g'$ not shown, and the third term in the non-Abelian field-strength tensors gives rise to gauge-boson self interactions.

With the field-strength tensors associated to the gauge group displayed in Eq. (1.1.5), we can then write the first term in Eq. (1.1.3) as,

$$\begin{aligned} \mathcal{L}_{\text{Gauge}} &= -\frac{1}{4}G^a_{\mu\nu}G^{a,\mu\nu} - \frac{1}{4}W^i_{\mu\nu}W^{i,\mu\nu} - \frac{1}{4}B_{\mu\nu}B^{\mu\nu} \\ &= -\frac{1}{4}F_{\mu\nu}F^{\mu\nu}, \end{aligned} \tag{1.1.7}$$

which condenses the dynamics and (self-)interactions of the gauge fields.

Several times we have mentioned the concept of *gauge invariance* of the Lagrangian throughout the text, and it is about time to show why. Recalling that the contraction $F_{\mu\nu}F^{\mu\nu}$ should result in a Lorentz scalar, and taking the Abelian field $B_\mu$ as an example for simplicity, we apply a gauge transformation parametrised by $\alpha(x)$ as a

[5] In the case of Abelian gauge groups, such as $U(1)$, the structure constant is zero.

[6] In the adjoint representation, $N^2 - 1$ corresponds to the total number of generators as well.

Table 1.1: Some fundamental properties of gauge bosons [19].

| **Boson** | **Interaction** | **Mass** [GeV] | **Charge** [$e$] |
|---|---|---|---|
| $\gamma$ | Electromagnetism | 0 | 0 |
| $g$ | Strong | 0 | 0 |
| $W^{\pm}$ | Weak | $80.379 \pm 0.012$ | $\pm 1$ |
| $Z$ | Weak | $91.1876 \pm 0.0021$ | 0 |

function of the space-time coordinate $x$ as,

$$B_\mu \to B'_\mu = B_\mu - \frac{1}{g'}\partial_\mu \alpha(x), \tag{1.1.8}$$

from where it is easy to see that $B_\mu B^\mu \neq B'_\mu B'^\mu$, hence not invariant under such a gauge transformation. Given the experimental evidence for the massiveness of the $W^{\pm}$- and $Z$-bosons, one might be tempted to include a mass term by hand in the Lagrangian. However, from Eq. (1.1.8) it is evident that a mass term like $m^2 W^i_\mu W^{i,\mu}$ is forbidden. Hence, in the unbroken theory the gauge bosons are massless, and it is through the Higgs mechanism in Sec. 1.1.3 that gauge bosons acquire mass dynamically.

In summary, in QCD the index $a$ runs from 1 to 8, giving 8 massless gluons for the 8 generators of the gauge group $SU(3)_C$. For $SU(2)_L$, the index $i$ runs from 1 to 3, giving rise to three massive weak bosons. For QED and $U(1)$, we have 1 massless photon. The main properties of the gauge bosons after SSB are shown in Table 1.1.

### 1.1.2 Fermion sector

As mentioned before, the fundamental matter particles are spin-1/2 fermions, obeying Fermi-Dirac statistics: *quarks* and *leptons*. Evidence related to the spin structure of weak interactions revealed that only left-handed fermions, in particular neutrinos, take part in interactions mediated by the $W$-boson— if existing at all, right-handed neutrinos are *sterile* (do not interact weakly through the $W$-boson). This implies that there is a distinction within the SM between left- and right-handed fermions, meaning that we are dealing with a *chiral* theory: one can decompose the fermion

fields into their chiral components,

$$\psi = \psi_L + \psi_R, \tag{1.1.9}$$

where $\psi$ denotes a matter field, and the subscripts $L$ and $R$ correspond to the left- and right-handed projections, respectively. In terms of projection operators $P_L$ and $P_R$, the chiral components of a fermion field $\psi$ are,

$$\begin{aligned} \psi_L \equiv P_L\psi &= \frac{1}{2}\left(1-\gamma^5\right)\psi, \\ \psi_R \equiv P_R\psi &= \frac{1}{2}\left(1+\gamma^5\right)\psi, \end{aligned} \tag{1.1.10}$$

with $\gamma^5 = i\gamma^0\gamma^1\gamma^2\gamma^3$ the fifth Dirac matrix.

Quarks and leptons come in three families or generations, and each generation is represented under the SM gauge group[7] as,

$$\begin{aligned} Q_L &= \begin{pmatrix} u_L \\ d_L \end{pmatrix} \in (\mathbf{3},\mathbf{2},1/3), \quad u_R \in (\mathbf{3},\mathbf{1},4/3), \quad d_R \in (\mathbf{3},\mathbf{1},-2/3), \\ L_L &= \begin{pmatrix} \nu_L \\ \ell_L \end{pmatrix} \in (\mathbf{1},\mathbf{2},-1), \quad \ell_R \in (\mathbf{1},\mathbf{1},-2). \end{aligned} \tag{1.1.11}$$

Quarks, in the first row above, are $SU(3)_C$ triplets, which means they carry colour charge. Leptons, in the second row, are $SU(3)_C$ singlets and do not interact via the strong force[8]. Above, $u$, $d$, $\nu$, and $\ell$, stand for up-type quarks, down-type quarks, neutrinos, and charged leptons, respectively.

Mass terms for fermions mix left- and right-hand components, and spoil gauge invariance,

$$\begin{aligned} \mathcal{L}_{\text{Fermion, mass}} = im\overline{\psi}\psi &= im\left(\overline{\psi}_L + \overline{\psi}_R\right)\left(\psi_L + \psi_R\right) \\ &= im\left(\overline{\psi}_L\psi_R + \overline{\psi}_R\psi_L\right), \end{aligned} \tag{1.1.12}$$

since $\psi_L$ and $\psi_R$ have different quantum numbers under the EW gauge group. Hence,

[7] Although each family has a copy of these representations, they only differ by their mixings and masses.

[8] Strictly speaking, quarks and leptons are in the triplet and trivial representation of $SU(3)_C$, respectively.

a fermion mass term like the one shown above violates gauge invariance and in the unbroken theory fermions end up being massless, the same way as gauge bosons do.

For massless fermions, the kinetic term of the Lagrangian reads,

$$\begin{aligned}\mathcal{L}_{\text{Fermion, kinetic}} = i\overline{\psi}\not{\partial}\psi &= i\left(\overline{\psi}_L + \overline{\psi}_R\right)\not{\partial}\left(\psi_L + \psi_R\right) \\ &= i\overline{\psi}_L\not{\partial}\psi_L + i\overline{\psi}_R\not{\partial}\psi_R,\end{aligned} \tag{1.1.13}$$

where $\not{\partial} \equiv \gamma^\mu\partial_\mu$, and it is made evident that kinetic terms decompose into left- and right-handed sectors— this would allow us to ignore the right-handed fermions for weak interactions. However, fermions interact with each other via the gauge bosons, so the actual gauge-invariant kinetic term of the Lagrangian involving the fermion sector reads,

$$\begin{aligned}\mathcal{L}_{\text{Fermion, kinetic}} = \sum_{k=1}^{3}\Big[&\overline{Q}_L^k i\gamma^\mu D_\mu Q_L^k + \overline{u}_R^k i\gamma^\mu D_\mu u_R^k + \overline{d}_R^k i\gamma^\mu D_\mu d_R^k \\ &+ \overline{L}_L^k i\gamma^\mu D_\mu L_L^k + \overline{\ell}_R^k i\gamma^\mu D_\mu \ell_R^k\Big],\end{aligned} \tag{1.1.14}$$

summing explicitly over the fermion families. We further define the covariant derivative[9] $D_\mu$ acting on a fermion field $\psi$ as,

$$D_\mu\psi = \partial_\mu\psi - ig_S\frac{\lambda^a}{2}G_\mu^a\psi - ig\frac{\sigma^i}{2}W_\mu^i\psi - ig'\frac{Y}{2}B_\mu\psi, \tag{1.1.15}$$

which contain the gauge fields corresponding to the SM gauge group. In the equation above, the $\lambda^a$ and $\sigma^i$ are the Gell-Mann and Pauli matrices, respectively, and when divided by 2 these can be identified with the generators of the gauge groups $SU(3)_C$ and $SU(2)_L$. The purpose of introducing the covariant derivative is to make the term $D_\mu\psi$ covariant, such that $\overline{\psi}\gamma^\mu D_\mu\psi$ is gauge invariant.

From Eq. (1.1.15), with $T^i = \sigma^i/2$ the three generators of $SU(2)_L$ and $Y$ the hypercharge of $U(1)_Y$, the algebra followed by the EW sector is,

$$\left[T^i, T^j\right] = i\epsilon^{ijk}T^k, \quad \left[T^i, Y\right] = 0, \quad [Y, Y] = 0. \tag{1.1.16}$$

[9]Note that the second term in the definition of $D_\mu$ vanishes in the case of leptonic fields.

Table 1.2: Some fundamental properties of quarks [19]. Since quarks are found in bound states, except for the top which decays before hadronising, and not observed as physical particles, their masses are determined indirectly from the influence in hadronic states. Note that antiquarks carry opposite electric charge.

| **Generation** | **Flavour** | **Mass** [GeV] | **Charge** [$e$] |
|---|---|---|---|
| 1 | up ($u$) | $0.00216^{+0.00049}_{-0.00026}$ | $+2/3$ |
| | down ($d$) | $0.00467^{+0.00048}_{-0.00017}$ | $-1/3$ |
| 2 | charm ($c$) | $1.27 \pm 0.02$ | $+2/3$ |
| | strange ($s$) | $0.093^{+0.011}_{-0.005}$ | $-1/3$ |
| 3 | top ($t$) | $172.76 \pm 0.30$ | $+2/3$ |
| | bottom ($b$) | $4.18^{+0.03}_{-0.02}$ | $-1/3$ |

Defining $T^{\pm} = T^1 \pm iT^2$, and the charged and neutral physical fields as,

$$W^{\pm}_{\mu} = \frac{1}{\sqrt{2}}\left(W^1_{\mu} \mp iW^2_{\mu}\right), \quad \begin{pmatrix} Z_{\mu} \\ A_{\mu} \end{pmatrix} = \begin{pmatrix} \cos\theta_W & -\sin\theta_W \\ \sin\theta_W & \cos\theta_W \end{pmatrix} \begin{pmatrix} W^3_{\mu} \\ B_{\mu}, \end{pmatrix} \tag{1.1.17}$$

it is possible to rewrite the covariant derivate $D_{\mu}$ in terms of the physical gauge fields, barring the gluon field term for illustration purposes only, as,

$$D_{\mu} = \partial_{\mu} - i\frac{g}{\sqrt{2}}\left(T^+W^+_{\mu} + T^-W^-_{\mu}\right) - ig_Z\left(T_3 - Q\sin^2\theta_W\right)Z_{\mu} - ieQA_{\mu}, \tag{1.1.18}$$

where $\theta_W$ is the *weak mixing angle*, *a.k.a. Weinberg angle*, defined as,

$$\tan\theta_W = \frac{g'}{g}. \tag{1.1.19}$$

From Eq. (1.1.18), $g_Z = g/\cos\theta_W$, and $e = g\sin\theta_W = g'\cos\theta_W$ the coupling strength of the electromagnetic interaction. In the doublet representations of $SU(2)_L$, where $T_3$ are the eigenvalues of the third component of $SU(2)_L$ generators, the upper fields have $T_3 = 1/2$, and the lower fields have $T_3 = -1/2$. The electromagnetic charge $Q$ is related to the weak isospin $T_3$ and weak hypercharge $Y$ by the Gell-Mann–Nishijima relation [20, 21],

$$Q = T_3 + \frac{Y}{2}. \tag{1.1.20}$$

In summary, we have two types of fermions: quarks and leptons, grouped into three generations with two fermions each. They differ by their electric charge, as well as by their masses. All fermions, except for the neutrinos, are electrically charged,

Table 1.3: Some fundamental properties of leptons [19]. Unlike quarks, the masses of leptons can be measured directly and the ones shown here correspond to their pole masses. In the case of neutrinos, upper bounds are reported. Note that antileptons carry opposite electric charge.

| **Generation** | **Flavour** | **Mass** [GeV] | **Charge** [$e$] |
|---|---|---|---|
| 1 | electron ($e^-$) | $5.11 \times 10^{-4} \pm 3.1 \times 10^{-12}$ | $-1$ |
| | electron-neutrino ($\nu_e$) | $< 460 \times 10^{-9}$ | 0 |
| 2 | muon ($\mu^-$) | $0.10566 \pm 2.4 \times 10^{-9}$ | $-1$ |
| | muon-neutrino ($\nu_\mu$) | $< 0.00019$ | 0 |
| 3 | tau ($\tau^-$) | $1.77686 \pm 1.2 \times 10^{-4}$ | $-1$ |
| | tau-neutrino ($\nu_\tau$) | $< 0.0182$ | 0 |

and hence interact with electromagnetic fields. Given that the SM seems to be a chiral theory, only left-handed fermions and right-handed antifermions take part in weak interactions mediated by the $W$-boson. Quarks carry colour charge and are affected by the strong force, while leptons are insensitive to it— since each quark has a colour quantum number, these are three-fold degenerate in EW interactions. The main properties of quarks and leptons after SSB are shown in Tables 1.2 and 1.3, respectively.

With the information encoded in Eqs. (1.1.7) and (1.1.14), we are now ready to move on and discuss the mechanism by which the particle content we have introduced so far acquires mass by breaking the symmetry of the theory but leaving the Lagrangian invariant under gauge transformations: the Higgs mechanism.

### 1.1.3 Higgs sector

So far we have discussed what the kinetic terms are for the gauge and fermion sectors of the SM Lagrangian. As pointed out in Secs. 1.1.1 and 1.1.2, although we have described a gauge theory of strong interactions, weak isospin and hypercharge, we have a theory of massless particles. However, experimental findings of massive fermions and (three) gauge bosons of weak interactions contradict our Lagrangian density. Requiring the theory to obey gauge symmetry prohibits any explicit mass terms for the gauge fields, and we cannot write gauge invariant mass terms for

fermions. Generating masses in the SM implies that the EW symmetry must be broken somehow, so let us get to it. The following description of the Higgs mechanism and Higgs physics in general is inspired by comprehensive texts like Refs. [22–30].

From the continuity equation of Classical Electrodynamics [31, 32],

$$\partial_\mu J^\mu = 0, \tag{1.1.21}$$

where $J^\mu = \left(\rho, \vec{J}\right)$ is the four-current with sources $\rho$ and $\vec{J}$ the charge and current densities, respectively, we know that electric charge is a conserved quantity— this means that the symmetry group of electromagnetic interactions, $U(1)_Q$, is unbroken. Hence, the mechanism which gives mass to the weak bosons and breaks the symmetry of the gauge group should do so as noted in Eq. (1.1.2),

$$SU(2)_L \times U(1)_Y \to U(1)_Q,$$

so as to keep $U(1)_Q$ unbroken, which SSB does. Strictly speaking, since we are dealing with a gauge theory, and the EW symmetry group is the one being broken, we should call this *electroweak symmetry breaking* (EWSB), instead of SSB as we have done until now.

Since the Lagrangian of the theory needs to be Lorentz invariant, and scalars do not break the Lorentz group, a complex scalar charged under the SM gauge group is introduced,

$$\Phi = \begin{pmatrix} \phi^+ \\ \phi^0 \end{pmatrix} = \frac{1}{\sqrt{2}} \begin{pmatrix} \phi_1 + i\phi_2 \\ \phi_3 + i\phi_4 \end{pmatrix} \in (\mathbf{1}, \mathbf{2}, 1), \tag{1.1.22}$$

where $\phi_j$ are real scalar fields. With this new multiplet, we can now sketch the general form of the Lagrangian associated to the scalar sector,

$$\mathcal{L}_{\text{Higgs}} = D_\mu \Phi^\dagger D^\mu \Phi - V\left(\Phi^\dagger \Phi\right) - \mathcal{L}_{\text{Yukawa}}, \tag{1.1.23}$$

where the first term encodes the couplings of the scalar to the gauge fields, the second term corresponds to the potential of the scalar field, and the last term (known as the *Yukawa sector*) stands for the interactions between the scalar and the fermions.

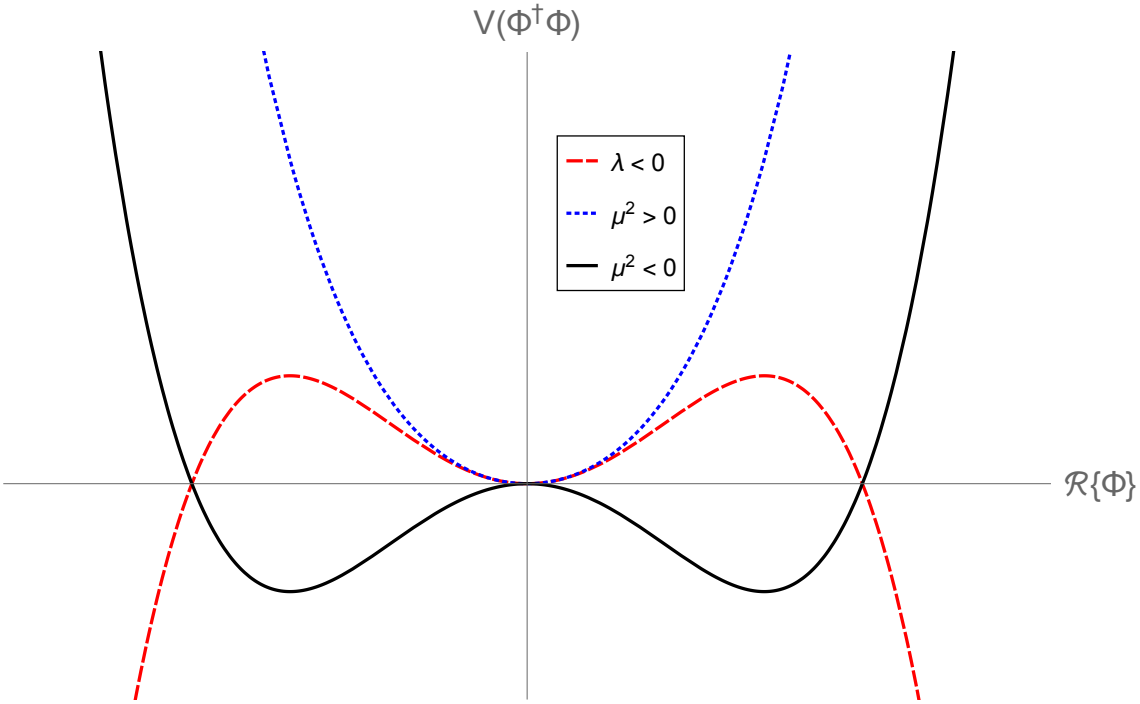


Figure 1.1: Example scalar potentials $V\left(\Phi^\dagger\Phi\right) = \mu^2\left(\Phi^\dagger\Phi\right) + \lambda\left(\Phi^\dagger\Phi\right)^2$ for different signs of the mass $\mu^2$ and self-coupling $\lambda$ parameters. **Dashed red:** $\lambda < 0$ dominates over the sign of $\mu^2$, and the potential is unbounded from below. **Dotted blue:** Both $\mu^2$ and $\lambda > 0$ yield a minimum at the origin, and the EW symmetry remains unbroken in the vacuum. **Solid black:** For $\mu^2 < 0$ and $\lambda > 0$ the EW gauge symmetry is spontaneously broken in the ground state as the vacuum is away from $|\Phi| = 0$ and degenerate. See text for details.

The potential $V\left(\Phi^\dagger\Phi\right)$, responsible for EWSB, has the form,

$$V\left(\Phi^\dagger\Phi\right) = \mu^2\left(\Phi^\dagger\Phi\right) + \lambda\left(\Phi^\dagger\Phi\right)^2, \tag{1.1.24}$$

where $\mu^2$ and $\lambda$, the coefficients of the mass term and the self-coupling, respectively, are real numbers. We now need to determine what the ground state (*vacuum*) of the scalars is, which we will do by minimising the potential,

$$V'\left(\Phi^\dagger\Phi\right) = 0 \Rightarrow |\Phi|^2 = -\frac{\mu^2}{2\lambda}. \tag{1.1.25}$$

If $\lambda < 0$, the potential is unbounded from below and there is no stable ground state. If both $\mu^2$ and $\lambda > 0$, the potential finds its minimum at $|\Phi| \equiv \sqrt{\Phi^\dagger\Phi} = 0$, which keeps EW symmetry unbroken in the vacuum. Finally, if $\mu^2 < 0$ and $\lambda > 0$, the potential finds a degenerate minimum away from $|\Phi| = 0$, which spontaneously breaks the EW gauge symmetry as the ground state is not invariant under $SU(2)_L \times U(1)_Y$ transformations. Fig. 1.1 shows a sketch of the shape of the scalar potential for different signs of the mass $\mu^2$ and self-coupling $\lambda$ parameters. Hence, the non-zero vacuum expectation value (*vev*, $v$) of the scalar doublet is,

$$\langle\Phi\rangle = \sqrt{-\frac{\mu^2}{2\lambda}} \equiv \frac{v}{\sqrt{2}}, \tag{1.1.26}$$

where $v = \left(\sqrt{2}G_F\right)^{-1/2} \sim 246\,\text{GeV}$ is fixed by the Fermi constant $G_F$ [33].

Since the Higgs doublet is written in terms of four real scalar fields $\phi_j$ as shown in Eq. (1.1.22), the *vev* can lie in any of these fields. However, as $U(1)_Q$ remains an unbroken symmetry, this *vev* must be chosen in the electrically neutral component of the doublet, *i.e.*, $\phi_3$ or $\phi_4$. For simplicity, let us choose $\langle\phi_4\rangle = v$, and set to zero the *vev* of the remaining fields. It is possible to "gauge away" the unphysical degrees of freedom $\phi_1$, $\phi_2$, and $\phi_3$, which are Nambu-Goldstone bosons [34–36]. In the unitary gauge, the Higgs doublet then becomes,

$$\Phi = \frac{1}{\sqrt{2}}\begin{pmatrix} 0 \\ \\ v + h \end{pmatrix}, \tag{1.1.27}$$

where we denote $h$ as the physical Higgs boson. Recalling that the symmetry-breaking pattern of the gauge group is the one shown in Eq. (1.1.2), it is possible to check what the broken symmetries are given the Higgs doublet in Eq. (1.1.27): by acting with the generators $T$ of the gauge group into $\Phi$, invariance implies $T\Phi = 0$, which only holds for $U(1)_Q$, as expected.

Expanding the potential in Eq. (1.1.24) around the *vev*,

$$V\left(\Phi^\dagger\Phi\right) = \frac{\mu^2}{2}(v+h)^2 + \frac{\lambda}{4}(v+h)^4, \tag{1.1.28}$$

one can see that there are Higgs self-interactions parametrised by $\lambda$, whereas the mass of the Higgs boson is,

$$m_h \equiv \sqrt{2\lambda}v. \tag{1.1.29}$$

To fully describe the Higgs potential $V\left(\Phi^\dagger\Phi\right)$, measurements of the free parameters $\mu^2$ and $\lambda$ are needed, since these are not predicted by the SM. In 2012, the discovery of the Higgs boson at the Large Hadron Collider (LHC) [37] by the ATLAS and CMS collaborations [38, 39] was announced, reporting $m_h \sim 125\,\text{GeV}$. However, Higgs self-interactions remain elusive experimentally.

Having looked into the Higgs potential $V\left(\Phi^\dagger\Phi\right)$, we now turn our attention to the gauge-Higgs couplings in Eq. (1.1.23). Using the definitions shown in Eq. (1.1.17) for the physical fields, the interaction between the Higgs and the gauge bosons reads,

$$\left|D_\mu\Phi\right|^2 = \frac{1}{2}\left(\partial_\mu h\right)^2 + \frac{1}{4}g^2(v+h)^2W_\mu^+W^{-,\mu} + \frac{1}{8}(v+h)^2\left(g^2+g'^2\right)Z_\mu Z^\mu. \tag{1.1.30}$$

One can now see that the Lagrangian of the Higgs field in Eq. (1.1.23) contains the terms,

$$\mathcal{L}_{\text{Higgs}} \supset \frac{1}{4}g^2v^2W_\mu^+W^{-,\mu} + \frac{1}{8}v^2\left(g^2+g'^2\right)Z_\mu Z^\mu, \tag{1.1.31}$$

giving rise to the masses for the $W^\pm$- and $Z$-bosons,

$$m_W^2 = \frac{g^2v^2}{4}, \qquad m_Z^2 = \frac{m_W^2}{c_{\theta_W}^2}, \tag{1.1.32}$$

where the second relation is a consequence of the definition for $c_{\theta_W}^2$ in Eq. (1.1.19),

and is uniquely specified by the mixing between the EW gauge groups. Finally, as the Higgs does not couple to the $A_\mu$ field, the photon does not acquire mass and the $U(1)_Q$ symmetry remains unbroken. *What just happened?*

We started with a theory that has no masses. Then, we introduced an interaction between the (EW) gauge fields and some constant scalar background field with four degrees of freedom, whatever that might be. As the *vev* of the scalar field is a non-zero parameter, the gauge symmetry is (spontaneously) broken by fixing a value for its ground state. After EWSB, only one of the four degrees of freedom we started with remains physical (the Higgs boson), while the other three act as longitudinal modes obtained by the $W^\pm$ and $Z$ gauge bosons becoming massive—*the three unphysical degrees of freedom generate the masses of three gauge bosons.* In short, if a local gauge symmetry gets broken, the gauge boson associated to its generator acquires a non-zero mass[10].

The doublet nature of the Higgs field allows for interactions with fermion fields $\psi$, called *Yukawa couplings* $\mathcal{Y}_\psi^{ij}$, which correspond to the last piece of the Higgs Lagrangian in Eq. (1.1.23), allowing fermions to acquire mass. From Eq. (1.1.11), the Yukawa piece of the Lagrangian reads,

$$\mathcal{L}_{\text{Yukawa}} = \mathcal{Y}_\ell^{ij}\overline{L}_{L,i}\Phi\ell_{R,j} + \mathcal{Y}_u^{ij}\overline{Q}_{L,i}\Phi^{\text{c}}u_{R,j} + \mathcal{Y}_d^{ij}\overline{Q}_{L,i}\Phi d_{R,j} + \text{h.c.}, \tag{1.1.33}$$

where $\Phi^{\text{c}}$, also an $SU(2)_L$ doublet with hypercharge $Y = -1$, allows for Yukawa interactions with up-type quarks, and is defined as,

$$\Phi^{\text{c}} \equiv i\sigma^2\Phi^* = \begin{pmatrix} \phi^{0^*} \\ -\phi^{+^*} \end{pmatrix}. \tag{1.1.34}$$

Note that, in order to maintain gauge invariance, Eq. (1.1.33) contains both left- and right-handed $SU(2)_L$ multiplets. Masses of fermions can be read off directly

[10] Gauge bosons of unbroken symmetries remain massless.

from the Lagrangian, and for this let us consider the term involving the tau lepton,

$$\mathcal{Y}_\tau \overline{L}_{L,\tau} \Phi \ell_{R,\tau} + \text{h.c.} = m_\tau \tau^+ \tau^- + \frac{\mathcal{Y}_\tau}{\sqrt{2}} h \tau^+ \tau^-, \tag{1.1.35}$$

where we identify $m_\tau \equiv \mathcal{Y}_\tau v/\sqrt{2}$. Not only masses, but fermion-Higgs interactions too are parametrised by $\mathcal{Y}_\psi$, the fermion $\psi$ Yukawa coupling, which is a free parameter of the theory.

From Eq. (1.1.33), the parameter $\mathcal{Y}_\psi^{ij}$ stands for 3×3 (since there are three generations of fermions) complex matrices: one for leptons $\mathcal{Y}_\ell^{ij}$, one for up-type quarks $\mathcal{Y}_u^{ij}$, and one for down-type quarks $\mathcal{Y}_d^{ij}$. As these matrices are not necessarily diagonal in the gauge basis, one needs to rotate the Yukawa matrices from the weak interaction flavour basis in such a way that in the mass basis these are diagonal[11]. With $V_L^\psi$ and $V_R^\psi$ unitary matrices that diagonalise the Yukawa matrices,

$$\tilde{Y}_\psi = V_L^\psi \mathcal{Y}_\psi V_R^{\psi\dagger}, \tag{1.1.36}$$

we obtain the diagonalised version of the Yukawa matrices, $\tilde{Y}_\psi$. As there is only one Yukawa matrix in the lepton sector due to the absence of right-handed neutrinos that can mix with their left-handed counterparts as explained before, gauge-lepton interactions remain diagonal with a suitable definition of the gauge eigenstates aligned with the mass eigenstates. For quarks, neutral-current interactions ($\gamma$- and $Z$-mediated) are insensitive to these rotations as the effects cancel. However, charged-current interactions mediated by the $W^\pm$-boson in Eq. (1.1.14) get modifications of the form,

$$\mathcal{L}_{\text{Fermion, kinetic}} \supset \overline{u}_L \gamma^\mu W_\mu^+ V_L^u V_L^{d\dagger} d_L + \text{h.c.}, \tag{1.1.37}$$

where we define the non-diagonal, unitary matrix $V_{\text{CKM}} \equiv V_L^u V_L^{d\dagger}$, known as the *Cabibbo-Kobayashi-Maskawa* (CKM) matrix [40, 41]. As a result, charged currents change the flavour (mass eigenstates) of the interacting quarks (gauge eigenstate).

At last we can show what the SM Lagrangian looks like. With the renormalisable[12]

[11] In other words, the fields are not necessarily aligned with the (physical) mass eigenstates.
[12] Operators with mass-dimension less than or equal to four.

and gauge-invariant fields and interactions described above it can be written as,

$$\mathcal{L}_{\rm SM} = -\frac{1}{4}F_{\mu\nu}F^{\mu\nu} + i\overline{\psi}\gamma^{\mu}D_{\mu}\psi + \left|D_{\mu}\Phi\right|^2 - V\left(\Phi^{\dagger}\Phi\right) - \mathcal{Y}_{\psi}^{ij}\overline{\psi}_i\Phi\psi_j + \text{h.c.}, \quad (1.1.38)$$

where, in summary, the first term describes the gauge sector; the second one corresponds to the kinetic terms of fermions; gauge-Higgs interactions are contained in the third term; the Higgs potential, responsible for EWSB, is the fourth term; the fifth term accounts for Yukawa interactions giving rise to fermion masses; finally, the Hermitian conjugate includes antiparticles.

## 1.2 Higgs phenomenology at colliders

In the previous section we discussed the gauge group of the SM Lagrangian and the interactions between fermions and gauge bosons, as well as the Higgs mechanism that gives rise to the mass spectrum of the particles contained in the theory. Let us now see some predictions of the SM Lagrangian in Eq. (1.1.38) related to the Higgs sector: Higgs production at colliders and its decay channels— so far, ATLAS and CMS have managed to establish a picture of consistency of Higgs measurements with the SM expectations [42–44]. The experimental evidence suggests an $m_h = 125.25 \pm 0.17\,\text{GeV}$, $\Gamma_h = 3.2^{+2.8}_{-2.2}\,\text{MeV}$ Higgs boson [19, 45–49], where $\Gamma_h$ corresponds to the total decay width of the Higgs.

### 1.2.1 Higgs production

As this Thesis is aimed at studying Higgs phenomenology at current (LHC) and future linear $e^+e^-$ colliders [50] such as the International Linear Collider (ILC) [51–53] or the Compact Linear Collider (CLIC) [54–56], we briefly outline what the main single-Higgs[13] production mechanisms favoured at high-energy experiments are.

[13] Since di-Higgs production has not been observed to date, we restrict to present the single-Higgs channels only.

At the LHC, there are four production modes of the Higgs boson. The *gluon-gluon fusion* (*ggh*) [57] is the dominant production mode because of the high gluon luminosity,

$$pp \to gg \to h,$$

induced by top- and bottom-quark loops. The *vector-boson fusion* (*VBF*) channel [58],

$$pp \to q\bar{q}' + V^*V^* \to jjh,$$

where $j$ refers to a quark that could have changed flavour under charged current interactions and $V = W^{\pm}/Z$, is mediated by the fusion of $W^{\pm}$ or $Z$ weak bosons and subleading with respect to the *ggh* mode[14]. Sizeable, but suppressed compared to *ggh* and *VBF*, the *Higgs-strahlung* (*Vh*) channel [59],

$$pp \to q\bar{q}' \to V^* \to Vh,$$

where $V = W^{\pm}/Z$, consists of Higgs radiation off of weak bosons $V$. Similar to *Vh*, a Higgs can be radiated off of top- or bottom- quark pairs $\left(t\bar{t}h/b\bar{b}h\right)$ [60],

$$pp \to q\bar{q}/gg \to Q\overline{Q}h,$$

where $Q = t/b$, subdominant with respect to the other production modes, completing our list. Other processes, such as Higgs produced in association with a single top-quark, are highly suppressed with respect to the ones mentioned above. The Feynman diagrams of the outlined processes are illustrated in Fig. 1.2.

At $e^+e^-$ colliders, there are three single-Higgs production modes[15]. At low centre-of-mass energies $\sqrt{s}$, the dominant channel is *Higgs-strahlung* (*Zh*),

$$e^+e^- \to Z^* \to Zh,$$

which, just as for the LHC's *Zh* channel, consists of Higgs radiation off of a $Z$-boson.

[14] From Fig. 1.4 it can be seen that the cross-section of the *ggh* process dominates over the rest of the production mechanisms, and the *VBF*'s cross-section is the second largest.

[15] Lepton colliders provide an excellent alternative to hadron colliders for observing di-Higgs production above the $m_{2h+Z}$ threshold.

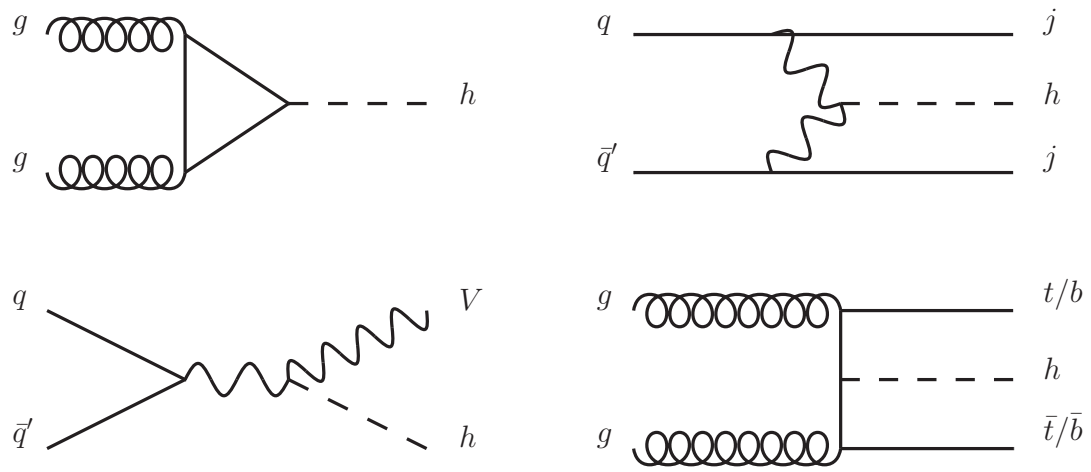


Figure 1.2: Feynman diagrams illustrating the four dominant single-Higgs production channels at the LHC (see text for details). **Top left:** *ggh*, the dominant production mode. **Top right:** *VBF*, subleading with respect to *ggh*. **Bottom left:** *Vh*, where a Higgs is produced in association with a weak boson $V = W^{\pm}/Z$. **Bottom right:** Higgs radiation off of a third-generation quark ($t\bar{t}h/b\bar{b}h$).

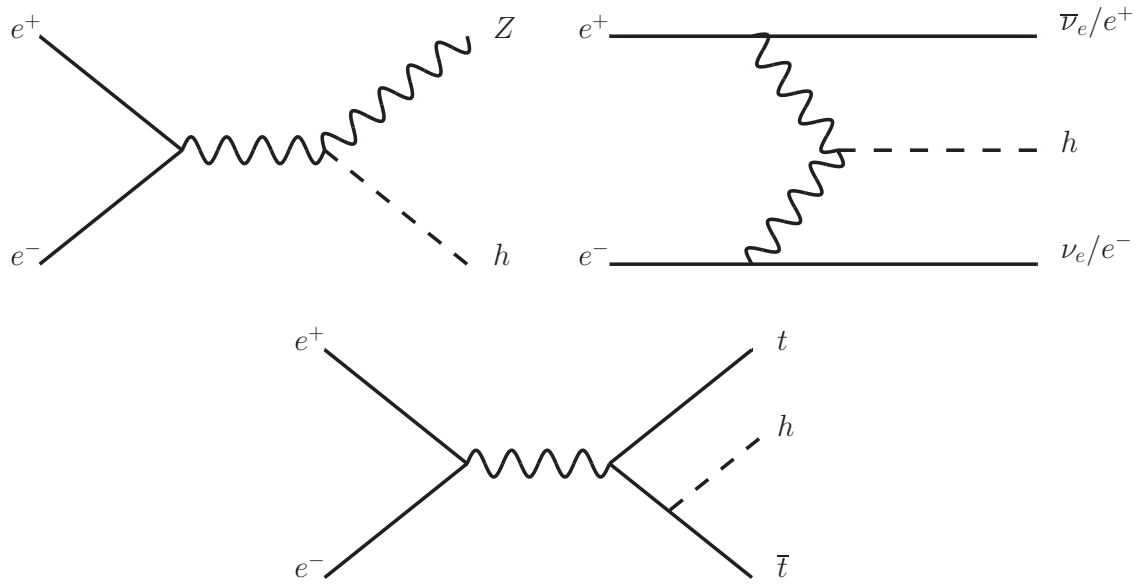


Figure 1.3: Feynman diagrams illustrating the three dominant single-Higgs production channels at $e^+e^-$ colliders (see text for details). **Top left:** *Zh* dominates at a centre-of-mass energy $\sqrt{s} \sim 250\,\text{GeV}$, and its cross-section $\sigma$ falls as $\sigma \sim 1/s$. **Top right:** *VBF*, which can be $W^{\pm}$- or $Z$-mediated, takes over *Zh* as $\sqrt{s}$ increases, with $\sigma \sim \ln^2\left|s/m_V^2\right|$. **Bottom:** Higgs radiation off of a top-quark pair, can be accessed once the $m_{t\bar{t}h}$ threshold is reached.

Its cross-section $\sigma$ reaches its maximum at $\sqrt{s} \sim 250\,\text{GeV}$, near the $m_{Zh}$ threshold, and then falls as $\sigma \sim 1/s$. As $\sqrt{s}$ increases, the *vector-boson fusion* (*VBF*) mode,

$$e^+e^- \to \overline{\nu}_e\nu_e/e^+e^- + W^{+*}W^{-*}/Z^*Z^* \to \overline{\nu}_e\nu_e h/e^+e^- h,$$

which can be either $W^\pm$- or $Z$- mediated, begins taking over with a cross-section that grows as $\sigma \sim \ln^2\left|s/m_V^2\right|$, where $m_V$ corresponds to the $V$ boson mass. Finally, similar to the LHC case, the Higgs can be radiated off of a top-quark pair,

$$e^+e^- \to Z/\gamma^* \to t\bar{t}h,$$

once the $m_{t\bar{t}h}$ threshold is reached. The Feynman diagrams of the single-Higgs production modes at $e^+e^-$ colliders are illustrated in Fig. 1.3, and the cross-sections of all the production channels outlined above are shown in Fig. 1.4 as a function of the centre-of-mass energy $\sqrt{s}$.

### 1.2.2 Higgs decays

As the Higgs mass is not predicted by the SM, this parameter has to be measured by experiments. Once this is done, the decay pattern of the Higgs boson is unambiguously determined. Since its couplings to fermions and gauge bosons are proportional to their masses, the Higgs tends to prefer decays into the heaviest particles allowed by phase-space restrictions. The decay processes of the Higgs boson can be categorised as:

- **Fermionic:** The Higgs boson couples to fermions with a strength proportional to the corresponding Yukawa coupling. For $m_h \sim 125\,\text{GeV}$, the preferred fermionic decay is the $h \to b\bar{b}$ channel.

- **Massive gauge bosons:** Even though there is not enough phase space for Higgs decays to a pair of on-shell weak bosons, the $h \to V^{(*)}V^*$ $\left(V = W^\pm/Z\right)$ decay mode to one or two off-shell weak bosons is still kinematically accessible.

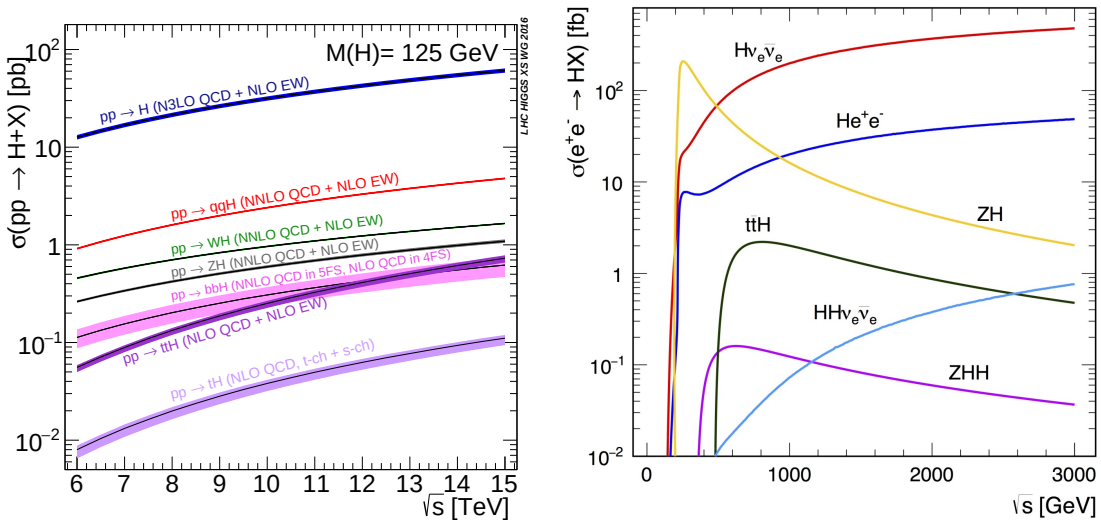


Figure 1.4: Higgs production cross-sections at colliders as a function of the centre-of-mass energy $\sqrt{s}$ (see text for details). **Left:** Cross-sections $\sigma$, in pb, as a function of the centre-of-mass energy $\sqrt{s}$, in TeV, relevant at the LHC for single production of an $m_h \sim 125\,\text{GeV}$ Higgs boson via *ggh* (blue), *VBF* (red), *Wh* (green), *Zh* (black), associated production with a pair of bottom quarks (pink), associated production with a pair of top quarks (purple), and associated production with a single top quark (magenta), at different orders in perturbation theory (shown in parentheses). The bands correspond to theory uncertainties. Taken from Ref. [46]. **Right:** Cross-sections $\sigma$, in fb, as a function of the centre-of-mass energy $\sqrt{s}$, in GeV, for Higgs production at $e^+e^-$ colliders. The dominant single-Higgs production channel at low energies is *Zh* (yellow). As $\sqrt{s}$ increases, *WBF* (red) and *ZBF* (blue) are enhanced. Above the $m_{t\bar{t}h}$ threshold, the Higgs can be produced in association with a pair of top quarks (green). Also displayed are some di-Higgs production channels. Taken from Ref. [61].

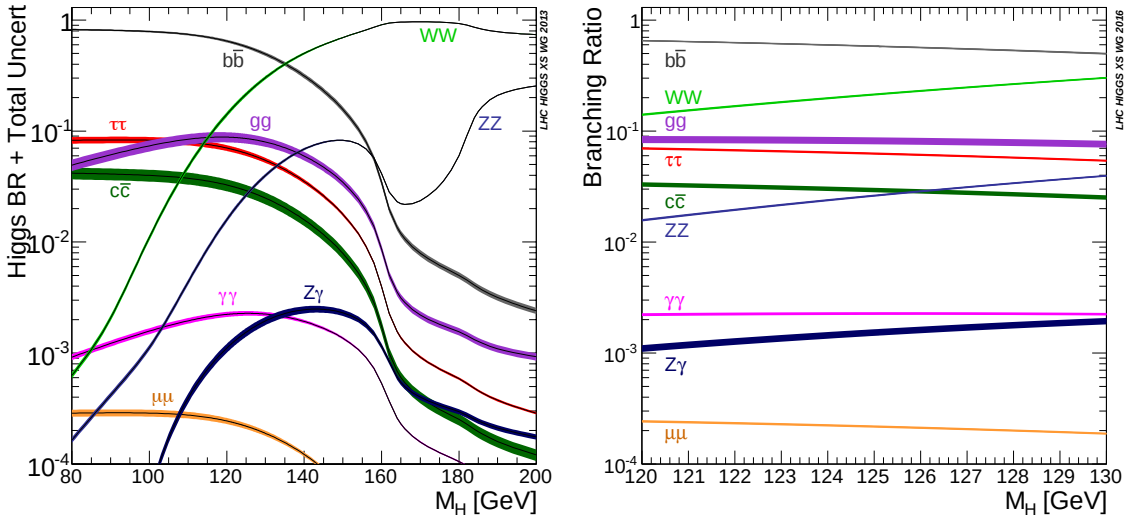


Figure 1.5: Higgs decay branching ratios as a function of the Higgs mass $m_h$, in GeV (see text for details). **Left:** As the mass of the Higgs boson varies in the range $[80, 200]$ GeV, the phase space available for its decays gets enhanced or reduced, which allows or restricts the preferred tree-level and loop-induced decays into the heaviest particles and massless gauge bosons, respectively. **Right:** *Idem* left panel, but in the range $m_h \pm 5\,\text{GeV}$, with $m_h = 125\,\text{GeV}$. The bands correspond to theory uncertainties. Both figures taken from Ref. [46].

- **Loop-induced:** Massless gauge bosons ($g$ and $\gamma$) do not couple to the Higgs field directly. However, the $h \to gg$ decay is mediated by quark loops, whereas the $h \to \gamma\gamma$ and $h \to Z\gamma$ channels are mediated by $W$-boson and charged-fermion loops.

The partial width $\Gamma_{h\to ab}$ of the Higgs decaying to a pair of particles $a,b$ and its total decay width $\Gamma_h$ are used to define the dimensionless quantity called *branching ratio*,

$$\text{BR}(h \to ab) = \frac{\Gamma_{h\to ab}}{\Gamma_h}, \tag{1.2.1}$$

which is a useful parameter to determine the fraction of Higgs decays to a given final state; Fig. 1.5 shows the branching ratios as a function of $m_h$. The ATLAS and CMS experiments at CERN have carried out direct searches of the decay modes $h \to b\bar{b}$ [62, 63], $h \to c\bar{c}$ [64, 65], $h \to \tau^+\tau^-$ [66, 67], $h \to \mu^+\mu^-$ [68, 69], $h \to WW^*$ [59, 70], $h \to$ invisibles [71, 72], $h \to \ell^+\ell^-\gamma$ [73, 74], as well as the *silver mode* $h \to \gamma\gamma$ [75, 76], and finally the *golden channel* $h \to ZZ^* \to 2\ell 2\ell'$ [77, 78]. Despite their low rates, as shown in Fig. 1.5, the clean final-state signatures of

the *silver* and *golden* channels allow us to extract *signal* events from *background* processes[16] in a narrow window around the nominal Higgs mass. Thus, these are the modes preferred by experiments to carry out precision measurements of Higgs properties, such as $m_h$ and $\Gamma_h$ [47–49].

Experimental searches have been useful to either observe certain decay modes, or set bounds on the rate at which others occur. As explained before, the *silver mode* along with the *golden channel* were the ones used to claim the discovery of a Higgs-like boson in 2012 by the ATLAS and CMS experiments at CERN. In Chapter 4 of this work we will explore the *golden channel* in the *ggh* production mode at the LHC, and Chapter 5 aims to study the *Zh* and *ZBF* single-Higgs production channels at high-energy $e^+e^-$ colliders.

## 1.3 Shortcomings of the Standard Model

Despite its several and accurate predictions, the SM fails to describe pressing issues which will be outlined below; thus it is often seen as an incomplete theory: many questions remain unanswered that a fundamental theory of Nature should try to address. Some deep questions that need to be answered are,

- **Electric charge.** In the SM we often deal with the electric charge as the coupling constant in processes involving charged fermions and photons. In the case of quarks, why the up (down) quark charge is exactly $e/3$ ($2e/3$)?

- **Patterns.** The number *three* seems to constantly appear in the SM. For instance, to date we are aware of the existence of three families for quarks and leptons. In the case of quarks, electric charges are quantised by a third, and the number of colours equals three. Is there a specific reason for this, or is it a happy accident of Nature?

[16] See Chapter 3 for more details.

- **Symmetries.** Why does Nature demand that the gauge group of the SM $G_{\text{SM}}$ follows the gauge symmetry of Eq. (1.1.1)?

- **Free parameters.** As a theory capable of predicting phenomena, the SM is built upon many parameters that do not seem to have theoretical predictions, but need to be measured by experiments, such as the Higgs self-coupling. Can we build a theory powerful enough to predict the values of the "free" parameters of the SM which can be later on confirmed by experiments?

The SM further fails to account for a set of observed phenomena that are not predicted by the theory and need to be explained,

- **Neutrino masses.** In the SM, the particle spectrum contains three massless left-handed neutrinos. However, there is clear experimental evidence to claim that neutrinos are actually not massless, contrary to the SM predictions. The quantum-mechanical effect of neutrino oscillation [79, 80], parametrised by the *Pontecorvo–Maki–Nakagawa–Sakata* (PMNS) matrix [81, 82], has been observed [83–86] and requires neutrinos to be massive [87, 88]. However, we are unaware of their absolute masses. Moreover, the *Dirac* or *Majorana* nature of these fermions remains elusive [89]. The most popular SM extension to give masses to neutrinos is the so-called *seesaw mechanism* [90], in which a massive right-handed neutrino is added to the particle content of the SM.

- **Dark matter.** Our available evidence to claim for the existence of *dark matter* (DM) is supported and based on gravitational effects, and cannot be accounted for only by the observed luminous matter. Observations of the Coma cluster in 1933 by Fritz Zwicky [91] suggested that some galaxies were moving faster than predicted by Newtonian mechanics. Vera Rubin's studies in 1970 of rotation curves of spiral galaxies showed that there was a slow decrease with the galactic radius [92], providing hints for the existence of a new mass component. Lensing, large-scale structure, and anisotropies in the *Cosmic Microwave Background*

(CMB) contain data that support the existence of DM [93]. Results from the *Cosmic Background Explorer* (COBE) satellite [94] and the *Wilkinson Microwave Anisotropy Probe* (WMAP) [95] have shown that our Universe is highly dominated by a large amount of DM and dark energy (see next bullet point *Dark energy*). The *Planck* mission [96], as a dedicated search for the precision measurement of cosmological parameters, has determined the relation between the power spectrum of the CMB and the amount of matter in the Universe, concluding that DM is responsible for approximately 26% of the energy density of the Universe. Today's issue is to detect and characterise the nature of DM [97, 98] from cosmology [99, 100], or indrectly from collider experiments [101].

- **Dark energy**. From the *Dark matter* bullet point above, the *Planck* mission concluded that *dark energy* (DE) constitutes about 68% of the energy density in our Universe. An unknown form of energy, DE is supposed to be responsible for the accelerated expansion of the Universe [102].

- **Gravity.** The most evident missing piece in the SM is a particle-like description of gravity [103, 104]. To date, the best description of gravitational phenomena we have is Albert Einstein's Theory of General Relativity (GR). *String theory* [105] and *loop quantum gravity* [106] are the most popular attempts to either unify gravity with the other fundamental interactions, or quantise the gravitational field away from the other interactions, respectively.

- **Baryon asymmetry.** There is an observable difference between the baryonic and anti-baryonic matter in our Universe. In 1979, Andrei Sakharov[17] showed that there are certain rules to be fulfilled in order to achieve the aforementioned asymmetry [107], namely baryon number violation, $C$-symmetry and $CP$-symmetry violation, and phase out of thermal equilibrium. The amount

[17] The *father of the Soviet hydrogen bomb* was awarded the Nobel Peace Prize in 1975 "for his struggle for human rights in the Soviet Union, for disarmament and cooperation between all nations".

of baryon asymmetry in the Universe cannot be explained in the SM, even though *CP*-violation is present.

One more issue to be addressed is related to the Higgs boson and its mass, which receives radiative corrections due to quantum effects, known as the *fine-tuning problem*. As $m_h$ is well separated from the Planck scale $M_P \sim 10^{19}\,\text{GeV}$, there seems to be some kind of interplay between the *fine-tuning* of the Higgs mass and $M_P$. This is known as the *hierarchy problem* [108], and deserves a special mention...

### 1.3.1 The hierarchy problem

The mass of the Higgs boson receives quantum corrections, illustrated in Fig. 1.6, that can be large unless there is something that protects it from a divergent behaviour. Quantum contributions give rise to corrections of the form,

$$\delta m_h^2 \equiv m_h^2 - \left(m_h^0\right)^2 \propto \Lambda_{\text{NP}}^2 \left[6\lambda + \frac{1}{4}\left(9g^2 + 3g'^2\right) - y_t^2\right], \tag{1.3.1}$$

where $m_h^0$ is the Higgs bare mass, and $\Lambda_{\text{NP}}$ the cut-off scale of the momentum running in the loops. From Eqs. (1.1.29), (1.1.32), and (1.1.35), it is possible to see that corrections to the Higgs mass squared are proportional to the square masses of the particles running in the loops. If there exist new heavier states that couple directly to the Higgs boson, their contributions to the Higgs mass squared are proportional to the square mass of these states,

$$\delta m_h^2 \propto \lambda_{h\vartheta} m_\vartheta^2, \tag{1.3.2}$$

where we have assumed the existence of a new scalar $\vartheta$ with mass $m_\vartheta \gg m_h$ and coupling strength to the Higgs $\lambda_{h\vartheta}$. In both cases, if $\delta m_h^2 \gg m_h^2$ then there must be a large cancellation taking place so that we recover the experimentally measured $m_h \sim 125\,\text{GeV}$. Since in the SM $\delta m_h^2 < m_h^2$, then $m_h$ is protected from fine-tuning. However, when new heavy states that couple to the Higgs in some way are introduced,

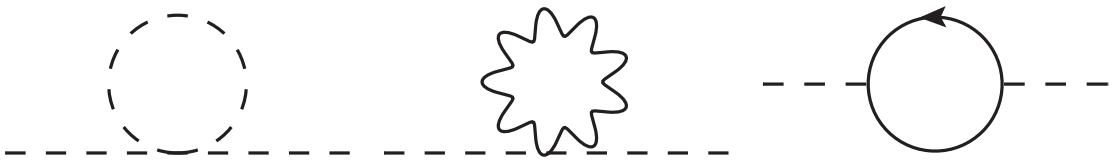

Figure 1.6: Feynman diagrams illustrating the one-loop contributions associated to the quantum corrections received by the Higgs mass squared. From left to right, the scalar, gauge, and fermion diagrams are shown.

then the issue of the Higgs mass receiving large corrections appears. In other words, *why is the Higgs boson so light?*

All of these problems are clear evidence of the need for new physics above the EW scale that address these issues, motivating the need to extend the SM somehow. These extensions are commonly referred to as *physics beyond the SM* (BSM), and some ideas will be outlined next.

## 1.4 Going beyond the Standard Model

Solving the issues outlined in Sec. 1.3 is not an easy thing to do. As we have seen before, the SM is a theory valid at the EW scale; however, it cannot be extrapolated to arbitrarily high energies since gravitational effects might become relevant above $M_P$, and QED develops a Landau pole[18] at an energy scale $Q \sim 10^{286}\,\text{eV}$ [4]. So, if we want to come up with a theory valid up to very high energies, such as $M_P$, that not only answers our questions but is also able to make accurate and testable predictions, we would want its low-energy behaviour to reproduce the SM[19]. In this sense, the SM is an *effective theory*, *i.e.*, the low-energy approximation, valid up to a finite energy scale $\Lambda_{\text{NP}}$, of a fundamental theory; to date we can estimate that $\Lambda_{\text{NP}}$ must be $\mathcal{O}(\text{TeV})$.

One of the goals of the high-energy and high-luminosity runs of the LHC will be

[18] Energy scale at which perturbation theory breaks down due to a coupling constant becoming infinite.

[19] For example, one can think of Newtonian mechanics as the low-energy approximation of Special Relativity.

to discover new physics at energies higher than the EW scale, or to observe those particles that have so far escaped detection. The extended particle spectrum of the SM is known as a *simplified model*— contrary to ultraviolet-complete (UV) models, simplified models contain just a few new particles and interactions described by Lagrangians that respect the symmetries of the SM, providing robust tools to interpret data collected at colliders that can be later matched to UV models. Hence, simplified models can be seen as effective theories of UV models, but that have extended the particle spectrum of the SM.

The common feature of many simplified-model extensions of the SM is the existence of new heavy fields, the so-called *bottom-up approach*. On the other hand, a *top-down approach* studies specific, complex UV models and its implications on the low-energy phenomenology. Although the study of BSM extensions of the SM from a simplified-model perspective is beyond the scope of this Thesis, we outline below some of these for illustration purposes,

- **Supersymmetry** (SUSY) introduces a wider particle spectrum mapping bosons into fermions, and vice versa, cancelling some divergences of the quantum corrections affecting the Higgs mass [109–112]. However, experimental bounds do not seem to favour the minimal SUSY extensions of the SM [113, 114]. For more information, see Refs. [115–119].

- **Grand Unification Theories** (GUT) attempt to encode the description of fundamental particles and their interactions into a single theoretical framework based on the guiding principle of gauge symmetry. Analogous to the EW unification, its major goal is to unify the strong and the EW interactions into a single force at high energies [120–128].

- **Extra dimensions** introduce additional gauge fields that can interact with the Higgs, controlling the quadratic divergences of its mass [129, 130].

- **Vector-like quarks** (VLQ) are hypothetical, massive quarks, whose left- and right-handed projections belong to the same representation of the SM gauge

group. In the SM, the charged-current Lagrangian involving chiral fermions has a *vector−axial* $(V-A)$ structure in Eq. (1.1.37), while for VLQ has only a $V$ component [131–141].

- **Little Higgs** models extend the gauge group of the SM to naturally accommodate a light Higgs boson, with vector-like fermionic partners cancelling the quadratic divergences of the Higgs mass [142–147].

- **Composite Higgs** is aimed at describing the Higgs as a bound state, and not as a fundamental particle [148–155]. It is analogous to the case of the pion ($\pi$) in QCD: it went from a fundamental scalar to a bound state of quarks [156].

- **Two-Higgs-Doublet Models** (2HDM) incorporate two copies of the SM doublet $\Phi_1$ and $\Phi_2$, at least one of which carry a non-zero *vev* [157–162]. These models contain five physical states after EWSB: two *CP*-even neutral scalars $h$ and $H$ ($m_H > m_h$), two charged Higgsses $H^{\pm}$, and a *CP*-odd pseudoscalar $A$. One can also come across with models postulating three Higgs doublets [163, 164].

A common feature of the models outlined above is that the Higgs boson and the rest of the SM particles are conjectured to be part of a wider spectrum. We must, however, measure precisely the properties of the SM Higgs— *what if the particle discovered in 2012 is nothing but an additional scalar which happens to resemble the SM Higgs?* Precision measurements must be carried out in the Higgs sector to determine its coupling strengths to gauge bosons and fermions, since any variation from the SM expectations might be a hint for new physics.

In the context of the *bottom-up approach* employed by simplified-model studies, we can extend the SM starting with its Lagrangian and adding more terms constructed out of SM fields,

$$\mathcal{L}_{\text{EFT}} = \mathcal{L}_{\text{SM}} + \sum_i \frac{c_i^{(D)}}{\Lambda_{\text{NP}}^{D-4}} \mathcal{O}_i^{(D)}, \tag{1.4.1}$$

where $\Lambda_{\rm NP}$ is the scale of new physics we had previously introduced, and $c_i^{(D)}$ are the dimensionless *Wilson coefficients* of the perturbative expansion standing for the coupling strength of each dimension-$D$ ($D > 4$) operator $\mathcal{O}_i^{(D)}$. Each term $\mathcal{O}_i^{(D)}/\Lambda_{\rm NP}^{D-4}$ must be consistent with the mass-dimension four of the SM Lagrangian. Eq. (1.4.1) corresponds to the effective theory description [165–167] associated with the SM. The Wilson coefficients encode the high-energy behaviour of new physics and need to be measured, whereas the operators parametrise the long-distance physics. Contrary to the simplified-model approach, this way of encapsulating the low-energy effects of an unknown UV theory does not require additional degrees of freedom, and one only has to deal with new higher-dimensional Lorentz structures arising from the dimension-four SM operators. It is then within the framework of effective theories that the following Chapters are devoted to study the variations of the Higgs couplings to $Z$-bosons at the LHC, as well as showing how these can be probed at future linear $e^+e^-$ colliders.

# Chapter 2

# Effective Field Theory

In Chapter 1 we introduced some of the basic elements that construct the best theoretical framework we have to date to describe the interactions between the building blocks of the Universe, the Standard Model of Particle Physics. Its predictions have been put to the test several times throughout the years, and it has been found that the results agree well with a plethora of measurements. Nevertheless, the Standard Model fails at explaining several physical phenomena, which is an evidence of the need for a more powerful theory that is able to include suitable candidates that provide an answer to the questions raised by the experimental data. In coming up with a robust theory, one should bear in mind that the Standard Model remains a framework with powerful predictive power up to the electroweak scale.

There are many competing theories available on the market[1] that extend the particle spectrum of the Standard Model in the so-called *simplified-model* approach. These contain just a few new particles and interactions described by Lagrangians that respect the symmetries of the Standard Model, which could be later matched to UV-complete models. If it exists, the ultimate theory of Nature should reproduce in its low-energy limit the accurate predictions of the Standard Model. In this sense, not only the Standard Model but simplified models, too, are *effective theories*, valid up to a finite energy scale $\Lambda_{\mathrm{NP}}$, of a fundamental theory.

[1] For a non-exhaustive list, see Sec. 1.4 of this Thesis.

We can estimate that $\Lambda_{\rm NP}$ must be $\mathcal{O}$(TeV). As explained in Chapter 3, the energy reach of the Large Hadron Collider limits its potential to perform direct searches for physics beyond the Standard Model above a few TeV. Although currently there are plans to build more powerful colliders able to reach higher centre-of-mass energies, these would take several years from now to begin collecting data. Since direct production of new physics has remained elusive, and we are unaware of what is the value of $\Lambda_{\rm NP}$, then indirect searches and precision measurements are the best alternative to look for potential deviations from the theory predictions that carry the imprint of said new physics[2].

In looking for deviations from the Standard Model expectations, we need to find a way to parametrise our lack of knowledge on the type of interactions that would induce such measurable and testable deviations. One option is to extend the Standard Model starting with its Lagrangian and adding more terms constructed out of its particle content. This new set of operators of higher mass dimension that respects the underlying symmetries of the theory encapsulates the low-energy effects of an unknown UV-complete model. Thus, additional higher-dimensional Lorentz structures and modified vertices encode the effects of physics beyond the Standard Model in an effective-theory fashion, without the need to worry about additional degrees of freedom and their interactions with the fields known to date.

In this Chapter we give a brief description of the Effective Field Theory framework and its interplay with the Standard Model of Particle Physics. Using Fermi's theory of muon decay, we motivate the need to study the Standard Model as an Effective Field Theory. Further, we introduce some key concepts needed to get to grips with the notion of parametrising unknown high-energy physics through its low-energy manifestations. The following description of the basic elements building up the Standard Model as an Effective Field Theory is inspired by comprehensive texts like Refs. [168–184].

[2]In Chapter 3 we describe some key aspects of direct and indirect searches for new physics at colliders.

## 2.1 Warmup: basic idea

Let us begin with the following statement: *in studying a physical system, one does so from a distance for sake of simplicity.* In other words, when tackling a physics problem we only care about the relevant degrees of freedom. Let us take the case of an undergraduate student who is being taught about geometrical optics. For the student to understand Fermat's principle, it is not necessary to know the short-distance behaviour of light-matter interactions, nor the long-distance physics governing the laws of electric dipole radiation. However, a more experienced student would argue that an expensive experiment might be sensitive to polarisation effects, and so more calculations would be needed to account for any discrepancies between the theory prediction and the experimental outcome. Putting it differently, we are free to choose the physics needed to describe a system to the desired precision.

There is physics that is far away, in some sense, from the physics that one might be interested in. In such case, then the far-away physics can be removed from the theory when you are not talking about it, *i.e.*, the high- and low-energy degrees of freedom can be decoupled from each other. This is precisely the purpose of an effective theory: *to describe the physics at some scale $\lambda$, we do not need to know the detailed dynamics of what is going on at $\Lambda \gg \lambda$* (or $\lambda \gg \Lambda$). Nevertheless, given a full theory that describes a physical phenomenon, the subdominant effects can be computed to correct the leading-order approximation[3]. From an Effective Field Theory (EFT) perspective, one can say that high-energy effects show up as small modifications to low-energy interactions when studying a physical system in the long-distance regime, where a short-distance description is not needed.

As explained in Chapter 1, we know that the SM is not a complete theory of Nature, and so we expect new resonant physics to appear at a yet unknown energy scale $\Lambda_{\rm NP}$. The EFT framework provides us with a powerful toolkit that allows us to construct

[3]For example, consider the relativistic corrections $\mathcal{O}\left(v^2/c^2\right)$ to Newton's second law of motion, which are subdominant for $v \ll c$.

an effective description of the particle world, taking the SM as an IR-complete theory, while remaining agnostic about the fundamental UV theory that lies beyond $\Lambda_{\rm NP}$. Conversely, if we know what is the high-energy theory and want to look at certain low-energy phenomena, the EFT structure is useful when calculations are somewhat nasty in the IR. In short, effective theories are useful to "parametrise our ignorance" [168] of the physics at some energy, far away from the scale that we are probing, in terms of free parameters contained in the EFT Lagrangian.

Let us consider the Lagrangian of a UV-complete theory $\mathcal{L}_{\rm UV}(\phi, \Phi)$, where $\phi$ is a field of mass $m$, $\Phi$ is a field of mass $M \gg m$, and these are allowed to interact with each other. Since the dynamics of said system are encoded in $\mathcal{L}_{\rm UV}$, one can make computations of processes involving these two fields at an energy scale $E \geq M$, where the kinematic threshold allows $\Phi$ to be produced on-shell. But what happens if we are interested in calculating the cross-section of certain modes at $E \sim m$, *i.e.*, with only $\phi$'s in the external states and $\Phi$ being too massive for its resonant production? To simplify calculations in the latter case, using the path-integral formulation of QFT [1] we can 'integrate out' $\Phi$ from $\mathcal{L}_{\rm UV}$, obtaining an effective theory describing a system with $\phi$'s only. To do this, we must use the partition function $Z_{\rm UV}$ of the UV-complete theory,

$$Z_{\rm UV}\left[j_\phi, j_\Phi\right] = \int \mathcal{D}\phi\mathcal{D}\Phi \exp\left\{i \int \mathrm{d}^4x \left[\mathcal{L}_{\rm UV}(\phi, \Phi) + j_\phi\phi + j_\Phi\Phi\right]\right\}, \tag{2.1.1}$$

which, differentiated with respect to the currents $j_i$ ($i = \{\phi, \Phi\}$), gives the $n$-point correlation functions of $\phi$'s and $\Phi$'s. In the equation above, $\int \mathcal{D}\phi\mathcal{D}\Phi$ denotes a functional integral over all fields $\phi$ and $\Phi$ present in the Lagrangian of the theory. Integrating over the field configurations $\mathcal{D}\Phi$, the partition function $Z_{\rm EFT}$ of the effective theory is,

$$Z_{\rm EFT}\left[j_\phi\right] = \int \mathcal{D}\phi \exp\left\{i \int \mathrm{d}^4x \left[\mathcal{L}_{\rm EFT}(\phi) + j_\phi\phi\right]\right\}, \tag{2.1.2}$$

where $\mathcal{L}_{\rm EFT}(\phi)$ corresponds to the Lagrangian of the effective theory that does not know anything about $\Phi$. Thus, one might be tempted to claim that we would only

need to require,

$$Z_{\rm EFT}\left[j_\phi\right] = Z_{\rm UV}\left[j_\phi, 0\right]. \tag{2.1.3}$$

However, $\mathcal{L}_{\rm EFT}(\phi) \neq \mathcal{L}_{\rm UV}(\phi, 0)$ in general[4], and simply setting $j_\Phi = 0$ means that $\Phi$'s are never external, but these can appear as internal propagators. In the low-energy regime $E \sim m \ll M$ the exchange of $\Phi$'s looks like an interaction between $\phi$'s only [184]. If the momentum transfer carried by $\Phi$ is $p \ll M$, then the propagator can be expanded as,

$$\frac{1}{p^2 - M^2} = -\frac{1}{M^2}\left(1 - \frac{p^2}{M^2}\right)^{-1} \approx -\frac{1}{M^2} + \frac{p^2}{M^4} - \dots \tag{2.1.4}$$

and one can see that higher-order corrections are suppressed in the low-momentum limit due to the appearance of the heavy mass scale in the denominator of the expansion. Since $\Phi$ is too massive to be produced on-shell, we are blind to the physics involving said field. In integrating out the heavy fields, one should bear in mind that although $\mathcal{L}_{\rm UV}$ and $\mathcal{L}_{\rm EFT}$ differ in the UV, their predictions must agree in the IR and in their overlap region.

Following Ref. [185], let us wrap things up by considering the Lagrangian $\mathcal{L}(\phi, \psi, \Phi)$ of a model consisting of a heavy field $\Phi$, and light fields $\phi$ and $\psi$,

$$\mathcal{L}(\phi, \psi, \Phi) = \mathcal{L}_{\rm H}(\phi, \psi, \Phi) + \mathcal{L}_{\rm L}(\phi, \psi), \tag{2.1.5}$$

with $M_\Phi \gg m_{\phi,\psi}$. Note that we have split $\mathcal{L}(\phi, \psi, \Phi)$ into its "heavy" and "light" interactions. We now use the path integral to integrate out the heavy field $\Phi$ as,

$$\int \mathcal{D}\Phi \exp\left[i \int \mathrm{d}^4x \mathcal{L}(\phi, \psi, \Phi)\right] = \exp\left[i \int \mathrm{d}^4x \mathcal{L}_{\rm EFT}(\phi, \psi)\right], \tag{2.1.6}$$

where $\mathcal{L}_{\rm EFT}(\phi, \psi)$ corresponds to the effective Lagrangian,

$$\mathcal{L}_{\rm EFT}(\phi, \psi) = \mathcal{L}_{\rm L}(\phi, \psi) + \Delta\mathcal{L}(\phi, \psi). \tag{2.1.7}$$

The corrections $\Delta\mathcal{L}(\phi, \psi)$ consist of a tower of higher-dimensional operators constructed out of the fields contained in $\mathcal{L}_{\rm EFT}(\phi, \psi)$, and correspond to an infinite

[4] This could be the case if the fields $\phi$ and $\Phi$ were completely decoupled from each other.

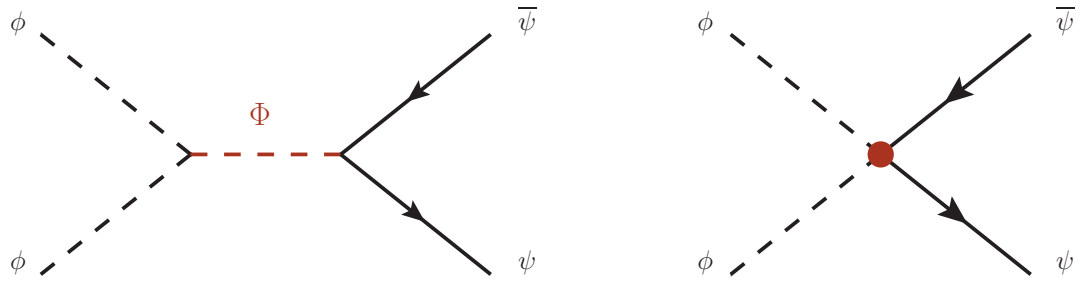


Figure 2.1: Feynman diagrams illustrating the interactions described in the **left:** full theory, and **right:** effective theory. At energy scales $\Lambda \ll M_\Phi$, the propagator looks like a contact interaction between light fields. These diagrams are meant for illustration purposes only.

series in decreasing relevance of whatever expansion we are doing,

$$\Delta\mathcal{L}(\phi,\psi) = \sum_i \frac{c_i^{(D)}}{\Lambda_{\rm NP}^{D-4}}\mathcal{O}_i^{(D)}, \tag{2.1.8}$$

with the desired precision telling us where to truncate the series[5]. The $c_i^{(D)}$ are the dimensionless *Wilson coefficients*, which stand for the coupling strength of each dimension-$D$ ($D > 4$) operator $\mathcal{O}_i^{(D)}$ [167]. The infinite series is constructed out of the most general possible interactions consistent with the symmetries that we are imposing [174]. Although the Wilson coefficients are unknown, it is possible to fit them to experimental data. In Fig. 2.1 we illustrate the idea of integrating out the heavy field $\Phi$ from the theory to recover a contact interaction between the remaining degrees of freedom $\phi$ and $\psi$.

Heavy particles might show up if we probe those energies directly. However, in the EFT we are probing the physics at low energy, and the way that the high-energy degrees of freedom would show up is by a contribution to one of the $\mathcal{O}_i^{(D)}$ operators. Suppose we added a new particle with mass $M = 20\,\text{TeV}$. If we perform an expansion $p/M$ as in Eq. (2.1.4), then what happens is that we get an operator $\mathcal{O}$ where that particle has been removed. Its mass will show up in the denominator of the expansion as $\Lambda_{\rm NP}$ (which can be thought of as the propagator). New particles do not show up in the operator, but affect the prefactors $c_i^{(D)}/\Lambda_{\rm NP}^{D-4}$ in Eq. (2.1.8). In this sense,

[5]Note that the effective theory is only valid below $\Lambda_{\rm NP}$, as beyond this scale the EFT is no longer predictive.

the Wilson coefficients encode the high-energy behaviour of new physics, and the operators parametrise the long-distance physics by inducing a new set of vertices and interactions, the so-called *anomalous couplings*.

## 2.2 Power counting

From Eq. (2.1.8), one can see that the EFT Lagrangian $\mathcal{L}_{\text{EFT}}$ is constructed out of a large number of dimension-$D$ operators $\mathcal{O}_i^{(D)}$ entailing new interactions not included in the original theory. It is also possible to notice that the higher the mass dimension the bigger the suppression factor owed to the expansion parameter,

$$\eta = \left(\frac{1}{\Lambda_{\text{NP}}}\right)^{D-4} \tag{2.2.1}$$

of the infinite series. To see this, consider computing an amplitude where we insert an arbitrary higher-dimensional operator $\mathcal{O}^{(D)}$, and assume that we want to probe such an interaction at an energy $E \ll \Lambda_{\text{NP}}$. Said amplitude scales roughly as,

$$\mathcal{A} \sim \left(\frac{E}{\Lambda_{\text{NP}}}\right)^{D-4}, \tag{2.2.2}$$

and it is clear that, depending on the desired accuracy, it is possible to neglect consistently the contributions of order larger than the chosen $D$ in $\eta$ [178]. Thus, truncating the series in Eq. (2.1.8) at the desired dimension $D$ gives a finite set of terms, from where observables can then be expanded in powers of $E/\Lambda_{\text{NP}}$ [179].

In practice, the operators $\mathcal{O}_i^{(D)}$ are constructed out of the SM scalar $\Phi$, fermion $\psi$, and gauge $V_\mu$ fields, and the dimension $D$ is determined from the field content of $\mathcal{O}$. Since the action,

$$S = \int \mathrm{d}^4x \mathcal{L}, \tag{2.2.3}$$

is a dimensionless quantity[6], it is possible to apply reverse engineering to work out

[6] In natural units, $\hbar = c = 1$.

the mass dimension of each SM field by looking into its Lagrangian,

$$\mathcal{L}_{\rm SM} = -\frac{1}{4}F^a_{\mu\nu}F^{a,\mu\nu} + i\overline{\psi}\gamma^\mu D_\mu\psi + \left|D_\mu\Phi\right|^2 - V(\Phi) - \mathcal{Y}^{ij}_\psi\overline{\psi}_i\Phi\psi_j + \text{h.c.}, \tag{2.2.4}$$

introduced in Chapter 1. From Eq. (2.2.3), one can notice that,

$$[x] = -1 \Rightarrow \begin{cases} \left[\partial_\mu\right] = 1 \\ \left[\mathcal{L}_{\rm SM}\right] = 4 \end{cases} \tag{2.2.5}$$

Since $F_{\mu\nu} = \partial_\mu V_\nu - \partial_\nu V_\mu$,

$$\left[D_\mu\right] = 1, \quad \left[F_{\mu\nu}\right] = 2. \tag{2.2.6}$$

Thus,

$$[\Phi] = 1, \quad [\psi] = \frac{3}{2}, \quad \left[V_\mu\right] = 1. \tag{2.2.7}$$

Once we know what is the mass dimension of each field in $\mathcal{L}_{\rm SM}$, it is possible to write down the most generic structure of an operator $\mathcal{O}$. Following the convention adopted in Ref. [183],

$$\mathcal{O} = \left(\overline{\psi}\psi\right)^{N_\psi}\left(F_{\mu\nu}\right)^{N_F}\left(D_\mu\right)^{N_D}(\Phi)^{N_\Phi} \Rightarrow [\mathcal{O}] = 3N_\psi + 2N_F + N_D + N_\Phi, \tag{2.2.8}$$

where the exponents $N_{\rm object}$ correspond to the number of insertions of said object in the operator under consideration. One can notice that the coefficients on the right-hand side of the expression above correspond to the mass dimension of the (composite) structures $\overline{\psi}\psi$, $F_{\mu\nu}$, $D_\mu$, and $\Phi$.

Let us now look at an example in a scalar field theory to illustrate another important concept, following Refs. [174, 184]. Consider the action,

$$S(\phi) = \int \mathrm{d}^4x \left[\frac{1}{2}\left(\partial_\mu\phi\right)^2 - \frac{1}{2}m^2\phi^2 - \frac{\lambda}{4!}\phi^4 - \frac{\tau}{6!}\phi^6\right], \tag{2.2.9}$$

What we want to do here is to understand how each term in the equation above behaves when we rescale the space-time coordinates as,

$$x_\mu \to \zeta x'_\mu. \tag{2.2.10}$$

The limits $\zeta \to 0$ and $\zeta \to \infty$ correspond to the high- and low-energy ends of the theory[7], respectively. Changing the coordinates and normalising the kinetic term by rescaling $\phi \to \phi'\zeta^{-1}$ yields,

$$S'\left(\phi'\right) = \int \mathrm{d}^4x' \left[\frac{1}{2}\left(\partial_\mu\phi'\right)^2 - \frac{1}{2}m^2\zeta^2\phi'^2 - \frac{\lambda}{4!}\phi'^4 - \frac{\tau}{6!\zeta^2}\phi'^6\right], \tag{2.2.11}$$

such that the kinetic term dominates the action integral. Now, let us compare Eq. (2.2.9) and Eq. (2.2.11) by taking the low-energy limit $\zeta \to \infty$ of the latter. Depending on their behaviour, each term in Eq. (2.2.11) can be categorised [165,166] as,

- **Relevant.** As we approach the IR, these terms become more and more important, as is the case of the mass term.
- **Marginal.** No matter if we are in the IR or the UV, these terms are equally important as they were before, such as the $\phi'^4$ term.
- **Irrelevant.** The more we go to larger distances, the more suppressed the effects of these operators are, for which $\phi'^6$ is an example.

We can as well relate the mass dimension $D$ of each operator and the space-time dimension $d = 4$ of the action integral with the categories above. Notice that,

- $\phi^2$: $D = 2 < 4$, *relevant*.
- $\phi^4$: $D = 4$, *marginal*.
- $\phi^6$: $D = 6 > 4$, *irrelevant*.

These imply that, for finite (large) $\zeta$, the dimension of the operators tells us their importance. With these ideas in mind, it becomes more evident that the expansion parameter $\eta$ in Eq. (2.2.1) plays an important role to determine at which dimension

[7] The rescaling $x \to 0\,(\infty)$ zooms in (out) to smaller (larger) distances, hence probing higher (lower) energies.

$D$ should we truncate the series in Eq. (2.1.8) and neglect higher-order corrections. From Eq. (2.2.2),

$$\mathcal{A} \sim \left(\frac{E}{\Lambda_{\text{NP}}}\right)^{D-4},$$

we can see that as $E$ approaches $\Lambda_{\text{NP}}$, the terms neglected in the series become more relevant [183]. With the EFT looking towards the IR of the underlying theory [174], we find yet another reason to have a cut-off scale $\Lambda_{\text{NP}}$ for the effective theory.

## 2.3 Top-down & bottom-up

As mentioned previously, the EFT framework allows us to separate the energy scales relevant to the study of a physical phenomenon from those that are not necessary for an adequate description of the system under consideration. If one is able to write the Lagrangian of a theory in the form of Eq. (2.1.5), then the UV is said to be *decoupled* from the lower energies of the spectrum [186]. In the low-energy effective theory, the possible effects induced by heavy fields of mass $M$ impact the values of the couplings, which can be probed by precision measurements, or are suppressed by factors of $1/M$ [174]. In this sense, at the UV one might want to simplify the known theory to compute observables where not all the degrees of freedom are relevant. Further, at the IR one can remain agnostic about the UV that lies beyond $\Lambda_{\text{NP}}$ and still use Eqs. (2.1.7) and (2.1.8) to perform calculations. These approaches to construct an effective theory are called *top-down* and *bottom-up*, respectively, and we will now have a quick look into these.

### 2.3.1 Fermi theory of muon decay

Let us illustrate the *top-down* approach at constructing an EFT by introducing Fermi's theory of muon decay, involving four-fermion contact interactions[8]. The

[8]Strictly speaking, Enrico Fermi used this type of interaction in a *bottom-up* fashion to explain the energy spectrum of $\beta$-decay in the early 1930's [187], when the $W$-boson had not been discovered yet, and a few years after Wolfgang Pauli proposed the existence of the neutrino. However, for

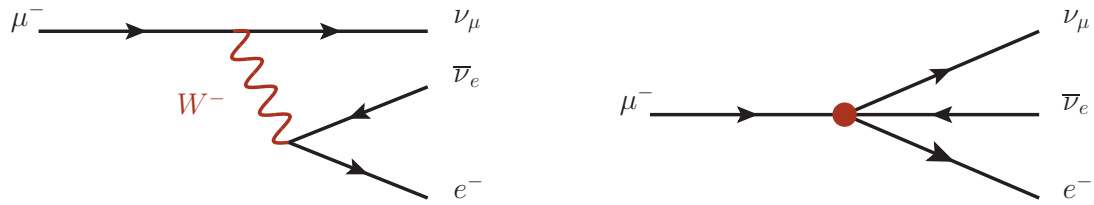


Figure 2.2: Leading-order Feynman diagrams illustrating the muon decay in the **left:** Standard Model, and **right:** Fermi effective theory. Note that the $W$-boson is present in the full theory, but is integrated out in the effective theory giving rise to a four-fermion contact interaction.

four-lepton vertex, shown in the right panel of Fig. 2.2, is described by,

$$\mathcal{L}_{\text{EFT}} \supset G_F \mathcal{O}_{\text{Fermi}} = \frac{G_F}{4} \left[\overline{\nu}_\mu \gamma^\alpha \left(1 - \gamma^5\right) \mu\right] \left[\overline{e} \gamma_\alpha \left(1 - \gamma^5\right) \nu_e\right] + \text{h.c.}, \tag{2.3.1}$$

where $G_F$ is the Fermi constant, and the lepton fields stand for their associated spinor. The low-energy weak interactions, well below the $W$-boson mass $m_W \sim 80\,\text{GeV}$ (see Table 1.1), are accurately described by these vertices since the mass scale $m_\mu \ll m_W$, and the propagator can be expanded as shown in Eq. (2.1.4). Further, $G_F$ absorbs the effect of the $W$-boson, which cannot be produced on-shell, and the high-energy physics are encoded in the leading order expansion containing the four-momenta of the low-energy degrees of freedom. Notice that $\mathcal{O}_{\text{Fermi}}$ in Eq. (2.3.1) is a dimension-six operator, following the power-counting rules shown in Eq. (2.2.8), which implies that $[G_F] = -2$.

Taking the SM as our starting point, we focus on the degrees of freedom relevant to describe the decay of the muon at leading order, as shown in the left panel of Fig. 2.2. The decay process,

$$\mu^- \to \nu_\mu e^- \overline{\nu}_e, \tag{2.3.2}$$

is mediated by the $W$-boson, and its interactions with leptons are given by the charged-current Lagrangian,

$$-\mathcal{L}_{\text{SM}} \supset \frac{g}{2\sqrt{2}} \left[W_\alpha \sum_{\ell=e,\mu} \overline{\nu}_\ell \gamma^\alpha \left(1 - \gamma^5\right) \ell + W_\alpha^\dagger \sum_{\ell=e,\mu} \overline{\ell} \gamma^\alpha \left(1 - \gamma^5\right) \nu_\ell\right], \tag{2.3.3}$$

illustrative purposes we can use the SM as a UV-complete theory, and the guiding principle applies to muon decay, too.

From Eq. (2.3.3) one can derive the amplitude for the tree-level process shown in Eq. (2.3.2), which in the Landau gauge reads,

$$i\mathcal{M}_{\rm SM} = \left(\frac{-ig}{2\sqrt{2}}\right)^2 \left[\overline{\nu}_\mu \gamma^\alpha \left(1-\gamma^5\right)\mu\right] \frac{-i\left(g_{\alpha\beta} - p_\alpha p_\beta/p^2\right)}{p^2 - m_W^2} \left[\overline{e}\gamma^\beta \left(1-\gamma^5\right)\nu_e\right], \quad (2.3.4)$$

with $p^\alpha$ the four-momentum transfer, which is limited by the three-body decay kinematics as,

$$0 \leq p^2 \leq m_\mu^2, \quad (2.3.5)$$

in the limit where the other leptons (electron and neutrinos) are massless. Since $m_\mu^2/m_W^2 \approx 1.73 \times 10^{-6}$, the $W$-boson can be safely integrated out, and the decay of the muon is thus approximated by the four-lepton interaction,

$$\mathcal{M}_{\rm SM} \approx -\frac{g^2}{8m_W^2} \left[\overline{\nu}_\mu \gamma^\alpha \left(1-\gamma^5\right)\mu\right] \left[\overline{e}\gamma_\alpha \left(1-\gamma^5\right)\nu_e\right] \left(1 + \mathcal{O}\left(\frac{p^2}{m_W^2}\right)\right), \quad (2.3.6)$$

which follows from the binomial expansion of the denominator in Eq. (2.3.4). Keeping $n$ terms in this expansion, the accuracy of the equation above with respect to the full theory goes like $\left(p^2/m_W^2\right)^n$. The amplitude in Eq. (2.3.6) does not develop a pole at $m_W$, and so one can construct an EFT that does not know anything about the interchange of a virtual $W$-boson. The EFT Lagrangian,

$$\mathcal{L}_{\rm EFT} \supset \frac{c}{4\Lambda^2} \left[\overline{\nu}_\mu \gamma^\alpha \left(1-\gamma^5\right)\mu\right] \left[\overline{e}\gamma_\alpha \left(1-\gamma^5\right)\nu_e\right] + \text{h.c.}, \quad (2.3.7)$$

reproduces the leading-order amplitude in Eq. (2.3.6) if,

$$\Lambda = m_W, \quad c = -\frac{g^2}{2}, \quad (2.3.8)$$

known as the *matching conditions*, which roughly speaking are the boundary conditions[9] such that the full Lagrangian in Eq. (2.1.5) describes the same physics as the effective Lagrangian in Eq. (2.1.7), just below the cut-off scale $\Lambda \sim m_W$. As long as the energy scale $E \ll m_W$, Eq. (2.3.7) describes all charged-current processes involving electrons, muons, and neutrinos [184], which is a valid approximation of the

[9] One can think of the matching conditions as the continuity conditions for $S$-matrix elements between the effective and full theories, which differ by their particle content, but must describe the same IR physics. See, e.g., Refs. [168, 169, 174, 176, 179] for more information on the subject.

EW process in the SM. In this sense, one can understand the effect of "integrating out" the propagator as contracting the $W$-boson to a point in the Feynman diagram (see Fig. 2.2). The effective coupling encapsulates the high-energy behaviour induced by the virtual propagator, now absent in the interaction vertex, and the dimension-six operator describes the long-distance physics[10].

From Eqs. (2.3.4) and (2.3.6), one can see that the expansion parameter $p^2/m_W^2 \ll 1$ suppresses all higher-order corrections to the amplitude, fixing $\Lambda_{\rm NP} \sim m_W$. As $p^2 \to m_W^2$, the perturbative expansion breaks down since more and more terms are needed to keep the predictive power of the effective theory under control. As long as one stays in the EFT validity regime, *i.e.*, $p^2 \ll m_W^2$, Eq. (2.3.7) can be used as an effective theory that gives good approximations of the full EW sector in the SM. Nevertheless, one should notice that the information concerning the massive propagator is not available to a large-distance observer, and so the validity scale of the EFT cannot be extracted only from large-distance measurements [184].

### 2.3.2 SMEFT

In the previous subsection we introduced the *top-down* approach to construct an EFT. Given a physical process at an energy scale $E$, pick your UV-complete theory and determine which heavy ($M \gg E$) degrees of freedom are not relevant to provide a low-energy description of said process. Once you identify these, integrate them out from the full theory to obtain the Lagrangian of your EFT, shrinking the massive propagators to point interactions. The amplitudes of the process under consideration can be written as a power series of the expansion parameter $(E/M)^{2n}$, where $n$ determines the number of terms included in the expansion, as well as the accuracy to which the effective amplitude will reproduce that of the full theory. Make sure that $E^2/M^2 \ll 1$ not to break the perturbative expansion as $E \to M$. And you're all set! But what happens if we do not know what the structure of the UV theory

[10] Notice that in the SM all the terms involved in the Lagrangian are dimension-four operators, except for the mass term of the scalar field which is a dimension-two operator.

looks like, and want to go to higher energies instead of larger distances?

As outlined in Chapter 1, we know that the SM is not the ultimate theory of Nature, despite its many accurate predictions. This motivates the need for a more powerful description of the short-distance physics that take place in our Universe well beyond $m_h$. Given that no new resonant physics has appeared at the LHC (apart from the Higgs boson in 2012), we can take the SM as our starting point and construct new operators out of its particle content to look for deviations from the SM expectations at experiments. This *bottom-up* approach helps us in constructing an EFT where the SM is the low-energy limit of an unknown UV-complete theory. Hence, looking into the IR theory we can set constraints on the Wilson coefficients that encode the short-distance physics of the higher-dimensional operators containing new tensor structures that can be probed at colliders.

Let us take Eqs. (2.1.7) and (2.1.8) to write our effective Lagrangian, barring Hermitian conjugation, as,

$$\mathcal{L}_{\rm EFT} = \mathcal{L}_{\rm SM} + \sum_i \frac{c_i^{(D)}}{\Lambda_{\rm NP}^{D-4}} \mathcal{O}_i^{(D)}, \tag{2.3.9}$$

where, as before, the $c_i^{(D)}$ are the dimensionless *Wilson coefficients*, which stand for the coupling strength of each dimension-$D$ ($D > 4$) operator $\mathcal{O}_i^{(D)}$ [167]; $\mathcal{L}_{\rm SM}$ is the dimension-four SM Lagrangian (see Chapter 1), and $\Lambda_{\rm NP}$ is the scale of NP. Notice that with each increasing ($D$), the corresponding $c_i^{(D)}$ are suppressed by increasing powers of $\Lambda_{\rm NP}^{D-4}$.

Remaining agnostic about the UV theory implies that we should make some minimal assumptions to construct the higher-dimensional operators, namely,

1. These are built out of all SM fields only.

2. Should respect the SM gauge symmetry $SU(3)_C \times SU(2)_L \times U(1)_Y$.

3. Need to be invariant under the Poincaré group.

Beyond the previous numbered assumptions, one can make some additional choices, such as a universal flavour structure of the fermion families. Further, one can choose EW symmetry to be linearly realised, *i.e.*, that the Higgs and the would-be Goldstones form a doublet charged under the EW gauge group (see Eq. (1.1.22)), the so-called *linear EFT* (SMEFT). The are other scenarios in which the $m = 125\,\text{GeV}$ scalar discovered in 2012 at the LHC is thought to be a singlet, *i.e.*, does not form a doublet with the Goldstones as in the SM, and as such are treated independently[11]. In the latter case, EW symmetry is said to be *non-linearly realised* [188], known as *non-linear Higgs EFT* (HEFT).

The first higher-dimensional correction to $\mathcal{L}_{\text{SM}}$ occurs at $D = 5$, which only consists of the so-called *Weinberg operator* [189],

$$\mathcal{O}^{(5)}_{\text{Weinberg}} = \left(\widetilde{\Phi}^\dagger L_\ell\right)^T i\gamma^2\gamma^0 \left(\widetilde{\Phi}^\dagger L_{\ell'}\right) + \text{h.c.}, \tag{2.3.10}$$

where $L$ is the lepton doublet, and $\Phi$ is the SM Higgs doublet (see Appendix A for an explanation on the notation). This operator violates lepton number, and generates a Majorana mass term for the neutrinos after EWSB. Since a mass term for the neutrinos is forbidden in the SM, adding this term to $\mathcal{L}_{\text{SM}}$ makes it compatible with the experimental evidence of neutrino oscillations. Further, it has been shown in Ref. [190] that operators of odd mass dimension cannot preserve simultaneously baryon and lepton number[12].

Let us consider next the set of dimension-six operators in the SMEFT, where the Wilson coefficients are suppressed by a factor of $1/\Lambda^2_{\text{NP}}$. These give the leading baryon- and lepton-number-conserving BSM contributions to $\mathcal{L}_{\text{EFT}}$ in Eq. (2.3.9). In 1985, W. Buchmüller and D. Wyler [167] derived a set of 80 said operators. However, in 2010, B. Grzadkowski, M. Iskrzyński, M. Misiak, and J. Rosiek, showed that some linear combinations of operators in Ref. [167] were redundant and van-

[11] This topic is beyond the scope of this Thesis, and we restrict to the linear realisation of EW symmetry.

[12] One can choose baryon- and lepton-number conservation to be an assumption in constructing the set of higher-dimensional operators of the effective theory, which is our case of study.

ished by the equations of motion. The so-called *Warsaw basis* [191] is this new, reduced set of gauge-invariant operators[13] containing 59 independent terms (2499 for three generations of fermions). Other popular operator bases[14] are the *Hagiwara–Ishihara–Szalapski–Zeppenfeld* (HISZ) [192], and the *Strongly-Interacting Light Higgs* (SILH) [193–195].

The dimension-six SMEFT Lagrangian contains operators of the form,

$$\mathcal{L}_{\text{EFT}}^{(6)} \supset \left\{\Phi^6, D^2\Phi^4, \psi^2\Phi^3, F^2\Phi^2, \psi^2 F\Phi, \psi^2 D\Phi, F^3, \psi^4\right\}, \tag{2.3.11}$$

following the convention introduced in Eq. (2.2.8). These operators induce new vertices not allowed by the SM. Further, they can contribute to tree-level interactions that are already present at the dimension-four level, provided they have the same field content after EWSB through the introduction of either two additional powers of $\Phi$ or two more derivatives [175, 180]. These contributions scale respectively as,

$$\frac{g_\star^2 v^2}{\Lambda_{\text{NP}}^2}, \quad \frac{p^2}{\Lambda_{\text{NP}}^2}, \tag{2.3.12}$$

where $g_\star^2$ corresponds to the coupling parameter of the interaction [193, 196]. These impact directly the total rate of the process, as well as the momentum that is being exchanged in the corresponding vertex, which can be probed in the high-energy tails of differential distributions at colliders (see Chapter 3).

Although these violate lepton- and baryon-number conservation, a set of dimension-seven operators can be found in Refs. [197, 198]. Dimension-eight operators are spanned by the bases in Refs. [199, 200]. Thus, the leading effective Lagrangian respecting lepton- and baryon-number conservation reads,

$$\mathcal{L}_{\text{EFT}} = \mathcal{L}_{\text{SM}} + \sum_i \frac{c_i^{(6)}}{\Lambda_{\text{NP}}^2}\mathcal{O}_i^{(6)} + \sum_j \frac{d_j^{(8)}}{\Lambda_{\text{NP}}^4}\mathcal{O}_j^{(8)}, \tag{2.3.13}$$

where it is easy to notice that the Wilson coefficients of the dimension-eight operators are suppressed by a factor of $1/\Lambda_{\text{NP}}^4$. In general, the leading BSM effects are encoded

[13] The list of bosonic operators relevant to this Thesis is shown in Appendix A. For the complete set of operators, including the fermionic ones, see Ref. [191].

[14] These operator bases are related to each other via the equations of motion.

in the $D = 6$ operators. The amplitude corresponding to the Lagrangian above can be parametrised as,

$$\mathcal{M}_{\text{EFT}} = \mathcal{M}_{\text{SM}} + \frac{c_i}{\Lambda^2_{\text{NP}}}\mathcal{M}_{(6)} + \frac{d_j}{\Lambda^4_{\text{NP}}}\mathcal{M}_{(8)}, \tag{2.3.14}$$

and one can obtain the inclusive cross-section,

$$|\mathcal{M}_{\text{EFT}}|^2 = |\mathcal{M}_{\text{SM}}|^2 + 2\Re\left[\frac{c_i}{\Lambda^2_{\text{NP}}}\mathcal{M}^*_{(6)}\mathcal{M}_{\text{SM}}\right] + \underbrace{2\Re\left[\frac{d_j}{\Lambda^4_{\text{NP}}}\mathcal{M}^*_{(8)}\mathcal{M}_{\text{SM}}\right] + \frac{c_i^2}{\Lambda^4_{\text{NP}}}\mathcal{M}^2_{(6)}}_{\text{Theoretical uncertainty}} + \dots \tag{2.3.15}$$

where the terms to the right of the $\mathcal{M}^*_{(6)}\mathcal{M}_{\text{SM}}$ piece can be used to estimate the theoretical uncertainty[15]. Note that one can receive contributions from the $(D = 6)^2$ and the interference $(D = 8) \times$ SM terms, simultaneously, that are suppressed by a factor of $1/\Lambda^4_{\text{NP}}$. In such scenarios, one needs to check whether the $1/\Lambda^2_{\text{NP}}$ piece dominates over the $1/\Lambda^4_{\text{NP}}$ one, since the latter terms, both $(D = 6)^2$ and $(D = 8) \times$ SM, might need to be taken into account. However, including dimension-eight contributions in SMEFT studies is not straightforward, and most of these are performed using dimension-six operators, as is our case. For the remainder of this Thesis, we restrict to the set of dimension-six operators in the Warsaw basis, unless stated otherwise.

In practice, observables measured at colliders are quantities more easily related to interactions in the *mass basis* than to unbroken-phase operators. Ref. [202] provides a translation for the Wilson coefficients entering a particular process in the Warsaw to those in the mass basis, and the *Higgs basis* is described in Ref. [203]. In Chapters 4 and 5 we use the parametrisation known as the *BSM primary effects* [204] to probe the correlations between anomalous couplings and EW precision measurements. As we have seen in this subsection, the *bottom-up* approach predicts that any impact on the value of the couplings, total rates, or distributions expected by the SM, might be a hint for the eagerly awaited BSM physics.

[15] For a systematic methodology to assign theoretical uncertainties in SMEFT studies see Ref. [201].

### 2.3.3 Renormalisation Group Equations

The basic idea of EFTs is to perform calculations at an energy scale that is blind to the effects of physics far away from such energy scale. In the previous subsections we outlined the *top-down* and *bottom-up* approaches to construct EFTs. In the former, one starts from a UV-complete theory and obtains an effective Lagrangian upon integrating out the heavy degrees of freedom. In the latter, one needs to remain agnostic about the UV physics: higher-dimensional operators built out of all the fields in the theory encode the information of the long-distance physics, and the unknown high-energy effects are encapsulated in the Wilson coefficients of the perturbative expansion. In both cases, the effective theory description is valid up to a cut-off scale $\Lambda_{\rm NP}$. The boundary conditions are set by the matching procedure: both the EFT and the full theory must describe the same physics for the light fields just below $\Lambda_{\rm NP}$, relating the Wilson coefficients of the effective Lagrangian to the couplings of the UV theory.

If we go beyond tree-level processes, *a wild unphysical scale dependence appears*[16] in the calculations. This new scale $\mu_{\rm M}$ now corresponds to the "matching scale"; since momentum running in the loops is unconstrained, we are free to choose the value of such scale, given that actual physical observables cannot explicitly depend on it [177]. However, performing the loop-level matching induces scale-dependent Wilson coefficients $c_i\left(\mu_{\rm N}\right)$ through *dimensional transmutation*. Fixing $\mu_{\rm M}$ to arbitrarily low values yields large logarithms in our results of the form,

$$\ln\left|\frac{\Lambda_{\rm NP}}{\mu_{\rm M}}\right|, \tag{2.3.16}$$

where $\Lambda_{\rm NP}$ corresponds to the energy scale of physics that were integrated out. To remove these large logarithms, one needs to go to higher and higher orders in perturbation theory [179], or use the Renormalisation Group (RG) improved perturbation theory to sum up these logarithms to all orders [174].

[16] Disclaimer for the untrained eye: a reference to *Pokémon* was suitable in this case.

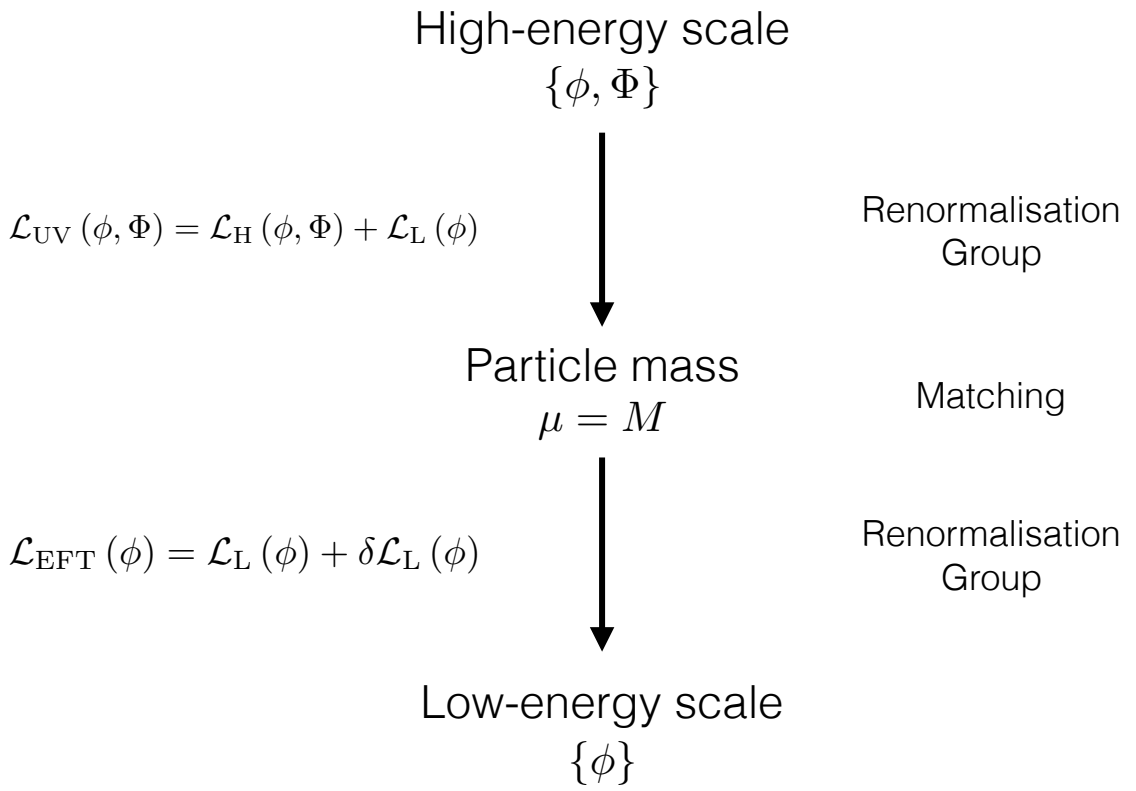


Figure 2.3: Interplay between matching and the RGEs. Start at a high energy scale $\mu_H$ with a UV-complete theory containing heavy ($\Phi$) and light ($\phi$) fields, of masses $M$ and $m$ respectively, and Lagrangian $\mathcal{L}_{\rm UV}(\phi,\Phi) = \mathcal{L}_{\rm H}(\phi,\Phi) + \mathcal{L}_{\rm L}(\phi)$. Using the RGEs, evolve the theory to lower energy scales until $\mu = M$ is reached, where the $\Phi$ fields can be integrated out. Since the particle content changed for $\mu < M$, and hence its parameters, one needs an effective theory with no heavy particles, described by the Lagrangian $\mathcal{L}_{\rm EFT}(\phi) = \mathcal{L}_{\rm L}(\phi) + \delta\mathcal{L}_{\rm L}(\phi)$, where the term $\delta\mathcal{L}$ parametrises the corrections due to the matching condition. In both the effective and the UV-complete theories, the physics of the light fields $\phi$ should be the same at $\mu = M$. Reproduced from Ref. [168].

One might want to perform loop-level calculations of low-energy observables at energy scales $E \ll \mu_{\rm M} \sim \Lambda_{\rm NP}$, resumming all the large logarithms of the theory. Since the Wilson coefficients were fixed at the matching scale $\mu_{\rm M}$ as $c_i(\mu_{\rm M})$, we need to run the value of these couplings down to $c_i(E)$ using the Renormalisation Group Equations (RGEs),

$$\mu \frac{{\rm d}c_i(\mu)}{{\rm d}\mu} = \frac{1}{16\pi^2}\gamma_{ij}c_j(\mu)\,, \tag{2.3.17}$$

where $\gamma_{ij}$ is the *anomalous dimension matrix*, which encodes the information of the mixing between operators as they evolve through different energy scales. A schematic representation of the interplay between matching and the RGEs is shown in Fig. 2.3.

In the studies presented in Chapters 4 and 5 we do not take the RGE effects into account, since we perform these at a fixed energy scale. Thus, relevant subjects for an in-depth description of the RGE, such as *renormalisation* and *dimensional regularisation*, among others, are beyond the scope of this Thesis. For a review on those and other topics in the context of the SM and EFTs, as well as some RGE results, see, e.g., Refs. [1, 2, 4, 170–173, 179, 184, 205, 206].

Having introduced the (very) basic elements of Effective Field Theory, we now move a bit away from theory concepts to broadly talk about direct and indirect searches for hints of new physics at high-energy colliders.

# Chapter 3

# Collider Phenomenology

In Chapter 1 we introduced the basic ideas underpinning the SM, and Chapter 2 helped us to understand the concept of the SM as an EFT. At this stage we know that the theory, although powerful by itself, has several shortcomings, and alternatives have been proposed throughout the years to address these issues (see Secs. 1.3 and 1.4). Following the *bottom-up approach* explained before, what we as physicists have in our toolkit to describe Nature with BSM physics is a bunch of Lagrangians constructed out of SM fields and either new Lorentz structures (*effective theories*) or new degrees of freedom (*simplified models*). We can predict how the interactions allowed by our Lagrangians should behave, and what the phenomenological implications of these are.

However, as Richard Feynman once said, *it doesn't matter how beautiful your theory is, it doesn't matter how smart you are. If it doesn't agree with experiment, it's wrong.* In short, *we need experiments to test our theories.* We want particles to be produced so we can then go and measure their masses, couplings, electric charge, etc. And this is the purpose of high-energy colliders: take two bunches of particles $A$ and $B$, give them enough energy, smash them together, and see what particles $C$, $D$, $E\ldots$ come out of the reaction.

This is Quantum Mechanics, though, and the particles we are interested in to be produced on the collision might not live long enough to reach our detectors: they

can decay on-the-fly producing a bunch of other particles, and we will need to indirectly characterise these particles through their decay products. But perhaps there are other objects that produce the same particles we detect, so we need to learn how to extract *signal events* from *background noise*. Essentially we would be detectives standing on the crime scene: two cars collided head-to-head[1], and we need to reconstruct the dynamics of the crash by looking at what the scatter pattern of the spark plugs, brake pads, screws, and many other parts looks like over the pavement of a street... on a rainy day, at night. But we are smart and know how to build big collider experiments with robust detectors to ease things a bit for us—now we only need to understand what particles look like in the detectors, and learn how to analyse and interpret the data.

The broad description of collider physics presented next is inspired by comprehensive texts like Refs. [207–209]. We consider two types of collider-target[2] experiments: electron-positron ($e^+e^-$), such as the ILC or CLIC, and proton-proton ($pp$). Since the LHC is the biggest $pp$ accelerator built to date, we will use it as our benchmark study case. We first address the case of a $pp$ collider, and then we will explain what makes an $e^+e^-$ experiment different from the former. We remit the reader to Refs. [37, 52, 54] for specific details on the technical design of the LHC, ILC, and CLIC, respectively.

## 3.1 The benchmark case: a proton-proton collider

The LHC is a collider-target experiment designed to accelerate protons to very high energies. In order to reach the nominal collision energy, a series of accelerators boost the energy of the proton beams before injecting them into the 27 km ring. As they need to follow a circular path, the trajectory of the beams is bent using magnetic

[1] Luckily there were no fatalties nor injuries.
[2] We will neglect fixed-target colliders.

fields produced by superconducting electromagnets that surround the beam-carrying channels. The curvilinear motion of the protons produces synchrotron radiation that needs to be compensated for by radio-frequency cavities, with a per-cycle loss,

$$\Delta E \propto \frac{1}{R}\left(\frac{E}{m}\right)^4, \tag{3.1.1}$$

with $R$ the radius of curvature, $E$ the beam energy, and $m$ the mass of the particle. To prevent protons from moving in the transverse plane, called *betatron oscillations*, beams are focused in the vertical-horizontal plane and forced to move towards the centre of the channel using quadrupole magnets, narrowing the beams and allowing them to overlap at the interaction point.

### 3.1.1 Collision energy

The beams carrying the bunches of protons move in opposite directions around the ring. The energy $E$ and three-momentum $\vec{p}$ of a single proton of mass $m$ is encoded in the proton's four-momentum $p \equiv p^\mu = (E, \vec{p})$ obeying the *on-shell* condition,

$$p^2 \equiv p_\mu p^\mu = E^2 - \vec{p}\cdot\vec{p} = m^2. \tag{3.1.2}$$

It is customary to adopt a coordinate system in which the protons are moving in the $\hat{z}$ direction, with the $\hat{x}$ axis pointing to the centre of the ring and $\hat{y}$ completes the right-handed set, since quadrupole magnets focus the beams in the plane transverse to the channel (*transverse plane* $\hat{x} - \hat{y}$), . In the relativistic limit, with $E \gg m$, $p^2 \to 0$,

$$p^\mu = (E, 0, 0, E). \tag{3.1.3}$$

The energy transfer in the centre-of-mass frame between any two protons $A$ and $B$ of the incoming beams follows from four-momentum conservation and can be expressed in terms of the Lorentz-invariant Mandelstam variable $s$ as,

$$s \equiv (p_A + p_B)^2 = (E_A + E_B)^2, \tag{3.1.4}$$

since in the centre-of-mass frame $p_z^A = -p_z^B$. At the LHC, the collision energy is equally shared between both beams, $E_A = E_B$, and the nominal collision energy $\sqrt{s}$ is then,

$$\sqrt{s} = 2E_A. \tag{3.1.5}$$

Protons, however, are not fundamental particles: these are composite objects made up of not only "valence" quarks (proton = $|\text{uud}\rangle$), but "sea" quarks and gluons, too. One can then have several combinations for the partons involved in the *hard scatter*, *i.e.*, the actual collision: $qq'$, $q\overline{q}$, $q\overline{q}'$, $qg$, $gg$... All these combinations lead to different charge and spin assignment in the initial state, hence opening up the possibilities of producing intermediate-state resonances, and giving access to a large variety of particles allowed in the final state of the collision. But since protons are "extended" objects, and there are $\mathcal{O}\left(10^{11}\right)$ protons per crossing bunch, many interactions might be taking place at the same time, often referred to as *underlying event*.

*What does proton compositeness have to do with the collision energy?* Protons are bound states of partons charged under the $SU(3)_C$ group, meaning that they are affected by the strong interaction and partons can radiate gluons. But we are talking about electrically charged particles (in the case of quarks) too, so these couple to photons as well, which can also be emitted by the incoming quarks— photon and gluon radiation can smear the energy of the colliding particles. Moreover, parton $i$ carries a fraction $x_i$ of the proton's momentum $\vec{p}_{\text{proton}}$,

$$\vec{p}_i = x_i \vec{p}_{\text{proton}}, \tag{3.1.6}$$

which leads to the so-called *parton distribution functions* (PDFs) $f_{i/p}\left(x, \mu_F^2\right)$ [210, 211], which parametrise the distribution of partons inside the proton[3]. More precisely, $f_{i/p}\left(x, \mu_F^2\right)$ represents the density of (valence or sea) partons of type $i$ ($\{q, \overline{q}, g\}$) as a function of their momentum fraction $x$ in Eq. (3.1.6) when a proton $p$ is probed at an energy scale $\mu_F^2$. Fig. 3.1 shows the difference between parton distributions at two

[3]When talking about PDFs, one would need to discuss the *factorisation theorem* [212], as well as the DGLAP equation [213–215]. However, these topics are beyond the scope of this Thesis.

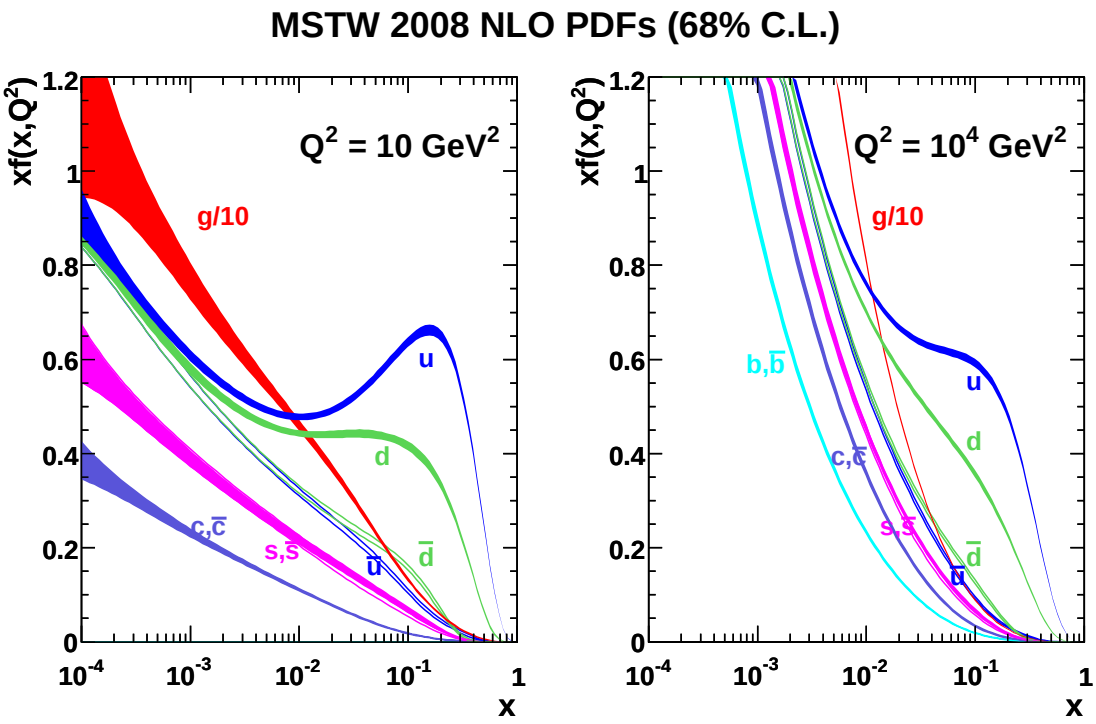


Figure 3.1: Illustration of the change of parton distributions, from **left:** $\mu_F^2 = Q^2 = 10\,\mathrm{GeV}^2$ to **right:** $\mu_F^2 = Q^2 = 10^4\,\mathrm{GeV}^2$. Taken from Ref. [216].

different scales. Hence, the *effective* energy transfer $\hat{s}$ in the collision expressed in terms of the momentum fraction $x$ of the interacting partons follows from Eqs. (3.1.3) and (3.1.4),

$$\begin{aligned} q^\mu = (xE, 0, 0, xE) \Rightarrow \hat{s} &= (x_A + x_B)^2 E^2 - (x_A - x_B)^2 E^2 \\ &= 4 x_A x_B E^2 \\ &= x_A x_B s, \end{aligned} \tag{3.1.7}$$

where $E$ corresponds to the beam energy, $x_A$ and $x_B$ to the momentum fraction carried by the interacting parton from proton $A$ and $B$ respectively, and $s$ is the nominal centre-of-mass energy squared.

In summary, the composite nature of the colliding protons leads not only to a plethora of charge and spin assignments, but to a per-event energy-varying collision due to the PDFs. The effective and nominal centre-of-mass energies $\sqrt{\hat{s}}$ and $\sqrt{s}$, respectively, are related as,

$$\sqrt{\hat{s}} = \sqrt{x_A x_B}\,\sqrt{s}, \tag{3.1.8}$$

which makes evident the major impact that PDFs have in the nominal collision energy. Figure 3.2 shows the cross-sections of some relevant SM processes that can be produced at $p\bar{p}$, such as the Tevatron [217], and $pp$ colliders, as a function of $\sqrt{s}$.

### 3.1.2 Collision rate

Since protons travel in bunches[4], and beams overlap at the interaction points, it is customary to define the interaction rate $N$ as,

$$N = \frac{n_1 n_2 f}{A}\sigma, \tag{3.1.9}$$

where $n_i$ are the number of protons in bunch $i$, $f$ is the frequency at which collisions take place (can be as high as 40 MHz at the LHC), $A$ is the area of the bunch at collision point, and $\sigma$ is the cross-section of the $pp$ collision. From Eq. (3.1.9), we define the *instantaneous luminosity* $L$, a measure of how tightly packed together the bunches are, as,

$$L = \frac{n_1 n_2 f}{A}, \tag{3.1.10}$$

where for convenience $A$ is measured in *femtobarns* (fb), with $1\,\text{fb} = 10^{-43}\text{m}^2$. Hence, it follows from Eq. (3.1.9) that the cross-section $\sigma$ is measured in femtobarns, too, and the instantaneous luminosity is given in units of $(\text{fb}\,\text{s})^{-1}$.

The machine collides protons and collects data during several days, weeks, months ... The total number of recorded events over a given period of time $t$ is known as the *integrated luminosity* $\mathcal{L}$ (not to be confused with the Lagrangian density),

$$\mathcal{L} = \int L\,\text{d}t \tag{3.1.11}$$

where $L$ is the instantaneous luminosity defined in Eq. (3.1.10). Since it began running on November 2009 and until the end of the *Run 2* phase on December 2018, the LHC has delivered $\mathcal{L} = 189.3\,\text{fb}^{-1}$ of data. It has performed collisions at different $\sqrt{s}$: 1.8 TeV and 2.36 TeV during its first days of operations before the

[4]There are roughly 2000 bunches of protons per beam, with nearly $10^{11}$ protons each. The length of a single bunch is about 30 cm.

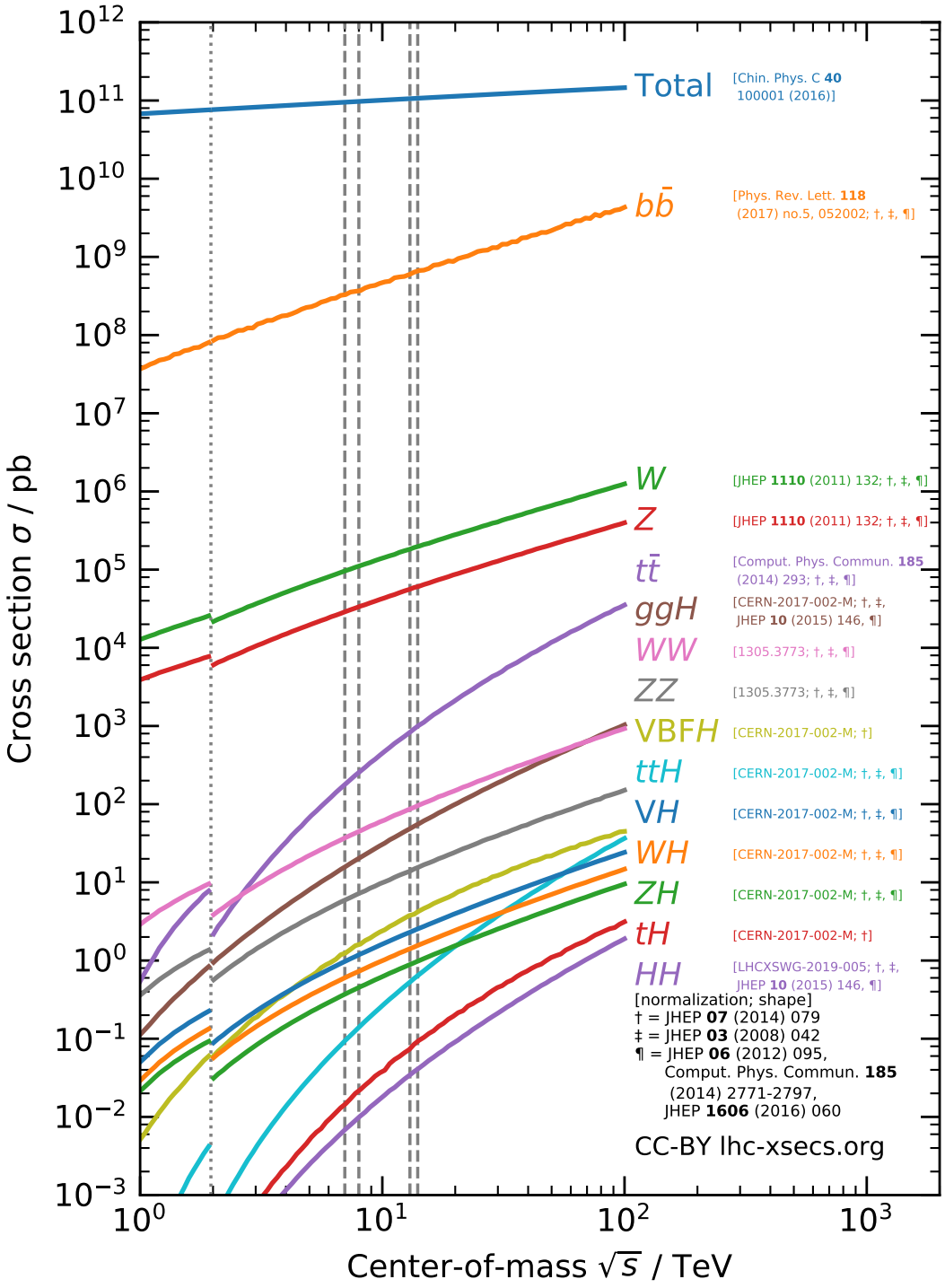


Figure 3.2: Production cross-sections $\sigma$, in pb, of some SM processes at hadron colliders as a function of the centre-of-mass energy $\sqrt{s}$, in TeV. The dotted vertical line corresponds to the $\sqrt{s} = 1.96\,\text{TeV}$ Tevatron; curves to its left are cross-sections at $p\bar{p}$ colliders, and curves to its right are cross-sections at $pp$ colliders. From left to right, vertical dashed lines correspond to the $\sqrt{s} = 7, 8, 13$, and $14\,\text{TeV}$ LHC, respectively. Taken from Ref. [218].

2009 shutdown over the winter; in March 2010 it began the *Run 1* phase, period over which the Higgs boson was discovered, with the centre-of-mass energy increased to 7 TeV and later on to 8 TeV until 2013; and finally the *Run 2* phase at 13 TeV. The high-energy stage, *Run 3*, is expected to begin at the start of March 2022; the machine will run at $\sqrt{s} = 14\,\text{TeV}$ and is expected to collect $\mathcal{L} = 300\,\text{fb}^{-1}$ of data. The plan is to perform a high-luminosity run (HL-LHC) that would operate at $\sqrt{s} = 14\,\text{TeV}$ and collect $\mathcal{L} = 3000\,\text{fb}^{-1}$ of data after *Run 3*.

### 3.1.3 Detectors and kinematics

Experiments have big and robust detectors that help us in studying, directly or indirectly, the particles that are produced as a result of the $pp$ collisions. Let us take the Compact Muon Solenoid (CMS) [219], one of the four main experiments at the LHC along with ALICE [220], ATLAS [221], and LHCb [222], as an example to broadly describe what its coordinate system and components are.

CMS is a cylindrical detector, forward/backward symmetric about the interaction point. As mentioned in the above paragraphs, the $\hat{x}$ axis points to the center of the ring, the $\hat{z}$ axis points in the direction of the beam, and $\hat{y}$ completes the right-handed set, with the plane formed by the $\hat{x}$ and $\hat{y}$ axes known as the *transverse plane*. As the geometry of the detector suggests, cylindrical coordinates are more suitable to describe the physics than the Cartesian ones. The polar angle $\theta$ between the direction of the particle and the beam is measured from the $\hat{z}$ axis in the $\hat{y} - \hat{z}$ plane, with $\theta \in [0, \pi]$, and the azimuthal angle $\phi$ is measured from the $\hat{x}$ axis in the transverse plane, where $\phi \in [0, 2\pi)$. An illustration of the coordinate system is shown in Fig. 3.3.

Let us consider a bunch of particles, each with four-momentum $p^\mu = (E, \vec{p})$ obeying Eq. (3.1.2), reaching our detector. From four-momentum conservation in Eq. (3.1.3), the vector sum of the transverse components of the particles produced after the $pp$ collision should vanish. From Eq. (3.1.7), one can see that the possible ambiguities

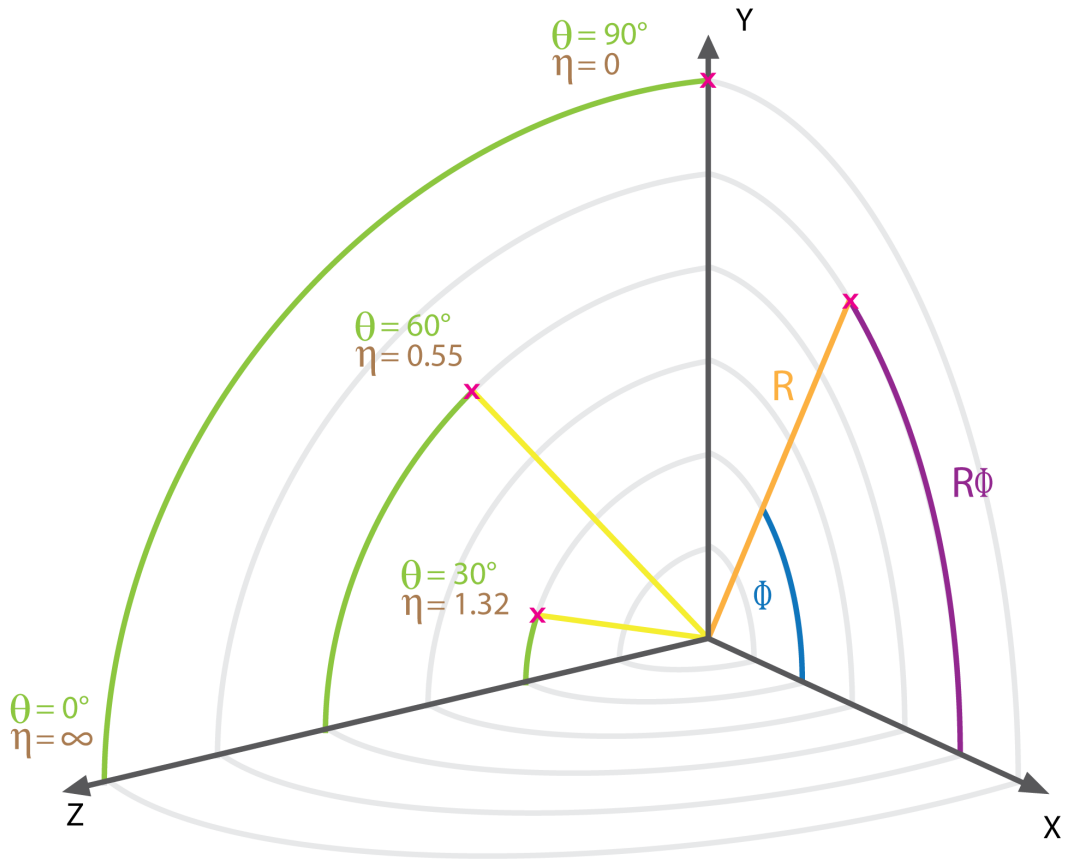


Figure 3.3: Cylindrical coordinate system used in the CMS detector (see text for details). The $\hat{x}$ axis points to the centre of the accelerator; the $\hat{z}$ axis points in the direction of the beam; finally, the $\hat{y}$ axis completes the right-handed set. Note that the polar angle $\theta$ (green), measured in the $\hat{y} - \hat{z}$ plane, gets replaced by the pseudorapidity $\eta$ (brown), with $\eta = -\ln|\tan(\theta/2)|$. The azimuthal angle $\phi$ (blue) is measured in the transverse $(\hat{x} - \hat{y})$ plane. Taken from Ref. [223].

related to the four-momenta of particles reaching the detectors are along the beam direction ($\hat{z}$), which means that variables defined in terms of only the transverse components are invariant under longitudinal boosts. As such, the aim is to describe the physics in terms of as many boost-invariant quantities as possible. We introduce the *transverse momentum* $p_T$,

$$p_T = \sqrt{p_x^2 + p_y^2} = |\vec{p}| \sin\theta, \tag{3.1.12}$$

with $p_i$ the projection of $\vec{p}$ onto the $i$ axis, and $\theta$ the polar angle described above. We find in the azimuthal angle $\phi$ another quantity which remains invariant under longitudinal boosts, since it is measured about the $\hat{z}$ axis and lies in the transverse plane.

We define the *rapidity* $y$,

$$y = \frac{1}{2} \ln \left| \frac{E + p_z}{E - p_z} \right|, \tag{3.1.13}$$

which is additive under longitudinal boosts, with $E$ and $p_z$ the energy and the $z$-component of the three-momentum $\vec{p}$ of our particle, respectively. In the relativistic limit, or in the (nearly) massless case, $E \approx |\vec{p}|$ and one can define the quantity called *pseudorapidity* $\eta$,

$$\begin{aligned} y \xrightarrow{E \approx |\vec{p}|} \frac{1}{2} \ln \left| \frac{1 + \cos\theta}{1 - \cos\theta} \right| &= \ln \left| \cot\left(\frac{\theta}{2}\right) \right| \\ &= -\ln \left| \tan\left(\frac{\theta}{2}\right) \right| \equiv \eta, \end{aligned} \tag{3.1.14}$$

where $-\infty < \eta < \infty$. Differences in pseudorapidity are not necessarily invariant under longitudinal boosts, unlike rapidity differences. For massless particles, $y = \eta$, and these can be swapped at convenience; however, they differ for massive objects. Thus, it is recommended to use $y$ whenever possible.

Having introduced all these well-behaved (under longitudinal boosts) quantities, one can rewrite the four-vector of a particle of mass $m$ as,

$$p^\mu = \left(E, p_x, p_y, p_z\right) \to \left(E_T \cosh y, p_T \cos\phi, p_T \sin\phi, E_T \sinh y\right), \tag{3.1.15}$$

where $E_T = \sqrt{p_T^2 + m^2}$, and it is easy to see that $p^2 = m^2$. Finally, it is customary to quantify the separation between two particles reaching the detector, in the $y - \phi$ plane, in terms of the angular separation $\Delta R$,

$$\Delta R = \sqrt{(\Delta y)^2 + (\Delta \phi)^2}, \tag{3.1.16}$$

which is also an invariant quantity under longitudinal boosts.

Now that we have seen how to express the four-momentum of a particle in terms of the kinematic quantities measured at colliders, it is time to turn our attention to the components that build the detection system. To understand the nature of the particles produced on the collisions, it is necessary to look at their tracks and energy deposits. Detectors make use of a series of components designed to measure the momenta, charges, and energies of the final-state objects. In the SM, massive particles $\left(W^{\pm}, Z, h, t \dots\right)$ decay promptly[5], and their presence can only be inferred from the production and subsequent detection of their stable decay products. Due to colour confinement [224–226], quarks and gluons undergo a series of small-angle fragmentations and produce a bunch of collimated (color-neutral) hadrons, which can subsequently decay until stable bound states are formed, that are often referred to as *jets*[6]. The stable particles and objects (electrons, muons, jets, photons) reaching our detectors are characterised by their footprints in the different layers of the detection system illustrated in Fig. 3.4 and outlined next.

i. **Inner tracker.** Located immediately around the interaction point, it is used to identify the tracks of individual charged particles that can be matched to the vertices from which they were produced. Its pseudorapidity coverage is roughly $|\eta| \simeq 2.5$, and can estimate a particle's momentum and mass by determining the curvature of its track.

ii. **Electromagnetic Calorimeter (ECAL).** Surrounding the inner tracker, the

[5]The lifetime $\tau$ of a massive particle is related to its decay width $\Gamma$ as $\Gamma = \hbar/\tau$, where $\hbar$ is the reduced Planck constant $\hbar = h/2\pi$.

[6]For a more detailed explanation of jet definitions, see Ref. [209].

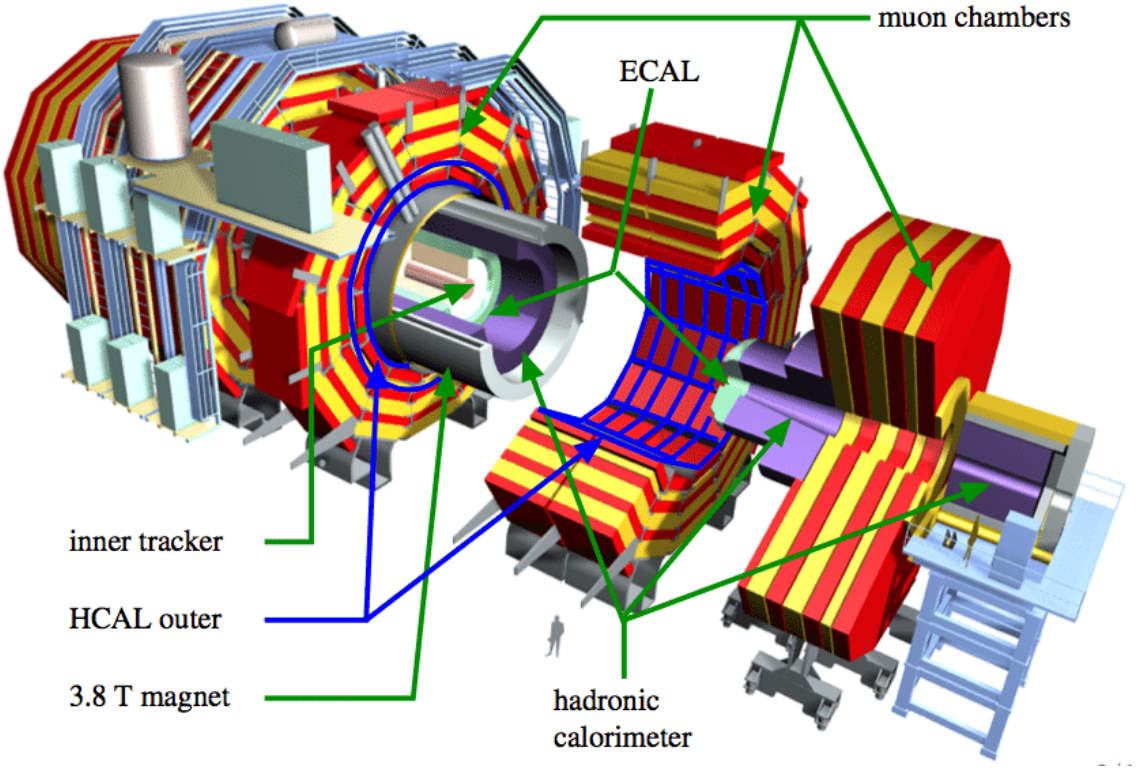


Figure 3.4: Sketch of the major components of the CMS detector surrounding the beam channel (see text for details). From the inside to the outside: inner tracker, electromagnetic calorimeter, hadronic calorimeter, magnet, and muon chambers. Taken from Ref. [227].

ECAL is designed to measure the energies of charged particles and photons by *bremsstrahlung* and pair production, respectively, provided the resulting particles are energetic enough to undergo a cascade of electromagnetic showers inside the material. The rapidity coverage of the ECAL is $|\eta| \simeq 3.0$.

iii. **Hadronic calorimeter (HCAL).** Similar to the ECAL where radiative processes allow for particle identification, the HCAL creates both electromagnetic and hadronic cascades, the latter driven by strong interactions between the material and the hadrons reaching this layer. Its pseudorapidity coverage $|\eta| \simeq 5.0$ is meant to create an environment as hermetic as possible around the interaction point.

iv. **Magnet.** Creates an homogeneous and strong magnetic field inside the solenoid in which the inner tracker is placed to determine the momentum of charged particles to high precision, as well as increasing the resolution of the calorimeters. Moreover, it also serves as a barrier for particles that manage to escape the calorimeters, except for muons.

v. **Muon chambers.** Due to its large mass, the muon barely interacts with the calorimeters. As such, muons are the only particles that can escape the innermost layers of the detection system left at this stage. Its pseudorapidity coverage is close to $|\eta| \simeq 2.7$.

The combined particle-reconstruction algorithms [228] for electrons and photons [229], muons [230], and jets [231] allow for a high level of accuracy on identifying these objects, while suppressing their mutual fake rates.

Particles can avoid detection for several reasons, namely escaping the detector through the forward region ($|\eta| > 5.0$) close to the beam channel; not being energetic enough to produce cascade showers in the calorimeters, or not interacting with the detector system at all, as is the case for neutrinos. Four-momentum conservation allows us to, in principle, quantify the amount of energy that was not detected.

However, we saw that for $pp$ collisions it is difficult to determine $\sqrt{\hat{s}}$ because of the ambiguity due to the PDFs, but not everything is lost: we can look into the *missing transverse momentum* vector $\left(\vec{\not{p}}_T\right)$. In an event, the overall transverse energy deposits should be zero from four-momentum conservation (see Eq. (3.1.2)), so the $\vec{\not{p}}_T$ observable balances the vector that results of summing the transverse momenta of all objects visible to the detection system,

$$\vec{\not{p}}_T = -\sum_{\text{visible}} \vec{p}_T, \tag{3.1.17}$$

with complex algorithms designed to estimate to a high level of accuracy the amount of missing transverse momentum $\not{p}_T = \left|\vec{\not{p}}_T\right|$ in an event [232].

Although robust analysis techniques and detection systems have been developed and constructed over the years, these have to deal with many sources of radiation present in each collision that can contaminate the energy deposits recorded by the calorimeters. If we want to study and characterise a specific *signal* process, we not only have to rely on the resolution of the detector, but we must also come up with strategies that allow us to accurately identify those noisy *background* processes that yield the same final-state configuration that we are after, suppress these, and extract the signal contributions by looking into as many observables and distributions as possible (invariant masses, $p_T$, $\Delta y \dots$), unique to the objects of our signal, that can be constructed from the four-momenta of the detected particles.

## 3.2 Interlude: EFT and collider phenomenology

Having seen the major components of the detection system, as well as the basic kinematic variables that can be extracted from measurements at $pp$ colliders, now it is time for us to briefly describe what the interplay between effective field theory and collider phenomenology is, mostly inspired by Refs. [185, 233]. For this, we will first discuss what the physics effects induced by resonances that can be produced on-shell are, to then broadly explain the search strategy for those effects induced by

heavy particles with masses above the energy attainable by the experiment.

### 3.2.1 Resonances: on-shell production

The discovery of a new, massive particle has a clear signature: a resonant signal. Let us assume that there is an undiscovered and unstable particle $N$ with mass $M_N$ within the energy reach of the LHC $\left(M_N < \sqrt{\hat{s}}\right)$, and decay width $\Gamma_N$, that can be produced on-shell through an $s$-channel process of the form $pp \to N$ with a subsequent two-body ($ab$) decay $N \to ab$. The propagator of the full process $pp \to N \to ab$ is of the form,

$$\frac{i}{\left(\hat{s} - M_N^2\right) + iM_N\Gamma_N},$$

and the Breit-Wigner resonance $R(\hat{s})$ parametrises the probability density of the process $pp \to N \to ab$ as,

$$R(\hat{s}) = \frac{1}{\left(\hat{s} - M_N^2\right)^2 + M_N^2\Gamma_N^2}, \tag{3.2.1}$$

which develops a kinematic peak around the pole mass $\hat{s} \approx M_N^2$, assuming a weakly-coupled particle ($\Gamma_N \ll M_N$). In practice, the massive particle $N$ is unstable and one has to detect and reconstruct the four-momenta $p_a$ and $p_b$ of the decay products $a$ and $b$, respectively. Four-momentum conservation implies,

$$\begin{aligned} p_N = p_a + p_b \Rightarrow p_N^2 &= (p_a + p_b)^2 \\ &= m_a^2 + m_b^2 + 2p_a \cdot p_b \\ &= M_N^2 \equiv M_{ab}^2, \end{aligned} \tag{3.2.2}$$

called the *invariant mass* of the $ab$-system, which is the most useful observable that one can use to discover a heavy resonance provided its mass is within the energy reach of the collider, and the four-momenta of its decay products can be fully reconstructed[7].

[7] If the four-momenta of the decay products cannot be unambiguously reconstructed, then one has to use other kind of observables such as the *transverse mass*, which is an end-point function of

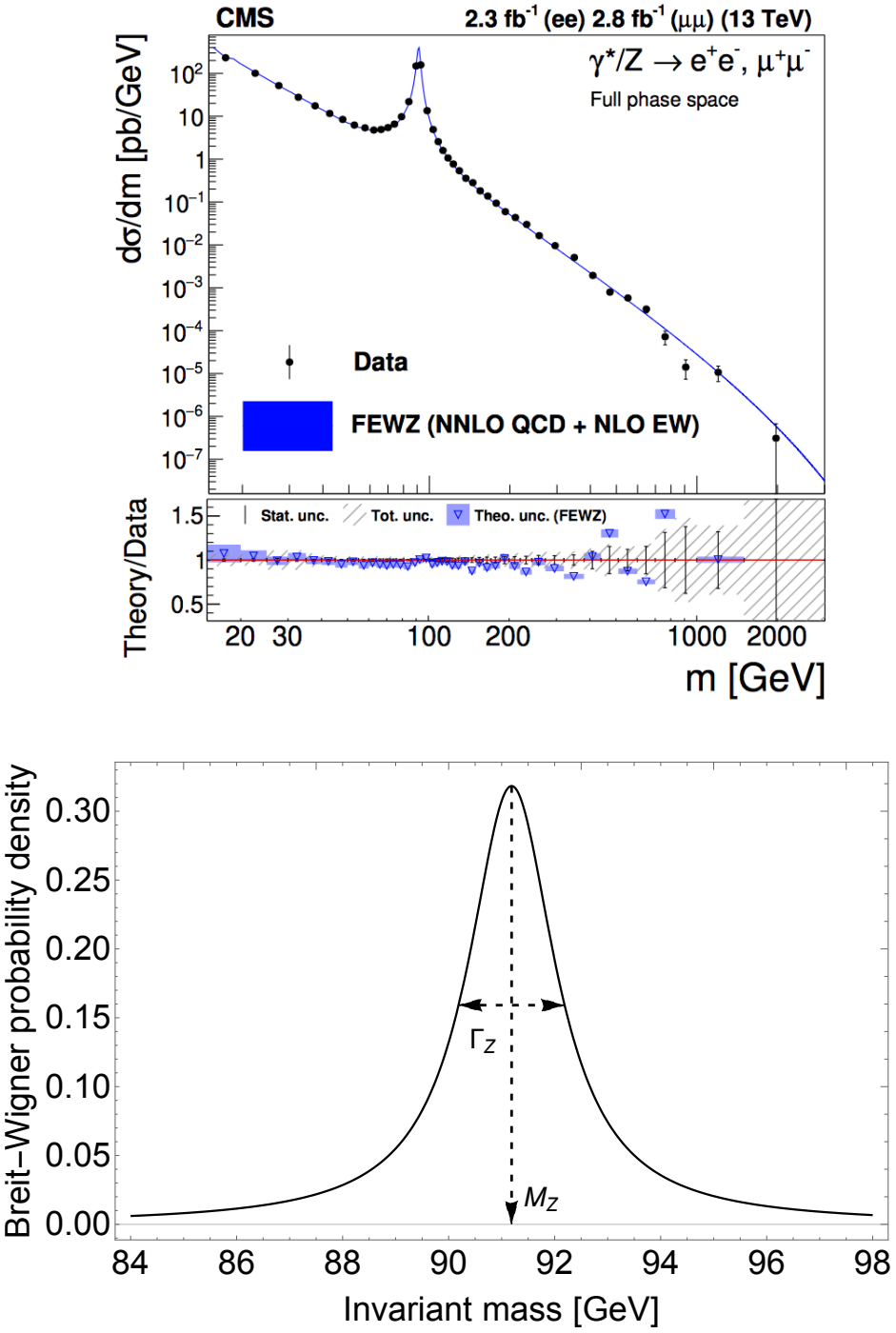


Figure 3.5: Invariant-mass distribution, in GeV, of the dilepton system in the Drell-Yan process $pp \to \ell^+\ell^-$ (see text for details). **Top:** Differential cross-section as a function of the invariant mass of the dilepton system, $\mathrm{d}\sigma/\mathrm{d}m$, in pb/GeV, in $pp$ collisions at $\sqrt{s} = 13\,\mathrm{TeV}$. Taken from Ref. [234]. **Bottom:** Line shape of the probability density function for a Breit-Wigner distribution peaking at the nominal mass $M_Z$ of the $Z$-boson. Note that the width $\Gamma_Z$ is measured at half-maximum of the distribution's peak. Reproduced from Ref. [235].

The cross-section $\sigma$ of the $s$-channel process $pp \to ab$, proportional to the Breit-Wigner resonance $\sigma(pp \to ab) \propto R(\hat{s})$, is energy-dependent and peaks at $M_N$. To illustrate this effect, Fig. 3.5 shows the cross-section of the Drell-Yan process $pp \to Z/\gamma^* \to \ell^+\ell^-$ ($\ell = e, \mu$) as a function of the invariant mass of the dilepton system, with a clear line shape associated to the on-shell production of a $Z$-boson as the massive propagator of such a process.

However, there is a major caveat concerning the potential reach of experiments to produce and observe a massive resonance, which is the attainable energy at colliders: if the scale of new physics is well beyond the energy threshold of the LHC, then such particles cannot be produced on-shell, so any direct evidence for their existence might remain elusive until a new, more energetic accelerator complex is built. For now, our best hope to constrain new physics effects rely on indirect searches.

### 3.2.2 Indirect searches: hints and clues

The lack of tantalising evidence for new resonant BSM physics during the LHC's Runs 1 and 2 seem to suggest that the next energy scale $\Lambda_{\text{NP}}$ at which experiments could find such resonances (if any exists) is well beyond the reach of current colliders. Several questions trying to address these issues arise, such as how to reconstruct a TeV-scale Lagrangian with the current data, or what the best strategies to look for certain observables would allow us to best anticipate incoming data. Although direct searches will be part of the LHC programme during its high-energy and high-luminosity stages, it is possible to look for hints of BSM physics in precision measurements since the existence of heavy degrees of freedom may impact the distributions and observables contained in the SM by showing deviations from the predictions of the theory.

From an EFT perspective, as outlined in Chapter 2, the extension of the SM Lagrangian by higher-dimensional operators would allow us to parametrise the effects of

the resonance's mass. See Ref. [207] for more details.

new BSM physics in terms of Lorentz structures made up of SM fields only, and any deviation from the SM predictions is expected to be a hint for effects of new physics at the low-energy regime. The leading BSM effects are encoded in dimension-six operators, and it is crucial to understand what the predictions of these are: new vertices ensuing from EFT can produce novel or enhanced effects in certain regions of the phase space, and it is vital to determine what the best observables to study the effects of certain operators or procceses are. *At what extent would current or future colliders be able to probe the presence of vertices and interactions arising from searches for non-resonant extensions of the SM?*

Since this Thesis studies gauge-Higgs interactions, let us use the Higgs sector to illustrate the idea behind indirect searches, as EFT effects can impact their kinematic distributions. For a given observable, experiments count the number of events per "bin", which get translated to cross-sections: these encode the information related to a certain process within the phase space defined by the detectors, as well as tests for non-standard couplings or production/decay modes. Upon looking for deviations sensitive to short-distance physics, the predictive power of the SM allowed us to use total rates [42–44] to parametrise deviations from the SM predictions in the form of *signal strengths* $\mu_i^f$, defined as the ratio of the measured rates to their SM predictions,

$$\mu_i^f = \frac{\sigma_i \cdot B^f}{\left(\sigma_i \cdot B^f\right)_{\text{SM}}}, \tag{3.2.3}$$

where $\sigma_i$ and $B^f$ are the production cross-section $\sigma(i \to h)$ and decay branching fraction $\text{BR}(h \to f)$, respectively (see Sec. 1.2). Although useful to shed light on Higgs couplings, signal-strength measurements are not physical quantities and fail at separating signal contributions to their different phase-space regions, which might be sensitive to BSM contributions that can be parametrised in a "model-independent" way by a bottom-up EFT approach.

In order to measure cross-sections in mutually exclusive regions of phase space, specific to the different production modes and inclusive on Higgs decays, the *Simplified*

*Template Cross Section* (STXS) measurements [236,237] provide kinematic templates that can potentially isolate possible BSM effects. The results of STXS measurements can be interpreted in an EFT fashion [238,239]. Consider the perturbative extension of the SM Lagrangian by new operators of dimension $D > 4$ [203],

$$\begin{aligned}\mathcal{L}_{\text{EFT}} &= \mathcal{L}_{\text{SM}} + \sum_i \frac{c_i^{(D)}}{\Lambda_{\text{NP}}^{D-4}} \mathcal{O}_i^{(D)} \\ &\equiv \mathcal{L}_{\text{SM}} + \mathcal{L}_{\text{BSM}},\end{aligned} \tag{3.2.4}$$

where, as before, $c_i^{(D)}$ are the Wilson coefficients and $\mathcal{O}_i^{(D)}$ are the dimension-$D$ operators[8]. The (square) amplitude of a generic process governed by the Lagrangian above is,

$$\begin{aligned}\mathcal{M} = \mathcal{M}_{\text{SM}} + \mathcal{M}_{\text{BSM}} \Rightarrow |\mathcal{M}|^2 &= |\mathcal{M}|^2_{\text{SM}} + 2\Re\left(\mathcal{M}^*_{\text{SM}}\mathcal{M}_{\text{BSM}}\right) + |\mathcal{M}|^2_{\text{BSM}} \\ &= |\mathcal{M}|^2_{\text{SM}} + |\mathcal{M}|^2_{\text{Interference}} + |\mathcal{M}|^2_{\text{BSM}}\,,\end{aligned} \tag{3.2.5}$$

where $|\mathcal{M}|^2_{\text{Interference}} \equiv 2\Re\left(\mathcal{M}^*_{\text{SM}}\mathcal{M}_{\text{BSM}}\right)$ is the interference of the dimension-$D$ amplitude with the SM. The Higgs boson production cross-section $\sigma$ in a generic STXS region $\Omega$ is then,

$$\sigma_\Omega = \sigma_{\Omega,\text{SM}} + \sigma_{\Omega,\text{Interference}} + \sigma_{\Omega,\text{BSM}}, \tag{3.2.6}$$

which makes clear that it is possible to build a bridge between cross-section measurements at colliders and higher-dimensional operators, provided distributions can be "binned" in mutually exclusive phase-space regions, sensitive to BSM effects.

While signal-strength and STXS measurements allow to look for small deviations in couplings and probe specific phase-space regions, respectively, new physics typically shows up modifying the tail of the differential distributions at high energies [233]. From Eq. (3.2.5), the interference piece of the amplitude[9],

$$|\mathcal{M}|^2_{\text{Interference}} = 2\Re\left(\mathcal{M}^*_{\text{SM}}\mathcal{M}_{\text{BSM}}\right) \propto \cos\theta, \tag{3.2.7}$$

[8] Since dimension-six operators entail the leading BSM effects, it is customary to deal with the $D = 6$ case and consistently drop the $\mathcal{O}\left(1/\Lambda^4_{\text{NP}}\right)$ terms as the latter are suppressed.

[9] Note that for a fixed dimension $D$, and allowing only one operator $\mathcal{O}^{(D)}$ insertion at a time, the cross-section of the interference term $\sigma_{\text{Interference}}$ behaves linearly with respect to the corresponding Wilson coefficient $c^{(D)}$.

where $\theta$ is a generic angle related to the kinematics of the process. Since the cross-section $\sigma_{\text{Interference}}$ of the interference piece of a process is proportional to the square amplitude $|\mathcal{M}|^2_{\text{Interference}}$,

$$\sigma_{\text{Interference}} \propto \int \mathrm{d}\Omega \, |\mathcal{M}|^2_{\text{Interference}} \Rightarrow \sigma_{\text{Interference}} \propto \int_0^{\pi} \mathrm{d}\theta \cos\theta, \tag{3.2.8}$$

with $\mathrm{d}\Omega$ the phase-space volume element, it is clear that the interference piece will vanish upon integration over $\theta$, and any clues of the impact of this kinematic angle would be missed should we analyse total rates only [185]. Retaining these effects is crucial to extract hints for new physics, which is a strong motivation to carry out differential analyses as a complementary strategy to total-rate searches [240]. Differential observables such as the $p_T$ of Higgs decay products [75, 241–243] can show deviations in the tails of their distributions which get translated into EFT interpretations of Higgs properties [244], and along with signal-strength measurements are used to set constraints on higher-dimensional operators [245, 246]. A schematic representation of direct and indirect searches at colliders is shown in Fig. 3.6.

Since experiments provide measurements, these need not only interpretation, but strategies that allow us to anticipate incoming data, too. Meaningful results rely heavily on the energy reach of the accelerator complex, as well as on its precision: *in order to probe high-energy effects, we require high-energy collisions and high-precision measurements*. As we saw before, although the LHC is a high-energy collider, its centre-of-mass energy is limited due to the PDFs of the incoming beams, and hadronic activity is somewhat annoying to deal with. Future $e^+e^-$ colliders, high-energy and precision experiments that circumvent these problems, can carry out complementary direct and indirect searches in our quest to look for new physics effects at higher and higher energies, and these will be broadly described next.

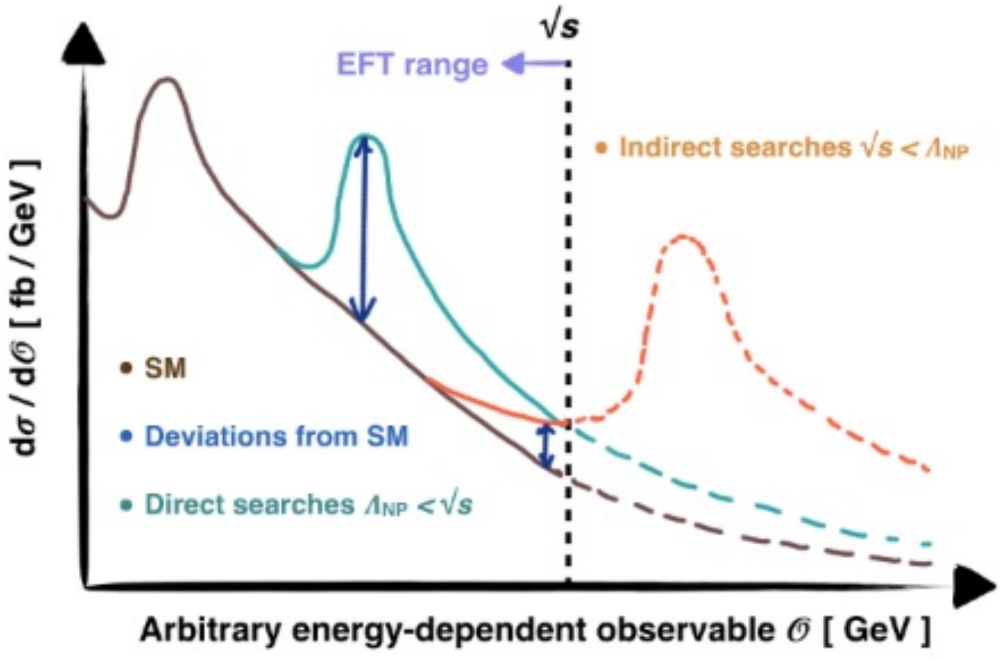


Figure 3.6: Schematic representation of direct and indirect searches for discovering BSM physics at colliders assuming the existence of a new heavy degree of freedom at energy scale $\Lambda_{\text{NP}}$. The differential distribution of the cross-section with respect to an arbitrary energy-dependent observable $\mathcal{O}$, $\mathrm{d}\sigma/\mathrm{d}\mathcal{O}$, in fb/GeV, is shown. If the scale of new physics is attainable at colliders, *i.e.*, $\Lambda_{\text{NP}} < \sqrt{s}$, the resonance can be produced on-shell (turquoise) and a clear deviation from the SM prediction (brown) can be seen, both in total rates and differential distributions. If instead $\sqrt{s} < \Lambda_{\text{NP}}$, then it is expected that a departure from the SM prediction in the high-energy tail of the differential distribution (orange) can be extracted from data and interpreted in an EFT fashion. Reproduced and modified from Ref. [183].

## 3.3 A clean environment: electron-positron colliders

As we have seen, *pp* colliders are machines that can accelerate protons to high energy, with a plethora of charge and spin assignments owed to the interacting partons at the hard scatter level. However, the presence of coloured objects in the initial state produce large amounts of radiation in the form of jets. Moreover, the associated PDFs introduce an ambiguity when one tries to compute the collision energy, and the highly hadronic environment can turn out to be cumbersome to deal with while trying to extract the signal from the overwhelmingly large QCD backgrounds.

Electron-positron accelerators offer a convenient alternative when it comes to collider experiments. Since leptons are colour singlets, any presence of hadronic activity in the detectors can only be related to the production and further decay of massive resonances. Furthermore, as electrons and positrons are fundamental particles, unlike protons, the nominal centre-of-mass energy $\sqrt{s}$ is fixed and determined by the energy of each beam, contrary to a *pp* collider. Figure 3.7 shows the cross-sections of some relevant SM processes that can be produced in $e^+e^-$ collisions as a function of $\sqrt{s}$.

However, as the incoming beams undergo acceleration before the collision, there is radiation in the form of collinear photons that tend to escape detection through the beam channel. Additionally, because of the small masses of electrons and positrons compared to the proton's, it can be seen from Eq. (3.1.1) that there is more per-cycle energy loss on an $e^+e^-$ than on a *pp* collider, which limits the achievable energy at the interaction point. For example, the Large Electron-Positron Collider (LEP) [248] was the LHC's predecessor and collided electron-positron beams at $\sqrt{s} = 209\,\text{GeV}$ in the same tunnel that the latter occupies nowadays. Hence, a much higher energy can be achieved at *pp* colliders compared to the $e^+e^-$ ones. To mitigate the energy loss due to synchrotron radiation, linear colliders (such as ILC or CLIC) can be used to achieve an even higher $\sqrt{s}$, although the incoming beams have to be accelerated over a large distance.

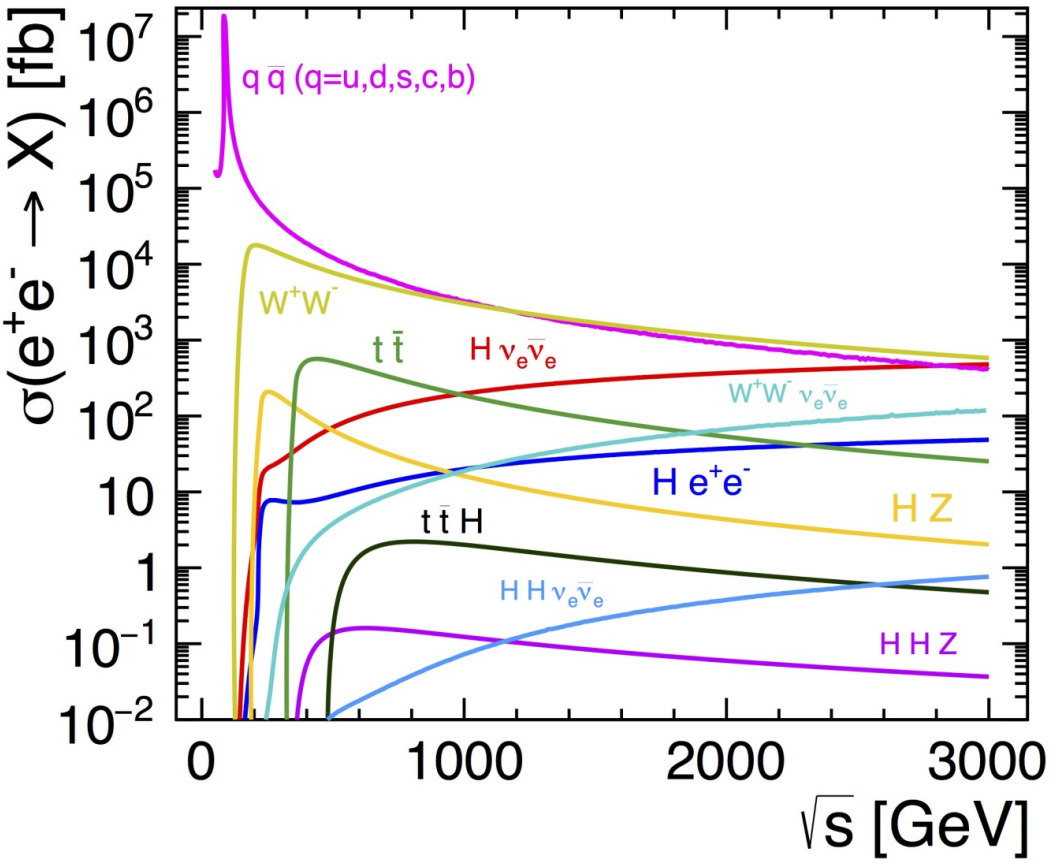


Figure 3.7: Production cross-sections $\sigma$, in fb, of some SM processes at $e^+e^-$ colliders as a function of the centre-of-mass energy $\sqrt{s}$, in GeV. Taken from Ref. [247].

In terms of the kinematics and the detection systems, $pp$ and $e^+e^-$ colliders are similar. Both types of experiments use cylindrical coordinates to characterise the four-momenta of final-state particles in the detector, although it is customary for the latter not to make use of the (pseudo) rapidity since there is no ambiguity in the collision energy of the incoming beams, and the polar angle $\theta$ suffices to describe the trajectory of a particle in the $\hat{y} - \hat{z}$ plane. Detectors such as the International Large Detector (ILD) [249] at the ILC use a layout for the detection systems similar to CMS, although the technologies implemented might vary, but overall one has to deal with the exact same set of reconstructed final-state objects. The main difference between $pp$ and $e^+e^-$ colliders in terms of the observables is the missing transverse momentum vector $\vec{\not{p}}_T$: while in the former case one needs to stick to transverse variables as explained before, the latter allows to introduce the more general *missing momentum* vector $\vec{\not{p}}$,

$$\vec{\not{p}} = -\sum_{\text{visible}} \vec{p}, \tag{3.3.1}$$

as a consequence of Eq. (3.1.2). However, as we will see in Chapter 5, four-momentum conservation can be exploited in different ways to implement analyses that target inclusive searches, so stay tuned!

Note that, unlike $pp$ colliders, in electron-positron collisions the net charge has to be zero, and there are only two possible spin assignments $|\Delta S|$ depending on the properties of the interacting $e^+e^-$ pair: $|\Delta S| = 0,\ 1$. It is possible to resolve the spin dependence of certain production processes and decay channels by reconstructing complete quark and lepton momenta, providing access to their $SU(2)\times U(1)$ quantum numbers through the observation and categorisation of spin asymmetries that are difficult to measure at $pp$ colliders, a critical ingredient for our understanding of the electroweak sector and the Higgs mechanism. The cross-sections of spin-dependent processes can be enhanced or suppressed for their study since the point-like, initial-state particles only couple through electroweak interactions: experimentally it is possible to make use of *beam polarisation* to have a certain degree of control over the chiral couplings between the $e^+e^-$ beams and the weak bosons, which play an

important role in high-energy searches for vector resonances, as well as extracting signal contributions from background processes.

### 3.3.1 The role of beam polarisation

As we saw in Sec. 1.1.2, the SM is a chiral theory since it distinguishes fermions' handedness. The opportunity at $e^+e^-$ colliders to implement beam polarisation allows us to access to the structure of interactions between fermions and weak bosons through their chiral couplings, as well as to determine the best strategies to enhance signals' cross-sections while suppressing background processes merely from an experimental configuration. Below we will broadly outline the impact of *longitudinal* beam polarisation in the physics programme of future linear electron-positron colliders, inspired by comprehensive texts like Refs. [54, 250–253]. For technical details on polarised beams, from their generation to their transportation, and for a discussion on *transverse* polarisation, see Refs. [254, 255].

For a particle of mass $m$ with momentum $\vec{p}$ and intrinsic angular momentum (spin) $\vec{\Sigma}$, we introduce the *helicity* operator $\hat{h}$ as,

$$\hat{h} = \frac{\vec{\Sigma} \cdot \vec{p}}{2\,|\vec{p}|}, \tag{3.3.2}$$

which is to be understood as the *component of spin in the direction of motion*. A particle with a helicity eigenvalue $h = +1/2$ is called *right handed*, whereas a particle with a helicity eigenvalue $h = -1/2$ is called *left handed*[10]. We define the longitudinal beam polarisation $\mathcal{P}$ as,

$$\mathcal{P} = \frac{N_R - N_L}{N_R + N_L}, \tag{3.3.3}$$

where $N_{L(R)}$ corresponds to the number of left- (right-) handed particles in a beam. Therefore, it corresponds to the number asymmetry between left- and right-handed particles in a beam: with this notation, $\mathcal{P} = 100\%$ $(-100\%)$ corresponds to a fully right- (left-) handed polarisation.

[10] In the massless limit, chirality and helicity are equivalent.

From basic tree-level QFT calculations of QED processes, such as $e^+e^- \to \mu^+\mu^-$, assuming that we do not know what the polarisation of the initial state is and neglecting the electron's mass (in the high-energy limit), then to get the *unpolarised* cross-section $\sigma_{00}$ we have to average over the four possible chiral states [1,4] as,

$$\sigma_{00} = \frac{1}{4}\left\{\sigma_{\mathrm{RR}} + \sigma_{\mathrm{LL}} + \sigma_{\mathrm{RL}} + \sigma_{\mathrm{LR}}\right\}, \tag{3.3.4}$$

where $\sigma_{\mathrm{RL}}$ corresponds to a right-handed (left-handed) positron (electron), and so on. Now let us consider the case where the electron (positron) beam has a polarisation $\mathcal{P}_{e^-}$ $\left(\mathcal{P}_{e^+}\right)$. The *polarised* cross-section $\sigma_{e^+,e^-}$ of an arbitrary process in $e^+e^-$ collisions is computed from the chiral cross-sections $\sigma_{\mathrm{RR}}$, $\sigma_{\mathrm{LL}}$, $\sigma_{\mathrm{RL}}$, $\sigma_{\mathrm{LR}}$ [252] and is given by,

$$\begin{aligned}\sigma_{e^+,e^-} = \frac{1}{4}\Big\{ &\left(1+\mathcal{P}_{e^+}\right)\left(1+\mathcal{P}_{e^-}\right)\sigma_{\mathrm{RR}} + \left(1-\mathcal{P}_{e^+}\right)\left(1-\mathcal{P}_{e^-}\right)\sigma_{\mathrm{LL}} \\ &+ \left(1+\mathcal{P}_{e^+}\right)\left(1-\mathcal{P}_{e^-}\right)\sigma_{\mathrm{RL}} + \left(1-\mathcal{P}_{e^+}\right)\left(1+\mathcal{P}_{e^-}\right)\sigma_{\mathrm{LR}}\Big\},\end{aligned} \tag{3.3.5}$$

and it can be seen that an apt choice of beam polarisation can enhance or suppress the polarised cross-section. Note that in $s$-channel (annihilation) diagrams, the helicities of the interacting initial-state particles are coupled to each other, whereas in $t$-channel (exchange) processes the initial states couple their helicities directly to the final-state objects. In the SM, $2 \to 2$ exchange processes in $e^+e^-$ collisions will only lead to final-state leptons, while annihilation channels allow for the production of quarks as well.

For illustration purposes Fig. 3.8 shows the different longitudinal spin configurations that can be achieved at $e^+e^-$ colliders with polarised beams. In Fig. 3.9 we show the interplay between beam polarisation and the cross-sections for single-Higgs production in association with a pair of leptons in $e^+e^-$ collisions, where it is made evident that polarised beams impact directly the chiral couplings of the initial-state electron-positron pair to weak bosons, which are the mediators of such processes (see Fig. 1.3).

Annihilation processes with polarised beams are of particular interest. From the

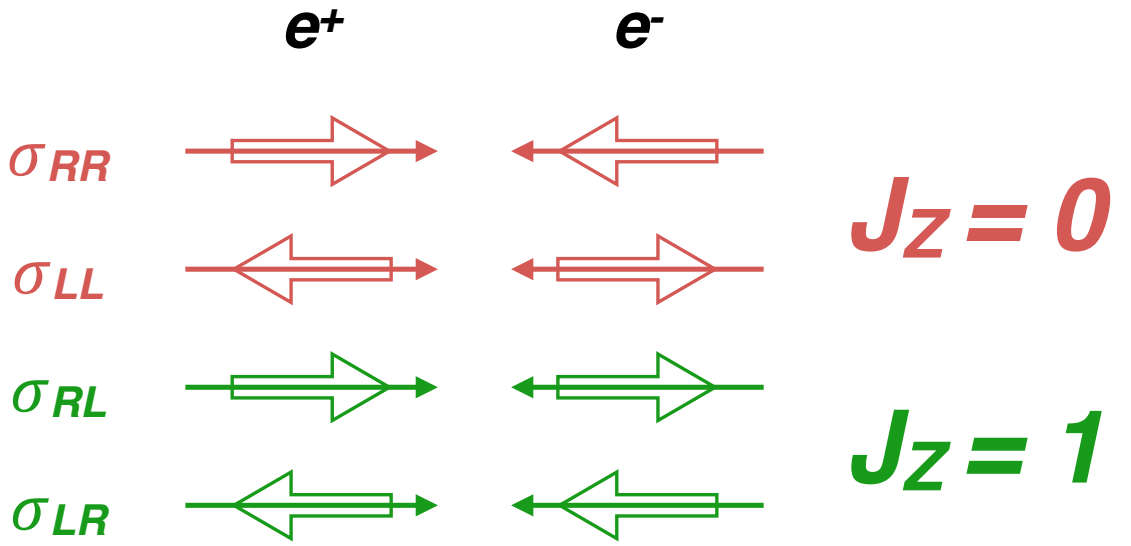


Figure 3.8: The various spin-assignment configurations in the beam direction at $e^+e^-$ colliders. The solid, thin arrow represents the direction of motion of positrons (second column) and electrons (third column), and the double arrow the projection of their spin in the $\hat{z}$ axis. For any given particle, the *right-handed* (*left-handed*) configuration corresponds to the case where both the arrows of motion and spin point in the same (opposite) direction. The first column shows the cross-section $\sigma_{e^+e^-}$ for each spin configuration of the $e^+e^-$ pair. The last column indicates the total spin projection onto the beam direction $J_Z$. Reproduced from Ref. [250].

various configurations shown in Fig. 3.8, in the SM only the $J_Z = 1$ processes are allowed at $e^+e^-$ colliders[11] through the interchange of a vector boson ($Z/\gamma^*$). BSM physics could potentially contribute to both spin configurations, and measuring the properties of the final-state objects using different settings for the initial-state polarisation would allow us to shed light on processes that might be produced at these colliders. Since each initial-state spin assignment probes on itself different processes and couplings, $e^+e^-$ can be thought of as *four colliders in one*, providing an option to enhance (suppress) the cross-sections of signal (background) processes, while accessing observables that allow to access the couplings driving the collisions.

Both $pp$ and $e^+e^-$ colliders are powerful machines that allow us to study the particle spectrum of the SM and explore whether new physics shows up at high energy scales. While $pp$ colliders can accelerate proton beams at higher energies and combine dif-

[11] Although the $J_Z = 0$ recombination into a scalar particle (Higgs boson) is possible, the $e^+e^- \to h$ process is suppressed by the small masses (Yukawa couplings) of electrons and positrons.

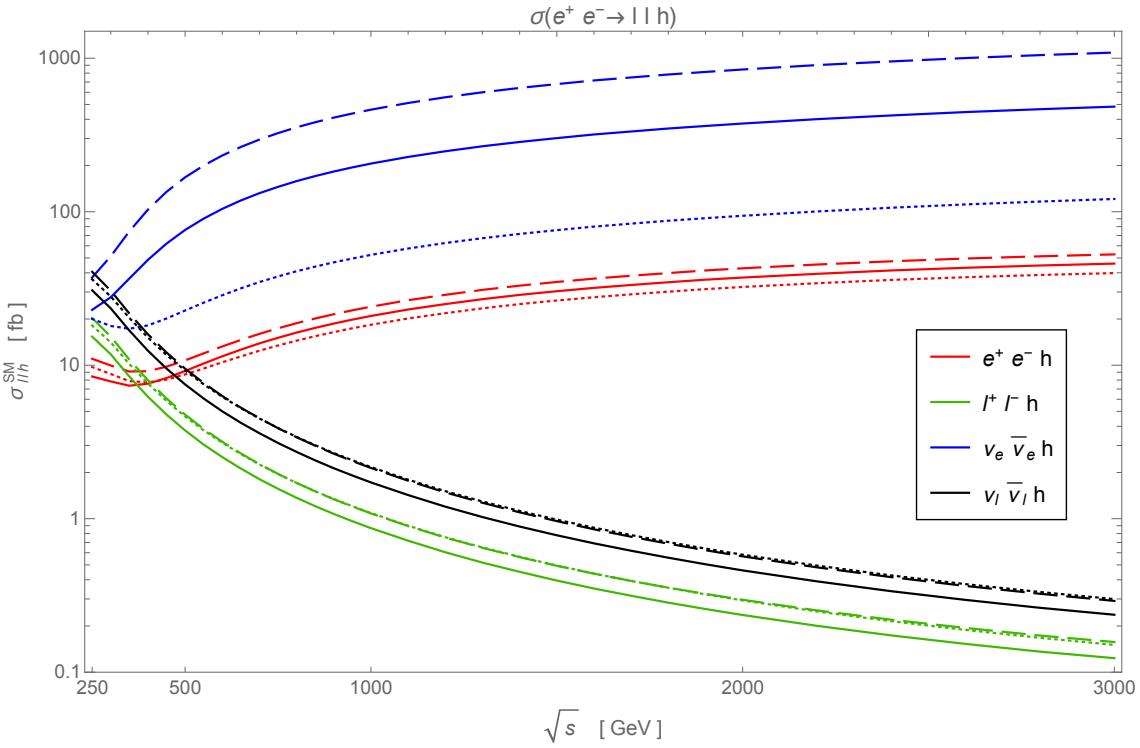


Figure 3.9: Impact of beam polarisation $P_{e^+}, P_{e^-}$ in the cross-sections $\sigma^{\rm SM}_{\ell\ell h}$, in fb, as a function of the centre-of-mass energy $\sqrt{s}$, in GeV, for the production of a Higgs boson in association with a pair of leptons at $e^+e^-$ colliders. We consider the case of unpolarised beams (solid), $P_{e^+}, P_{e^-} = +50\%, -50\%$ (dashed), and $P_{e^+}, P_{e^-} = -50\%, +50\%$ (dotted), with $\ell = \{\mu, \tau\}$.

ferent charge and spin assignments at the cost of dominant QCD backgrounds, $e^+e^-$ colliders can make use of a clean environment, as well as the impact of beam polarisation to enhance or suppress cross-sections, and exploit four-momentum conservation to extract signal processes from background noise to perform precision measurements to a high level of accuracy. In Chapters 4 and 5 we will explore the potential reach of the LHC and future linear $e^+e^-$ colliders, respectively, at constraining the possible contributions from high-energy underlying physics by combining differential distributions and total rates in the gauge-Higgs sector, illustrating more clearly what the interplay between EFT and collider phenomenology looks like.

# Chapter 4

# The Differential Golden Channel in the SMEFT

In this Chapter, based on Ref. [256], we perform our first investigation into the interplay between effective theories and measurements at colliders by considering the LHC's capability to constrain effective operators in the so-called *golden channel*. Using a technique analogous to Fourier analysis, called the *method of moments*, it is possible to use the conservation of angular momentum to disentangle the relative contributions of the decay channel $h \to 4\ell$ to its various phase-space regions in a fully differential fashion. Deviations from the distributions predicted by the SM allow us to set constraints on the gauge-Higgs anomalous couplings affecting the kinematics of the leptons originating from the decay of the Higgs boson. All equations, tables, and figures, are taken from Ref. [256].

## 4.1 Motivation

One of the main goals of the LHC is to perform and improve precision studies of Higgs couplings to weak bosons, as these will allow us to understand and disentangle the nature of EWSB. The data provided so far by the LHC that accounts for the gauge-Higgs couplings [57, 59, 70, 244, 257] needs to be complemented by differential

studies of relevant processes, such as Higgs decays to gauge bosons and $VBF/Vh$ Higgs production. Such studies would allow us to resolve the tensor structure of these couplings: upon including higher-order operators in the SMEFT expansion[1], new tensor structures for these couplings arise unavoidably. As outlined in Chapter 3, it is of great importance to develop differential strategies that probe anomalous couplings in the gauge-Higgs sector to anticipate the incoming data of the HL-LHC.

Using the method of moments [296,297], in this Chapter we present a fully differential analysis of the golden channel, $h \to 4\ell$ [298–302]. From the conservation of angular momentum, it is possible to write the full angular distributions of the final-state leptons as a sum of basis functions. The extraction of the so-called *angular moments*, analogous to Fourier analysis, allows us to study the differential distributions of the leptons reaching the detectors, hence probing the tensor structure of the gauge-Higgs coupling that corrects the SM process in the D6 SMEFT.

Current multivariate techniques, such as Optimal Observables [303], the Matrix Element Likelihood Analysis (MELA) [304, 305], or even machine-learning based methodologies [306], can be complemented by the method of moments. Although MELA is largely used by the experiments to study gauge-Higgs couplings, and it might be difficult to surpass its power, we show that the more transparent and intuitive method of moments is able to achieve bounds comparable to those of the matrix-element approach. If a deviation from the SM prediction is observed in a particular angular moment it would not only provide a hint for the distributions receiving EFT contributions but also information about the corresponding helicity amplitudes.

In Ref. [292], the method of moments was used to set bounds on the operators affecting the *Higgs-strahlung* process at the LHC. The combination of the constraints from $Vh$ and the projections obtained from our analysis of the golden channel results in stringent bounds on the EFT deformations of the gauge-Higgs couplings affected by

[1] A non-exhaustive list of other relevant SMEFT studies can be found in Refs. [167,175,176,191, 193–195, 204, 233, 240, 245, 258–295].

these processes, since complementary directions in the parameter space are probed. The remainder of this Chapter is divided as follows. The D6 operators contributing to the various vertices that are deformed for the $pp \to 4\ell$ process in the Warsaw basis are listed in Sec. 4.2. Section 4.3 shows the derivation of the amplitude's angular dependence. The method of moments is introduced in Sec. 4.4. In Sec. 4.5 we outline the collider analysis along with the angular extraction, followed by our results in Sec. 4.6. Finally, a summary is presented in Sec. 4.7.

## 4.2 The $pp \to h \to 4\ell$ in the dimension-six SMEFT

Due to its dominant cross-section compared to the remaining single-Higgs production modes at the LHC, we study the gluon-initiated $pp \to h \to 4\ell$ process, with $\ell = \{e, \mu\}$[2]. In the SM, the dominant contribution to this final-state topology is from the $h \to Z^{(*)}Z^* \to 4\ell$ process, with at least one off-shell $Z$-boson (in most of the events analysed, the resonant propagator of the $Z$-boson enhances its on-shellness). The Feynman diagram illustrating the $ggh$ process can be seen in Fig. 1.2, and the single-Higgs production cross-sections at the LHC as a function of the centre-of-mass energy are shown in Fig. 1.4.

Although the $h \to 4\ell$ decay can be driven in the SMEFT by anomalously large $h\ell^+\ell^-$ couplings, these topologies are tightly bounded[3], and as such are not comparable to the standard $h \to Z^{(*)}Z^* \to 4\ell$ channel[4]. The current bounds on the branching fractions for $h \to \gamma\gamma$ [308, 309] and $h \to Z\gamma$ [73, 74][5], and the fact that these are

[2] As discussed in Sec. 4.5, imposing a hard cut on the missing transverse energy, $\not{E}_T$, mostly eliminates stable leptons arising from $Z \to \tau\tau$, where the $\tau$'s decay leptonically.

[3] ATLAS searches for the $h \to e^+e^-$ channel [307] have set the (observed) limit on Higgs decays to electrons $\text{BR}(h \to e^+e^-) < 3.6 \times 10^{-4}$ at 95% confidence level, while the expected value is $\text{BR}(h \to e^+e^-) < 3.5 \times 10^{-4}$, which shows a great consistency with the SM expectation. In the case of Higgs decays to muons, the expected branching fraction is $\text{BR}(h \to \mu^+\mu^-) = 2.18 \times 10^{-4}$, and CMS have constrained its value to $\text{BR}(h \to \mu^+\mu^-) \in [0.8, 4.5] \times 10^{-4}$ [69].

[4] Higgs production cross-section measurements in the $h \to 4\ell$ decay channel [244] yield a global signal strength $\mu = 1.01 \pm 0.11$, in excellent agreement with the SM prediction.

[5] For HL-LHC projections, see Ref. [310].

loop-suppressed processes, makes us not consider the possibility of leptons arising from intermediate-state photons as these would need to be enhanced by at least one order of magnitude to have any sizeable impact. Moreover, the contact interaction $hZ\ell^+\ell^-$ gives rise to a new diagram that is not present in the standard theory.

Various vertices of the SM diagram for the $h \to 4\ell$ process can receive EFT corrections, namely $hZZ$ and $Z\ell^+\ell^-$, condensed in the following broken-phase Lagrangian [27, 204],

$$\begin{aligned}\Delta\mathcal{L}_6 \supset\ & \delta\hat{g}^h_{ZZ}\frac{2m_Z^2}{v}h\frac{Z^\mu Z_\mu}{2} + \sum_\ell \delta g^Z_\ell Z_\mu \bar{\ell}\gamma^\mu\ell + \sum_\ell g^h_{Z\ell}\frac{h}{v}Z_\mu\bar{\ell}\gamma^\mu\ell \\ & + \kappa_{ZZ}\frac{h}{2v}Z^{\mu\nu}Z_{\mu\nu} + \tilde{\kappa}_{ZZ}\frac{h}{2v}Z^{\mu\nu}\widetilde{Z}_{\mu\nu},\end{aligned} \tag{4.2.1}$$

where for simplicity we only include the first-generation leptons, such that the fermionic bilinear $\ell = \{e_L, e_R, \nu^e_L\}$. We further assume that the above Lagrangian can be extended to include the second and third generations, such that the lepton couplings to the $Z$-boson $\delta g^Z_\ell$ and $g^h_{Z\ell}$ are flavour-diagonal and universal in the interaction basis[6].

In the unitary gauge, the aforementioned vertices arise from operators containing the Higgs doublet. Table 4.1 shows the list of operators, in the Warsaw basis [191], contributing to the process under consideration, as well as those affecting single-Higgs production at the LHC. The correlations between D6 operators and the said

[6] This way, strong constraints can be imposed on these couplings [264, 311].

Table 4.1: List of D6 operators in the Warsaw basis contributing to various vertices of the $pp \to h \to 4\ell$ process in Eq. (4.2.1), such as the anomalous $hVV^*/hV\overline{f}f$, the effective $ggh$, Yukawa, and chromomagnetic couplings. Details about the notation can be found in Ref. [191], as well as in Appendix A.

| | |
|---|---|
| $\mathcal{O}_{H\Box} = \left(H^\dagger H\right) \Box \left(H^\dagger H\right)$ | $\mathcal{O}_{HB} = \lvert H\rvert^2 B_{\mu\nu} B^{\mu\nu}$ |
| $\mathcal{O}_{HD} = \left(H^\dagger D_\mu H\right)^* \left(H^\dagger D_\mu H\right)$ | $\mathcal{O}_{HWB} = H^\dagger \sigma^i H W^i_{\mu\nu} B^{\mu\nu}$ |
| $\mathcal{O}_{H\ell} = iH^\dagger \overleftrightarrow{D}_\mu H \overline{e}_R \gamma^\mu e_R$ | $\mathcal{O}_{HW} = \lvert H\rvert^2 W_{\mu\nu} W^{\mu\nu}$ |
| $\mathcal{O}^{(1)}_{HL} = iH^\dagger \overleftrightarrow{D}_\mu H \overline{L} \gamma^\mu L$ | $\mathcal{O}_{H\widetilde{B}} = \lvert H\rvert^2 B_{\mu\nu} \widetilde{B}^{\mu\nu}$ |
| $\mathcal{O}^{(3)}_{HL} = iH^\dagger \sigma^i \overleftrightarrow{D}_\mu H \overline{L} \sigma^i \gamma^\mu L$ | $\mathcal{O}_{H\widetilde{W}B} = H^\dagger \sigma^i H W^i_{\mu\nu} \widetilde{B}^{\mu\nu}$ |
| $\mathcal{O}_{tG} = \overline{Q}_3 \widetilde{H} T^a \sigma_{\mu\nu} t_R G^{a,\mu\nu}$ | $\mathcal{O}_{H\widetilde{W}} = \lvert H\rvert^2 W^i_{\mu\nu} \widetilde{W}^{i,\mu\nu}$ |
| $\mathcal{O}_{bG} = \overline{Q}_3 H T^a \sigma_{\mu\nu} b_R G^{a,\mu\nu}$ | $\mathcal{O}_{y_b} = \lvert H\rvert^2 \left(\overline{Q}_3 H b_R + \text{h.c.}\right)$ |
| $\mathcal{O}_{HG} = \left(H^\dagger H\right) G^a_{\mu\nu} G^{a,\mu\nu}$ | $\mathcal{O}_{y_t} = \lvert H\rvert^2 \left(\overline{Q}_3 \widetilde{H} t_R + \text{h.c.}\right)$ |

vertices are,

$$
\begin{aligned}
\delta g^Z_\ell =& -\frac{g Y_\ell s_{\theta_W}}{c^2_{\theta_W}} \frac{v^2}{\Lambda^2} c_{HWB} - \frac{g}{c_{\theta_W}} \frac{v^2}{\Lambda^2} \left(\left|T^\ell_3\right| c^{(1)}_{HL} - T^\ell_3 c^{(3)}_{HL} + \left(1/2 - \left|T^\ell_3\right|\right) c_{H\ell}\right) \\
&+ \frac{\delta m^2_Z}{m^2_Z} \frac{g}{2 c_{\theta_W} s^2_{\theta_W}} \left(T^\ell_3 c^2_{\theta_W} + Y_\ell s^2_{\theta_W}\right), \\
\delta \hat{g}^h_{ZZ} =& \frac{v^2}{\Lambda^2} \left(c_{H\Box} + \frac{c_{HD}}{4}\right), \\
g^h_{Z\ell} =& -\frac{2g}{c_{\theta_W}} \frac{v^2}{\Lambda^2} \left(\left|T^\ell_3\right| c^{(1)}_{HL} - T^\ell_3 c^{(3)}_{HL} + \left(1/2 - \left|T^\ell_3\right|\right) c_{H\ell}\right), \\
\kappa_{ZZ} =& \frac{2v^2}{\Lambda^2} \left(c^2_{\theta_W} c_{HW} + s^2_{\theta_W} c_{HB} + s_{\theta_W} c_{\theta_W} c_{HWB}\right), \\
\kappa_{GG} =& \frac{2v^2}{\Lambda^2} c_{HG}, \\
\widetilde{\kappa}_{ZZ} =& \frac{2v^2}{\Lambda^2} \left(c^2_{\theta_W} c_{H\widetilde{W}} + s^2_{\theta_W} c_{H\widetilde{B}} + s_{\theta_W} c_{\theta_W} c_{H\widetilde{W}B}\right),
\end{aligned}
\tag{4.2.2}
$$

where our input parameters are $(m_W, m_Z, \alpha_{\text{em}})$. It is important to notice that in the equation for $\delta g^Z_\ell$, the term,

$$
\frac{\delta m^2_Z}{m^2_Z} = \frac{v^2}{\Lambda^2} \left(2 t_{\theta_W} c_{HWB} + \frac{c_{HD}}{2}\right), \tag{4.2.3}
$$

shows that a linear combination of two of the previously listed operators contribute

to a shift in $m_Z$, which is one of our input parameters.

In Eq. (4.2.2), only the anomalous couplings $\delta\hat{g}^h_{ZZ}$, $\kappa_{ZZ}$, and $\widetilde{\kappa}_{ZZ}$ are relevant for our study, since the remaining ones can be probed more stringently in other processes. To begin with, the anomalous couplings $\delta g^Z_\ell$ have been tightly constrained at LEP [312] by the leptonic partial width of the $Z$-boson $\Gamma\left(Z \to \ell^+\ell^-\right)$ [264, 311], and so we neglect any corrections due to these couplings.

Any contributions from the couplings $g^h_{Z\ell}$ can be ignored since these can be stringently constrained at the HL-LHC. It can be seen that $g^h_{Z\ell}$ receive corrections from the same operators affecting $\delta g^Z_\ell$ using the D6 SMEFT correlations, apart from $c_{HWB}$ and $c_{HD}$ (which enters into the corresponding equation through the shift in $m_Z$) that contribute to $\delta g^Z_\ell$. Moreover, $c_{HWB}$ and $c_{HD}$ contribute to the anomalous (charged) *Triple Gauge Couplings* (TGCs) [313],

$$\begin{aligned} \delta g^Z_1 &= \frac{1}{2s^2_{\theta_W}}\frac{\delta m^2_Z}{m^2_Z}, \\ \delta\kappa_\gamma &= \frac{1}{t_{\theta_W}}\frac{v^2}{\Lambda^2}c_{HWB}, \end{aligned} \tag{4.2.4}$$

and so these Wilson coefficients can be constrained by other processes. Finally, plugging the above expressions for the TGCs into the correlations for $g^h_{Z\ell}$ and $\delta g^Z_\ell$ in Eq. (4.2.2) we obtain[7],

$$g^h_{Z\ell} = \frac{2g}{c_{\theta_W}} Y_\ell t^2_{\theta_W}\delta\kappa_\gamma + 2\delta g^Z_\ell - \frac{2g}{c_{\theta_W}}\left(T^\ell_3 c^2_{\theta_W} + Y_\ell s^2_{\theta_W}\right)\delta g^Z_1. \tag{4.2.5}$$

While the $\delta g^Z_\ell$ couplings have been tightly constrained at LEP as explained above, projections of the HL-LHC show that TGCs can be bounded at the per-mille level [283, 285]. Hence, tight constraints on the contact-term couplings $g^h_{Z\ell}$ using the correlation shown in Eq. (4.2.5) are expected at the HL-LHC[8]. Furthermore, future linear $e^+e^-$ colliders running at the TeV scale are machines suitable to constrain the $g^h_{Z\ell}$ couplings by probing the corresponding contact interaction through either the

[7] A derivation of these correlations is shown in Refs. [27, 204].

[8] In Ref. [284], it was shown that the contact-term couplings involving quarks can be constrained above the per-mille level at the HL-LHC.

*Higgs-strahlung* or *ZBF* channels, which is the focus of Chapter 5.

The corrections to Higgs production in the $pp \to h$ process involve five additional operators, listed in Table 4.1: Yukawa operators $\mathcal{O}_{y_b,y_t}$, chromomagnetic operator $\mathcal{O}_{tG,bG}$, and effective gluon-Higgs operator $\mathcal{O}_{HG}$ [314, 315]. As will be discussed in the following sections, we perform our study in the rest frame of the Higgs boson, so that these operators will only affect the total rate and do not have an impact on the leptons' distributions, since these can be decoupled. However, since the couplings $\delta\hat{g}^h_{ZZ}$ affect only the total rate too, the effects of the D6 operators mentioned above yield the redefinition,

$$\left(1+\delta\hat{g}^h_{ZZ}\right) \to \left(1+\delta\hat{g}^h_{ZZ}\right)\left(1+f\left(c_{HG},c_{y_t},c_{y_b},c_{tG},c_{bG}\right)\right), \tag{4.2.6}$$

where $f\left(c_{HG},c_{y_t},c_{y_b},c_{tG},c_{bG}\right)$ corresponds to a linear combination of the shown Wilson coefficients [314, 315]. Hence, the contributions due to the operators affecting the $pp \to h$ process need to be studied using other production modes, such as $t\bar{t}h$ or $h$+jets, and decay channels more sensitive to the effects of these couplings.

Non-Higgs processes also receive EFT contributions. Considering the dominant background $q\bar{q} \to 4\ell$, corrections arise from the TGCs and $Z$-coupling deviations $\delta g^Z_\ell$ which, as previously mentioned, can be tightly constrained by looking into other processes. As discussed in Sec. 4.5, the subleading $gg \to 4\ell$ background is much smaller than the dominant $q\bar{q} \to 4\ell$ process and the SM-driven signal $pp \to h \to 4\ell$, and so EFT modifications parametrised by anomalous vertices, such as $t\bar{t}g$ or $t\bar{t}Z$, will not be considered. Although the $gg \to h \to 4\ell$ amplitude interferes with the $gg \to ZZ \to 4\ell$ continuum, we neglect this effect since, as explained in Sec. 4.5, our signal region is defined at invariant masses close to $m_h$, where the modification to the total cross-section is negligible with respect to the $gg \to h \to 4\ell$ process [316].

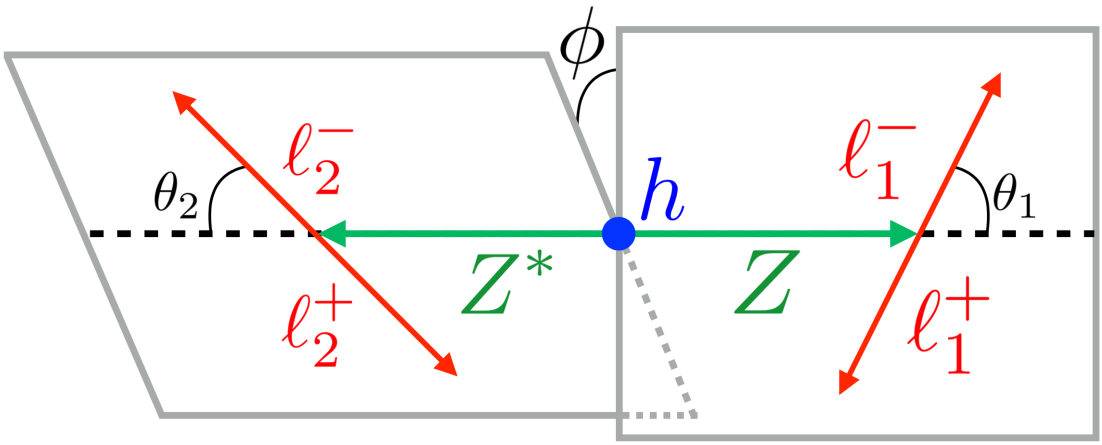


Figure 4.1: Definition of the various scattering angles for the sequential decay $h \to ZZ^* \to \left(\ell_1^+\ell_1^-\right)\left(\ell_2^+\ell_2^-\right)$ (see text for details). Following the convention used in Ref. [317], we use two different reference frames to compute i) the azimuthal angle $\phi$ between the planes containing the lepton pairs in the Higgs rest frame, and ii) the polar angle $\theta_i$ ($i = \{1, 2\}$) of the lepton in its parent $Z$-boson rest frame measured with respect to the direction of motion of $Z_i$ in the Higgs rest frame. Both frames contain back-to-back objects.

## 4.3 Angular dependence of the $h \to 4\ell$ amplitude

As explained in the previous section, due to the dominant cross-section at the LHC of single-Higgs production through the $ggh$ mode, the main contribution to the $pp \to h \to 4\ell$ process comes from $gg \to h \to 4\ell$, where Higgs decays are mediated by a $Z^{(*)}Z^*$ pair in the SM. In the D6 SMEFT, two processes can contribute to the $h \to 4\ell$ mode: the first involves modifications to the $hZZ$ vertex through the insertion of the $\delta\hat{g}^h_{ZZ}$, $\kappa_{ZZ}$, and $\tilde{\kappa}_{ZZ}$ couplings in a diagram similar to the SM process with two intermediate $Z$-bosons, and the second corresponds to an amplitude that contains a contact interaction of the form $hZ\ell^+\ell^-$ as shown in Eq. (4.2.5), induced by the $\mathcal{O}_{HL,\ell}$ operators (see Table 4.1), with the single $Z$-boson decaying leptonically [9].

Our goal is to analyse the angular variables and their differential distributions, which we describe next. As shown in Fig. 4.1, the final-state lepton pairs are defined by three angles in two different reference frames, and we use the fact that in the

[9] In both diagrams there are two fermion currents, where at least one is coupled to a vector.

experiment the leptons can be characterised by their electric charges. However, in calculating the analytic expressions of the angular distributions it is more convenient to consider the final-state leptons with definite helicity[10], so we will refer to the angles defined by the positive-helicity lepton for the remainder of this section, unless stated otherwise[11]. In what follows, we will modify our notation and denote the two-lepton states as an $\ell_+\ell_-$ system, where the subscript $+$ $(-)$ indicates a positive-(negative-) helicity lepton. From this point on, we will drop the superscripts referring to the lepton's charge, and will use instead $\bar{\ell}$ to refer to the antilepton $\left(\ell^+\right)$, unless stated otherwise, to aid readibility.

In Fig. 4.1, the polar angles $\theta_i$ $(i = \{1, 2\})$ are measured from the three-momentum of $\ell_{i,+}$ to the direction of motion of its parent $\ell_{i,+}\ell_{i,-}$ system, evaluated in the $\ell_{i,+}\ell_{i,-}$ rest frame, where we have back-to-back lepton momenta. Further, for each $\ell_+\ell_-$ system we consider the azimuthal angle $\varphi_i$ that describes the orientation of the plane containing the two-lepton momenta, evaluated in the four-lepton centre-of-mass frame[12], with respect to the scattering plane; then, we define $\phi$ as the relative azimuthal angle between the two said planes. A more concise explanation on the definition of these angles and planes is given in Sec. 4.5.2.

As noted above, the structure of the lepton currents is such that in the massless limit each $\ell_+\ell_-$ system has two opposite-helicity leptons, with $\lambda = \pm 1/2$. In the $\ell_+\ell_-$ centre-of-mass frame, the total angular momentum $J$ of each two-lepton state and its projection $M$ along the direction of motion of the $\ell_+\ell_-$ system uniquely determine the angular dependence of the amplitude. More specifically, the total amplitude is proportional to the *Wigner d-functions*[13] $d^J_{M,\Delta\lambda=1}(\theta_i, \varphi_i)$ for both final-state $\ell_+\ell_-$ pairs, where the angles are evaluated with respect to the momentum of the positive-helicity leptons as explained above, and $\Delta\lambda \equiv \lambda_{\ell_+} - \lambda_{\ell_-} = 1$. Since the $\ell_+\ell_-$ pair comes from the decay of a $Z$-boson, $J = 1$ and $M = \{0, \pm 1\}$ depending

[10] In the massless limit each outgoing lepton and antilepton have opposite helicities.

[11] A translation from fixed helicity to fixed charge is provided in subsection 4.3.3.

[12] This frame is equivalent to the frame where the Higgs boson is at rest.

[13] The study of the analytic structure of said functions is beyond the scope of this Thesis. For details on the subject, see Ref. [318].

on the helicity of the vector. Hence, the Wigner $d$-functions describing the angular dependence of the amplitude are,

$$\begin{aligned} d^1_{+1,\Delta\lambda=+1}(\theta_i,\varphi_i) &= \cos^2(\theta_i/2)\, e^{+i\varphi_i}, \\ d^1_{-1,\Delta\lambda=+1}(\theta_i,\varphi_i) &= \sin^2(\theta_i/2)\, e^{-i\varphi_i}, \\ d^1_{0,\Delta\lambda=+1}(\theta_i,\varphi_i) &= \frac{\sin\theta_i}{\sqrt{2}}. \end{aligned} \tag{4.3.1}$$

Consequently, studying the helicity amplitudes corresponding to the $h \to ZZ^*$ and $h \to Z\bar{\ell}\ell$ processes is crucial, and these are shown in subsections 4.3.1 and 4.3.2.

### 4.3.1 Helicity amplitudes for $ZZ^*$ production

The process $h \to ZZ^*$ consists of a scalar particle decaying into two states— in the scalar rest frame, the two-body system has a total angular momentum $J = 0$. To guarantee that $M = 0$, the two final-state objects, having back-to-back momenta, should have the same helicities[14]. Hence, the helicity configurations that are allowed for the $ZZ^*$ final states are, following our earlier notation to denote the helicity of an object, $Z_+Z_+$, $Z_-Z_-$, and $Z_0Z_0$, with their corresponding helicity amplitudes $\mathcal{A}_{++}$, $\mathcal{A}_{--}$, and $\mathcal{A}_{00}$, respectively.

The $hZZ^*$ interactions that we are looking into can deviate from the SM if these are indeed induced by the two $CP$-even $\delta\hat{g}^h_{ZZ}$ and $\kappa_{ZZ}$ effective couplings, which contribute to $\mathcal{A}_{++}$, $\mathcal{A}_{--}$, and $\mathcal{A}_{00}$, whereas the $CP$-odd $\widetilde{\kappa}_{ZZ}$ coupling only contributes to the transverse amplitudes $\mathcal{A}_{++}$ and $\mathcal{A}_{--}$. The helicity amplitudes for the $h \to ZZ^*$ process are,

$$\begin{aligned} \mathcal{A}_{++} &= -2\frac{\left(\delta\hat{g}^h_{ZZ}+1\right)m_Z^2}{v} + 2\frac{\kappa_{ZZ}}{v}\gamma_a m_Z m_{Z^*} - 2i\frac{\widetilde{\kappa}_{ZZ}}{v}\gamma_b m_Z m_{Z^*}, \\ \mathcal{A}_{--} &= -2\frac{\left(\delta\hat{g}^h_{ZZ}+1\right)m_Z^2}{v} + 2\frac{\kappa_{ZZ}}{v}\gamma_a m_Z m_{Z^*} + 2i\frac{\widetilde{\kappa}_{ZZ}}{v}\gamma_b m_Z m_{Z^*}, \\ \mathcal{A}_{00} &= -2\frac{\left(\delta\hat{g}^h_{ZZ}+1\right)m_Z^2}{v}\gamma_a - 2\frac{\kappa_{ZZ}}{v}\frac{1}{m_Z m_{Z^*}}, \end{aligned} \tag{4.3.2}$$

[14] It is important to remember that $M$ can take $(2J+1)$ values, $M \in [-J,\ldots,0,\ldots,J]$.

where the Lorentz factors $\gamma_{a,b}$ are defined as,

$$\begin{aligned}\gamma_a &\equiv \frac{1}{m_Z m_{Z^*}}\left(E_1 E_2 + |\vec{q}|^2\right) = \frac{1}{m_Z m_{Z^*}} q_Z \cdot q_{Z^*},\\ \gamma_b &\equiv \frac{1}{m_Z m_{Z^*}} |\vec{q}|\,(E_1 + E_2) = \frac{1}{m_Z m_{Z^*}} |\vec{q}|\, m_h,\end{aligned} \tag{4.3.3}$$

where $\vec{q} = \vec{q}_Z = -\vec{q}_{Z^*}$ are the three-momenta of the $Z$-bosons in the rest frame of the Higgs, and $m^2_{Z^{(*)}} = q^2_{Z^{(*)}}$ is the squared invariant mass of the on- (off-) shell $Z$-boson. In Eq. (4.3.2) above, the term independent from $\delta\hat{g}^h_{ZZ}$, $\kappa_{ZZ}$, and $\widetilde{\kappa}_{ZZ}$ corresponds to the SM amplitude.

Although we have analysed the structure of the $h \to ZZ^*$ amplitude, the final lepton angles that we are interested in are actually determined by the helicities of the vector bosons. Summing over the allowed polarisations of the intermediate bosons, the $h \to ZZ^* \to \ell_+\ell_-\ell_+\ell_-$ helicity amplitude is,

$$\begin{aligned}&\mathcal{M}\left(h \to ZZ^* \to \ell^1_+\ell^1_-\ell^2_+\ell^2_-\right) = g^Z_{\ell_1} g^{Z^*}_{\ell_2}\,\mathcal{A}\left(h \to ZZ^* \to \ell^1_+\ell^1_-\ell^2_+\ell^2_-\right)\\ &\sim \sum_{\bar{\lambda}\bar{\lambda}'} \mathcal{A}\left(h \to Z_{\bar{\lambda}} Z^*_{\bar{\lambda}'}\right) \frac{-g^Z_{\ell_1}}{q^2_Z - m^2_Z + i\Gamma_Z m_Z}\mathcal{A}\left(Z_{\bar{\lambda}} \to \ell^1_+\ell^1_-\right)\\ &\qquad\qquad \times \frac{-g^{Z^*}_{\ell_2}}{q^2_{Z^*} - m^2_Z + i\Gamma_Z m_Z}\mathcal{A}\left(Z^*_{\bar{\lambda}'} \to \ell^2_+\ell^2_-\right)\\ &\propto \sum_{\bar{\lambda}} \mathcal{A}\left(h \to Z_{\bar{\lambda}} Z^*_{\bar{\lambda}}\right) \frac{-g^Z_{\ell_1}}{q^2_Z - m^2_Z + i\Gamma_Z m_Z} d^1_{\bar{\lambda},\Delta\lambda=1}(\theta_1,\varphi_1)\\ &\qquad\qquad \times \frac{-g^{Z^*}_{\ell_2}}{q^2_{Z^*} - m^2_Z + i\Gamma_Z m_Z} d^1_{\bar{\lambda},\Delta\lambda=1}(\theta_2,-\varphi_2)\,,\end{aligned} \tag{4.3.4}$$

where $\mathcal{A}\left(h \to ZZ^* \to \ell^1_+\ell^1_-\ell^2_+\ell^2_-\right)$ and $\mathcal{A}\left(Z^{(*)}_{\bar{\lambda}^{(\prime)}} \to \ell^{1(2)}_+\ell^{1(2)}_-\right)$ are the amplitudes with the $Z$-lepton couplings factorised in front. In the equation above, the parameter

$$g^{Z^{(*)}}_{\ell_i} = \frac{g}{2c_{\theta_W}}\left(T_{3,\ell} - Q_\ell s^2_{\theta_W}\right)$$

corresponds to the SM chirality-dependent coupling of the $Z$-boson to the lepton $\ell = \ell_{L,R}$. Fixing the helicity results in different chiralities for leptons and antileptons, since *positive helicity corresponds to left-hand chirality for positive-charge leptons, and to right-hand chirality for negative-charge leptons* (discussed in Sec. 4.3.3). In Eq. (4.3.4), $\bar{\lambda}^{(\prime)}$ is the helicity of the $Z^{(*)}$-boson, and in going from the second to the

third line we use the fact that $\bar{\lambda} = \bar{\lambda}'$ in the rest frame of the Higgs.

The polarisation of the intermediate vectors determines the form of the angular dependence, which is made explicit in Eq. (4.3.4) and encoded in the Wigner $d$-functions. Since the Breit-Wigner propagators are independent of the vectors' helicities, these can be factored out. However, the $\mathcal{A}(h \to Z_{\bar{\lambda}} Z^*_{\bar{\lambda}})$ helicity amplitude depends on the polarisation $\bar{\lambda}$ and receives BSM corrections, so the lepton angular observables are sensitive to deviations from the SM that impact their differential distributions. Then, the $\mathcal{A}_{++}$, $\mathcal{A}_{--}$, and $\mathcal{A}_{00}$ amplitudes are each multiplied by products of two Wigner $d$-functions $d^1_{\bar{\lambda},\Delta\lambda=1}$, encoded in a set of angular functions $f_{++}$, $f_{--}$, and $f_{00}$, as,

$$\begin{aligned} f_{++} &= \cos^2\left(\frac{\theta_1}{2}\right)\cos^2\left(\frac{\theta_2}{2}\right)e^{+i\phi}, \\ f_{--} &= \sin^2\left(\frac{\theta_1}{2}\right)\sin^2\left(\frac{\theta_2}{2}\right)e^{-i\phi}, \\ f_{00} &= \frac{\sin\theta_1 \sin\theta_2}{2}, \end{aligned} \tag{4.3.5}$$

where $\phi = \varphi_1 - \varphi_2$. Notice that, if we choose to compute the angles for the negative-helicity lepton, the $d^1_{\bar{\lambda},\Delta\lambda=-1}$ Wigner $d$-functions enter in the amplitude.

Although so far we have assumed that there is an on-shell $Z$-boson, it might be the case that both vectors are off-shell, in which case $m_Z m_{Z^*} \to m_{Z_1^*} m_{Z_2^*}$ in Eqs. (4.3.2) and (4.3.3). However, the cross-section of said process is suppressed with respect to the one with an on-shell $Z$-boson due to the resonant enhancement of the latter, as can be seen from Eq. (4.3.4). As discussed in Sec. 4.5, the collider analysis selects one pair of leptons with invariant mass around $m_Z$, which happens in the majority of the cases.

### 4.3.2 Helicity amplitudes for $Z\bar{\ell}\ell$ production through $hZ\bar{\ell}\ell$ contact interactions

We now discuss the contribution of the anomalous couplings $g^h_{Z\ell}$ to the angular distributions derived in subsection 4.3.1. As we mentioned before, we do not consider

the effect of these vertices in our numerical analysis, although we keep track of them in our analytical expressions. Here we show how the corrections due to $g^h_{Z\ell}$ in the $h \to 4\ell$ amplitude can be understood as a shift in the coupling $g^{Z^*}_{\ell_2}$ of the off-shell $Z$-boson to the leptons in Eq. (4.3.4). Even in the case of the amplitude with an insertion of a $hZ\bar{\ell}\ell$ contact term, the angular modulation turns out to be completely described by $d^1_{M,\Delta\lambda=1}(\theta,\varphi)$ functions.

Under Lorentz transformations, the fermion bilinear in the operator $hZ_\mu\bar{\ell}\gamma^\mu\ell$ does so as a vector, which means that the contact interaction has the form $hZ_\mu V^\mu$, where $V^\mu$ is a spin-one object. Hence, the two-lepton system $\ell_+\ell_-$ in the $g^h_{Z\ell}$ vertex has $J = 1$. As discussed in the previous sections, the $h \to ZV$ decay evaluated in the rest frame of the scalar must have $J = 0$, implying that $Z$ and $V$ have the same helicity, which holds independently of the form of the interaction. Consequently, in the centre-of-mass frame of the $\ell_+\ell_-$ system, the quantum number $M$ equals the helicity of the emitted $Z$-boson. Thus, the angular modulation in these contact interactions is the same as that for leptons produced from the decay of an intermediate $Z$-boson; in other words, the angular observables are described by $d^1_{M,\Delta\lambda=1}(\theta,\varphi)$ and are determined by the helicity $\bar{\lambda} = M$ of the $Z$-boson present in the contact interaction.

In the SM, the $hZZ$ vertex is $hZ_\mu Z^\mu$. It can be seen that the form of the contact interaction $hZ_\mu V^\mu$ is analogous to the SM case, so the amplitudes are the same for all the helicity configurations $\mathcal{A}_{++}$, $\mathcal{A}_{--}$, and $\mathcal{A}_{00}$: the $g^h_{Z\ell}$ contribution to the $h \to Z2\ell \to 4\ell$ process is equivalent to a shift in the SM $\mathcal{M}(h \to ZZ^* \to 4\ell)$ amplitude in Eq. (4.3.4), which can be expressed as a shift in the $g^{Z^*}_{\ell_2}$ coupling,

$$g^{Z^*}_{\ell_2} \to g^{Z^*}_{\ell_2} - g^h_{Z\ell_2}\frac{m_Z^2 - m_{Z^*}^2 - i\Gamma_Z m_Z}{2m_Z^2}. \tag{4.3.6}$$

So far, our heuristic reasoning has assumed that there is an on-shell $Z$-boson involved in the described vertex. However, it is possible to have an off-shell $Z$-boson radiated off the $g^h_{Z^*\ell}$ contact interaction, although its cross-section is suppressed with respect to the on-shell case since the former does not receive resonance enhancement.

### 4.3.3 Visible angular modulation

Experimentally, it is not possible to determine the helicities of the final-state leptons. For this reason, although so far we have evaluated the angles for leptons with $\lambda = +\frac{1}{2}$, in the angular analysis of the $h \to 4\ell$ helicity amplitudes the electric charge is instead fixed. We now consider the angles subtended by the negatively charged leptons $\ell^i$ (see Fig. 4.1 and Sec. 4.5 for further details), since at colliders it is possible to resolve the electric charge of the leptons reaching the detectors. Our squared amplitude should then be summed over the four possible helicity configurations $\overline{\ell^1_\pm}\ell^1_\mp$, $\overline{\ell^2_\pm}\ell^2_\mp$,

$$\left|\mathcal{M}\left(h \to \overline{\ell^1}\ell^1\overline{\ell^2}\ell^2\right)\right|^2 = \sum_{\lambda,\lambda'} \left|\mathcal{M}\left(h \to \overline{\ell^1_{-\lambda}}\ell^1_\lambda \overline{\ell^2_{-\lambda'}}\ell^2_{\lambda'}\right)\right|^2 . \tag{4.3.7}$$

In the cases with $\ell^i_{\lambda=+\frac{1}{2}}$, the differential distribution coincides with the emission angles $\theta^i$ and $\varphi^i$ entering in Eq. (4.3.4). Whenever $\ell^i_{\lambda=-\frac{1}{2}}$, the measured angles $\theta^i$ and $\varphi^i$ refer to the negative-helicity leptons and, in consequence, the angular distributions are described by the Wigner $d$-functions,

$$d^1_{\lambda,\Delta\lambda=-1}(\theta,\varphi) = d^1_{\lambda,\Delta\lambda=+1}(\pi-\theta,\pi+\varphi). \tag{4.3.8}$$

As mentioned in subsection 4.3.1, since positive helicity corresponds to positive charge in the case of left-handed leptons and to negative charge for right-handed leptons, taking the angles $\theta$ and $\phi$ (or equivalently $\varphi$) into account for negative-charge leptons leaves the angular definition for right-handed leptons unchanged. In the case of left-handed chirality $(\theta,\phi) \to (\pi-\theta,\phi+\pi)$ in the angular functions shown in Eq. (4.3.5). Thus, the total squared amplitude of the physical process $h \to 4\ell$ observed at the collider can be expressed as,

$$\begin{aligned}\left|\mathcal{M}\left(h \to \overline{\ell^1}\ell^1\overline{\ell^2}\ell^2\right)\right|^2 =& \Big( g^{Z\,2}_{\ell_R} g^{Z^*\,2}_{\ell_R} \left|\mathcal{A}\left(\theta_1,\theta_2,\phi\right)\right|^2 \\ &+ g^{Z\,2}_{\ell_L} g^{Z^*\,2}_{\ell_L} \left|\mathcal{A}\left(\pi-\theta_1,\pi-\theta_2,\phi\right)\right|^2 \\ &+ g^{Z\,2}_{\ell_L} g^{Z^*\,2}_{\ell_R} \left|\mathcal{A}\left(\pi-\theta_1,\theta_2,\pi+\phi\right)\right|^2 \\ &+ g^{Z\,2}_{\ell_R} g^{Z^*\,2}_{\ell_L} \left|\mathcal{A}\left(\theta_1,\pi-\theta_2,\pi+\phi\right)\right|^2 \Big),\end{aligned} \tag{4.3.9}$$

with $\mathcal{A}(\theta_1, \theta_2, \phi) = \mathcal{A}\left(h \to \ell^1_+ \ell^1_- \ell^2_+ \ell^2_-\right)(\theta_1, \theta_2, \phi)$ the helicity amplitude in Eq. (4.3.4), where the angles are evaluated with respect to the positive-helicity leptons, and the $Z$-lepton couplings $g^{Z^{(*)}}_{\ell_{L(R)}}$ have been factorised out.

## 4.4 The method of moments

Using the results derived in the previous section, we now show that the squared amplitude of the $h \to 4\ell$ process can be expressed as the sum of a set of angular functions, both in the SM and D6 SMEFT. In doing so, we discuss both the technique that allows us to extract the coefficients of these functions, so-called *angular moments*, and the corresponding estimates of the uncertainties. As mentioned in Sec. 4.1, the method of moments is analogous to Fourier analysis; for illustrative purposes, an overview of the basic elements of Fourier analysis in calculating Fourier series is presented in Appendix B.

### 4.4.1 Angular moments for $h \to 4\ell$

The total cross-section of the $gg \to h \to 4\ell$ process is obtained by summing the squared amplitudes in Eq. (4.3.9), noting that it is induced by the contributions of the cases studied in subsections 4.3.1 and 4.3.2. As seen from Eq. (4.3.5), it is a

linear combination of the functions,

$$
\begin{aligned}
f_1 &= \sin^2\theta_1 \sin^2\theta_2, \\
f_2 &= \left(\cos^2\theta_1 + 1\right)\left(\cos^2\theta_2 + 1\right), \\
f_3 &= \sin\left(2\theta_1\right)\sin\left(2\theta_2\right)\cos\phi, \\
f_4 &= \left(\cos^2\theta_1 - 1\right)\left(\cos^2\theta_2 - 1\right)\cos\left(2\phi\right), \\
f_5 &= \sin\theta_1 \sin\theta_2 \cos\phi, \\
f_6 &= \cos\theta_1 \cos\theta_2, \\
f_7 &= \left(\cos^2\theta_1 - 1\right)\left(\cos^2\theta_2 - 1\right)\sin\left(2\phi\right), \\
f_8 &= \sin\theta_1 \sin\theta_2 \sin\phi, \\
f_9 &= \sin\left(2\theta_1\right)\sin\left(2\theta_2\right)\sin\phi,
\end{aligned}
\tag{4.4.1}
$$

which depend on the angles of the negatively charged leptons as discussed previously (see Fig. 4.1), and where the $f_7$, $f_8$, and $f_9$ functions appear in the *CP*-odd terms (linear in the $\widetilde{\kappa}_{ZZ}$ coupling). Our results are in agreement with those shown in Ref. [317].

The nine angular functions shown in Eq. (4.4.1) arise in the computation of the cross-section in Eq. (4.3.9), and the angular moments are the coefficients accompanying said functions. These angular moments can be written as a function of the couplings

$\delta\hat{g}^h_{ZZ}$, $\kappa_{ZZ}$, $\widetilde{\kappa}_{ZZ}$, and $g^h_{Z\ell}$, as,

$$
\begin{aligned}
a_1 &= \mathcal{G}^4\left((1+\delta a)+\frac{bm_{Z^*}\gamma_b^2}{m_Z\gamma_a}\right)^2,\\
a_2 &= \mathcal{G}^4\left(\frac{(1+\delta a)^2}{2\gamma_a^2}+\frac{2c^2m_{Z^*}^2\gamma_b^2}{m_Z^2\gamma_a^2}\right),\\
a_3 &= -\mathcal{G}^4\left(\frac{1+\delta a}{2\gamma_a}+\frac{bm_{Z^*}\gamma_b^2}{2m_Z\gamma_a^2}\right)^2,\\
a_4 &= \mathcal{G}^4\left(\frac{(1+\delta a)^2}{2\gamma_a^2}-\frac{2c^2m_{Z^*}^2\gamma_b^2}{m_Z^2\gamma_a^2}\right),\\
a_5 &= -\varepsilon^2\mathcal{G}^4\left(\frac{2\,(1+\delta a)^2}{\gamma_a}+\frac{2\,(1+\delta a)\,bm_{Z^*}\gamma_b^2}{m_Z\gamma_a^2}\right),\\
a_6 &= \varepsilon^2\mathcal{G}^4\left(\frac{2\,(1+\delta a)^2}{\gamma_a^2}+\frac{8c^2m_{Z^*}^2\gamma_b^2}{m_Z^2\gamma_a^2}\right),\\
a_7 &= \mathcal{G}^4\frac{2\,(1+\delta a)\,cm_{Z^*}\gamma_b}{m_Z\gamma_a^2},\\
a_8 &= -\varepsilon^2\mathcal{G}^4\left(\frac{4\,(1+\delta a)\,cm_{Z^*}\gamma_b}{m_Z\gamma_a}+\frac{4bcm_{Z^*}^2\gamma_b^3}{m_Z^2\gamma_a^2}\right),\\
a_9 &= -\mathcal{G}^4\left(\frac{(1+\delta a)\,cm_{Z^*}\gamma_b}{m_Z\gamma_a}+\frac{bcm_{Z^*}^2\gamma_b^3}{m_Z^2\gamma_a^2}\right),
\end{aligned}
\tag{4.4.2}
$$

where $\varepsilon^2$ can be understood in the SM as a measure of the asymmetry between $Z$-boson couplings to left- and right-handed leptons,

$$
\varepsilon^2=\left(\frac{\left(g^Z_{\ell_L}\right)^2-\left(g^Z_{\ell_R}\right)^2}{\left(g^Z_{\ell_L}\right)^2+\left(g^Z_{\ell_R}\right)^2}\right)^2\approx 0.16^2=0.0256. \tag{4.4.3}
$$

From Eqs. (4.4.2) and (4.4.3) it can be seen that the angular moments $a_5$, $a_6$, and $a_8$ are numerically suppressed and contribute only marginally to the numerical bounds. To understand the suppression of these angular moments, let us consider how $f_6$ in Eq. (4.4.1) depends on $\cos\theta_1\cos\theta_2$ by looking at Eq. (4.3.9): in the second term, $\cos\theta_1\cos\theta_2$ retains its sign after $(\theta_1,\theta_2)\to(\pi-\theta_1,\pi-\theta_2)$, whereas having only one left-handed lepton with negative helicity in the third and fourth terms implies $\cos\theta_1\cos\theta_2\to-\cos\theta_1\cos\theta_2$, which gives rise to a factor of $\varepsilon^2$ in the squared amplitude, making its contribution numerically small. The charge-helicity interplay can lead to a partial or even complete cancellation of the angular distributions since

it is not possible to access the helicity of the lepton at the detector level[15].

In Eq. (4.4.2),

$$\mathcal{G}^4 = \left(\left(g^Z_{\ell_L}\right)^2 + \left(g^Z_{\ell_R}\right)^2\right)\left(\left(g^{Z^*}_{\ell_L}\right)^2 + \left(g^{Z^*}_{\ell_R}\right)^2\right), \tag{4.4.4}$$

contains the effect of the contact terms $g^h_{Z\ell}$ through the shift of the $g^{Z^*}_{\ell_2}$ coupling in Eq. (4.3.6), and we choose a normalisation such that $a_1^{\rm SM} = \mathcal{G}^4$. The Lorentz factors $\gamma_{a,b}$ are defined in Eq. (4.3.3), and the variables $\delta a$, $b$, and $c$, are,

$$\begin{aligned} \delta a &= \delta\hat{g}^h_{ZZ} - \kappa_{ZZ}\gamma_a \frac{m_{Z^*}}{m_Z}\frac{m_Z^2 - m_{Z^*}^2}{2m_Z^2}, \\ b &= \kappa_{ZZ}, \\ c &= -\frac{\widetilde{\kappa}_{ZZ}}{2}. \end{aligned} \tag{4.4.5}$$

### 4.4.2 Basics of the method of moments

As seen in the previous subsection, the squared amplitude of the $h \to 4\ell$ process under study can be written as a linear combination of a set of angular functions $f_i(\theta_1, \theta_2, \phi)$ that are parametrised by the angular moments $a_i$. We now explain how to extract the $a_i$ coefficients considering the method of moments [296, 297], a powerful technique for smaller datasets [319, 320].

For clarity, we can view this technique as an analog of Fourier analysis (see Appendix B). The basic idea is, given a set of angular functions $\{f_i\}_i$, to seek for a dual basis $\left\{w_j\right\}_j$ of 'weight functions' $w_j(\theta_1, \theta_2, \phi)$ that can extract all the coefficients $a_i$ unambiguously,

$$\begin{aligned} &\int_0^\pi \mathrm{d}\theta_1 \int_0^\pi \mathrm{d}\theta_2 \int_0^{2\pi} \mathrm{d}\phi \sum_i (a_i f_i)\, w_j \sin\theta_1 \sin\theta_2 = a_j, \\ \Rightarrow \quad &\int_0^\pi \mathrm{d}\theta_1 \int_0^\pi \mathrm{d}\theta_2 \int_0^{2\pi} \mathrm{d}\phi f_i w_j \sin\theta_1 \sin\theta_2 = \delta_{ij}, \end{aligned} \tag{4.4.6}$$

where the linear combination $\sum_i a_i f_i$ corresponds to the total rate, as described before. This essentially means that the weight $w_j$ is able to project the total rate onto the angular coefficients $a_j$, and we can assume these weight functions $w_i(\theta_1, \theta_2, \phi)$ to be

[15] This statement implies that, in general, by averaging over all the helicity configurations the information encoded *a priori* in the angular functions (see Eq. (4.3.5)) is partly washed away.

linear combinations of the functions in the original basis,

$$w_j = \lambda_{ij} f_i. \tag{4.4.7}$$

Using Eq. (4.4.6) it is possible to show that $\lambda_{ij} = M_{ij}^{-1}$, with,

$$M_{ij} = \int_0^{\pi} \mathrm{d}\theta_1 \int_0^{\pi} \mathrm{d}\theta_2 \int_0^{2\pi} \mathrm{d}\phi f_i f_j \sin\theta_1 \sin\theta_2. \tag{4.4.8}$$

In other words, we assume that the $\left\{w_j\right\}_j$ set is a linear transformation of the $\{f_i\}_i$ set (Eq. (4.4.7)), with the orthogonality condition (Eq. (4.4.6)) fixing such a transformation matrix $M_{ij}$ (Eq. (4.4.8)).

For the set of basis functions listed in Eq. (4.4.1), the transformation matrix is,

$$M = \begin{pmatrix} \frac{512\pi}{225} & \frac{128\pi}{25} & 0 & 0 & 0 & 0 & 0 & 0 & 0 \\ \frac{128\pi}{25} & \frac{6272\pi}{225} & 0 & 0 & 0 & 0 & 0 & 0 & 0 \\ 0 & 0 & \frac{256\pi}{225} & 0 & 0 & 0 & 0 & 0 & 0 \\ 0 & 0 & 0 & \frac{256\pi}{225} & 0 & 0 & 0 & 0 & 0 \\ 0 & 0 & 0 & 0 & \frac{16\pi}{9} & 0 & 0 & 0 & 0 \\ 0 & 0 & 0 & 0 & 0 & \frac{8\pi}{9} & 0 & 0 & 0 \\ 0 & 0 & 0 & 0 & 0 & 0 & \frac{256\pi}{225} & 0 & 0 \\ 0 & 0 & 0 & 0 & 0 & 0 & 0 & \frac{16\pi}{9} & 0 \\ 0 & 0 & 0 & 0 & 0 & 0 & 0 & 0 & \frac{256\pi}{225} \end{pmatrix}, \tag{4.4.9}$$

where we organise the basis functions $f_i$ according to the order shown in Eq. (4.4.1). It is simpler to work in a basis such that $M_{ij}$ is diagonal, and so we perform an orthogonal rotation of the first two moments,

$$\begin{aligned} \hat{f}_1 &= \cos\beta f_1 - \sin\beta f_2, \\ \hat{f}_2 &= \sin\beta f_1 + \cos\beta f_2, \end{aligned} \tag{4.4.10}$$

by an angle,

$$\tan\beta = -\frac{1}{2}\left(5 + \sqrt{29}\right). \tag{4.4.11}$$

In the fully-orthogonal basis, where $M_{ij}$ and thus its inverse $\lambda_{ij}$ are diagonal, the

rotated matrix $M \to \hat{M}$ is,

$$\hat{M} = \hat{\lambda}^{-1} = \text{diag}\left(\frac{64\pi}{225}\xi_+, \frac{64\pi}{225}\xi_-, \frac{256\pi}{225}, \frac{256\pi}{225}, \frac{16\pi}{9}, \frac{8\pi}{9}, \frac{256\pi}{225}, \frac{16\pi}{9}, \frac{256\pi}{225}\right), \tag{4.4.12}$$

with $\xi_\pm = \left(53 \pm 9\sqrt{29}\right)$. Further, the (rotated) weight functions can be expressed as,

$$w_i = \hat{M}^{-1}_{ij} \hat{f}_j, \tag{4.4.13}$$

with $\vec{\hat{f}} = \left\{\hat{f}_1, \hat{f}_2, f_3, f_4, f_5, f_6, f_7, f_8, f_9\right\}$. We can now convolute the various differential distributions from our recorded events with these weight functions to extract the angular moments in the diagonal basis,

$$\{\hat{a}_1, \hat{a}_2, a_3, a_4, a_5, a_6, a_7, a_8, a_9\}\,. \tag{4.4.14}$$

In case needed, one can simply rotate back these moments to the original, non-diagonal basis.

### 4.4.3 Estimates of moments and uncertainties

The weight functions $w_j$ allow us to project the total rate $\sum_i a_i f_i$ of the $h \to 4\ell$ process onto the angular coefficients $a_j$, as shown in Eq. (4.4.6) of the previous subsection. From the analytic expressions for the $a_j$, it is clear that in doing so we assume that the weights are defined over a continuous phase space. However, in practice we have a finite number of events delivered by the collider. In this subsection we show how to estimate the angular moments, as well as the uncertainty in this procedure, starting from the experimental dataset, or from the Monte Carlo samples in case we want to obtain projections.

Looking at Eq. (4.4.6), it is noticeable that the angular moments represent the expectation values of the weights $w_j$ for a probability distribution $\sum_i a_i f_i$, which happens to be the total cross-section, normalised to the total squared amplitude.

Let us consider the random variable $\widetilde{a}_i$ for each recorded event,

$$\widetilde{a}_i = N w_i, \tag{4.4.15}$$

where $N$ corresponds to the total number of observed events, which helps us in changing the normalisation of Eq. (4.4.6) to $N$. To obtain the observed value of the angular moments one needs to take the average over all events,

$$a_i = N\overline{w}_i = \sum_{n=1}^{\hat{N}} w_i\left(\theta_{1,n}, \theta_{2,n}, \phi_n\right), \tag{4.4.16}$$

which corresponds to the discrete version of Eq. (4.4.6). In the experiment this is the way to extract the angular moments.

Since our goal is to anticipate the incoming data of the HL-LHC, we perform a projection using Monte Carlo samples with and without insertions of the EFT couplings, where the SM case corresponds to no EFT insertions and consists of both Higgs and non-Higgs backgrounds. As we are able to control the parameters of the simulations, the Monte Carlo samples have a much larger number of events $N_{\text{MC}}^{\text{SM,EFT}}$ than the actual number of expected events $\hat{N}^{\text{SM,EFT}}$ at $\mathcal{L} = 3\,\text{ab}^{-1}$.

Given a sufficiently large number of events, the weight functions $w_i$ converge to a (multivariate) Gaussian distribution[16], for which the estimate of the expectation value,

$$\overline{w}_i = \frac{1}{N_{\text{MC}}} \sum_{n=1}^{N_{\text{MC}}} w_i\left(\theta_{1,n}, \theta_{2,n}, \phi_n\right), \tag{4.4.17}$$

and covariance matrix,

$$\sigma_{ij} = \frac{1}{N_{\text{MC}} - 1} \sum_{n=1}^{N_{\text{MC}}} \left[w_i - \overline{w}_i\right]\left[w_j - \overline{w}_j\right], \tag{4.4.18}$$

are given by the above equations for both the SM- and EFT-driven Monte Carlo samples. We can evaluate the estimates for the expectation values of the angular moments $a_i$ as,

$$a_i^{\text{SM,EFT}} \equiv \left\langle N^{\text{SM,EFT}} \right\rangle \overline{w}_i^{\text{SM,EFT}} = \hat{N}^{\text{SM,EFT}} \overline{w}_i^{\text{SM,EFT}}, \tag{4.4.19}$$

[16] As expected from the *Central Limit Theorem*.

where we asumme that $N^{\rm SM,EFT}$ is a Poisson-distributed variable with both mean and variance given by $\hat{N}^{\rm SM,EFT}$. As discussed in Sec. 4.6, in our statistical analysis we take the null hypothesis to be the SM expectation and assume that an excess over the SM is observed at the detectors due to the presence of EFT insertions.

In practice, one is supposed to evaluate the $\overline{w}_i^{\rm SM,(EFT)}$ in an expected (observed) dataset containing $\hat{N}^{\rm SM,(EFT)}$ events which is in principle much smaller than the number of events in the Monte Carlo samples. The covariance $\overline{\sigma}_{ij}$ matrix of the random variable $\overline{w}_i^{\rm SM,EFT}$ in Eq. (4.4.17), which provides good estimates of the expectation value of the weight functions $w_i$, follows from Eq. (4.4.18) and can be written as,

$$\overline{\sigma}_{ij} = \frac{\sigma_{ij}}{\hat{N}}, \tag{4.4.20}$$

which holds for both the SM and EFT cases. In performing the projections of the angular moments, we find that as $N_{\rm MC}^{\rm SM,EFT}$ increases and is large enough ($\mathcal{O}(100)$), the $\overline{w}_i$ and $\sigma_{ij}$ approach fixed values since the estimates converge to the true values of the parameters. Thus, the $\overline{\sigma}_{ij}$ values decrease for increasing $\hat{N}$, becoming more precise.

As we deal with estimators, we must take into account their statistical uncertainties; the latter are computed as covariances of functions of the random variables $N$ and $\overline{w}_i$,

$$\begin{aligned} \text{cov}\left(a_i, a_j\right) &= \sum_{kl} \overline{\sigma}_{kl} \left(\frac{\partial a_i}{\partial w_k}\frac{\partial a_j}{\partial w_l}\right)\Bigg|_{w=\overline{w},N=\hat{N}} + \hat{N}\left(\frac{\partial a_i}{\partial N}\frac{\partial a_j}{\partial N}\right)\Bigg|_{w=\overline{w},N=\hat{N}} \\ &= \left(\frac{\sqrt{\hat{N}}}{\hat{N}}\right)^2 a_i a_j + \hat{N}\sigma_{ij}. \end{aligned} \tag{4.4.21}$$

Since our null hypothesis is the SM prediction, the uncertainties entering into our final statistical analysis in Sec. 4.6 correspond to those of the SM expectation. We assume a flat systematic covariance on the SM prediction given by $\kappa_{\rm syst}^2 a_i^{\rm SM} a_j^{\rm SM}$, where we take $\kappa_{\rm syst} = 0.02$ in line with the experimental search described in Ref. [310].

Finally, the total covariance of the set of estimated SM angular moments is,

$$\Sigma_{ij} = \left( \left( \frac{\sqrt{\hat{N}^{\rm SM}}}{\hat{N}^{\rm SM}} \right)^2 + \kappa^2_{\rm syst} \right) a_i^{\rm SM} a_j^{\rm SM} + \hat{N}{\rm SM}\sigma_{ij}^{\rm SM}. \tag{4.4.22}$$

## 4.5 Collider analysis

In this section we discuss the collider analysis performed to suppress the background processes $q\overline{q} \to 4\ell$, $gg \to 4\ell$, and $Z/\gamma^*+$ jets, and extract the $gg \to h \to 4\ell$ signal events[17] to set bounds on the operators under consideration. Details of the Monte Carlo samples are presented in Appendix C.

### 4.5.1 Analysis setup

The analysis strategy employed in this study is based on the experimental search[18] described in Ref. [257]. A simplified detector analysis is implemented with the help of HepMC [321] and FastJet [322], where we select visible final-state objects within $|\eta| < 4.7$ and require $p_T > 0.5\,\text{GeV}$. The preselection of electrons (muons) is performed within the acceptance region of the detector $|\eta| < 2.5$ (2.4), with $p_T > 7$ (5) GeV. Leptons are further tagged as isolated if the total hadronic activity around a cone of radius $R = 0.3$, centred in the lepton's direction, is less than 35% of its transverse energy $E_T$. The missing transverse energy $\not{E}_T$, which corresponds to the magnitude of the total transverse momentum of the event, is calculated from the transverse components of all particles fulfilling the preselection criteria, and its corresponding vector $\vec{\not{E}}_T$ points in the opposite direction of the overall transverse momentum. Hadrons, photons, and non-isolated leptons are clustered into jets using the anti-$k_t$ algorithm [323] with a radius parameter 0.4 and $p_T > 30\,\text{GeV}$.

[17] Note that the SM-driven process $gg \to h \to 4\ell$ is a background in itself, and the signal events come from interactions ensuing from the EFT corrections explained in the previous sections.

[18] Our analysis is calibrated against the experimental search, and we find that our results are compatible with the experimental numbers within 96%.

Table 4.2: Set of cuts showing the effect of each stage of the selection on the fraction of retained Monte Carlo events for the SM-driven $gg \to h \to 4\ell$ signal, as well as on the $q\overline{q} \to 4\ell$ and $gg \to 4\ell$ irreducible backgrounds.

| Selection cut | SM $gg \to h$ | $q\overline{q} \to 4\ell$ | $gg \to 4\ell$ |
|---|---|---|---|
| Jet veto | 0.419 | 0.779 | 0.319 |
| $\not{E}_T < 25\,\text{GeV}$ | 0.348 | 0.667 | 0.248 |
| 2 pairs of isolated OSSF leptons, $\Delta R(\ell_i, \ell_j) > 0.02$, $M_{\ell^+\ell'^-} > 4\,\text{GeV}$ | 0.127 | 0.036 | 0.130 |
| $p_{T,\ell_1} > 20\,\text{GeV}$, $p_{T,\ell_2} > 10\,\text{GeV}$, $p_{T,\ell_3} > 10\,\text{GeV}$ | 0.121 | 0.031 | 0.124 |
| $M(Z_1) \in [40, 120]$ GeV, $M(Z_2) \in [12, 120]$ GeV | 0.110 | 0.021 | 0.112 |
| $M(4\ell) \in [118, 130]$ GeV | 0.095 | 0.001 | 0.001 |

The detector response in the reconstruction of final-state objects, such as electrons, muons, and jets, is simulated by applying a flat Gaussian smearing [324], as implemented in Rivet [325], to their energy, $p_T$, and three-momentum components, respectively. In the case of leptons, the mass- and direction-preserving smearing functions are applied before the selection takes place; for jets, the mass-preserving smearing is applied after the clustering stage. A flat leptonic reconstruction efficiency of 0.92 is assumed, and we consider a rapidity-dependent jet-to-electron fake rate of 0.016 (0.044) for jets with $\left|y^j\right| < 1.48$ $\left(1.48 < \left|y^j\right| < 2.5\right)$ [229].

The selection strategy is optimised to select signal candidates from events with no jet activity, $\not{E}_T < 25\,\text{GeV}$, and exactly two pairs of opposite-sign same-flavour (OSSF) leptons. To mimic the way in which Ref. [257] treats preselected leptons, we require $\Delta R\left(\ell_i, \ell_j\right) > 0.02$, and to protect the selection against events where leptons originate from the decay of low-mass resonances we further impose $M_{\ell^+,\ell'^-} > 4\,\text{GeV}$ (irrespective of flavour). Hard leptons are selected by demanding a cut on the leading lepton's $p_T > 20\,\text{GeV}$, and require that at least two of the trailing leptons fulfil $p_T > 10\,\text{GeV}$.

Once a four-lepton topology satisfying the previous criteria is selected, we combine pairs of OSSF leptons into $Z_1 Z_2$ candidates, where $Z_1$ corresponds to the two-lepton system with an invariant mass closest to the nominal $Z$-boson mass $m_Z = 91.1876\,\text{GeV}$ [326], and $Z_2$ is the remaining pair. Since low-mass dilepton resonances

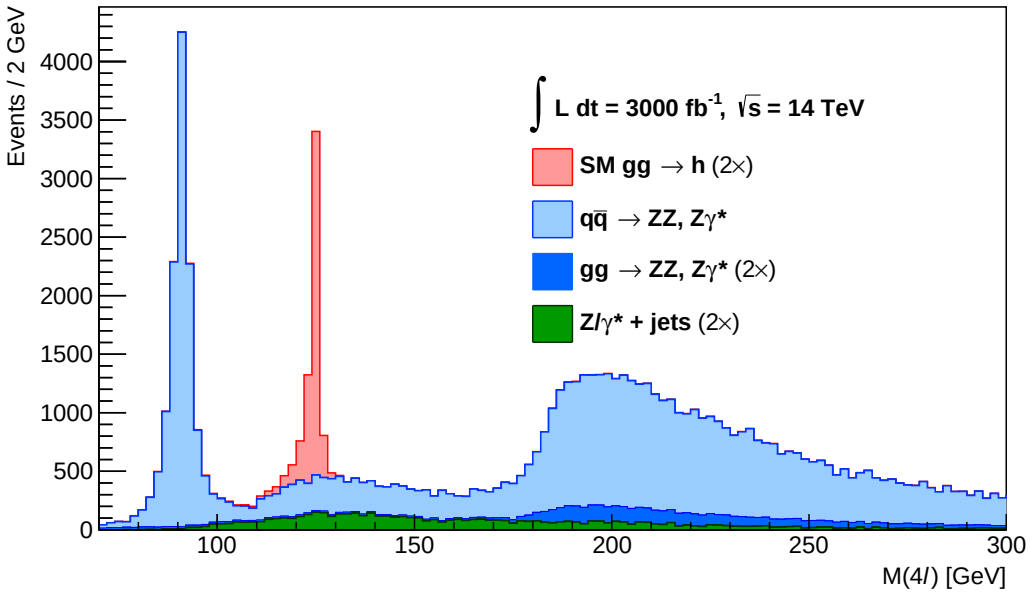


Figure 4.2: Invariant-mass distribution $M(4\ell)$, in GeV, of the four-lepton system after performing the reconstruction of the $Z_1 Z_2$ pairs (see text for details). Shown are the stacked histograms of the SM $gg \to h$ (red) signal, quark-initiated $q\bar{q} \to 4\ell$ (light blue), gluon-initiated $gg \to 4\ell$ (dark blue), and $Z/\gamma^* +$ jets (green) backgrounds, all of which are normalised to the expected number of events at the HL-LHC $\left(\mathcal{L} = 3000\,\text{fb}^{-1}\right)$. Except for the $q\bar{q} \to 4\ell$ background, all distributions are scaled $(2\times)$ for visualisation purposes. **Note:** The settings used in generating the $gg \to h \to 4\ell$ MC samples (see Appendix C) are such that the effect of off-shell Higgs production is negligible away from $m_h \pm 1\,\text{GeV}$, and hence not visible on top of the continuum backgrounds above (below) 140 GeV (100 GeV) after smearing the momenta of final-state leptons.

can be produced in association with an on-shell $Z$-boson, we reject these events by demanding that $M(Z_1) \in [40, 120]$ GeV and $M(Z_2) \in [12, 120]$ GeV. To conclude the selection, we define the signal region of the four-lepton system to be within the mass range $M(4\ell) \in [118, 130]$ GeV, given that a sharp peak is expected to rise near the nominal Higgs-boson mass $m_h = 125\,\text{GeV}$ [45, 46, 48, 49] on top of a continuum background, as shown in Fig. 4.2. In Table 4.2, we illustrate the impact of the selection cuts on the fraction of retained (Monte Carlo) events for the SM-driven signal and the irreducible backgrounds. In Fig. 4.3, we show the invariant-mass distributions of the reconstructed $Z_1 Z_2$ pairs surviving the selection.

### 4.5.2 Angular extraction

As previously explained in Sec. 4.3.3, the determination of the helicity of a final-state lepton has major experimental limitations. To overcome this situation we define the various scattering angles, as illustrated in Fig. 4.1, with respect to the negatively charged leptons originating from the decay of their parent $Z_i$-boson, with $i = \{1, 2\}$, and which we refer to from now on as $\ell_i^-$.

In order to extract the angular observables and analyse their differential distributions as described in sections 4.3 and 4.4, we Lorentz-boost the four-lepton system from the laboratory frame to the centre-of-momentum frame $S'$ where the Higgs boson is at rest, and we have back-to-back $Z$-boson momenta. In $S'$ a new Cartesian coordinate system $\left\{\hat{x}', \hat{y}', \hat{z}'\right\}$ is constructed on an event-by-event basis as follows: the positive $\hat{z}'$ axis points in the direction of motion of the $Z_1$ candidate; $\hat{y}'$ is normal to the plane generated by $\hat{z}'$ and $\hat{B}$, where $\hat{B} = (0, 0, 1)$ corresponds to the vector which in the laboratory frame defines the beam direction; finally, the $\hat{x}'$ axis completes the right-hand set. The azimuthal angle $\varphi_{i,S'}$ formed in $S'$ between $\ell_i^-$ and the scattering plane is calculated as,

$$\tan \varphi_{i,S'} = \left( \frac{\ell^-_{i,\hat{y}'}}{\ell^-_{i,\hat{x}'}} \right), \tag{4.5.1}$$

where $\ell^-_{i,\hat{e}'}$ corresponds to the projection of $\ell_i^-$'s three-momentum onto the $\hat{e}'$ axis in

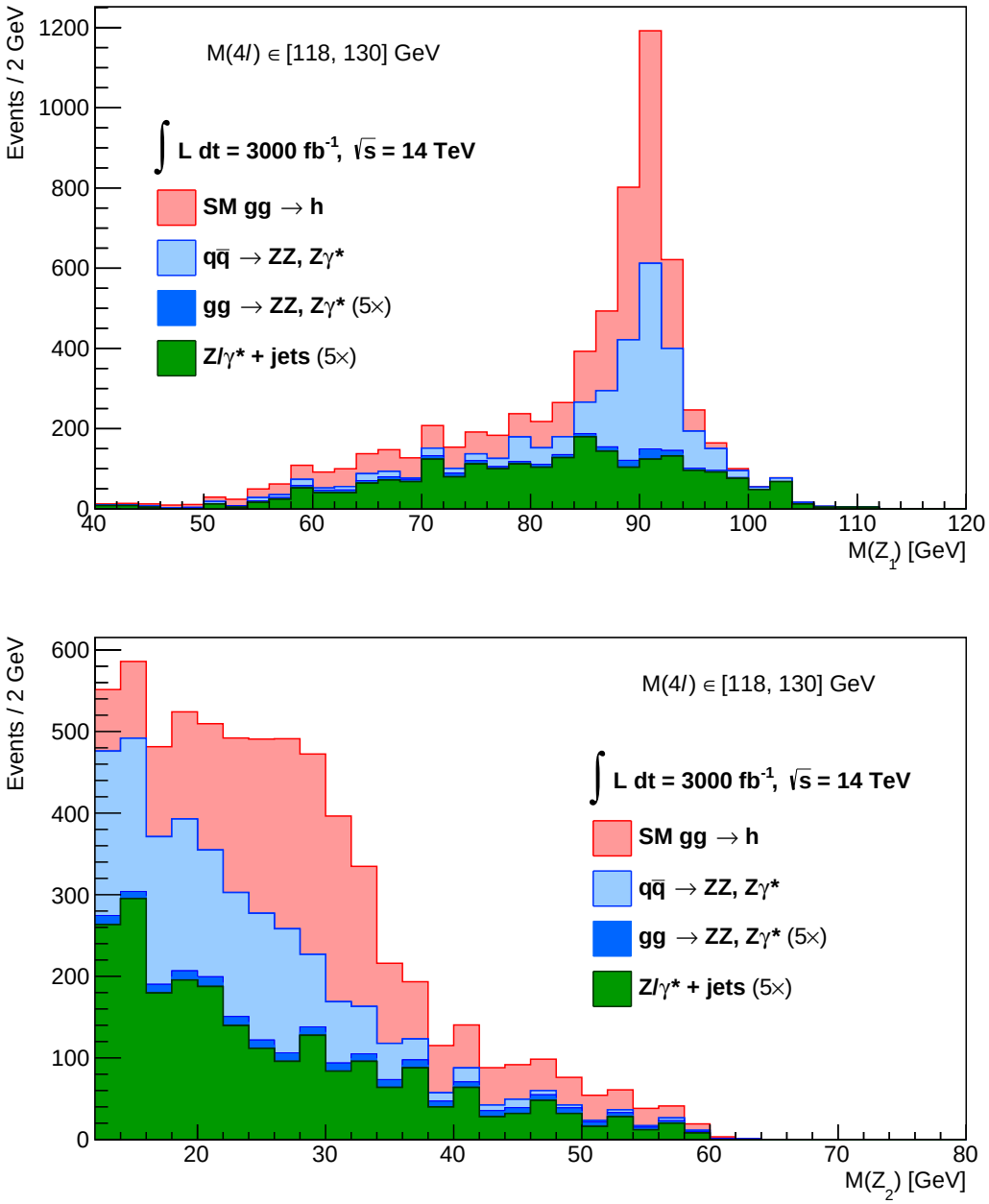


Figure 4.3: Invariant-mass distributions $M(Z_i)$, in GeV, of the $Z_1$ (top) and $Z_2$ (bottom) candidates after defining the signal region $M(4\ell) \in [118, 130]$ GeV (see text for details). The shown stacked histograms follow the same colour coding and normalisation as Fig. 4.2. The $gg \to 4\ell$ and $Z/\gamma^* + \text{jets}$ background distributions are scaled $(5\times)$ for visualisation purposes.

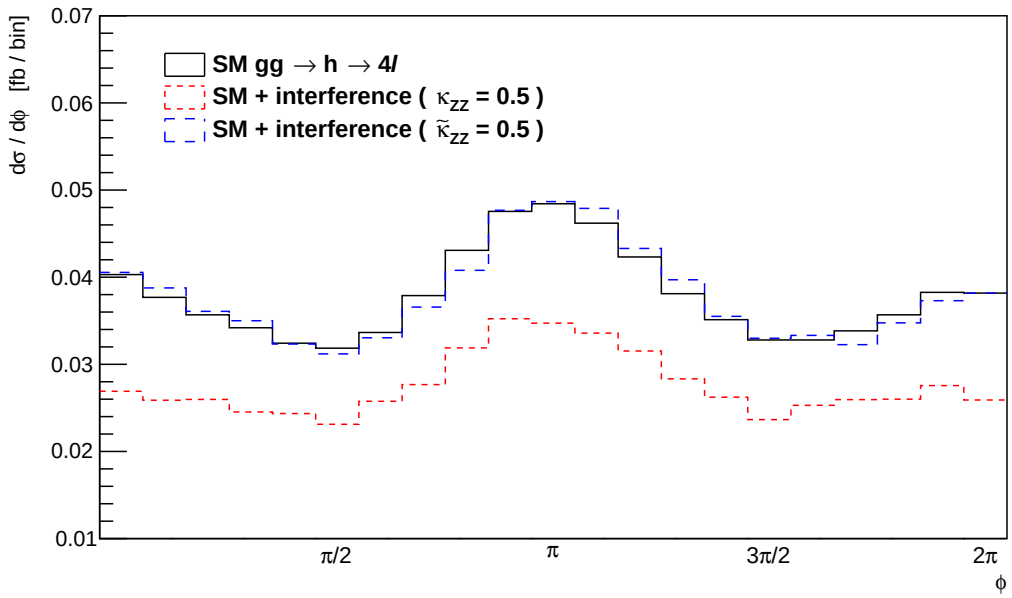


Figure 4.4: Differential distribution of the cross-section $\sigma$, with respect to the azimuthal angle $\phi$ between the scattering planes, $\mathrm{d}\sigma/\mathrm{d}\phi$, in fb/bin, for the SM-driven $gg \to h \to 4\ell$ process (solid black), as well as the SM + interference terms for the $CP$-even $\kappa_{ZZ} = 0.5$ (dotted red) and $CP$-odd $\tilde{\kappa}_{ZZ} = 0.5$ (dashed blue) operators. Note that the interference term of the $CP$-odd operator closely matches the expectation of the SM, while the $CP$-even histogram clearly departs from the black curve. In generating the MC samples, the interference effects occur at the level of the final-state leptons. See text for details.

$S'$, and $\varphi \in [0, 2\pi)$. Finally, the azimuthal angle $\phi_{S'}$ between the planes formed by the leptons pairs in $S'$ is defined as,

$$\tan\phi_{S'} \equiv \tan\left(\phi_{2,S'} - \phi_{1,S'}\right), \tag{4.5.2}$$

with $\phi \in [0, 2\pi)$. We show the (differential) azimuthal distribution of the signal process $gg \to h \to 4\ell$ in Fig. 4.4. Finally, each pair of OSSF leptons constructing the $Z_1Z_2$ candidates is Lorentz-boosted from $S'$ to the rest frame $S''$ of its parent $Z$-boson where, similarly to the case in going from the laboratory frame to $S'$, we have back-to-back lepton momenta. The polar angle $\theta_{i,S''}$ between $\ell_i^-$ in $S''$ and the direction of motion of its parent $Z$-boson in $S'$ is defined as,

$$\cos\theta_{i,S''} \equiv \frac{\vec{p}_{\ell_i^-,S''} \cdot \vec{q}_{Z_i,S'}}{\left|\vec{p}_{\ell_i^-,S''}\right| \left|\vec{q}_{Z_i,S'}\right|}, \tag{4.5.3}$$

where the vector $\vec{k}_{M_i,N}$ corresponds to the three-momentum of particle $M_i$ in frame $N$, and $\theta \in [0, \pi]$.

## 4.6 Results

We now discuss the statistical analysis used to obtain the bounds on the relevant anomalous couplings $\delta\hat{g}^h_{ZZ}$, $\kappa_{ZZ}$, and $\widetilde{\kappa}_{ZZ}$. We define a $\chi^2$ function as,

$$\chi^2\left(\delta\hat{g}^h_{ZZ}, \kappa_{ZZ}, \widetilde{\kappa}_{ZZ}\right) = \sum_{ij}\left(a_i^{\rm EFT} - a_i^{\rm SM}\right)\Sigma^{-1}_{ij}\left(a_j^{\rm EFT} - a_j^{\rm SM}\right), \tag{4.6.1}$$

where the covariance matrix $\Sigma_{ij}$ is defined in Eq. (4.4.22). In performing the analysis we neglect the contributions of the $g^h_{Z\ell}$ couplings of the $hZ\bar{\ell}\ell$ contact terms since, as discussed in Secs. 4.2 and 4.3, these are best constrained using other processes (see, e.g., Chapter 5 of this Thesis).

In Fig. 4.5 we show the 68% confidence-level (CL) bounds, obtained using Eq. (4.6.1), in the $\kappa_{ZZ} - \delta\hat{g}^h_{ZZ}$ space. Here, the green band corresponds to the bound obtained including only the information related to the total rate of the $gg \to h \to 4\ell$ process, and it is evident that there is flat direction, $\kappa_{ZZ} \approx 3.7\ \delta\hat{g}^h_{ZZ}$, which is lifted by

introducing the differential information of the angular moments described in Sec. 4.4. Also shown are the bounds obtained by including the interference-only term between the SM and EFT (red ellipse), which almost coincide with the bounds that include the EFT squared term (purple ellipse). This overlap implies that, if $\Lambda$ is the UV cut-off of the EFT expansion, truncating the cross-section at $\mathcal{O}\left(1/\Lambda^2\right)$ already includes most of the BSM effects that are encoded by the D6 operators; hence, the $1/\Lambda^4$ level does not need to be taken into account, and neglecting dimension-eight operators can be considered consistent. For $\delta\hat{g}^h_{ZZ} = 0$, and assuming no systematic uncertainties, we obtain the bound,

$$|\kappa_{ZZ}| < 0.05, \tag{4.6.2}$$

which is comparable to MELA's $|\kappa_{ZZ}| < 0.04$ [304].

In obtaining the bounds in Fig. 4.5 we have taken $\widetilde{\kappa}_{ZZ} = 0$. However, we have checked that a non-zero value of the $\widetilde{\kappa}_{ZZ}$ coupling does not have a visible impact in the plot, *i.e.*, to a very good approximation we obtain the same bounds if $\widetilde{\kappa}_{ZZ}$ is marginalised over. The reason for this is that the angular moments $a_7 - a_9$ in Eq. (4.4.2) hardly contribute to $\chi^2$ in Eq. (4.6.1), since these are the only moments containing a linear term in $\widetilde{\kappa}_{ZZ}$; the dominant contribution is given by the $a_1 - a_6$ angular moments which depend on $\widetilde{\kappa}^2_{ZZ}$, and so the $\chi^2$ function mildly depends on $\widetilde{\kappa}_{ZZ}$. It is for these reasons that a very weak bound on $\widetilde{\kappa}_{ZZ}$ is obtained,

$$|\widetilde{\kappa}_{ZZ}| \lesssim 0.5, \tag{4.6.3}$$

after marginalising over the $\delta\hat{g}^h_{ZZ}$ and $\kappa_{ZZ}$ couplings. This result is not competitive with the projection $|\widetilde{\kappa}_{ZZ}| < 0.05$ from the $pp \to W^{\pm}h/Zh$ processes in Ref. [292].

We combine the bounds reported above with the projections in Refs. [292,310], which consider the $pp \to W^{\pm}h\left(b\bar{b}\right)/Zh\left(b\bar{b}\right)$ and $pp \to h \to W^+W^- \to 2\ell 2\nu$ processes, respectively. To perform such a combination, we need to i) assume that the function $f$ in Eq. (4.2.6), as well as the EFT deformations rescaling the branching ratio of the decay $h \to b\bar{b}$, can be constrained in a global fit that takes into account all the processes relevant to Higgs physics; ii) use the constraints on the $Z\ell^+\ell^-$ couplings,

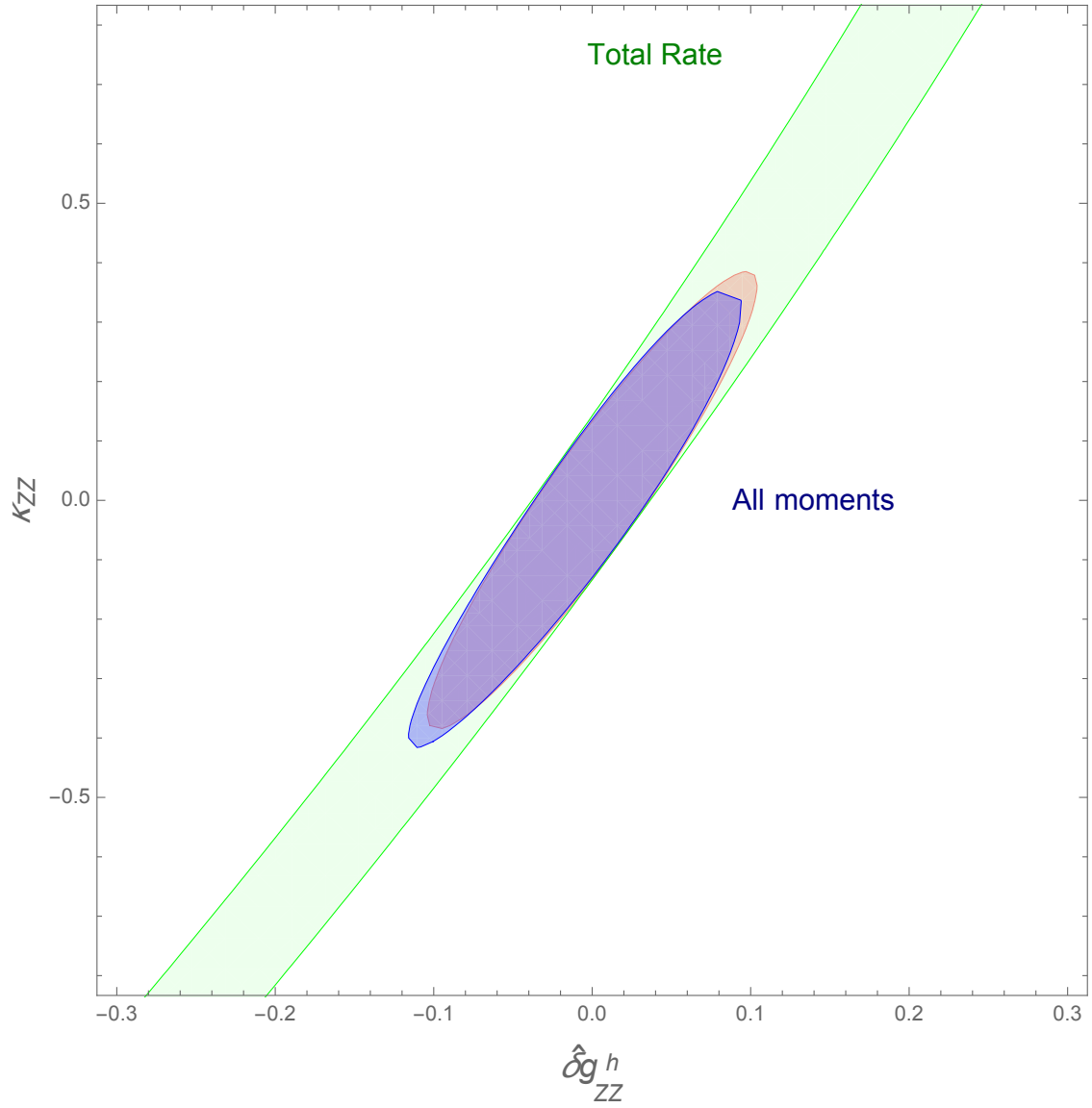


Figure 4.5: Bounds at 68% CL on the *CP*-even anomalous couplings. The green band corresponds to the bound obtained including only the information related to the total rate of the $gg \to h \to 4\ell$ process, which keeps a flat direction $\kappa_{ZZ} \approx 3.7\ \delta\hat{g}^{h}_{ZZ}$ unconstrained. The purple ellipse, corresponding to the EFT squared term, shows the bounds including all the angular moments. The red ellipse, obtained by including only the interference terms between the SM and EFT, also shows the results of the angular-moment analysis.

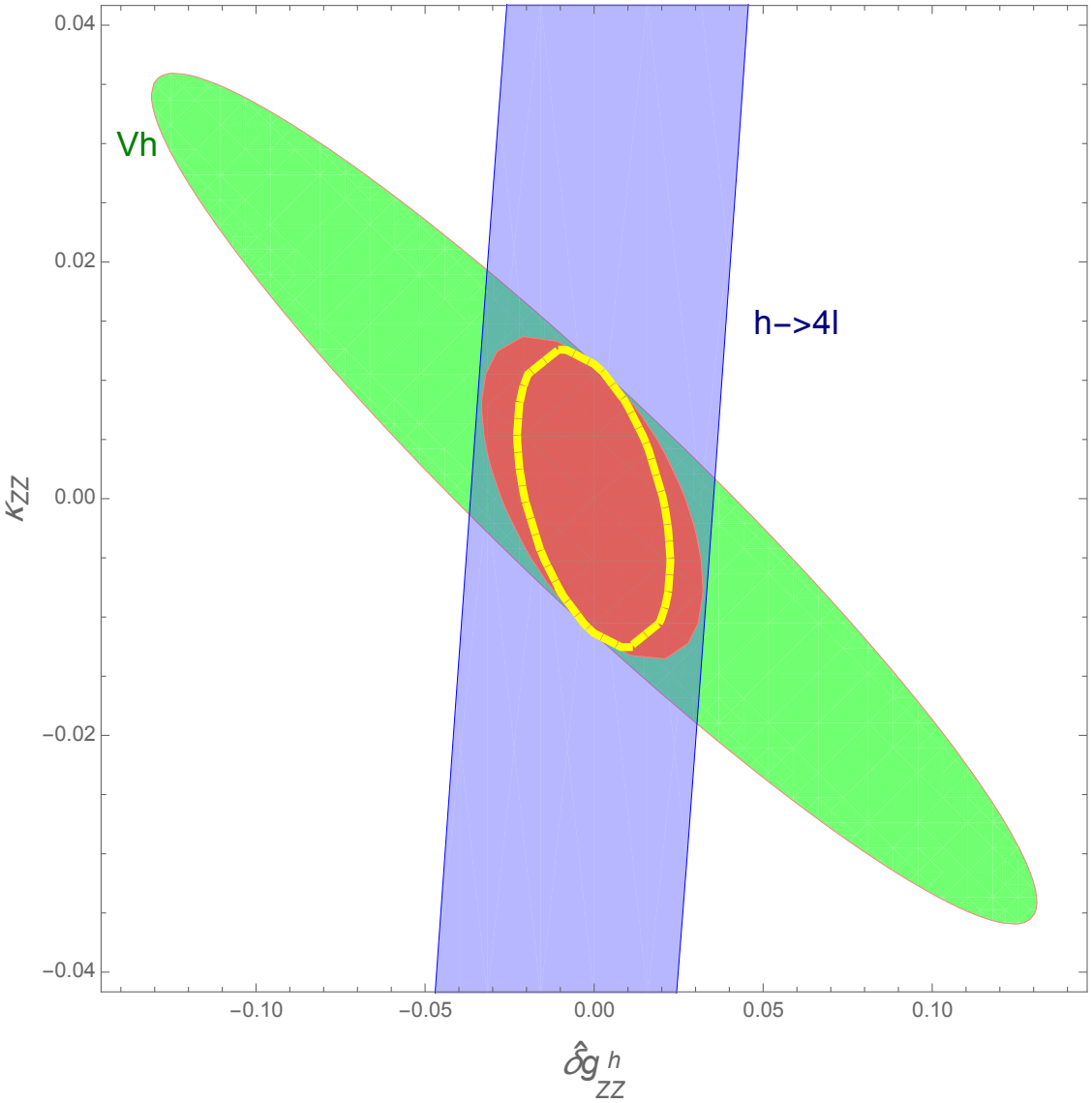


Figure 4.6: Bounds at 68% CL on the *CP*-even anomalous couplings after combination with the results of the angular moment analysis of the $pp \to W^{\pm}h/Zh$ processes carried out in Ref. [292], and with the projection of the $pp \to h \to W^{+}W^{-}$ process in Ref. [310]. The blue band shows the results of our differential study of the golden channel. The green ellipse shows the bounds from the $pp \to W^{\pm}h/Zh$ processes, and the red region corresponds to the combination of these angular-moment studies. The (dashed) yellow ellipse shows the final bound after combining the angular analyses with the total rate of $pp \to h \to W^{+}W^{-}$.

and iii) use the EFT correlations between the anomalous gauge-Higgs couplings involving the weak bosons [292]. In Fig. 4.6 we show the final bounds obtained after combining the angular analyses $gg \to h \to 4\ell$ and $pp \to Vh\left(b\bar{b}\right)$ with the total rate for $pp \to h \to W^+W^- \to 2\ell 2\nu$. Since these processes probe different linear combinations of $\delta\hat{g}^h_{ZZ}$ and $\kappa_{ZZ}$, we get strong bounds on these couplings at the per-cent level.

Although transparent, our approach can be criticised for several reasons, namely being based on leading-order matrix elements, not taking detector effects and selection cuts into account, or not being optimised to include parton-shower effects. We then compare our results with a *Boosted Decision Tree* (BDT) analysis, which does not rely on any *a priori* assumptions and does not have the aforementioned shortcomings. To make sure that we are comparing apples with apples, we perform a simple BDT analysis[19] with the angular observables $\theta_1$, $\theta_2$, and $\phi$, obtained from the Monte Carlo samples as outlined in Sec. 4.5. Since the $\delta\hat{g}^h_{ZZ}$ coupling does not leave differential signatures as it only rescales the SM matrix element, we only vary $\kappa_{ZZ}$ and obtain the bound $|\kappa_{ZZ}| < 0.052$, with the hypothesis of zero systematic uncertainties. This bound can be directly compared with the angular-moment result of $|\kappa_{ZZ}| < 0.051$; these numbers are very close to each other, and the nominal difference might be due to statistical reasons. This validation shows that the effects outlined above (leading-order matrix elements, parton-shower effects not included, and lack of detector effects or selection cuts) do not affect the extent at which the method of moments is sensitive to this particular final-state topology.

## 4.7 Conclusions

A fully differential study of the golden channel $h \to 4\ell$ in the *ggh* production mode has been carried out. Owing to the experimental resolution in reconstructing leptonic

[19] We choose the *Gradient Boost Decision Tree* (BDTG) algorithm, which is suitable for handling events with negative weights that arise upon including next-to-leading order and interference-only samples.

final states, a wealth of differential information can be extracted from these final-state topologies. We show that in the centre-of-mass frame of the four-lepton system, or equivalently the rest frame of the Higgs boson, three angles suffice to characterise and determine the direction of the leptons reaching the detectors. Thus, to probe the tensor structure of the Higgs couplings to gauge bosons at colliders and set bounds on potential new contributions in the D6 SMEFT, a detailed differential study of the three-dimensional space is needed.

In this Chapter we showed that the full angular distributions can be written as a linear combination of a set of basis functions in both the SM and the D6 SMEFT, where the coefficients accompanying these angular functions, the so-called angular moments, encode the full angular information of the process under consideration. We presented the derivation of the analytical expressions for these angular moments, including D6 EFT deformations. Moreover, we employed the method of moments, analogous to Fourier analysis, to extract said angular moments from our Monte Carlo samples, which are simulated and analysed using a strategy that follows closely that of the CMS experiment at the LHC during Run 2.

Further, we projected bounds on the gauge-Higgs couplings deformations that are parametrised by $\delta\hat{g}^h_{ZZ}$, $\kappa_{ZZ}$, and $\tilde{\kappa}_{ZZ}$ in Eq. (4.2.1), using the angular moments associated to the SM and D6 SMEFT predictions. As shown in Fig. 4.5, carrying out the angular analysis eliminates the flat directions arising from including only the information of the total rates in the statistical analysis. Finally, we performed a combination of our results with those of Ref. [292], where the method of moments was used to analyse the $pp \to Vh$ process, which allowed us to obtain strong bounds, shown in Fig. 4.6, on the anomalous gauge-Higgs couplings.

# Chapter 5

# Future Linear $e^+e^-$ Colliders as Higgs Microscopes

In this Chapter, based on Ref. [327], we perform our second investigation into the interplay between effective theories and measurements at colliders by considering the capability of future linear $e^+e^-$ colliders, such as ILC and CLIC, at constraining dimension-six operators through the *Higgs-strahlung* and *Z-boson fusion* single-Higgs production mechanisms. The leading contributions to these processes in the SMEFT are given by a subset of three operators, which are used to perform a 'high-energy fit'. The clean environment of electron-positron accelerators along with the fixed and controllable centre-of-mass energy of the collision allow us to set strong bounds on the so-called *leptonic high-energy primaries*. All equations, tables, and figures, are taken from Ref. [327].

## 5.1 Motivation

Particle physics has as one of its ultimate goals to reach higher and higher energies to probe smaller and smaller length scales. Where direct measurements are limited to the energy reach of the colliders, indirect searches are suitable avenues to test higher energies than the former, as explained in Chapter 3. At LEP, $Z$-pole precision

measurements were able to probe energies up to a few TeV, well beyond the nominal collision energy $\sqrt{s_{\rm LEP}} = 209\,\text{GeV}$, and some of these measurements have provided the most stringent constraints on the new-physics scale to date. Indirect effects of BSM physics are sensitive to irrelevant operators of the SMEFT[1], which convey the stamp of new physics at energy scales higher than that of the process under study.

As described in Chapter 2, the scaling of indirect effects due to D6 operators in the SMEFT behaves as $m_W^2/\Lambda^2$ or $s/\Lambda^2$, where $s$ corresponds to the centre-of-mass energy squared, and $\Lambda$ is the UV cut-off of the EFT expansion or, equivalently, the scale of new physics. Future linear $e^+e^-$ colliders, such as ILC or CLIC, have a clear advantage[2] over LEP, given their higher $\sqrt{s}$ [3], at probing indirect effects that scale as $s/\Lambda^2$. Compared to low-energy measurements performed at LEP, the same EFT effects probed at future lepton colliders are larger by a factor of $s/s_{\rm LEP}$. The aim of this study is to show that high-energy $e^+e^-$ collisions allow us to explore scales up to tens of TeV, the smallest length scales probed in the EW and Higgs sectors.

In this Chapter we identify a subset of D6 operators in the SMEFT, sensitive to the highest possible energy scale, that give the leading high-energy contributions in standard EW and Higgs processes at $e^+e^-$ collisions, such as $e^+e^- \to Zh, W^+W^-$ and single-Higgs production through *Z-boson fusion* (*ZBF*). We find, for a single generation of leptons, that only three linear combinations of operator coefficients, the so-called leptonic high energy primaries, give the leading high-energy contributions to all these channels, and in doing so we perform a 'high-energy fit' taking into account only this subset of EFT insertions. Further, we exploit the relation at high energies between the amplitudes of these processes due to i) the *Goldstone Boson Equivalence Theorem*, which relates the $e^+e^- \to Zh$ and $e^+e^- \to W^+W^-$ modes, and ii) the crossing symmetry that connects the *Higgs-strahlung* channel to *ZBF*.

[1] A non-exhaustive list of other relevant SMEFT studies can be found in Refs. [167, 175, 176, 191, 193–195, 204, 233, 240, 245, 258–295].

[2] In Refs. [283, 284, 295] it is shown that in some cases even the LHC can surpass the energy reach attained by indirect measurements at LEP.

[3] See Section 3.3 for a brief comparison between linear and circular $e^+e^-$ colliders.

Table 5.1: List of processes included in the high-energy fit performed in this study for $\sqrt{s} = 1\,\text{TeV}$ ($\text{ILC}_{1000}$) and $\sqrt{s} = 3\,\text{TeV}$ ($\text{CLIC}_{3000}$). See text for details.

| Process | $\text{ILC}_{1000}$ | $\text{CLIC}_{3000}$ |
|---|---|---|
| $e^+e^- \to Z\left(\ell^+\ell^-\right)h$ | ✓ | ✓ |
| $e^+e^- \to e^+e^-h$ | ✓ | ✓ |
| $e^+e^- \to W^\pm(2j)W^\mp(2j)$ | × | ✓ |
| $e^+e^- \to W^\pm(2j)W^\mp\left(\ell^\mp\nu_\ell\right)$ | × | ✓ |

The remainder of this Chapter is divided as follows. In Sec. 5.2 we list the D6 operators that give the leading high-energy contributions to the processes mentioned above. We outline the collider analyses that help us in extracting signal contributions from major background processes in Sec. 5.3, followed by the projected sensitivities to EFT couplings in Sec. 5.4. Finally, a summary is presented in Sec. 5.5.

## 5.2 The leptonic high-energy primaries

In this section we identify the set of D6 operators in the SMEFT giving the leading high-energy contributions to *Zh*, $W^+W^-$, and *ZBF* processes at electron-positron colliders. The aim is to perform a 'high-energy fit' of said leptonic operators; in doing so we assume and further verify numerically that the Wilson coefficients of other D6 operators, generated at the same scale, are negligible compared to those giving the dominant contribution at high energies, namely the $\sqrt{s} = 1\,\text{TeV}$ ILC and $\sqrt{s} = 3\,\text{TeV}$ CLIC. The linear combinations of operator coefficients entering the high-energy amplitudes of the standard electroweak processes considered in our study, outlined above, are the so-called leptonic high-energy primaries [283].

For our $\sqrt{s} = 1\,\text{TeV}$ projections we take into account the *Zh* and *ZBF* single-Higgs production mechanisms, and incorporate the $e^+e^- \to W^+W^-$ to our $\sqrt{s} = 3\,\text{TeV}$ projections. We perform our own collider analyses for the *Higgs-strahlung* and *ZBF* processes (see Sec. 5.3), and further include the results of the $e^+e^- \to W^+W^-$ mode described in Ref. [56]. A summary of these processes is shown in Table 5.1. We note that, in each case, the same set of three leptonic high-energy primaries dominate

the SMEFT contribution at high energies[4]. A statistic combination of the results from each channel gives very stringent bounds on this three-dimensional space[5]. In the following subsections we describe the high-energy behaviour of these processes in the SMEFT, as well as the underlying theory relating each other.

### 5.2.1 The high-enery $e^+e^- \to Zh, W^+W^-$ processes in the dimension-six SMEFT

In the high-energy limit $\sqrt{s} \gg m_W$, bosons produced with longitudinal polarisation are correlated as a consequence of the Goldstone Boson Equivalence Theorem [328, 329]. This way, and up to a factor of $m_W/\sqrt{s}$, the external legs of a Feynman diagram containing longitudinally-polarised gauge bosons can be represented by Goldstone lines. Thus, one can study the high-energy behaviour of these processes in the symmetric phase, where the symmetry group of the SM $SU(2)_L \times U(1)_Y$ remains unbroken— the EW bosons remain massless, and the Higgs doublet contains not only the physical $h$-boson, but the Goldstones as well. It is for this reason that in the high-energy regime the EW processes $e^+e^- \to Zh, W^+W^-$ are correlated[6], given that these are dominated by the longitudinal final-state modes $Z_Lh, W_L^+W_L^-$.

The amplitude for these processes involving diboson production in the SM at high energies can be computed by evaluating the left diagram in Fig. 5.1. In the D6 SMEFT, the leading contributions are given in the right diagram (Fig. 5.1), and these arise from the contact terms $e^+e^-hG_0$ and $e^+e^-G^+G^-$, where $G_0$ and $G^\pm$ are the Goldstone bosons. In the absence of a propagator connecting the leptons with the Goldstones, the D6 diagram corresponds to an amplitude that grows quadratically with energy, and so one can expand the operators in Table 5.2 to read off

[4] In Ref. [56] a study of the Drell-Yan process, not included here, shows its sensitivity to very high scales, where an independent set of operators from the ones we consider in our study gives the leading contribution to the high-energy amplitude of said process.

[5] Strictly speaking, to obtain the best possible bounds one should also take into account the deformations involved in single-Higgs production through *W-boson fusion* (*WBF*) $e^+e^- \to \nu_e\bar{\nu}_e h$, as its high-energy limit in the SMEFT can also be completely described by the same set of operators.

[6] See Refs. [283, 284] for the study of said processes in hadronic collisions.

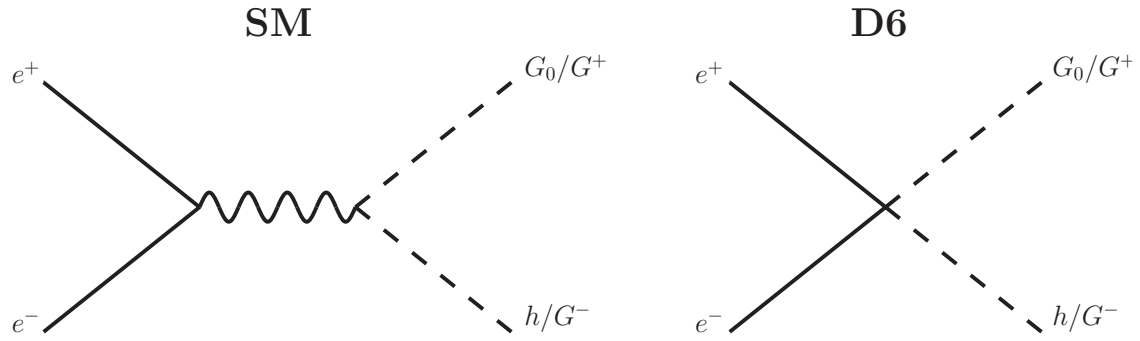


Figure 5.1: Feynman diagrams illustrating the interplay between the Goldstone Boson Equivalence Theorem and the leading high-energy contributions to $e^+e^- \to Zh, W^+W^-$ amplitudes in the **left:** SM, and **right:** D6 SMEFT. The dashed lines represent the corresponding Goldstone bosons.

Table 5.2: List of D6 operators contributing to $e^+e^- \to Zh, W^+W^-$, and *ZBF* processes at high energies.

| SILH Basis | Warsaw Basis |
|---|---|
| $\mathcal{O}_W = i\left(H^\dagger \sigma^i \overleftrightarrow{D^\mu} H\right) D^\nu W^i_{\mu\nu}$ | $\mathcal{O}_L^{\ell,(3)} = \left(\overline{L}\sigma^i\gamma^\mu L\right)\left(iH^\dagger\sigma^i\overleftrightarrow{D}_\mu H\right)$ |
| $\mathcal{O}_B = i\left(H^\dagger \overleftrightarrow{D^\mu} H\right) \partial^\nu B_{\mu\nu}$ | $\mathcal{O}_L^{\ell,(1)} = \left(\overline{L}\gamma^\mu L\right)\left(iH^\dagger\overleftrightarrow{D}_\mu H\right)$ |
| $\mathcal{O}_{HW} = i\left(D^\mu H\right)^\dagger \sigma^i \left(D^\nu H\right) W^i_{\mu\nu}$ | $\mathcal{O}_R^e = \left(\overline{e}_R\gamma^\mu e_R\right)\left(iH^\dagger\overleftrightarrow{D}_\mu H\right)$ |
| $\mathcal{O}_{HB} = i\left(D^\mu H\right)^\dagger \left(D^\nu H\right) B_{\mu\nu}$ | |
| $\mathcal{O}_{2W} = \left(D^\mu W^i_{\mu\nu}\right)^2$ | |
| $\mathcal{O}_{2B} = \left(\partial^\mu B_{\mu\nu}\right)^2$ | |

the amplitudes for these processes from the coefficients of the contact interactions $e^+e^-hG_0$ and $e^+e^-G^+G^-$. In the high-energy limit $s \gg m_Z^2$,

$$\begin{aligned}
\frac{\delta\mathcal{A}_{e_Re_R\to W^+W^-}}{\mathcal{A}^{\rm SM}_{e_Re_R\to W^+W^-}} &= \frac{\delta\mathcal{A}_{e_Re_R\to Zh}}{\mathcal{A}^{\rm SM}_{e_Re_R\to Zh}} = \frac{1}{2q^Z_{e_R}}\frac{s}{m_Z^2}\alpha_{e_R}, \\
\frac{\delta\mathcal{A}_{e_Le_L\to Zh}}{\mathcal{A}^{\rm SM}_{e_Le_L\to Zh}} &= \frac{1}{2q^Z_{e_L}}\frac{s}{m_Z^2}\left(\alpha_{L1}+\alpha_{L3}\right), \\
\frac{\delta\mathcal{A}_{e_Le_L\to W^+W^-}}{\mathcal{A}^{\rm SM}_{e_Le_L\to W^+W^-}} &= \frac{1}{2q^Z_{e_L}}\frac{s}{m_Z^2}\left(\alpha_{L1}-\alpha_{L3}\right),
\end{aligned} \tag{5.2.1}$$

where $\mathcal{A}^{\rm SM}$ are the SM amplitudes, $\delta\mathcal{A}$ correspond to the EFT contributions, and $q^Z_\ell = \left(T_3^\ell - Q_\ell s^2_{\theta_W}\right)$. The terms $\alpha_{e_R}$, $\alpha_{L1}$, and $\alpha_{L3}$ stand for the leptonic high-energy primaries, a linear combination of Wilson coefficients of D6 operators in the SMEFT. We make use of the SILH Lagrangian [193] to parametrise the BSM physics effects,

$$\begin{aligned}
\alpha_{L1} = \frac{\alpha_{e_R}}{2} &= \frac{m_W^2 t^2_{\theta_W}}{\Lambda^2}\left(c_B + c_{HB} - c_{2B}\right), \\
\alpha_{L3} &= -\frac{m_W^2}{\Lambda^2}\left(c_W + c_{HW} - c_{2W}\right),
\end{aligned} \tag{5.2.2}$$

from where it can be seen that only two out of the three directions remain independent. The primaries $\alpha_{L1}$ and $\alpha_{L3}$ can be written in terms of some universal *pseudo-observables* as,

$$\begin{aligned}
\alpha_{L1} = \frac{\alpha_{e_R}}{2} &= -t^2_{\theta_W}\left(\delta\kappa_\gamma - \hat{S} - \delta g_1^Z c^2_{\theta_W} + Y\right), \\
\alpha_{L3} &= \delta g_1^Z c^2_{\theta_W} + W,
\end{aligned} \tag{5.2.3}$$

where the set of anomalous couplings above can be independently constrained and best probed in other processes at high-energy collisions. We use the Warsaw basis [191] (see Appendix A) to write the expressions for the high-energy primaries in the general case as,

$$\begin{aligned}
\alpha_{e_R} &= -\frac{c_R^e v^2}{\Lambda^2}, \\
\alpha_{L1} &= -\frac{c_L^{\ell,(1)} v^2}{\Lambda^2}, \\
\alpha_{L3} &= -\frac{c_L^{\ell,(3)} v^2}{\Lambda^2}.
\end{aligned} \tag{5.2.4}$$

In terms of the anomalous couplings in Eq. (5.2.3), the expressions for the high-energy

primaries in the general case shown in Eq. (5.2.4) take the form,

$$\begin{aligned}\alpha_{L1} &= \frac{c_{\theta_W}}{g}\left(\delta g^Z_{e_L} + \delta g^Z_{\nu_L}\right) + s^2_{\theta_W}\delta g^Z_1 - t^2_{\theta_W}\delta\kappa_\gamma,\\ \alpha_{L3} &= \frac{c_{\theta_W}}{g}\left(\delta g^Z_{e_L} - \delta g^Z_{\nu_L}\right) + c^2_{\theta_W}\delta g^Z_1,\\ \alpha_{e_R} &= \frac{2c_{\theta_W}}{g}\delta g^Z_{e_R} + 2s^2_{\theta_W}\delta g^Z_1 - 2t^2_{\theta_W}\delta\kappa_\gamma.\end{aligned} \tag{5.2.5}$$

We show in Appendix F a derivation of these relations.

### 5.2.2 The *ZBF* channel: crossing symmetry

From Fig. 5.2, it can be seen that the diagram corresponding to the *ZBF* channel can be obtained by rotating the one for the *Higgs-strahlung* mode— these processes are related by *crossing symmetry*[7]. Thus, by replacing $s \to t$ in the relevant expressions of Eq. (5.2.1) one obtains the corresponding amplitude for the *ZBF* mode,

$$\begin{aligned}\frac{\delta\mathcal{A}_{e_RZ\to e_Rh}}{\mathcal{A}^{\rm SM}_{e_RZ\to e_Rh}} &= \frac{\delta\mathcal{A}_{e_Re_R\to Zh}}{\mathcal{A}^{\rm SM}_{e_Re_R\to Zh}}(s\to t) = \frac{1}{2q^Z_{e_R}}\frac{t}{m_Z^2}\alpha_{e_R},\\ \frac{\delta\mathcal{A}_{e_LZ\to e_Lh}}{\mathcal{A}^{\rm SM}_{e_LZ\to e_Lh}} &= \frac{\delta\mathcal{A}_{e_Le_L\to Zh}}{\mathcal{A}^{\rm SM}_{e_Le_L\to Zh}}(s\to t) = \frac{1}{2q^Z_{e_L}}\frac{t}{m_Z^2}\left(\alpha_{L1}+\alpha_{L3}\right),\end{aligned} \tag{5.2.6}$$

where $s$ and $t$ are the usual Mandelstam variables.

## 5.3 Collider analyses

In this section we discuss the collider analyses that help us in extracting the signal contributions from the background processes at future linear $e^+e^-$ colliders [50, 51, 55]. As explained previously, we focus on the *Higgs-strahlung* $e^+e^- \to \ell^+\ell^- h$, where $\ell = \{e, \mu, \tau\}$, and *ZBF* $e^+e^- \to e^+e^- h$ channels, targeting a semi-inclusive search of Higgs-boson decays that do not yield charged leptons in the final state to avoid redundancies in reconstructing the dilepton system[8]. Even though interference between these processes arises in the case of $Zh$ with final-state electrons, the invariant mass

[7] See, e.g., Ref. [295] for an analysis of these processes at the LHC.

[8] Although it is not an inclusive search, we still keep $\sim 90\%$ of Higgs decays.

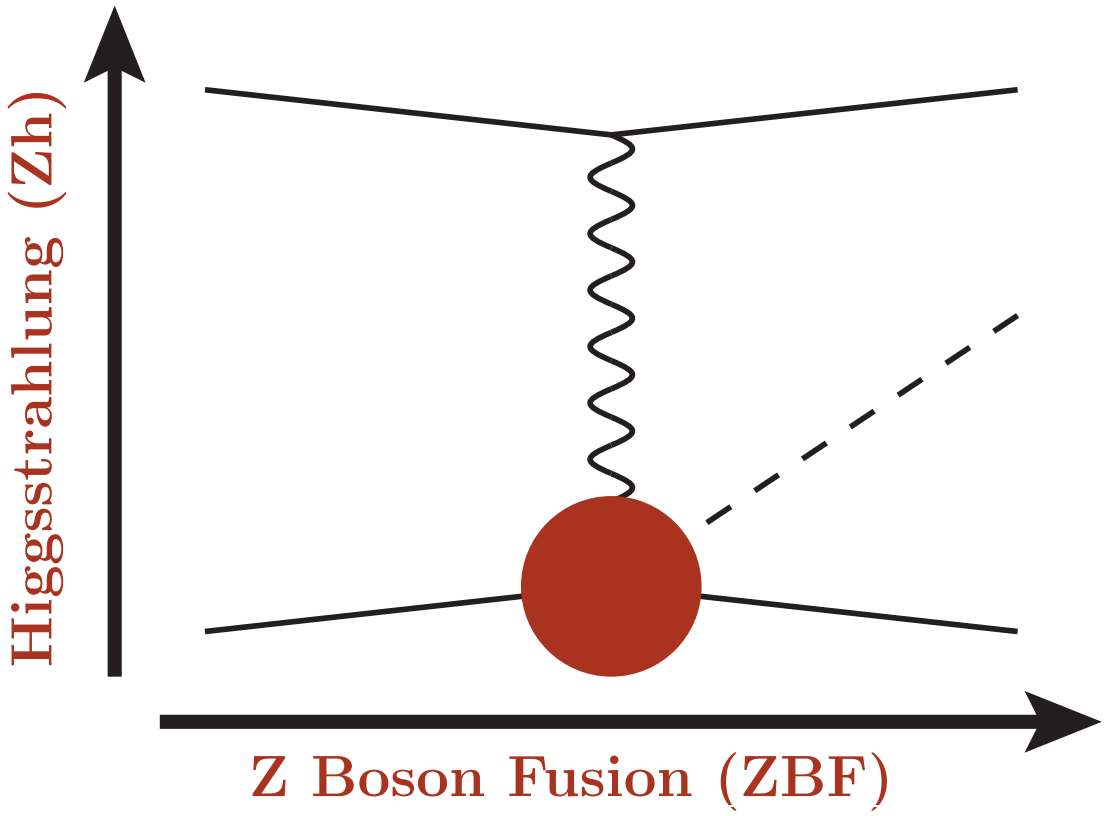


Figure 5.2: Feynman diagram illustrating the crossing symmetry between $Zh$ and $ZBF$ single-Higgs production. Note that by exchanging the Mandelstam variables $s \leftrightarrow t$ in the amplitude of a given process one can go from one channel to the other. Consequently, the same direction in the parameter space of the SMEFT controls $Zh$ at high $s$ and $ZBF$ at high $t$.

of the dilepton system is in itself a powerful discriminating variable that allows us to define mutually exclusive analysis categories.

We choose to sacrifice event rates, owed to the suppression of the leptonic decay channel of the $Z$-boson compared to the hadronic one, for a clean and unambiguous signal in the final state. Thus, the event topologies for the signal processes are characterised by exactly two leptons, satisfying an opposite-sign same-flavour (OSSF) requirement, and additional activity reaching the detectors in the form of jets, photons, missing energy, or a combination of these. Details of the Monte Carlo samples for the signal and background processes considered in our analyses, as well as the parameters of the colliders and the nomenclature employed, are presented in Appendix E.

It is possible for us to exploit the energy and momentum conservation since at $e^+e^-$ colliders the four-momentum $p_{e^+e^-}$ of the incoming beams is well known. In events where the Higgs is produced in association with a pair of charged, final-state leptons, one can uniquely specify Higgs-boson decays,

$$p_h = p_{e^+e^-} - p_{\ell^+\ell^-}, \tag{5.3.1}$$

with $p_{\ell^+\ell^-}$ the four-momentum of the final-state two-lepton system. The equation above can be used to implement model-independent studies of the width of the Higgs boson, $\Gamma_h$, as well as its inclusive production rate. In our analyses we make use of the dimensionful variable called the *recoil mass*,

$$m^2_{\text{recoil}} \equiv s - 2\sqrt{s}E_{\ell^+\ell^-} + m^2_{\ell^+\ell^-}, \tag{5.3.2}$$

which acts as a powerful discriminating observable against background process, and follows from Eq. (5.3.1). Given the Higgs' small width $\Gamma_h \sim 4.088\,\text{MeV}$ [46, 47], the $m_{\text{recoil}}$ distribution should show a narrow resonance centred at $m_h = 125\,\text{GeV}$ [45, 46, 48, 49] for events where the Higgs is produced on-shell. For a derivation of Eq. (5.3.2), see Appendix D.

Initial- (ISR) and final-state radiation (FSR), as well as *beam-strahlung* effects, yield

collinear photons that can have a visible impact on the $m_{\text{recoil}}$ distribution. Given that said collinear photons tend to escape the acceptance region of the detector, experimentally it is possible to control the smearing of the $m_{\text{recoil}}$ observable by imposing certain selection cuts on the $p_T$ of the final-state two-lepton system, as non-detected photons do not contribute largely to the overall transverse momentum of the recorded events.

### 5.3.1 Event selection of the *Zh* channel

In order to suppress background contributions from the SM-driven $e^+e^- \to \ell^+\ell^- h$ process, where $\ell = \{e, \mu, \tau\}$, at $\text{ILC}_{250,1000}$ and $\text{CLIC}_{3000}$[9], we implement a simplified cut-and-count analysis on the final-state objects after performing a fast detector simulation. The *Higgs-strahlung* channel is in itself a great avenue to select leptons originating from the decay of an on-shell $Z$-boson and, in doing so, make use of Eq. (5.3.2) to reconstruct the Higgs boson in a "model-independent" way, since the information of its decay products is encoded in Eq. (5.3.1).

As an $s$-channel process, the cross-section of the *Zh* mode decays with the centre-of-mass energy as $\sigma \sim 1/s$, being at low energies the dominant single-Higgs production mechanism at $e^+e^-$ colliders, as explained in Chapter 1. The $\text{ILC}_{250}$ is a Higgs factory that allows us to use the *Higgs-strahlung* channel to probe gauge-Higgs couplings through the reconstruction of $Z$-bosons decaying leptonically, a clean signature for the study of said process. However, at $\text{ILC}_{1000}$ and $\text{CLIC}_{3000}$ its cross-section is suppressed with respect to the $t$-channel *ZBF* process, and in order to enhance the total rate of the *Zh* mode at high energies one can target the hadronic decay channel of the $Z$-boson since its branching ratio is the largest. Nevertheless, even though the hadronic modes of the $Z$-boson are dominant with respect to the leptonic ones, $Z \to q\bar{q}$ decays are less clean, and the QCD activity associated with these $Z$-boson decays might present additional challenges requiring a detailed background analysis.

[9] Similar studies that target inclusive, or $h \to b\bar{b}$, Higgs decays can be found in, *e.g.*, Refs. [265, 330, 331].

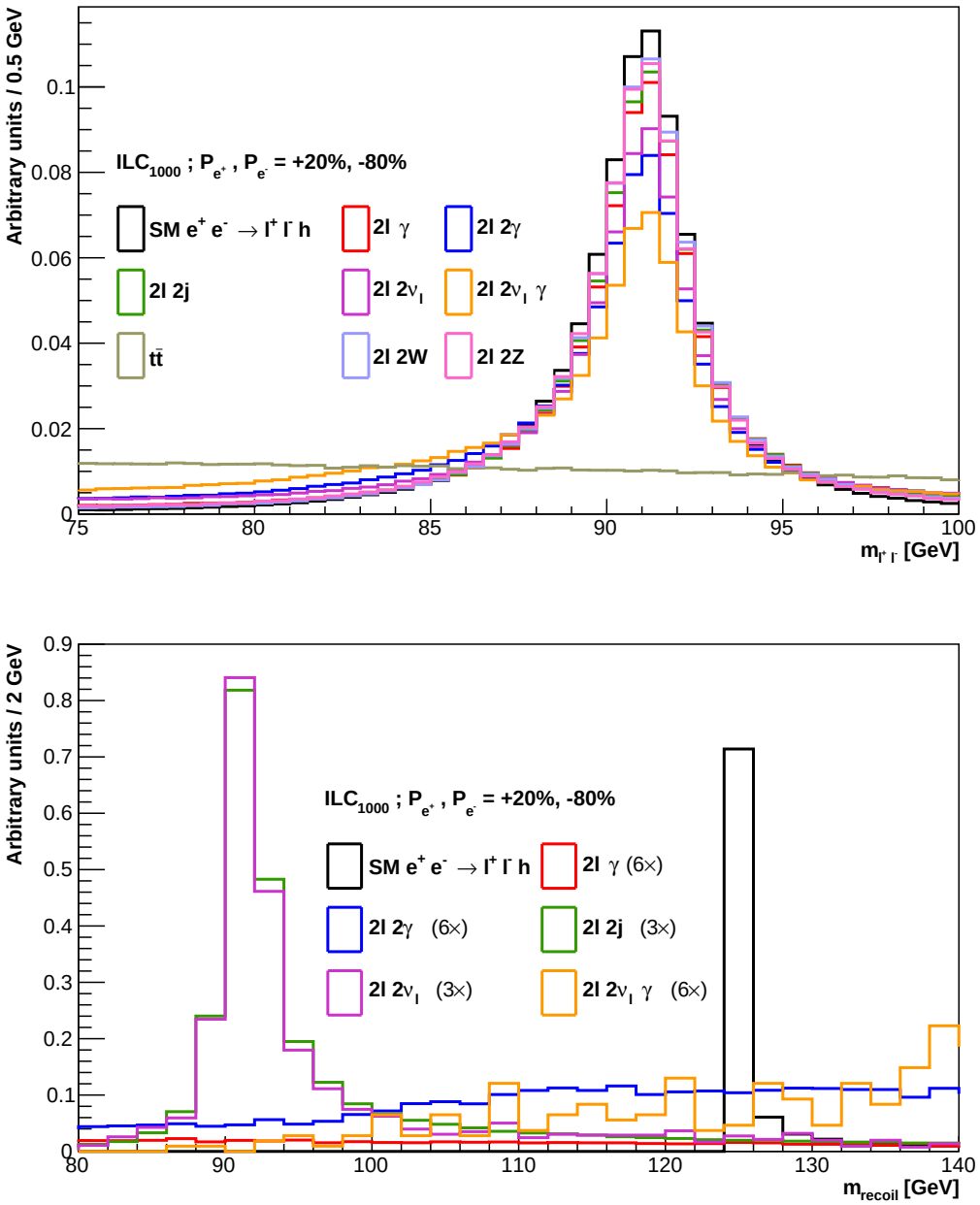


Figure 5.3: The $m_{\ell^+\ell^-}$ and $m_{\text{recoil}}$ distributions of the ILC$_{1000}$ $Zh$ selection with the *left* polarisation for the SM-driven $e^+e^- \to \ell^+\ell^- h$ (black), $2\ell\gamma$ (red), $2\ell2\gamma$ (blue), $2\ell2j$ (green), $2\ell2\nu_\ell$ (magenta), $2\ell2\nu_\ell\gamma$ (orange), $t\bar{t}$ (brown), $2\ell2W$ (lilac), and $2\ell2Z$ (pink) processes. All histograms are normalised to unity. **Top:** $m_{\ell^+\ell^-}$ distribution, in GeV, before applying the $m_{\ell^+\ell^-} \in [86.0, 96.0]$ GeV cut. **Bottom:** $m_{\text{recoil}}$ distribution, in GeV, before requiring $m_{\text{recoil}} \in [123.0, 127.0]$ GeV, where at this stage of the event selection the $t\bar{t}$ process is already negligible, and the $2\ell2V$ backgrounds lie beyond the right edge of the plot. Some histograms in the bottom panel are scaled for visualisation purposes. See text for details.

Table 5.3: Interplay between $Zh$ event selection and surviving cross-sections $\sigma$, in fb, of the SM-driven $e^+e^- \to \ell^+\ell^- h$ signal, and its dominant background processes before (*in*) and after (*out*) the event selection at centre-of-mass energies $\sqrt{s} = \{250, 1000, 3000\}$ GeV. We show the *left* and *right* polarisation settings $P_{e^+}$,$P_{e^-}$ at each $\sqrt{s}$, and report these as *left/right*. The high-energy backgrounds $t\bar{t}$ and $2\ell 2V$ are negligible and not shown here. See text for details.

| $\sigma^{\text{stage}}_{\sqrt{s}}$ [fb] | SM $e^+e^- \to \ell^+\ell^- h$ | $2\ell\gamma$ | $2\ell 2\gamma$ | $2\ell 2\nu_\ell$ | $2\ell 2\nu_\ell\gamma$ | $2\ell 2j$ |
|---|---|---|---|---|---|---|
| $\sigma^{\text{in}}_{250}$ | 29.85/26.26 | 5107.28/4735.02 | 316.95/287.56 | 651.88/101.26 | 68.75/8.21 | 264.22/181.23 |
| $\sigma^{\text{out}}_{250}$ | 6.99/6.14 | $< 10^{-6}$ | 0.40/0.32 | 1.02/0.12 | 0.13/0.04 | 0.22/0.08 |
| $\sigma^{\text{in}}_{1000}$ | 1.45/1.45 | 105.60/87.80 | 19.46/16.48 | 318.14/37.86 | 39.18/4.91 | 28.24/17.80 |
| $\sigma^{\text{out}}_{1000}$ | 0.33/0.31 | 0.017/0.013 | 0.0064/0.0053 | 0.0046/0.0024 | 3/2 $\left(\times 10^{-4}\right)$ | 0.0140/0.0072 |
| $\sigma^{\text{in}}_{3000}$ | 0.17/0.17 | 6.17/5.09 | 1.65/1.37 | 376.87/43.02 | 61.51/7.18 | 2.29/1.31 |
| $\sigma^{\text{out}}_{3000}$ | 0.026/0.025 | 12/9 $\left(\times 10^{-4}\right)$ | 9.64/6.09 $\left(\times 10^{-5}\right)$ | 3.8/1.9 $\left(\times 10^{-4}\right)$ | 61.5/3.6 $\left(\times 10^{-6}\right)$ | 8.3/4.9 $\left(\times 10^{-4}\right)$ |

In practice, we apply a minimal set of energy-dependent selection cuts to the Monte Carlo events. We require the presence of exactly one pair of OSSF leptons with $m_{\ell^+\ell^-} \in [86, 96]$ GeV— in $e^+e^-$ collisions it is possible to achieve high resolution in detecting final-state leptons, providing a clean reconstruction of the $Z$-boson mass $m_Z \sim 91\,\text{GeV}$ [326], irrespective of $\sqrt{s}$. Further, at the $\text{ILC}_{250,1000}$ and $\text{CLIC}_{3000}$ we impose the requirement $p_T^{\ell^+\ell^-} \in \{[40, 70], [400, 900], [1350, 1500]\}$ GeV, respectively. Finally, we make use of Eq. (5.3.2) to apply a hard cut on the mass of the recoiling system $m_{\text{recoil}} \in [123, 127]$ GeV, which exploits the fact that the $m_{\text{recoil}}$ distribution exhibits a sharp, narrow peak at $m_h \sim 125\,\text{GeV}$ on top of a continuum background. In Fig. 5.3 we show the $m_{\ell^+\ell^-}$ and $m_{\text{recoil}}$ distributions of the $\text{ILC}_{1000}$ collider analysis with the *left* polarisation, and Table 5.3 illustrates the impact of the event selection on the cross-sections of the SM processes considered in this subsection at three centre-of-mass energies as well as for the *left* and *right* polarisation settings[10].

As the aim of this study is to project bounds in D6 contact operators that grow with energy, we find in the collider analysis of the $Zh$ channel that the results of the $\text{ILC}_{250}$ do not show sensitivity to the effects of said operators. Thus, we neglect these and focus only on the high-energy regime, *i.e.*, $\text{ILC}_{1000}$ and $\text{CLIC}_{3000}$. We reserve the discussion of the projected sensitivities to EFT couplings for Sec. 5.4.

### 5.3.2 Event selection of the *ZBF* channel

We now discuss the analysis used to tackle the $ZBF$ mechanism $e^+e^- \to e^+e^-h$, which does not seem to be of much interest in the literature [332–334]. For this $t$-channel mode, the cross-section grows with energy as $\sigma \sim \ln^2\left|s/m_Z^2\right|$, and the interference with the $Zh$ channel at $\text{ILC}_{250}$ makes it difficult to disentangle its kinematic features, such as $m_{e^+e^-}$ well above $m_Z$ or a high-energy $e^+e^-$ pair in opposite forward regions of the detector, due to the reduced phase space. However, Fig. 3.9 makes evident that at $\sim 500\,\text{GeV}$ its total rate takes over the $Zh$ one. Thus, the enhanced cross-section

[10] We note that the kinematic distributions used in implementing the selection cuts exhibit similar shapes in both the *left* and *right* polarisation settings.

of the *ZBF* channel at higher centre-of-mass energies provides access to observables involving *Z-h* interactions that are best probed at $\text{ILC}_{1000}$ and $\text{CLIC}_{3000}$.

Similar to the event selection of the *Zh* channel, here we also perform a simplified cut-based analysis on the Monte Carlo samples after running a fast detector simulation at $\text{ILC}_{250,1000}$ and $\text{CLIC}_{3000}$. The invariant mass of the dilepton system $m_{e^+e^-}$, along with the recoil mass $m_{\text{recoil}}$ in Eq. (5.3.2), are the main variables used to discriminate non-Higgs backgrounds— the $m_{\text{recoil}}$ distribution exhibits a resonant behaviour that peaks at $\sim 125\,\text{GeV}$ on top of a continuum background, while the broad $m_{e^+e^-}$ distribution exhibits large values well above $m_Z$ at the TeV colliders but receives large contamination from the *Higgs-strahlung* process at $\text{ILC}_{250}$. Being a forward process, the final-state electron-positron pair tends to favour larger values of $|y^e|$ as $\sqrt{s}$ increases. However, one faces an experimental limitation to tag these leptons because of the absence of electromagnetic calorimeters able to reconstruct their tracks in the forward region of the detector, thus reducing the available phase-space (and consequently its total rate) to study the *ZBF* process at higher energies.

In performing the event selection we impose a minimal set of cuts, beginning with the forward-process requirement $y^{e^+} \cdot y^{e^-} < 0$, as the electron and positron should lie in opposite hemispheres of the detector. Due to this feature, one can expect a large rapidity gap $\Delta y_{e^+e^-}$ that, for the reasons explained above, is not present at $\text{ILC}_{250}$; however, at $\text{ILC}_{1000}$ ($\text{CLIC}_{3000}$) we require $\left|\Delta y_{e^+e^-}\right| \in [3,5]$ ($[3.5,5]$). Further, the $m_{e^+e^-}$ distribution is used to suppress background contributions, and we impose the condition $m_{e^+e^-} \in \{[105,130],[600,880],[2100,2880]\}$ GeV at $\text{ILC}_{250,1000}$ and $\text{CLIC}_{3000}$, respectively. Experimentally it is possible to control the effects of ISR, FSR, and *beam-strahlung*, that smear the $m_{\text{recoil}}$ distribution by demanding $p_T^{e^+e^-} \in \{[20,50],[80,300],[150,800]\}$ GeV. The event selection concludes by defining our signal region $m_{\text{recoil}} \in [123,127]$ GeV. In Fig. 5.4 we show the $\left|\Delta y_{e^+e^-}\right|$ and $m_{e^+e^-}$ distributions of the $\text{CLIC}_{3000}$ collider analysis with the *right* polarisation, and Table 5.4 illustrates the impact of the event selection on the cross-sections of the SM background processes considered in this subsection at the three centre-of-mass

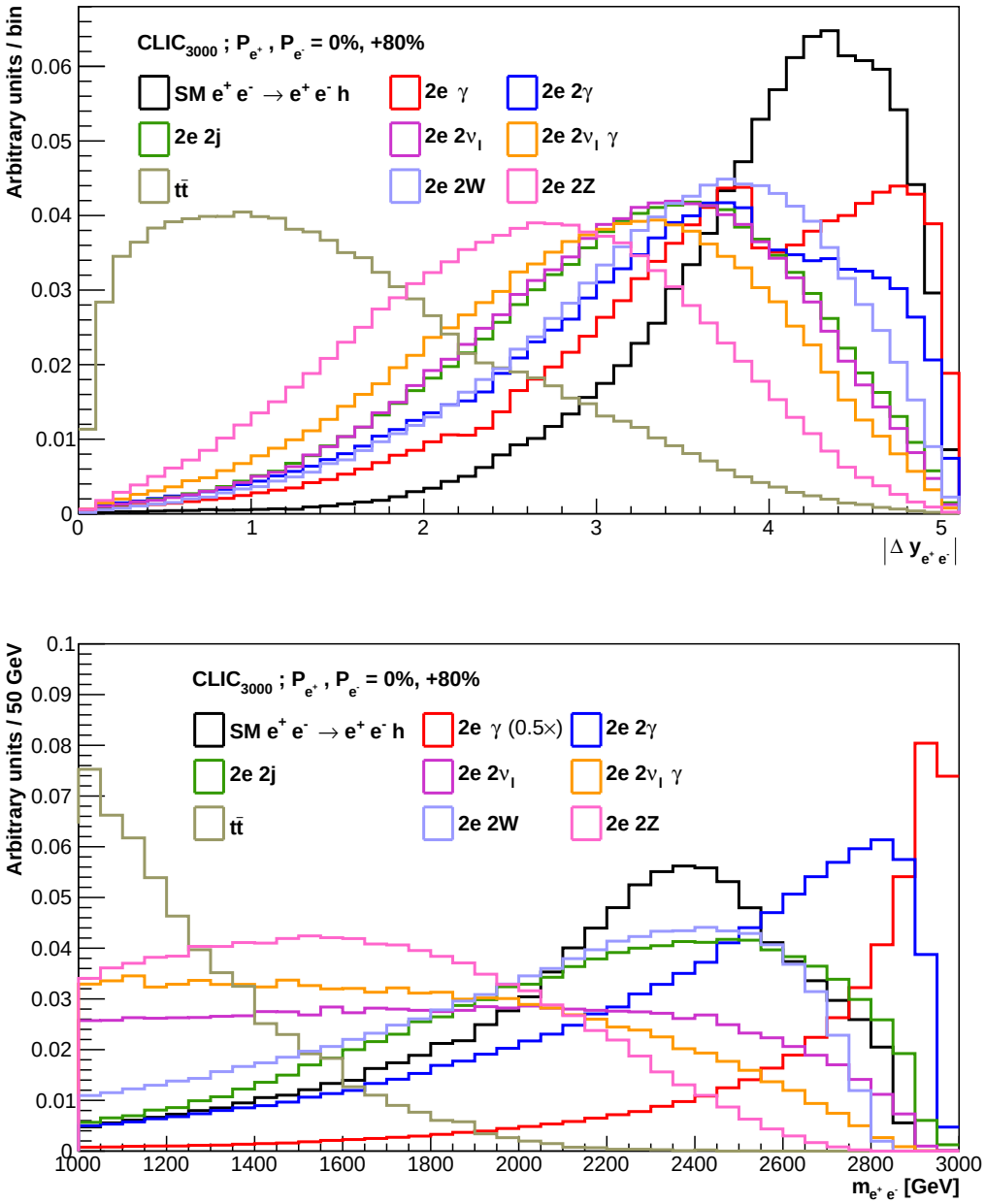


Figure 5.4: The $\left|\Delta y_{e^+e^-}\right|$ and $m_{e^+e^-}$ distributions of the CLIC$_{3000}$ *ZBF* selection with the *right* polarisation for the SM-driven $e^+e^- \to e^+e^-h$ (black), $2e\gamma$ (red), $2e2\gamma$ (blue), $2e2j$ (green), $2e2\nu_\ell$ (magenta), $2e2\nu_\ell\gamma$ (orange), $t\bar{t}$ (brown), $2e2W$ (lilac), and $2e2Z$ (pink) processes. All histograms are normalised to unity. **Top:** $\left|\Delta y_{e^+e^-}\right|$ distribution, illustrating the nature of the forward process $e^+e^- \to e^+e^-h$. **Bottom:** $m_{e^+e^-}$ distribution, in GeV, before imposing the cut $m_{e^+e^-} \in [2100, 2880]$ GeV, where the $2e\gamma$ distribution is scaled $(0.5\times)$ for visualisation purposes. See text for details.

Table 5.4: Interplay between $ZBF$ event selection and surviving cross-sections $\sigma$, in fb, of the SM-driven $e^+e^- \to e^+e^-h$ signal, and its dominant background processes before (*in*) and after (*out*) the event selection at centre-of-mass energies $\sqrt{s} = \{250, 1000, 3000\}$ GeV. We show the *left* and *right* polarisation settings $P_{e^+}$,$P_{e^-}$ at each $\sqrt{s}$, and report these as *left/right*. The high-energy processes $t\bar{t}$ and $2e2V$, as well as the $2e\gamma$ background, are negligible and not shown here. See text for details.

| $\sigma^{\text{stage}}_{\sqrt{s}}$ [fb] | SM $e^+e^- \to e^+e^-h$ | $2e2\gamma$ | $2e2\nu_\ell$ | $2e2\nu_\ell\gamma$ | $2e2j$ |
|---|---|---|---|---|---|
| $\sigma^{\text{in}}_{250}$ | 0.88/0.66 | 628.53/620.28 | 1348.33/99.46 | 59.79/4.29 | 125.27/115.97 |
| $\sigma^{\text{out}}_{250}$ | 0.26/0.19 | 0.37/0.34 | 1.57/0.13 | 0.11/0.01 | 0.033/0.024 |
| $\sigma^{\text{in}}_{1000}$ | 14.02/10.54 | 394.58/376.18 | 430.13/59.66 | 36.89/5.04 | 93.29/76.42 |
| $\sigma^{\text{out}}_{1000}$ | 2.52/1.92 | 0.034/0.030 | 0.099/0.016 | 0.0045/0.0017 | 0.024/0.012 |
| $\sigma^{\text{in}}_{3000}$ | 4.11/3.08 | 115.66/107.46 | 154.04/29.84 | 17.45/3.56 | 42.19/33.55 |
| $\sigma^{\text{out}}_{3000}$ | 0.22/0.15 | 0.0052/0.0054 | 0.0084/0.0022 | $8.4/4.7\ \left(\times 10^{-4}\right)$ | 0.0033/0.0018 |

energies as well as for the *left* and *right* polarisation settings[11].

As previously explained, the $t$-channel nature of the *ZBF* process implies that its cross-section dominates over the *Zh* mode at high energies and, similar to the event selection of the *Higgs-strahlung* channel, the results of the $\text{ILC}_{250}$ are not promising to probe the effects of the contact operators considered in our study. Thus, we neglect these and focus only on $\text{ILC}_{1000}$ and $\text{CLIC}_{3000}$. We reserve the discussion of the projected sensitivities to EFT couplings for Sec. 5.4.

## 5.4 Sensitivity to EFT couplings

We now present the sensitivity projections to the EFT couplings outlined in Sec. 5.2. As described in Sec. 5.3, we generate our signal Monte Carlo samples with the EFT couplings turned on, and apply the selection criteria to extract these from the background processes. We include the interference and EFT squared contributions as a function of the Wilson coefficients of the D6 operators listed in Table 5.2 for both *Zh* and *ZBF* processes.

Let us first look into the *Higgs-strahlung* process. The cut-and-count analysis described in Sec. 5.3 to suppress the background processes is enough to isolate the EFT-driven $e^+e^- \to \ell^+\ell^- h$ signal. As noted in Sec. 5.2, the absence of a propagator in the Feynman diagram shown in the right panel of Fig. 5.1 implies that the high-energy EFT and SM amplitudes have the same angular dependence (see also Ref. [284]), where the latter is the dominant background. To derive the sensitivity to EFT couplings we define a $\chi^2$ function,

$$\chi^2_{Zh} = \frac{\left(N^{\text{exp}}_{Zh} - N^{\text{obs}}_{Zh}\right)^2}{\sigma^2_{Zh}}, \tag{5.4.1}$$

where $N^{\text{exp}}_{Zh}$ denotes the number of events predicted by the SM (null hypothesis), and we assume that the number of observed events $N^{\text{obs}}_{Zh}$ differs from the SM prediction

[11] We note that the kinematic distributions used in implementing the selection cuts exhibit similar shapes in both the *left* and *right* polarisation settings.

because of the EFT insertions. The error $\sigma_{Zh}$,

$$\sigma_{Zh} = \sqrt{N_{Zh}^{\rm exp} + \left(\Delta_{\rm sys} N_{Zh}^{\rm exp}\right)^2}, \tag{5.4.2}$$

where we take $\Delta_{\rm sys} = 0.03$ in line with Ref. [56], includes the statistical and systematic uncertainties.

Let us now move on to the *ZBF* channel. Similar to the *Zh* case, the analysis strategy implemented to separate the SM $e^+e^- \to e^+e^-h$ process from the other backgrounds also isolates the EFT-driven signal, where the SM is the dominant source of background noise. In terms of the amplitudes, the EFT and the SM are alike except for a quadratic growth with $t$ of the former as described in Sec. 5.2, which we use to segregate the EFT process from the SM using the $p_T^h$ distribution as the discriminant. In doing so, we define the following $\chi^2$ function,

$$\chi^2_{ZBF} = \sum_i^N \frac{\left(N_{i,ZBF}^{\rm exp} - N_{i,ZBF}^{\rm obs}\right)^2}{\sigma_{i,ZBF}}, \tag{5.4.3}$$

where as done in the case of the *Zh* channel our null hypothesis corresponds to the SM prediction. In the equation above, $N_{i,ZBF}^{\rm exp}$ stands for the number of events predicted by the SM for the $i$-th bin in the $p_T^h$ distribution, and the binned uncertainty $\sigma_{i,ZBF}$ takes the form of Eq. (5.4.2) ($Zh \to i$*,ZBF*).

As far as the $e^+e^- \to W^+W^-$ process is concerned, we infer the $\chi^2_{WW}$ function from Table 15 in Ref. [56] for the hadronic and semileptonic channels. Finally, we combine all these processes (*Zh*, *ZBF*, and $W^+W^-$) as,

$$\chi^2_{\rm total} = \sum \chi^2_{Zh} + \sum \chi^2_{ZBF} + \sum \chi^2_{WW}, \tag{5.4.4}$$

where the sums run over the polarisation settings outlined in Appendix E for $\text{ILC}_{1000}$ and $\text{CLIC}_{3000}$.

### 5.4.1 Combination for universal case

Let us consider the case where new physics contributions are correlated with universal operators in Table 5.2. Expressing the Wilson coefficients of the operators contained in the SILH Lagrangian as a function of the universal parameters $\left(\delta\kappa_\gamma - \hat{S}\right)$ and $\delta g_1^Z$, we present our bounds in the two-dimensional planes shown in Fig. 5.5, where we neglect the $W$ and $Y$ parameters in Eq. (5.2.3) as these can be more stringently constrained in other processes [56, 283, 335, 336].

We show the results for $\text{ILC}_{1000}$ and $\text{CLIC}_{3000}$, as well as their comparison with LEP bounds [337] and HL-LHC projections [285]. In both cases, the *ZBF* channel allows us to set strong bounds at the per-mille level, surpassing LEP's. Nevertheless, the combination in Eq. (5.4.4) produces bounds that are an order of magnitude larger than the *ZBF* ones since at high $p_T^h$ the number of events filling the histograms becomes negligible, even though the cross-section of the *ZBF* process is dominant with respect to the *Zh* one. This effect can be seen in the top panel of Fig. 5.5, where at $\text{ILC}_{1000}$ the *Higgs-strahlung* process is more sensitive than the *ZBF* mode, and the *Zh* bounds are indistinguishable from the final ones. However, at $\text{CLIC}_{3000}$ the *Zh* and $e^+e^- \to W^+W^-$ processes probe two different directions in the parameter space, with the total combination giving stringent bounds.

We also show in Fig. 5.5, enclosed by the solid box, the energy scale,

$$\Lambda \sim \frac{m_W}{\sqrt{\delta g_1^Z c_{\theta_W}^2}}, \quad \frac{m_W}{\sqrt{\delta\kappa_\gamma - \hat{S}}}, \tag{5.4.5}$$

that can be probed in each case. Notice that scales as large as 4 TeV (10 TeV) can be probed at $\text{ILC}_{1000}$ ($\text{CLIC}_{3000}$), which is a confirmation that we indeed respect the considerations related to EFT validity. Finally, we note that the scales that can be accessed through our study far surpass the scales derived from LEP bounds on the $\hat{S}$-parameter corresponding to $\Lambda_{\text{LEP}} \sim 1.6 - 2.5$ TeV [193].

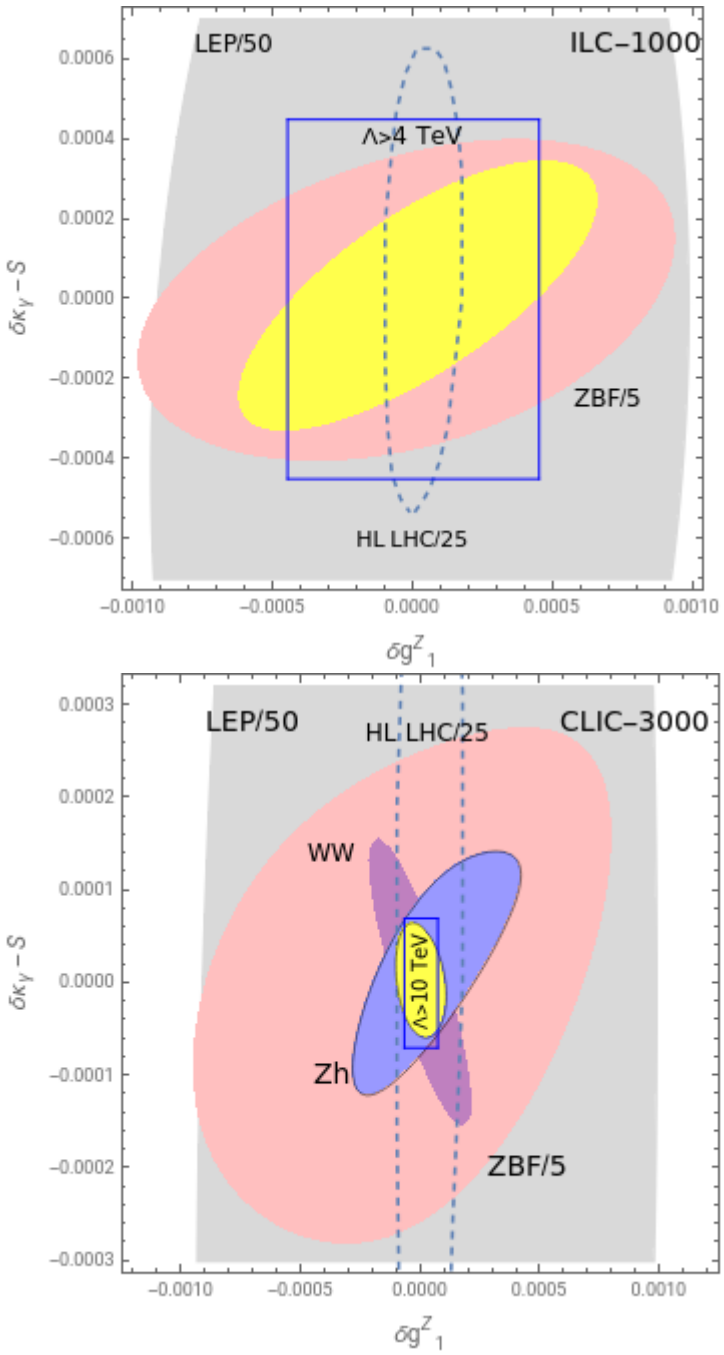


Figure 5.5: Projected sensitivities to EFT couplings for the case of universal new physics and their comparison with LEP bounds [337] and HL-LHC projections [285] at **top:** $\text{ILC}_{1000}$, and **bottom:** $\text{CLIC}_{3000}$. In both panels the grey area corresponds to LEP bounds; the region enclosed by the blue box shows the energy scale that can be accessed in each case; the dotted lines stand for the HL-LHC projections, and the pink area is the bounds obtained from the *ZBF* channel. In the top panel, the yellow area is the final bounds, which overlap with the bounds from the *Zh* channel. In the bottom panel, the blue region is the bounds from the *Higgs-strahlung* process; the purple area corresponds to the $W^+W^-$ process, and the yellow region shows the results of the overall combination. We assume $W = Y = 0$. See text for details.

### 5.4.2 Combination for general case

Let us now focus on the case where the three linearly independent combinations of the leptonic primaries under study contribute at high energies to new physics in the considered processes[12] as detailed in Sec. 5.2. The *Higgs-strahlung*, *ZBF*, and $e^+e^- \to W^+W^-$ channels can be used to probe different linear combinations of the Wilson coefficients corresponding to the operators listed in Table 5.2.

Looking at Eqs. (5.2.1) and (5.2.6), one can notice that the *Zh* and *ZBF* channels are not sensitive to the direction $(\alpha_{L1} - \alpha_{L3})$, and so including the bounds derived from the $W^+W^-$ process in Ref. [56] allows us to lift and further constrain an otherwise flat direction in the EFT space, as mentioned before. We show in Fig. 5.6 the two-dimensional bounds resulting after the third parameter is marginalised over, and the 95% confidence-level (CL) bounds on the individual leptonic high-energy primaries obtained after marginalising over the remaining two are,

$$\begin{aligned} \alpha_{L1} &\in [-8.5, 8.8] \times 10^{-5}, \\ \alpha_{L3} &\in [-9, 9] \times 10^{-4}, \\ \alpha_{e_R} &\in [-2.2, 1.5] \times 10^{-5}, \end{aligned} \tag{5.4.6}$$

with these bounds illustrated graphically in Fig. 5.7. Further, we show in Figs. 5.6 and 5.7 the energy scale that can be accessed, $\Lambda \sim v/\sqrt{\alpha_i}$, which can be as high as 20–30 TeV.

As shown in Eq. (5.2.5), one can write the leptonic high-energy primaries in terms of pseudo-observables measured at LEP,

$$\begin{aligned} \alpha_{L1} &= \frac{c_{\theta_W}}{g}\left(\delta g^Z_{e_L} + \delta g^Z_{\nu_L}\right) + s^2_{\theta_W}\delta g^Z_1 - t^2_{\theta_W}\delta\kappa_\gamma, \\ \alpha_{L3} &= \frac{c_{\theta_W}}{g}\left(\delta g^Z_{e_L} - \delta g^Z_{\nu_L}\right) + c^2_{\theta_W}\delta g^Z_1, \\ \alpha_{e_R} &= \frac{2c_{\theta_W}}{g}\delta g^Z_{e_R} + 2s^2_{\theta_W}\delta g^Z_1 - 2t^2_{\theta_W}\delta\kappa_\gamma, \end{aligned}$$

where these correlations allow us to directly compare our bounds with existing

[12] Note that this does not necessarily imply that the leptonic primaries are statistically independent parameters.

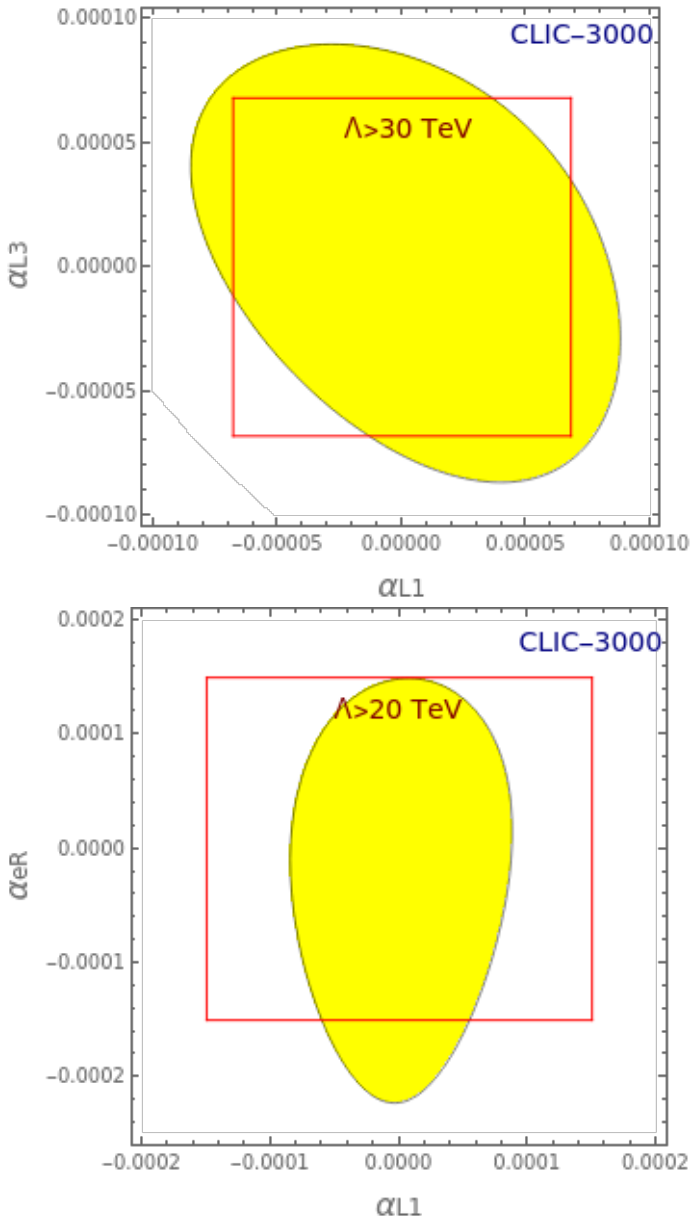


Figure 5.6: Projected sensitivities for the leptonic high-energy primaries, defined in Eq. (5.2.4), at $\text{CLIC}_{3000}$ in two-dimensional planes, where the remaining parameter has been marginalised over. See text for details.

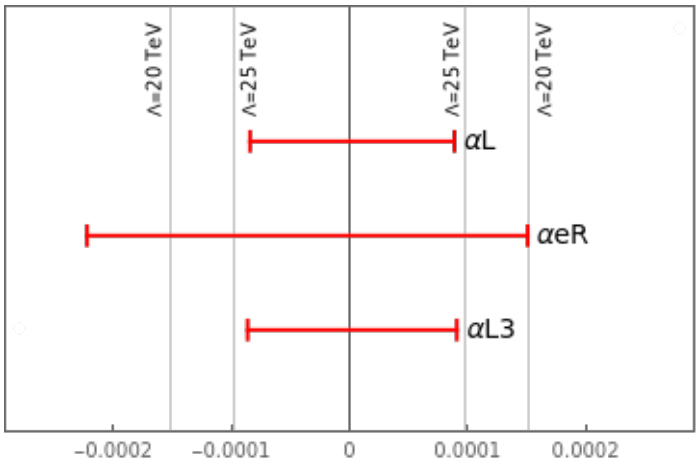


Figure 5.7: Projected sensitivities on the individual leptonic high-energy primaries, defined in Eq. (5.2.4), at $\text{CLIC}_{3000}$, after marginalising over the remaining two parameters. See text for details.

LEP ones and HL-LHC projections, arising mainly from constraints on anomalous (charged) *Triple Gauge Couplings* (TGCs) [313] on the right-hand side of the above expressions. The bounds obtained from leptonic $Z$-boson decays at LEP, given by Ref. [264], are,

$$\begin{aligned} \delta g^Z_{e_L} &\in [-1, 9] \times 10^{-4}, \\ \delta g^Z_{e_R} &\in [-4, 2] \times 10^{-4}. \end{aligned} \tag{5.4.7}$$

We note that our bounds in Eq. (5.4.6) are stronger than the $Z$-pole constraints at LEP, where we assume that EFT contributions to TGCs vanish[13].

## 5.5 Conclusions

The multi-dimensional parameter space of the SMEFT has been widely used to parametrise indirect effects of BSM physics— including all possible D6 operators that contribute to a given process is a systematic way to summarise the projections and bounds set by indirect searches. Nevertheless, to study the dominant high-energy deformations of a process due to EFT insertions one only has to include its most

[13]This statement is motivated by the fact that existing LEP bounds and HL-LHC projections are roughly 100× and 10× weaker, respectively, than those shown in Eq. (5.4.6).

sensitive effects, which in turn opens up the possibility to ask the question: *what is the highest energy scale that can be probed by the experiments?*

In this Chapter we addressed this question by considering the capabilities of future linear $e^+e^-$ colliders, such as the high-energy stages of ILC and CLIC, at studying standard electroweak processes, namely the *Higgs-strahlung* and *Z-boson fusion* single-Higgs production mechanisms, and their correlations with EFT effects that grow with energy. In doing so, we performed a 'high-energy fit' of the corresponding operators, including the results of the $e^+e^- \to W^+W^-$ channel described in Ref. [56].

We took into account the processes listed in Table 5.1. We identified that three linear combinations of the Wilson coefficients of the D6 operators listed in Table 5.2, the so-called *leptonic high-energy primaries*, entail the dominant high-energy contribution to these processes, shown in Eqs. (5.2.1), (5.2.2), (5.2.4), and (5.2.6). The growing-with-energy EFT effects of these operators are larger by a factor of $s/m_Z^2$ than those that do not grow with energy— these translate to roughly two orders of magnitude at the $\sqrt{s} = 1\,\text{TeV}$ ILC and $\sqrt{s} = 3\,\text{TeV}$ CLIC. Even if one takes into account EFT effects that are linear functions of the energy, these are still smaller by roughly one order of magnitude than the ones we consider in our study.

We showed in Figs. 5.5–5.7 and Eq. (5.4.6) our projections for the sensitivity to EFT couplings, and found that these estimates correspond to more stringent constraints on the considered anomalous couplings than existing LEP bounds and HL-LHC projections by at least two and one orders of magnitude, respectively. In addressing the question related to the energy scales that can be accessed at the colliders, we also showed in Figs. 5.5–5.7 our projections for the scales that these experiments can probe, and find that the effects considered in this study are capable of accessing energy scales up to tens of TeV. All these make future linear $e^+e^-$ colliders the ultimate miscroscopes to probe fundamental physics in the electroweak and gauge-Higgs sectors.

# Chapter 6

# Summary and Outlook

The SM is the best understanding we have to date of the interactions between elementary particles— it has been tested time and again, and is known to agree well with a plethora of experimental measurements. However, several physical phenomena suggest that the SM is not the ultimate theory possible for an adequate description of Nature. Thus, to account for the shortcomings of the SM, a more robust theory is needed. Because of its well-tested agreement with many observations, to construct a new framework that supersedes the SM it is necessary to begin by taking the current theory, and extend it to the energy scale of interest in some way. This means the ultimate theory (if any exists) that predicts the behaviour of the quantum fields composing our Universe should reproduce the SM in its low-energy limit.

It is possible to view the SM as an EFT, valid up to a high cut-off energy scale. In this framework, we parametrise our ignorance of the short-distance physics and the energies at which it becomes relevant. In doing so, the SM Lagrangian gets extended by operators of higher mass dimensions: these are built out of SM fields, and respect the underlying symmetries of the theory, with the coefficients of the perturbative expansion encoding the high-energy behaviour of new physics. This way of encapsulating the low-energy effects of an unknown theory does not require additional degrees of freedom. Thus, one has to deal with a new set of higher-dimensional Lorentz structures and modified vertices, the so-called anomalous couplings, that

extend the interactions allowed by the SM.

After the discovery of the Higgs boson in 2012, the Large Hadron Collider has yet not succeeded to deliver tantalising evidence for new resonant physics. As we are unaware of the exact energy scale at which such new resonant physics should show up, improving our current experiments and performing new precision measurements are among the most pressing issues that the particle physics community needs to address, since looking for deviations from the theory prediction might be a hint for physics beyond the SM. Thus, setting stringent bounds on loosely-constrained areas of the current framework is of great importance to determine whether discrepancies between theory and data can be found by the experiments. Due to the large masses of the Higgs and the weak bosons, gauge-Higgs interactions are thought to be a promising avenue that might shed light on what potentially lies beyond the SM.

In this Thesis we have investigated the interplay between effective theories and measurements at colliders by considering the capability of current and future experiments at segregating anomalous couplings through standard processes involving interactions between the Higgs and the gauge bosons.

In Chapter 1 we introduced the Standard Model of Particle Physics and listed some of its shortcomings, as well as the possible ways in which the particle physics community intends to extend it. Then, in Chapter 2 Fermi's theory of muon decay was used to give an overview of the EFT framework, and to motivate the study of the SM as an effective theory by extending its Lagrangian with higher-dimensional operators. From the collision energy to the detection system, in Chapter 3 we presented a non-exhaustive description of collider physics, and outlined the main differences between hadron and electron-positron colliders, as well as between direct and indirect searches. In Chapter 4 we used the method of moments to probe the tensor structure of the Higgs couplings to gauge bosons in the golden channel at the Large Hadron Collider, and we projected strong bounds which are competitive and complementary to the existing ones. Finally, in Chapter 5 we performed a 'high-energy fit' and set stringent constraints on the so-called leptonic high-energy primaries that can be probed in

the gauge-Higgs sector at future linear electron-positron colliders.

Past and present experiments have delivered a huge amount of data, testing the predictions of the SM. All these measurements, as well as the absence of new resonant physics at the Large Hadron Collider, seem to suggest that the scale of new physics is well separated from the electroweak scale. Several questions arise, such as how to reconstruct a TeV-scale Lagrangian with the current data, or which strategies are most effective in looking for certain differential observables and would allow us to best anticipate incoming statistics?

While the predictions of the SM Lagrangian have been addressed and tested experimentally, it now becomes crucial to understand what are the complete predictions from the dimension-six Lagrangian in the context of the SM EFT. New vertices can produce novel or enhanced effects in certain phase-space regions, and it is of vital importance to determine which the best observables to study the effects of certain operators or processes are. As shown in Chapters 4 and 5, some Higgs deformations have already been constrained by electroweak precision physics, and going to the regime of high energies or luminosities might be the only way to obtain newer information at collider experiments.

Correlations between $Z$-pole measurements and anomalous couplings inform the Higgs observables measured at colliders, which means that some physical processes are not independent and are instead related to each other. This can be useful if a departure from the SM predictions is observed; but if no deviations are found, these correlations can be used to set constraints on the size of the additional terms of the effective theory expansion. In other words, how well can we probe the tensor structure of gauge-Higgs couplings and be competitive with existing constraints from precision physics?

Although the nature of the boson discovered in 2012 is more or less consistent with the SM Higgs, some of its decay channels and interactions are still to be observed and measured. It is expected that some of these will be achieved during the High-Luminosity stage of the Large Hadron Collider, or even at future electron-positron

colliders. The precision expected at these machines is such that some projections show they have the potential to constrain couplings at the per-cent, or even per-mille, level. We can expect that the technical capabilities of the colliders to come can be exploited to achieve the precision needed for a successful physics programme.

As outlined in the previous paragraphs, the quest to come up with the ultimate theory of Nature seems to be far from being around the corner. Nevertheless, this Thesis could be a tiny contribution, one way or another, towards achieving this goal. With computational tools evolving and improving rapidly, comes a deeper understanding of the underlying theory of particle physics. Moreover, sophisticated analysis techniques, along with experiments reaching higher and higher energies, can benefit from precision measurements that might reveal hints of where to look for the eagerly awaited new physics.

All in all, despite the numerous theoretical and experimental challenges ahead, the years to come promise to be a good time to get on board and search for physics beyond the SM by *constraining anomalous couplings in the gauge-Higgs sector at high-energy colliders*.

# Appendix A

# Bosonic sector in the Warsaw basis

In this Appendix we list the dimension-six operators $\mathcal{O}^{(6)}$ in the Warsaw basis involving the scalar field $\phi$ and field-strength tensors $X_{\mu\nu} \in \left\{G^a_{\mu\nu},\, W^i_{\mu\nu},\, B_{\mu\nu}\right\}$, as presented in Ref. [191]. In what follows, dual field strength tensors are defined as,

$$\widetilde{X}_{\mu\nu} = \frac{1}{2}\epsilon_{\mu\nu\rho\sigma}X^{\rho\sigma}. \tag{A.0.1}$$

The complex conjugate of the Higgs field is,

$$\widetilde{\phi}^j = \epsilon_{jk}\left(\phi^k\right)^*. \tag{A.0.2}$$

Moreover, terms containing Hermitian derivatives have the following definition,

$$\phi^\dagger i\overset{\leftrightarrow}{D}_\mu\phi \equiv i\phi^\dagger\left(D_\mu - \overleftarrow{D}_\mu\right)\phi, \quad \phi^\dagger i\overset{\leftrightarrow}{D}{}^i_\mu\phi \equiv i\phi^\dagger\left(\tau^i D_\mu - \overleftarrow{D}_\mu\tau^i\right)\phi. \tag{A.0.3}$$

Gauge field strength tensors are defined according to Eq. (1.1.5) (see Sec. 1.1.1), and their covariant derivatives are,

$$\begin{aligned}
\left(D_\rho G_{\mu\nu}\right)^a &= \partial_\rho G^a_{\mu\nu} + g_S f^{abc}G^b_\rho G^c_{\mu\nu},\\
\left(D_\rho W_{\mu\nu}\right)^i &= \partial_\rho W^i_{\mu\nu} + g\epsilon^{ijk}W^j_\rho W^k_{\mu\nu},\\
D_\rho B_{\mu\nu} &= \partial_\rho B_{\mu\nu}.
\end{aligned} \tag{A.0.4}$$

Table A.1: **Class $X^3$:** Operators containing only gauge field strength tensors.

| | $X^3$ |
|---|---|
| $\mathcal{O}_G$ | $f^{abc}G_\mu^{a,\nu}G_\nu^{b,\rho}G_\rho^{c,\mu}$ |
| $\mathcal{O}_{\widetilde{G}}$ | $f^{abc}\widetilde{G}_\mu^{a,\nu}G_\nu^{b,\rho}G_\rho^{c,\mu}$ |
| $\mathcal{O}_W$ | $\epsilon^{ijk}W_\mu^{i,\nu}W_\nu^{j,\rho}W_\rho^{k,\mu}$ |
| $\mathcal{O}_{\widetilde{W}}$ | $\epsilon^{ijk}\widetilde{W}_\mu^{i,\nu}W_\nu^{j,\rho}W_\rho^{k,\mu}$ |

Table A.2: **Classes $\phi^6$ and $\phi^4 D^2$:** Operators affecting the scalar sector. Note that the 'box operator' $\Box$ is defined as $\Box \equiv \partial^\mu\partial_\mu$.

| | $\phi^6$ and $\phi^4 D^2$ |
|---|---|
| $\mathcal{O}_\phi$ | $\left(\phi^\dagger\phi\right)^3$ |
| $\mathcal{O}_{\phi\Box}$ | $\left(\phi^\dagger\phi\right)\Box\left(\phi^\dagger\phi\right)$ |
| $\mathcal{O}_{\phi D}$ | $\left(\phi^\dagger D^\mu\phi\right)^*\left(\phi^\dagger D_\mu\phi\right)$ |

Table A.3: **Class $\psi^2\phi^3$:** Operators affecting Yukawa interactions. Flavour indices are denoted by $p$ and $r$.

| | $\psi^2\phi^3$ + h.c. |
|---|---|
| $\mathcal{O}_{e\phi}$ | $\left(\phi^\dagger\phi\right)\left(\overline{\ell}_p e_r\phi\right)$ |
| $\mathcal{O}_{u\phi}$ | $\left(\phi^\dagger\phi\right)\left(\overline{q}_p u_r\widetilde{\phi}\right)$ |
| $\mathcal{O}_{d\phi}$ | $\left(\phi^\dagger\phi\right)\left(\overline{q}_p d_r\phi\right)$ |

Table A.4: **Class $X^2\phi^2$:** Purely bosonic operators.

| | $X^2\phi^2$ |
|---|---|
| $\mathcal{O}_{\phi G}$ | $\phi^\dagger\phi\, G^a_{\mu\nu}G^{a,\mu\nu}$ |
| $\mathcal{O}_{\phi\widetilde{G}}$ | $\phi^\dagger\phi\, \widetilde{G}^a_{\mu\nu}G^{a,\mu\nu}$ |
| $\mathcal{O}_{\phi W}$ | $\phi^\dagger\phi\, W^i_{\mu\nu}W^{i,\mu\nu}$ |
| $\mathcal{O}_{\phi\widetilde{W}}$ | $\phi^\dagger\phi\, \widetilde{W}^i_{\mu\nu}W^{i,\mu\nu}$ |
| $\mathcal{O}_{\phi B}$ | $\phi^\dagger\phi\, B_{\mu\nu}B^{\mu\nu}$ |
| $\mathcal{O}_{\phi\widetilde{B}}$ | $\phi^\dagger\phi\, \widetilde{B}_{\mu\nu}B^{\mu\nu}$ |
| $\mathcal{O}_{\phi WB}$ | $\phi^\dagger\tau^i\phi\, W^i_{\mu\nu}B^{\mu\nu}$ |
| $\mathcal{O}_{\phi\widetilde{W}B}$ | $\phi^\dagger\tau^i\phi\, \widetilde{W}^i_{\mu\nu}B^{\mu\nu}$ |

Table A.5: **Classes $\psi^2X\phi$ and $\psi^2\phi^2D$:** Fermionic dipole (left) and gauge-Higgs-fermion vertex (right) operators. Flavour indices are denoted by $p$ and $r$.

| | $\psi^2X\phi+$ h.c. | | $\psi^2\phi^2D$ |
|---|---|---|---|
| $\mathcal{O}_{eW}$ | $\left(\bar{\ell}_p\sigma^{\mu\nu}e_r\right)\tau^i\phi\, W^i_{\mu\nu}$ | $\mathcal{O}^{(1)}_{\phi\ell}$ | $\left(\phi^\dagger i\overleftrightarrow{D}_\mu\phi\right)\left(\bar{\ell}_p\gamma^\mu\ell_r\right)$ |
| $\mathcal{O}_{eB}$ | $\left(\bar{\ell}_p\sigma^{\mu\nu}e_r\right)\phi\, B_{\mu\nu}$ | $\mathcal{O}^{(3)}_{\phi\ell}$ | $\left(\phi^\dagger i\overleftrightarrow{D}^i_\mu\phi\right)\left(\bar{\ell}_p\tau^i\gamma^\mu\ell_r\right)$ |
| $\mathcal{O}_{uG}$ | $\left(\bar{q}_p\sigma^{\mu\nu}T^a u_r\right)\widetilde{\phi}\, G^a_{\mu\nu}$ | $\mathcal{O}_{\phi e}$ | $\left(\phi^\dagger i\overleftrightarrow{D}_\mu\phi\right)\left(\bar{e}_p\gamma^\mu e_r\right)$ |
| $\mathcal{O}_{uW}$ | $\left(\bar{q}_p\sigma^{\mu\nu}u_r\right)\tau^i\widetilde{\phi}\, W^i_{\mu\nu}$ | $\mathcal{O}^{(1)}_{\phi q}$ | $\left(\phi^\dagger i\overleftrightarrow{D}_\mu\phi\right)\left(\bar{q}_p\gamma^\mu q_r\right)$ |
| $\mathcal{O}_{uB}$ | $\left(\bar{q}_p\sigma^{\mu\nu}u_r\right)\widetilde{\phi}\, B_{\mu\nu}$ | $\mathcal{O}^{(3)}_{\phi q}$ | $\left(\phi^\dagger i\overleftrightarrow{D}^i_\mu\phi\right)\left(\bar{q}_p\tau^i\gamma^\mu q_r\right)$ |
| $\mathcal{O}_{dG}$ | $\left(\bar{q}_p\sigma^{\mu\nu}T^a d_r\right)\phi\, G^a_{\mu\nu}$ | $\mathcal{O}_{\phi u}$ | $\left(\phi^\dagger i\overleftrightarrow{D}_\mu\phi\right)\left(\bar{u}_p\gamma^\mu u_r\right)$ |
| $\mathcal{O}_{dW}$ | $\left(\bar{q}_p\sigma^{\mu\nu}d_r\right)\tau^i\phi\, W^i_{\mu\nu}$ | $\mathcal{O}_{\phi d}$ | $\left(\phi^\dagger i\overleftrightarrow{D}_\mu\phi\right)\left(\bar{d}_p\gamma^\mu d_r\right)$ |
| $\mathcal{O}_{dB}$ | $\left(\bar{q}_p\sigma^{\mu\nu}d_r\right)\phi\, B_{\mu\nu}$ | $\mathcal{O}_{\phi ud}$ | $i\left(\widetilde{\phi}^\dagger\overleftrightarrow{D}_\mu\phi\right)\left(\bar{u}_p\gamma^\mu d_r\right)$ |

# Appendix B

# Elements of Fourier analysis

In Chapter 4, the method of moments is introduced as a technique analogous to Fourier analysis. To illustrate and complement the idea, in this Appendix we will show the basic elements of the Fourier-series expansion of a function with arbitrary period defined on a finite interval, mostly inspired by Refs. [338, 339].

A function $f$ is called *T-periodic*, with $T > 0$, if it satisfies the identity,

$$f(x) = f(x+T) \quad \forall\, x. \tag{B.0.1}$$

Let $f$ be defined on the interval $[a, b]$. The function is continuous at $c \in [a, b]$ iff,

$$\lim_{x \to c} f(x) = \lim_{x \to c^+} f(x) = \lim_{x \to c^-} f(x), \tag{B.0.2}$$

where,

$$\lim_{x \to c^\pm} f(x) \equiv f\left(c^\pm\right),$$

corresponds to the limit of $f$ as $x$ approaches to $c$ from the right $(+)$ or from the left $(-)$. If the limits $f\left(a^+\right)$ and $f\left(b^-\right)$ exist, and $f$ is continuous and defined on the interval $(a, b)$[1], the function $f$ is *piecewise continuous* on $[a, b]$.

If $f$ is defined on the interval $[a, b]$, the function is said to be *piecewise smooth* if $f$ is piecewise continuous on $[a, b]$; $f'$ exists and is continuous in $(a, b)$[2], and $f'\left(a^+\right)$

[1] It is possible that there exist a finite number of points where $f$ is not continuous.

[2] Except possibly at a finite number of points $c$ where $f'\left(c^-\right)$ and $f'\left(c^+\right)$ exist.

and $f'\left(b^-\right)$ exist.

Let $g(x)$ and $h(x)$ be piecewise smooth functions on $[a,b]$. These are *orthogonal* over the interval $[a,b]$ if,

$$\langle g|h\rangle \equiv \int_a^b \mathrm{d}x\, g^* h = 0. \tag{B.0.3}$$

With these concepts at hand, we can turn our attention to the trigonometric system $\{1, \cos(nx), \sin(nx)\}$ $(n>0)$: these are orthogonal, periodic functions that satisfy the continuity and smoothness conditions[3] outlined above. The orthogonality properties of the trigonometric system on the interval $[-\pi,\pi]$[4] are such that,

$$\begin{aligned} \langle \cos(mx)|\cos(nx)\rangle = \ \langle \sin(mx)|\sin(nx)\rangle = 0 \quad & \text{if } m \neq n, \\ \langle \cos(mx)|\cos(mx)\rangle = \langle \sin(mx)|\sin(mx)\rangle = \pi \quad & \forall\, m \neq 0, \\ \langle \cos(mx)|\sin(nx)\rangle = 0 \quad & \forall\, m \text{ and } n. \end{aligned} \tag{B.0.4}$$

The set of these trigonometric functions forms a basis for the vector space (of their linear combinations) over $\mathbb{R}$ of continuous functions defined on $[a,b]$. We define a Fourier series as an expansion of a function $f$ in a series of the trigonometric functions sine and cosine with an expression of the form,

$$f(x) = a_0 + \sum_{n=1}^{\infty} \left(a_n \cos(nx) + b_n \sin(nx)\right). \tag{B.0.5}$$

The coefficients of the series expansion are extracted making use of the orthogonality properties in Eq. (B.0.4) as,

$$\begin{aligned} a_0 \equiv \langle f(x)|1\rangle \quad &\Rightarrow \quad a_0 = \frac{1}{2\pi}\int_{-\pi}^{\pi} \mathrm{d}x\, f(x), \\ a_n \equiv \langle f(x)|\cos(mx)\rangle \quad &\Rightarrow \quad a_m = \frac{1}{\pi}\int_{-\pi}^{\pi} \mathrm{d}x\, f(x)\cos(mx), \\ b_n \equiv \langle f(x)|\sin(mx)\rangle \quad &\Rightarrow \quad b_m = \frac{1}{\pi}\int_{-\pi}^{\pi} \mathrm{d}x\, f(x)\sin(mx), \end{aligned} \tag{B.0.6}$$

since,

$$\int_{-\pi}^{\pi} \mathrm{d}x\, \cos(mx) = \int_{-\pi}^{\pi} \mathrm{d}x\, \sin(mx) = 0. \tag{B.0.7}$$

[3] Also known as *Dirichlet conditions*.

[4] Since these functions are $2\pi$-periodic, the orthogonality properties hold for any interval of length $2\pi$.

So far we have worked with $2\pi$-periodic functions for simplicity. The results can be extended to functions with arbitrary period. Let us assume that $f$ is a function satisfying the Dirichlet conditions mentioned above, with period $T = 2p > 0$, and perform the following change of variables,

$$h(x) = f\left(\frac{p}{\pi}x\right), \tag{B.0.8}$$

such that $h$ is $2\pi$-periodic. The main result in Eq. (B.0.5) can be extended as,

$$f(x) = a_0 + \sum_{n=1}^{\infty}\left(a_n \cos\left(\frac{n\pi}{p}x\right) + b_n \sin\left(\frac{n\pi}{p}x\right)\right), \tag{B.0.9}$$

where the coefficients can be extracted using the prescription in Eq. (B.0.6) as,

$$\begin{aligned} a_0 &= \frac{1}{2p}\int_{-p}^{p} \mathrm{d}x\, f(x), \\ a_n &= \frac{1}{p}\int_{-p}^{p} \mathrm{d}x\, f(x)\cos\left(\frac{n\pi}{p}x\right), \\ b_n &= \frac{1}{p}\int_{-p}^{p} \mathrm{d}x\, f(x)\sin\left(\frac{n\pi}{p}x\right). \end{aligned} \tag{B.0.10}$$

The moral of this story in terms of the method of moments in Chapter 4 is as follows: given a set of functions $\{f_i\}_i$, we might assume there exists a dual basis of "weights" $\{w_i\}_i$ *orthonormal* to the set containing the $f$'s,

$$\int \mathrm{d}\Omega\, w_j f_i = \delta_{ij}, \tag{B.0.11}$$

such that the $w_j$'s are able to project the linear combination $a_i f_i$ (total rate) onto the coefficients $a_j$,

$$\int \mathrm{d}\Omega \sum_i (a_i f_i)\, w_j = a_j, \tag{B.0.12}$$

where we have assumed that the $\{w_i\}$ set is a linear transformation of the $\{f_i\}$ set, with the orthogonality condition fixing the transformation matrix,

$$w_i = \lambda_{ij} f_j \Rightarrow \lambda = M^{-1}, \quad \text{with } M_{ij} = \int \mathrm{d}\Omega\, f_i f_j. \tag{B.0.13}$$

# Appendix C

# The Golden Channel: Monte Carlo samples

In this Appendix we outline the details of the Monte Carlo samples used in Chapter 4 to obtain bounds on the relevant operator combinations.

Our UFO [340] model is implemented with the help of FeynRules [341], which we use to generate the Monte Carlo signal samples including the interference and squared terms ensuing from D6 interactions. Since the process under consideration is $gg \to h \to 4\ell$, we identify the quark- and gluon-initiated $q\bar{q} \to 4\ell$ and $gg \to 4\ell$ irreducible backgrounds, respectively, where $\ell = \{e, \mu, \tau\}$. Given that, in practice, at the LHC the overwhelmingly large QCD activity can produce jets that might fake charged leptons in the fiducial region of the detector, we take into account the reducible backgrounds $Z/\gamma^* + \text{jets}$, $t\bar{t}$, $W^+W^- + \text{jets}$, and $W^\pm Z + \text{jets}$. We find that the dominant source of fake backgrounds arises from the $Z/\gamma^* + \text{jets}$ process, which we generate as $pp \to \ell^+\ell^- + 2$ jets, and neglect the remaining reducible processes.

We consider a centre-of-mass energy $\sqrt{s} = 14\,\text{TeV}$ in generating our Monte Carlo events. Leading-order (LO) samples which include the full decay chain, consisting of the SM- and EFT-driven $gg \to h \to 4\ell$ process, as well as the main reducible background $Z/\gamma^* + \text{jets}$, are generated with MadGraph [342]. The dominant background process $q\bar{q} \to 4\ell$ is generated at next-to-leading order (NLO)

with POWHEG BOX v2 [343–345]. The PDF sets `NNPDF23_lo_as_0130` and `NNPDF31_nlo_hessian_pdfas` [346] are used to generate MadGraph events and quark-initiated background samples, respectively. The gluon-initiated $gg \to 4\ell$ events are generated at LO with MCFM 7 [347], using the `CTEQ6L` [348] PDF set. In all cases, the parton-level samples are passed on to Pythia 8 [349] for showering and hadronisation.

At the generator level, the quark-initiated $q\overline{q} \to 4\ell$ events are required to fulfil an invariant-mass cut for each pair of opposite-sign same-flavour (OSSF) leptons of $M_{\ell^+,\ell^-} \geq 4\,\text{GeV}$. The remaining samples must satisfy $\left|\eta^{\ell}\right| \leq 3$ and $\Delta R(\ell_i, \ell_j) \geq 0.015$, where $\Delta R = \sqrt{\Delta\eta^2 + \Delta\phi^2}$ is the angular distance between two objects in the $\eta - \phi$ plane. We impose an additional set of cuts in MadGraph, namely $p_T^{\ell_1} \geq 15\,\text{GeV}$, $p_T^{\ell_{2,3}} \geq 8\,\text{GeV}$, and $p_T^{\ell_4} \geq 3\,\text{GeV}$, where the leptons' indices indicate their ordering with respect to $p_T$. Moreover, we require the $Z/\gamma^* + \text{jets}$ samples to satisfy $p_T^j \geq 20\,\text{GeV}$, $\left|y^j\right| \leq 3$, $\Delta R(j,\ell) \geq 0.015$, $\Delta R\,(j_m, j_n) \geq 0.015$, as well as $M_{2\ell,2j} \in [95, 155]$ GeV. Finally, in MCFM 7 we apply the $p_T^{\ell} \geq 3\,\text{GeV}$, $M_{\ell^+,\ell^-} \geq 2.5\,\text{GeV}$, and $M_{4\ell} \geq 70\,\text{GeV}$ cuts. For a description of the geometry and major components of the detection system, see Chapter 3.

The LO production cross-section of the $gg \to h$ Monte Carlo events is scaled to the N$^3$LO-accurate prediction of the *LHC Higgs Cross-Section Working Group* [46] (LHC HXSWG, CERN Report 4), for $M_h = 125\,\text{GeV}$, which results in a $K$-factor of 3.155 applied to the SM- and EFT-driven samples. For consistency with the LHC HXSWG, we further set $\Gamma_h = 4.088\,\text{MeV}$. In the case of the $q\overline{q} \to 4\ell$ background, we consider a flat NNLO/NLO $K$-factor of 1.1 [350]. Moreover, we apply an NNLO/LO flat $K$-factor of 2.27 to the $gg \to 4\ell$ cross-section, in line with the experimental search described in Ref. [241]. Finally, a conservative approach is adopted by applying a flat $K$-factor of 0.91 [351] to the $Z/\gamma^* + \text{jets}$ events.

# Appendix D

# Derivation of the recoil mass observable

In this Appendix we derive the equation that describes the *recoil mass* observable, at $e^+e^-$ colliders, introduced in Chapter 5. For simplicity and illustration purposes, let us consider the process $e^+e^- \rightarrow Z + X$, with the $Z$-boson decaying leptonically $Z \rightarrow \ell^+\ell^-$, where $\ell = \{e, \mu\}$, and $X$ an arbitrary final state recoiling against the $Z$-boson. Hence, the full reaction is,

$$e^+e^- \rightarrow Z + X \rightarrow \ell^+\ell^- + X.$$

Let $p^{\mu}_{e^+}$ and $p^{\mu}_{e^-}$ be the four-momenta of the incoming positron and electron, respectively, each with mass $m_e$. For a centre-of-mass energy $\sqrt{s}$, each beam carries an energy $E$ such that $E_{e^+} = E_{e^-} \equiv E$ and $2E = \sqrt{s}$. In the relativistic limit, $E \gg m_e$, the four-momenta of the incoming particles in the laboratory frame can be written as,

$$p^{\mu}_{e^+} = (E, 0, 0, E), \quad p^{\mu}_{e^-} = (E, 0, 0, -E), \tag{D.0.1}$$

where we take the $+\hat{z}$ axis in the direction of the positron. The four-momentum of the incoming electron-positron pair $p^{\mu}_{e^+e^-}$ is simply,

$$\begin{aligned} p^{\mu}_{e^+e^-} \equiv p^{\mu}_{e^+} + p^{\mu}_{e^-} &= (2E, 0, 0, 0) \\ &= \left(\sqrt{s}, 0, 0, 0\right). \end{aligned} \tag{D.0.2}$$

Similarly for the decay products of the $Z$ boson,

$$q^{\mu}_{\ell^+} = \left(E_{\ell^+}, \vec{q}_{\ell^+}\right), \quad q^{\mu}_{\ell^-} = \left(E_{\ell^-}, \vec{q}_{\ell^-}\right), \tag{D.0.3}$$

the four-momentum of the final-state dilepton system $q^{\mu}_{\ell^+\ell^-}$ is,

$$q^{\mu}_{\ell^+\ell^-} = \left(E_{\ell^+\ell^-}, \vec{q}_{\ell^+\ell^-}\right), \tag{D.0.4}$$

with $q^{\ell^+\ell^-}_{\mu} q^{\mu}_{\ell^+\ell^-} = m_Z^2$ the invariant mass squared of the $Z$-boson. The four-momenta of the reaction under consideration can then be written as,

$$p_{e^+e^-} = q_{\ell^+\ell^-} + k_X, \tag{D.0.5}$$

where $k_X$ is the four-momentum of the arbitrary final state $X$ fixed by,

$$k_X = p_{e^+e^-} - q_{\ell^+\ell^-}. \tag{D.0.6}$$

Plugging Eqs. (D.0.2) and (D.0.4) in the expression for $k_X$ above, four-momentum conservation implies,

$$\begin{aligned} k^2 \equiv m_X^2 &= (p_{e^+e^-} - q_{\ell^+\ell^-})^2 \\ &= p^2_{e^+e^-} - 2p_{e^+e^-} \cdot q_{\ell^+\ell^-} + q^2_{\ell^+\ell^-} \\ &= s - 2\sqrt{s}E_{\ell^+\ell^-} + m^2_{\ell^+\ell^-}, \end{aligned} \tag{D.0.7}$$

which corresponds to the invariant mass $m_X^2$ of the set of objects recoiling against the dilepton system, or equivalently against the $Z$-boson. For a $2 \rightarrow 2$ process it is enough to reconstruct one of the intermediate-state objects to fix completely the kinematics of the object recoiling against it.

# Appendix E

# The Higgs at $e^+e^-$ colliders: Monte Carlo samples

In this Appendix we outline the details of the Monte Carlo samples used in Chapter 5 to define the analysis categories, extract the signal contributions from the background processes, and obtain bounds on the relevant operator combinations.

Our UFO [340] model is implemented with the help of FeynRules [341], which we use to generate the Monte Carlo signal samples including the interference and squared terms ensuing from D6 interactions. Since the analysis categories correspond to the ($Zh$) $e^+e^- \to \ell^+\ell^- h$, where $\ell = \{e, \mu, \tau\}$, and ($ZBF$) $e^+e^- \to e^+e^- h$ channels, we consider for both cases the following set of background processes: $2\ell\gamma$, $2\ell2\gamma$, $2\ell2\nu_\ell$, $2\ell2\nu_\ell\gamma$, and $2\ell2j$. Where the phase space permits, we also take into account $2\ell2V$ ($V = \{W, Z\}$), as well as the fully-leptonic $t\bar{t}$ process[1]. Further, for $Zh$-like backgrounds, $\ell = \{e, \mu, \tau\}$, whereas for the $ZBF$-like case, $\ell = \{e, \tau\}$[2].

For simplicity, we neglect reducible backgrounds that arise from charged leptons being faked by jets or photons reaching the electromagnetic calorimeters of the detector. Note that the SM-driven $Zh$ and $ZBF$ processes are the major sources of background noise in themselves, and the signal events come from interactions

[1] We find that these high-energy background processes are rendered negligible.

[2] Note that $v_\ell$ always stands for the set of all three neutrino flavours.

ensuing from the EFT corrections explained in Chapter 5.

We examine the centre-of-mass energies $\sqrt{s} = \{250, 1000, 3000\}$ GeV, where the first and second values correspond to the projected low- and high-energy phases of the International Linear Collider (ILC) [52, 53], respectively, and the last one to the high-energy run of the Compact Linear Collider (CLIC) [54, 56]. We adopt the nomenclature $\text{ILC}_{250,1000}$ ($\text{CLIC}_{3000}$) to refer to the ILC (CLIC) collider run at the $\sqrt{s}$ subscript. In line with the recommendations of Ref. [352], we incorporate longitudinal beam polarisation [250, 252, 253, 353] into our collider setup[3]. Denoting $\mathcal{L}$ as the integrated luminosity of the collider, and $P_{e^+}, P_{e^-}$ as the polarisation of the positron and electron beams[4], respectively, we use the following parameters to set up the environment of the $e^+e^-$ colliders considered in our study:

- $\text{ILC}_{250}$: $\sqrt{s} = 250\,\text{GeV}$, $\mathcal{L} = 2000\,\text{fb}^{-1}$, $P_{e^+}, P_{e^-} = \pm 30\%, \mp 80\%$.
- $\text{ILC}_{1000}$: $\sqrt{s} = 1000\,\text{GeV}$, $\mathcal{L} = 8000\,\text{fb}^{-1}$, $P_{e^+}, P_{e^-} = \pm 20\%, \mp 80\%$.
- $\text{CLIC}_{3000}$: $\sqrt{s} = 3000\,\text{GeV}$, $\mathcal{L} = 5000\,\text{fb}^{-1}$, $P_{e^+}, P_{e^-} = 0\%, \mp 80\%$.

From the list above, we call *left* and *right* polarisation the cases $P_{e^+} \geq 0, P_{e^-} < 0$, and $P_{e^+} \leq 0, P_{e^-} > 0$, respectively. Given that for each $\sqrt{s}$ there are two possible polarisation settings, we effectively have a two-in-one collider, where a different fraction of the total integrated luminosity corresponds to each *left* and *right* beams. We refer the reader to Chapter 3 for an explanation of the role of beam polarisation in $e^+e^-$ collisions.

We use MadGraph [342] to generate the leading-order (LO) Monte Carlo samples, and further pass on the parton-level events to Pythia 8 [349] for showering and hadronisation. We perform a fast detector simulation with the help of DELPHES 3 [354], where the `ILD Tune` [249, 355] and `CLICdet Stage3 Tune` [356, 357]

[3] Throughout the text, the term *polarisation* stands for longitudinal polarisation.

[4] In this notation, $P = +100\%$ stands for a fully right-handed polarised beam, and $P = -100\%$ corresponds to a fully left-handed polarised beam.

are used for the $\text{ILC}_{250,1000}$ and $\text{CLIC}_{3000}$ collider scenarios, respectively. We impose a minimal set of generator-level cuts, namely $p_T^{\ell,j,\gamma} > 5\,\text{GeV}$, $m_{jj} > 10\,\text{GeV}$, $\left|y^{j,\gamma}\right| \left(\left|y^{\ell}\right|\right) < 5$ (3), and $\Delta R_{a,b} > 0.1$, where $\Delta R_{a,b} = \sqrt{(\Delta\phi)^2 + (\Delta y)^2}$ is the angular distance between two objects $(a, b)$ in the $\phi - y$ plane[5].

The invariant mass of the dilepton system is the observable that helps us best in discriminating between the *Zh* and *ZBF* categories. For the *Zh*-like samples we require $m_{\ell^+\ell^-} \in [70, 110]\text{GeV}$, while for the *ZBF* ones we impose a $\sqrt{s}$-dependent cut $m^{\sqrt{s}}_{\ell^+\ell^-}$ as follows: $m^{250}_{\ell^+\ell^-} > 100\,\text{GeV}$, $m^{1000}_{\ell^+\ell^-} > 300\,\text{GeV}$, and $m^{3000}_{\ell^+\ell^-} > 1000\,\text{GeV}$. Further, since the *ZBF* channel is a forward process we require $y^{\ell^+} \cdot y^{\ell^-} < 0$ to ensure that the leptons lie in opposite hemispheres of the detector. For a description of the geometry and major components of the detection system, see Chapter 3.

[5]Note that, although the polar angle $\theta$ is used in lepton colliders to help defining the three-momentum of a particle reaching the detectors, here we use the rapidity $y$ to be consistent with the parameters of the generator and detector simulation. In the massless limit, $\theta \equiv 2\arctan\left(e^{-y}\right)$.

# Appendix F

# Anomalous couplings and the Higgs at $e^+e^-$ colliders

In this Appendix we show what the connection between the Wilson coefficients of the operators listed in Table 5.2 of Chapter 5 and anomalous couplings is.

The Lagrangian which is relevant to the universal case is,

$$\begin{aligned}\Delta\mathcal{L}_{\text{univ}} = &-\frac{\hat{T}}{2}\frac{m_Z^2}{2}Z_\mu Z^\mu - \frac{\hat{S}}{4m_W^2}\frac{gg'v^2}{2}\left(W^3_{\mu\nu}B^{\mu\nu}\right)\\ &-\frac{W}{2m_W^2}\left(\partial^\mu W^3_{\mu\nu}\right)^2 - \frac{Y}{2m_W^2}\left(\partial^\mu B_{\mu\nu}\right)^2\\ &+ ig\delta g_1^Z c_{\theta_W} Z^\mu\left(W^{+,\nu}W^-_{\mu\nu} - W^{-,\nu}W^+_{\mu\nu}\right)\\ &+ ig\left(\delta\kappa_Z c_{\theta_W} Z^{\mu\nu} + \delta\kappa_\gamma s_{\theta_W}\hat{A}^{\mu\nu}\right)W^+_\mu W^-_\nu,\end{aligned} \tag{F.0.1}$$

where $\delta\kappa_Z = \delta g_1^Z - t^2_{\theta_W}\delta\kappa_\gamma$. In the equation above, $\hat{S}$ and $\hat{T}$ are the usual Peskin-Takeuchi parameters [358]; $W$ and $Y$ correspond to two-other EW Precision Observables (EWPO) defined in Ref. [359], and $\delta g_1^Z$ and $\delta\kappa_\gamma$ are the TGCs defined in Ref. [313]. In the SILH basis [193], the Wilson coefficients are related to the above EWPO and TGCs by,

$$\begin{aligned}\hat{T} = \frac{v^2}{\Lambda^2}c_T, \quad \hat{S} = \frac{m_W^2}{\Lambda^2}\left(c_W + c_B\right), \quad Y = \frac{m_W^2}{\Lambda^2}c_{2B}, \quad W = \frac{m_W^2}{\Lambda^2}c_{2W},\\ \delta g_1^Z = -\frac{m_W^2}{\Lambda^2}\frac{1}{c^2_{\theta_W}}\left(c_W + c_{HW}\right), \quad \delta\kappa_\gamma = -\frac{m_W^2}{\Lambda^2}\left(c_{HW} + c_{HB}\right),\end{aligned} \tag{F.0.2}$$

where $c_T$ corresponds to the Wilson coefficient of the operator $\mathcal{O}_T = \left(H^\dagger \overleftrightarrow{D}_\mu H\right)^2/2$, and the input parameters are $(G_F, m_Z, \alpha_{\rm em})$. From the equations above, it is possible to derive the following correlations,

$$\begin{aligned} t_{\theta_W}^2\left(\delta\kappa_\gamma - \hat{S} - \delta g_1^Z c_{\theta_W}^2 + Y\right) &= -\frac{m_W^2}{\Lambda^2}\left(c_B + c_{HB} - c_{2B}\right), \\ \left(\delta g_1^Z c_{\theta_W}^2 + W\right) &= -\frac{m_W^2}{\Lambda^2}\left(c_W + c_{HW} - c_{2W}\right), \end{aligned} \tag{F.0.3}$$

used in Secs. 5.2 and 5.4 to obtain the two-dimensional bounds in the EFT parameter space shown in Fig. 5.5.

Following Ref. [204], the Lagrangian which is relevant to the general case is,

$$\begin{aligned} \Delta\mathcal{L}_6 = {} & \delta g_L^W\left(W_\mu^+ \overline{\nu}_L \gamma^\mu e_L + \text{h.c.}\right) + g_{W\ell}^h \frac{h}{v}\left(W_\mu^+ \overline{\nu}_L \gamma^\mu e_L + \text{h.c.}\right) \\ & + \sum_\ell \delta g_\ell^Z Z_\mu \bar{\ell}\gamma^\mu \ell + \sum_\ell g_{Z\ell}^h \frac{h}{v} Z_\mu \bar{\ell}\gamma^\mu \ell \\ & + ig\delta g_1^Z c_{\theta_W} Z^\mu\left(W^{+,\nu}\hat{W}_{\mu\nu}^- - W^{-,\nu}\hat{W}_{\mu\nu}^+\right) \\ & + ig\left(\delta\kappa_Z c_{\theta_W}\hat{Z}^{\mu\nu} + \delta\kappa_\gamma s_{\theta_W}\hat{A}^{\mu\nu}\right) W_\mu^+ W_\nu^-, \end{aligned} \tag{F.0.4}$$

where, for simplicity, $L$ is the first-generation lepton doublet, and $\ell = e_L, e_R, \nu_L^e$.

Taking the operators of the Warsaw basis [191] (see Appendix A) into account, listed in Table 5.2, we get the contributions,

$$\begin{aligned} \delta g_\ell^W &= \frac{g}{\sqrt{2}}\frac{v^2}{\Lambda^2} c_L^{\ell,(3)} + \frac{\delta m_Z^2}{m_Z^2}\frac{\sqrt{2} g c_{\theta_W}^2}{4 s_{\theta_W}^2}, \\ g_{W\ell}^h &= \sqrt{2} g \frac{v^2}{\Lambda^2} c_L^{\ell,(3)}, \\ \delta g_\ell^Z &= -\frac{g Y_\ell s_{\theta_W}}{c_{\theta_W}^2}\frac{v^2}{\Lambda^2} c_{HWB} + \frac{\delta m_Z^2}{m_Z^2}\frac{g}{2 c_{\theta_W} s_{\theta_W}^2}\left(T_3^\ell c_{\theta_W}^2 + Y_\ell s_{\theta_W}^2\right) \\ & \quad - \frac{g}{c_{\theta_W}}\frac{v^2}{\Lambda^2}\left(\left|T_3^\ell\right| c_L^{\ell,(1)} - T_3^\ell c_L^{\ell,(3)} + \left(1/2 - \left|T_3^\ell\right|\right) c_R^e\right), \\ g_{Z\ell}^h &= -\frac{2g}{c_{\theta_W}}\frac{v^2}{\Lambda^2}\left(\left|T_3^\ell\right| c_L^{\ell,(1)} - T_3^\ell c_L^{\ell,(3)} + \left(1/2 - \left|T_3^\ell\right|\right) c_R^e\right), \\ \delta g_1^Z &= \frac{1}{2 s_{\theta_W}^2}\frac{\delta m_Z^2}{m_Z^2}, \\ \delta\kappa_\gamma &= \frac{1}{t_{\theta_W}}\frac{v^2}{\Lambda^2} c_{HWB}, \end{aligned} \tag{F.0.5}$$

where, following Ref. [204], we use the $(m_W, m_Z, \alpha_{\rm em})$ input scheme. As mentioned

in Chapter 4, the input parameter $m_Z$ gets shifted by,

$$\frac{\delta m_Z^2}{m_Z^2} = \frac{v^2}{\Lambda^2}\left(2t_{\theta_W}c_{HWB} + \frac{c_{HD}}{2}\right), \tag{F.0.6}$$

due to the operators $\mathcal{O}_{HWB}$ and $\mathcal{O}_{HD}$ [292]. Finally, the correlations used in Secs. 5.2 and 5.4 can be derived using the above equations,

$$\begin{aligned}
c_L^{\ell,(1)}\frac{v^2}{\Lambda^2} &= -\frac{c_{\theta_W}}{g}\left(\delta g_{eL}^Z + \delta g_{\nu L}^Z\right) - s_{\theta_W}^2\delta g_1^Z + t_{\theta_W}^2\delta\kappa_\gamma,\\
c_L^{\ell,(3)}\frac{v^2}{\Lambda^2} &= -\frac{c_{\theta_W}}{g}\left(\delta g_{eL}^Z - \delta g_{\nu L}^Z\right) - c_{\theta_W}^2\delta g_1^Z,\\
c_R^e\frac{v^2}{\Lambda^2} &= -\frac{2c_{\theta_W}}{g}\delta g_{eR}^Z - 2s_{\theta_W}^2\delta g_1^Z + 2t_{\theta_W}^2\delta\kappa_\gamma.
\end{aligned} \tag{F.0.7}$$

# Bibliography


[1] M. E. Peskin and D. V. Schroeder, *An Introduction to Quantum Field Theory*. Perseus Books, 1995.

[2] S. Weinberg, *The Quantum Theory of Fields*. Cambridge University Press, 1995.

[3] F. Halzen and A. D. Martin, *Quarks & Leptons: An Introductory Course in Modern Particle Physics*. John Wiley & Sons, 1984.

[4] M. D. Schwartz, *Quantum Field Theory and the Standard Model*. Cambridge University Press, 2013.

[5] M. Thomson, *Modern Particle Physics*. Cambridge University Press, 2013.

[6] M. Gell-Mann, *Symmetries of Baryons and Mesons*, *Phys. Rev.* **125** (1962) 1067–1084.

[7] S. Weinberg, *Non-Abelian Gauge Theories of the Strong Interactions*, *Phys. Rev. Lett.* **31** (1973) 494–497.

[8] D. J. Gross and F. Wilczek, *Asymptotically-Free Gauge Theories. I*, *Phys. Rev. D* **8** (1973) 3633–3652.

[9] C. N. Yang and R. L. Mills, *Conservation of Isotopic Spin and Isotopic Gauge Invariance*, *Phys. Rev.* **96** (1954) 191–195.

[10] S. L. Glashow, *Partial Symmetries of Weak Interactions*, *Nuclear Physics* **22** (1961) 579–588.

[11] S. Weinberg, *A Model of Leptons*, *Phys. Rev. Lett.* **19** (1967) 1264–1266.

[12] A. Salam, *Weak and Electromagnetic Interactions*, *Conf. Proc. C* **680519** (1968) 367–377.

[13] G. 't Hooft, *Renormalizable Lagrangians for Massive Yang-Mills Fields*, *Nucl. Phys. B* **35** (1971) 167–188.

[14] G. 't Hooft and M. J. G. Veltman, *Regularization and Renormalization of Gauge Fields*, *Nucl. Phys. B* **44** (1972) 189–213.

[15] F. Englert and R. Brout, *Broken Symmetry and the Mass of Gauge Vector Mesons*, *Phys. Rev. Lett.* **13** (1964) 321–323.

[16] P. W. Higgs, *Broken Symmetries and the Masses of Gauge Bosons*, *Phys. Rev. Lett.* **13** (1964) 508–509.

[17] G. S. Guralnik, C. R. Hagen and T. W. B. Kibble, *Global Conservation Laws and Massless Particles*, *Phys. Rev. Lett.* **13** (1964) 585–587.

[18] J. Schwinger, *Quantum Electrodynamics. I. A Covariant Formulation*, *Phys. Rev.* **74** (1948) 1439–1461.

[19] Particle Data Group collaboration, P. A. Zyla, R. M. Barnett, J. Beringer, O. Dahl, D. A. Dwyer, D. E. Groom et al., *Review of Particle Physics*, *Progress of Theoretical and Experimental Physics* **2020** (2020) .

[20] K. Nishijima, *Charge Independence Theory of V Particles*, *Progress of Theoretical Physics* **13** (1955) 285–304.

[21] M. Gell-Mann, *The interpretation of the new particles as displaced charge multiplets*, *Il Nuovo Cimento (1955-1965)* **4** (1956) 848–866.

[22] J. D. Wells, *Lectures on Higgs Boson Physics in the Standard Model and Beyond*, in *38th British Universities Summer School in Theoretical Elementary Particle Physics*, 2009, 0909.4541.

[23] L. Reina, *TASI 2011: lectures on Higgs-Boson Physics*, in *Theoretical Advanced Study Institute in Elementary Particle Physics: The Dark Secrets of the Terascale*, pp. 39–106, 2013, 1208.5504, DOI.

[24] T. Plehn, *Lectures on LHC Physics*, *Lect. Notes Phys.* **844** (2012) 1–193, [0910.4182].

[25] J. Ellis, *Higgs Physics*, in *2013 European School of High-Energy Physics*, 2013, 1312.5672, DOI.

[26] H. E. Logan, *TASI 2013 lectures on Higgs physics within and beyond the Standard Model*, 1406.1786.

[27] A. Pomarol, *Higgs Physics*, in *2014 European School of High-Energy Physics*, pp. 59–77, 2016, 1412.4410.

[28] S. Dawson, C. Englert and T. Plehn, *Higgs Physics: It ain't over till it's over*, *Phys. Rept.* **816** (2019) 1–85, [1808.01324].

[29] C. Englert, *Higgs Physics*, *PoS* **TASI2018** (2019) 003.

[30] P. A. Waite, *Precision Physics in Extensions of the Standard Model*, Ph.D. thesis, Durham University, 2019.

[31] J. D. Jackson, *Classical electrodynamics; 2nd ed.* Wiley, 1975.

[32] D. J. Griffiths, *Introduction to Electrodynamics; 4th ed.* Pearson, 2013.

[33] T. van Ritbergen and R. G. Stuart, *Complete 2-Loop Quantum Electrodynamic Contributions to the Muon Lifetime in the Fermi Model*, *Phys. Rev. Lett.* **82** (1999) 488–491, [hep-ph/9808283].

[34] Y. Nambu, *Quasi-Particles and Gauge Invariance in the Theory of Superconductivity*, *Phys. Rev.* **117** (1960) 648–663.

[35] J. Goldstone, *Field theories with «Superconductor» solutions*, *Il Nuovo Cimento (1955-1965)* **19** (1961) 154–164.

[36] J. Goldstone, A. Salam and S. Weinberg, *Broken Symmetries*, *Phys. Rev.* **127** (1962) 965–970.

[37] L. Evans and P. Bryant, *LHC Machine*, *Journal of Instrumentation* **3** (2008) S08001–S08001.

[38] ATLAS collaboration, G. Aad et al., *Observation of a new particle in the search for the Standard Model Higgs boson with the ATLAS detector at the LHC*, *Phys. Lett. B* **716** (2012) 1–29, [1207.7214].

[39] CMS collaboration, S. Chatrchyan et al., *Observation of a New Boson at a Mass of 125 GeV with the CMS Experiment at the LHC*, *Phys. Lett. B* **716** (2012) 30–61, [1207.7235].

[40] N. Cabibbo, *Unitary Symmetry and Leptonic Decays*, *Phys. Rev. Lett.* **10** (1963) 531–533.

[41] M. Kobayashi and T. Maskawa, *CP-Violation in the Renormalizable Theory of Weak Interaction*, *Progress of Theoretical Physics* **49** (1973) 652–657.

[42] ATLAS AND CMS collaboration, G. Aad et al., *Measurements of the Higgs boson production and decay rates and constraints on its couplings from a combined ATLAS and CMS analysis of the LHC pp collision data at* $\sqrt{s} = 7$ *and 8 TeV*, *JHEP* **08** (2016) 045, [1606.02266].

[43] CMS collaboration, A. M. Sirunyan et al., *Combined measurements of Higgs boson couplings in proton–proton collisions at* $\sqrt{s} = 13$ *TeV*, *Eur. Phys. J. C* **79** (2019) 421, [1809.10733].

[44] ATLAS collaboration, G. Aad, B. Abbott, D. C. Abbott, O. Abdinov, A. Abed Abud, K. Abeling et al., *Combined measurements of Higgs boson production and decay using up to 80* $fb^{-1}$ *of proton-proton collision data at* $\sqrt{s} = 13$ *TeV collected with the ATLAS experiment*, *Phys. Rev. D* **101** (2020) 012002, [1909.02845].

[45] ATLAS AND CMS collaboration, G. Aad et al., *Combined Measurement of the Higgs Boson Mass in pp Collisions at $\sqrt{s} = 7$ and 8 TeV with the ATLAS and CMS Experiments*, *Phys. Rev. Lett.* **114** (2015) 191803, [1503.07589].

[46] THE LHC HIGGS CROSS SECTION WORKING GROUP collaboration, D. de Florian et al., *Handbook of LHC Higgs Cross Sections: 4. Deciphering the Nature of the Higgs Sector*, 1610.07922.

[47] CMS collaboration, A. M. Sirunyan et al., *Measurements of the Higgs boson width and anomalous HVV couplings from on-shell and off-shell production in the four-lepton final state*, *Phys. Rev. D* **99** (2019) 112003, [1901.00174].

[48] ATLAS collaboration, *Measurement of the Higgs boson mass in the $H \to ZZ^* \to 4\ell$ decay channel with $\sqrt{s} = 13$ TeV pp collisions using the ATLAS detector at the LHC*, tech. rep., CERN, Geneva, 2020.

[49] CMS collaboration, A. M. Sirunyan et al., *A measurement of the Higgs boson mass in the diphoton decay channel*, *Phys. Lett. B* **805** (2020) 135425, [2002.06398].

[50] CLICDP, ILD CONCEPT GROUP collaboration, A. F. Zarnecki, *On the physics potential of ILC and CLIC*, *PoS* **CORFU2019** (2020) 037, [2004.14628].

[51] H. Yamamoto, *Physics at International Linear Collider (ILC)*, *J. Phys. Soc. Jap.* **76** (2007) 111014, [0709.0899].

[52] T. Behnke, J. E. Brau, B. Foster, J. Fuster, M. Harrison, J. M. Paterson et al., *The International Linear Collider Technical Design Report - Volume 1: Executive Summary*, 1306.6327.

[53] D. M. Asner, T. Barklow, C. Calancha, K. Fujii, N. Graf, H. E. Haber et al., *ILC Higgs White Paper*, in *Community Summer Study 2013: Snowmass on the Mississippi*, 2013, 1310.0763.

[54] L. Linssen, A. Miyamoto, M. Stanitzki and H. Weerts, *Physics and Detectors at CLIC: CLIC Conceptual Design Report*. CERN Yellow Reports: Monographs. CERN, Geneva, 2012, 10.5170/CERN-2012-003.

[55] H. Abramowicz et al., *Higgs physics at the CLIC electron–positron linear collider*, *Eur. Phys. J. C* **77** (2017) 475, [1608.07538].

[56] J. de Blas et al., *The CLIC Potential for New Physics*, 1812.02093.

[57] ATLAS collaboration, M. Aaboud, G. Aad, B. Abbott, O. Abdinov, B. Abeloos, D. Abhayasinghe et al., *Measurements of gluon-gluon fusion and vector-boson fusion Higgs boson production cross-sections in the $H \to WW^* \to e\nu\mu\nu$ decay channel in pp collisions at $\sqrt{s} = 13$ TeV with the ATLAS detector*, *Phys. Lett. B* **789** (2019) 508–529, [1808.09054].

[58] ATLAS collaboration, G. Aad et al., *Search for Higgs boson production in association with a high-energy photon via vector-boson fusion with decay into bottom quark pairs at $\sqrt{s}$=13 TeV with the ATLAS detector*, *JHEP* **03** (2021) 268, [2010.13651].

[59] ATLAS collaboration, G. Aad, B. Abbott, D. Abbott, O. Abdinov, A. Abed Abud, K. Abeling et al., *Measurement of the production cross section for a Higgs boson in association with a vector boson in the $H \to WW^* \to \ell\nu\ell\nu$ channel in pp collisions at $\sqrt{s} = 13$ TeV with the ATLAS detector*, *Phys. Lett. B* **798** (2019) 134949, [1903.10052].

[60] CMS collaboration, A. M. Sirunyan et al., *Measurement of the Higgs boson production rate in association with top quarks in final states with electrons, muons, and hadronically decaying tau leptons at $\sqrt{s} = 13$ TeV*, *Eur. Phys. J. C* **81** (2021) 378, [2011.03652].

[61] R. K. Ellis et al., *Physics Briefing Book: Input for the European Strategy for Particle Physics Update 2020*, 1910.11775.

[62] ATLAS collaboration, G. Aad et al., *Measurements of Higgs bosons decaying to bottom quarks from vector boson fusion production with the ATLAS experiment at* $\sqrt{s} = 13$ *TeV*, *Eur. Phys. J. C* **81** (2021) 537, [2011.08280].

[63] CMS collaboration, A. M. Sirunyan et al., *Observation of Higgs boson decay to bottom quarks*, *Phys. Rev. Lett.* **121** (2018) 121801, [1808.08242].

[64] ATLAS collaboration, M. Aaboud et al., *Search for the Decay of the Higgs Boson to Charm Quarks with the ATLAS Experiment*, *Phys. Rev. Lett.* **120** (2018) 211802, [1802.04329].

[65] CMS collaboration, A. M. Sirunyan et al., *A search for the Standard Model Higgs boson decaying to charm quarks*, *JHEP* **03** (2020) 131, [1912.01662].

[66] ATLAS collaboration, G. Aad et al., *Test of CP invariance in vector-boson fusion production of the Higgs boson in the* $H \to \tau\tau$ *channel in proton−proton collisions at* $\sqrt{s} = 13$ *TeV with the ATLAS detector*, *Phys. Lett. B* **805** (2020) 135426, [2002.05315].

[67] CMS collaboration, A. Tumasyan et al., *Measurement of the inclusive and differential Higgs boson production cross sections in the decay mode to a pair of* $\tau$ *leptons in pp collisions at* $\sqrt{s} = 13$ *TeV*, 2107.11486.

[68] ATLAS collaboration, G. Aad et al., *A search for the dimuon decay of the Standard Model Higgs boson with the ATLAS detector*, *Phys. Lett. B* **812** (2021) 135980, [2007.07830].

[69] CMS collaboration, A. M. Sirunyan et al., *Evidence for Higgs boson decay to a pair of muons*, *JHEP* **01** (2021) 148, [2009.04363].

[70] CMS collaboration, A. M. Sirunyan, A. Tumasyan, W. Adam, F. Ambrogi, T. Bergauer, M. Dragicevic et al., *Measurement of the inclusive and differential Higgs boson production cross sections in the leptonic WW decay*

*mode at* $\sqrt{s} = 13$ *TeV*, *Journal of High Energy Physics* **2021** (2021) 3, [2007.01984].

[71] ATLAS collaboration, M. Aaboud et al., *Combination of searches for invisible Higgs boson decays with the ATLAS experiment*, *Phys. Rev. Lett.* **122** (2019) 231801, [1904.05105].

[72] CMS collaboration, A. M. Sirunyan et al., *Search for invisible decays of a Higgs boson produced through vector boson fusion in proton-proton collisions at* $\sqrt{s} = 13$ *TeV*, *Phys. Lett. B* **793** (2019) 520–551, [1809.05937].

[73] ATLAS collaboration, G. Aad et al., *A search for the* $Z\gamma$ *decay mode of the Higgs boson in pp collisions at* $\sqrt{s} = 13$ *TeV with the ATLAS detector*, *Phys. Lett. B* **809** (2020) 135754, [2005.05382].

[74] CMS collaboration, A. M. Sirunyan et al., *Search for the decay of a Higgs boson in the* $\ell\ell\gamma$ *channel in proton-proton collisions at* $\sqrt{s} = 13$ *TeV*, *JHEP* **11** (2018) 152, [1806.05996].

[75] ATLAS collaboration, M. Aaboud et al., *Measurements of Higgs boson properties in the diphoton decay channel with 36* $fb^{-1}$ *of pp collision data at* $\sqrt{s} = 13$ *TeV with the ATLAS detector*, *Phys. Rev. D* **98** (2018) 052005, [1802.04146].

[76] CMS collaboration, A. M. Sirunyan et al., *Measurements of Higgs boson production cross sections and couplings in the diphoton decay channel at* $\sqrt{\text{s}}$ *= 13 TeV*, *JHEP* **07** (2021) 027, [2103.06956].

[77] ATLAS collaboration, G. Aad et al., *Measurements of the Higgs boson inclusive and differential fiducial cross sections in the* $4\ell$ *decay channel at* $\sqrt{s}$ *= 13 TeV*, *Eur. Phys. J. C* **80** (2020) 942, [2004.03969].

[78] CMS collaboration, A. M. Sirunyan, A. Tumasyan, W. Adam, J. W. Andrejkovic, T. Bergauer, S. Chatterjee et al., *Measurements of production*

*cross sections of the Higgs boson in the four-lepton final state in proton–proton collisions at* $\sqrt{s}$ *=13 TeV*, *Eur. Phys. J. C* **81** (2021) 488, [2103.04956].

[79] A. Strumia and F. Vissani, *Neutrino masses and mixings and...*, hep-ph/0606054.

[80] B. Kayser, *Neutrino Mass, Mixing, and Flavor Change*, 0804.1497.

[81] B. Pontecorvo, *Inverse beta processes and nonconservation of lepton charge*, *Zh. Eksp. Teor. Fiz.* **34** (1957) 247.

[82] Z. Maki, M. Nakagawa and S. Sakata, *Remarks on the unified model of elementary particles*, *Prog. Theor. Phys.* **28** (1962) 870–880.

[83] Super-Kamiokande collaboration, Y. Fukuda, T. Hayakawa, E. Ichihara, K. Inoue, K. Ishihara, H. Ishino et al., *Measurements of the Solar Neutrino Flux from Super-Kamiokande's First 300 Days*, *Phys. Rev. Lett.* **81** (1998) 1158–1162, [hep-ex/9805021].

[84] SNO collaboration, Q. R. Ahmad, R. C. Allen, T. C. Andersen, J. D. Anglin, G. Bühler, J. C. Barton et al., *Measurement of the Rate of* $\nu_e + d \to p + p + e^-$ *Interactions Produced by* $^8B$ *Solar Neutrinos at the Sudbury Neutrino Observatory*, *Phys. Rev. Lett.* **87** (2001) 071301, [nucl-ex/0106015].

[85] KamLAND collaboration, T. Araki, K. Eguchi, S. Enomoto, K. Furuno, K. Ichimura, H. Ikeda et al., *Measurement of Neutrino Oscillation with KamLAND: Evidence of Spectral Distortion*, *Phys. Rev. Lett.* **94** (2005) 081801, [hep-ex/0406035].

[86] RENO collaboration, C. D. Shin et al., *Observation of reactor antineutrino disappearance using delayed neutron capture on hydrogen at RENO*, *JHEP* **04** (2020) 029, [1911.04601].

[87] J. Lesgourgues and S. Pastor, *Massive neutrinos and cosmology*, *Phys. Rept.* **429** (2006) 307–379, [astro-ph/0603494].

[88] M. C. Gonzalez-Garcia and M. Maltoni, *Phenomenology with Massive Neutrinos*, *Phys. Rept.* **460** (2008) 1–129, [0704.1800].

[89] P. B. Pal, *Dirac, Majorana and Weyl fermions*, *Am. J. Phys.* **79** (2011) 485–498, [1006.1718].

[90] S. M. Boucenna, S. Morisi and J. W. F. Valle, *The low-scale approach to neutrino masses*, *Adv. High Energy Phys.* **2014** (2014) 831598, [1404.3751].

[91] F. Zwicky, *Die Rotverschiebung von extragalaktischen Nebeln*, *Helv. Phys. Acta* **6** (1933) 110–127.

[92] V. C. Rubin and W. K. Ford, Jr., *Rotation of the Andromeda Nebula from a Spectroscopic Survey of Emission Regions*, *Astrophys. J.* **159** (1970) 379–403.

[93] H. Baer and X. Tata, *Dark matter and the LHC*, 0805.1905.

[94] G. F. Smoot, *COBE observations and results*, *AIP Conf. Proc.* **476** (1999) 1–10, [astro-ph/9902027].

[95] WMAP collaboration, C. L. Bennett et al., *Nine-Year Wilkinson Microwave Anisotropy Probe (WMAP) Observations: Final Maps and Results*, *Astrophys. J. Suppl.* **208** (2013) 20, [1212.5225].

[96] S. Galli, *Planck results 2015*, in *51st Rencontres de Moriond on Cosmology*, pp. 3–6, ARISF, 2016.

[97] G. Bertone, D. Hooper and J. Silk, *Particle dark matter: Evidence, candidates and constraints*, *Phys. Rept.* **405** (2005) 279–390, [hep-ph/0404175].

[98] M. Lisanti, *Lectures on Dark Matter Physics*, in *Theoretical Advanced Study Institute in Elementary Particle Physics: New Frontiers in Fields and Strings*, pp. 399–446, 2017, 1603.03797, DOI.

[99] PICO collaboration, C. Amole et al., *Dark Matter Search Results from the Complete Exposure of the PICO-60 $C_3F_8$ Bubble Chamber*, *Phys. Rev. D* **100** (2019) 022001, [1902.04031].

[100] PandaX-II collaboration, Q. Wang et al., *Results of dark matter search using the full PandaX-II exposure*, *Chin. Phys. C* **44** (2020) 125001, [2007.15469].

[101] O. Buchmueller, C. Doglioni and L. T. Wang, *Search for dark matter at colliders*, *Nature Phys.* **13** (2017) 217–223, [1912.12739].

[102] P. J. E. Peebles and B. Ratra, *The Cosmological Constant and Dark Energy*, *Rev. Mod. Phys.* **75** (2003) 559–606, [astro-ph/0207347].

[103] V. A. Rubakov, M. V. Sazhin and A. V. Veryaskin, *Graviton Creation in the Inflationary Universe and the Grand Unification Scale*, *Phys. Lett. B* **115** (1982) 189–192.

[104] G. Amelino-Camelia, *Quantum theory's last challenge*, *Nature* **408** (2000) 661–664, [gr-qc/0012049].

[105] D. Tong, *String Theory*, 0908.0333.

[106] C. Rovelli, *Loop quantum gravity*, *Living Rev. Rel.* **1** (1998) 1, [gr-qc/9710008].

[107] A. D. Sakharov, *Baryonic Asymmetry of the Universe*, *Sov. Phys. JETP* **49** (1979) 594–599.

[108] G. Burdman, *New solutions to the hierarchy problem*, *Braz. J. Phys.* **37** (2007) 506–513, [hep-ph/0703194].

[109] T. Moroi and Y. Okada, *Radiative corrections to Higgs masses in the supersymmetric model with an extra family and antifamily*, *Mod. Phys. Lett. A* **7** (1992) 187–200.

[110] K. S. Babu, I. Gogoladze, M. U. Rehman and Q. Shafi, *Higgs Boson Mass, Sparticle Spectrum and Little Hierarchy Problem in Extended MSSM*, *Phys. Rev. D* **78** (2008) 055017, [0807.3055].

[111] P. Athron, S. F. King, D. J. Miller, S. Moretti and R. Nevzorov, *Constrained Exceptional Supersymmetric Standard Model with a Higgs Near 125 GeV*, *Phys. Rev. D* **86** (2012) 095003, [1206.5028].

[112] M. Hirsch, M. E. Krauss, T. Opferkuch, W. Porod and F. Staub, *A constrained supersymmetric left-right model*, *JHEP* **03** (2016) 009, [1512.00472].

[113] ATLAS collaboration, G. Aad et al., *Search for new phenomena in final states with b-jets and missing transverse momentum in* $\sqrt{s} = 13$ *TeV pp collisions with the ATLAS detector*, *JHEP* **05** (2021) 093, [2101.12527].

[114] CMS collaboration, A. Tumasyan et al., *Combined searches for the production of supersymmetric top quark partners in proton-proton collisions at* $\sqrt{s} = 13$ *TeV*, 2107.10892.

[115] S. P. Martin, *A Supersymmetry primer*, *Adv. Ser. Direct. High Energy Phys.* **18** (1998) 1–98, [hep-ph/9709356].

[116] A. Bilal, *Introduction to supersymmetry*, hep-th/0101055.

[117] D. J. H. Chung, L. L. Everett, G. L. Kane, S. F. King, J. D. Lykken and L.-T. Wang, *The Soft supersymmetry breaking Lagrangian: Theory and applications*, *Phys. Rept.* **407** (2005) 1–203, [hep-ph/0312378].

[118] M. J. Strassler, *An Unorthodox introduction to supersymmetric gauge theory*, in *Theoretical Advanced Study Institute in Elementary Particle Physics (TASI 2001): Strings, Branes and EXTRA Dimensions*, pp. 561–638, 2003, hep-th/0309149, DOI.

[119] A. Signer, *ABC of SUSY*, *J. Phys. G* **36** (2009) 073002, [0905.4630].

[120] H. Georgi and S. L. Glashow, *Unity of All Elementary Particle Forces*, *Phys. Rev. Lett.* **32** (1974) 438–441.

[121] J. C. Pati and A. Salam, *Lepton Number as the Fourth Color*, *Phys. Rev. D* **10** (1974) 275–289.

[122] A. J. Buras, J. R. Ellis, M. K. Gaillard and D. V. Nanopoulos, *Aspects of the Grand Unification of Strong, Weak and Electromagnetic Interactions*, *Nucl. Phys. B* **135** (1978) 66–92.

[123] D. V. Nanopoulos, *PROTONS ARE NOT FOREVER*, *Stud. Nat. Sci.* **16** (1979) 91–114.

[124] H. Terazawa, *Unifying All Elementary-particle Forces Including Gravity*, in *19th International Conference on High-Energy Physics*, pp. 617–623, 1979.

[125] P. Nath and P. Fileviez Perez, *Proton stability in grand unified theories, in strings and in branes*, *Phys. Rept.* **441** (2007) 191–317, [hep-ph/0601023].

[126] C. Englert, D. J. Miller and D. D. Smaranda, *Phenomenology of GUT-inspired gauge-Higgs unification*, *Physics Letters B* **802** (2020) 135261, [1911.05527].

[127] C. Englert, D. J. Miller and D. D. Smaranda, *The Weinberg angle and 5D RGE effects in a SO (11) GUT theory*, *Phys. Lett. B* **807** (2020) 135548, [2003.05743].

[128] J. Wang, *Ultra Unification*, *Phys. Rev. D* **103** (2021) 105024, [2012.15860].

[129] I. Antoniadis, K. Benakli and M. Quiros, *Finite Higgs mass without supersymmetry*, *New J. Phys.* **3** (2001) 20, [hep-th/0108005].

[130] Y. Hosotani, S. Noda and K. Takenaga, *Dynamical gauge-Higgs unification in the electroweak theory*, *Phys. Lett. B* **607** (2005) 276–285, [hep-ph/0410193].

[131] J. A. Aguilar-Saavedra, *Identifying top partners at LHC*, *JHEP* **11** (2009) 030, [0907.3155].

[132] J. A. Aguilar-Saavedra, R. Benbrik, S. Heinemeyer and M. Pérez-Victoria, *Handbook of vectorlike quarks: Mixing and single production*, *Phys. Rev. D* **88** (2013) 094010, [1306.0572].

[133] M. Buchkremer, G. Cacciapaglia, A. Deandrea and L. Panizzi, *Model Independent Framework for Searches of Top Partners*, *Nucl. Phys. B* **876** (2013) 376–417, [1305.4172].

[134] O. Matsedonskyi, G. Panico and A. Wulzer, *On the Interpretation of Top Partners Searches*, *JHEP* **12** (2014) 097, [1409.0100].

[135] N. Gutierrez Ortiz, J. Ferrando, D. Kar and M. Spannowsky, *Reconstructing singly produced top partners in decays to Wb*, *Phys. Rev. D* **90** (2014) 075009, [1403.7490].

[136] M. Backović, T. Flacke, S. J. Lee and G. Perez, *LHC Top Partner Searches Beyond the 2 TeV Mass Region*, *JHEP* **09** (2015) 022, [1409.0409].

[137] L. Basso and J. Andrea, *Discovery potential for $T' \to tZ$ in the trilepton channel at the LHC*, *PoS* **EPS-HEP2015** (2015) 107, [1509.07646].

[138] J. Reuter and M. Tonini, *Top Partner Discovery in the $T \to tZ$ channel at the LHC*, *JHEP* **01** (2015) 088, [1409.6962].

[139] B. A. Dobrescu and F. Yu, *Exotic Signals of Vectorlike Quarks*, *J. Phys. G* **45** (2018) 08LT01, [1612.01909].

[140] ATLAS collaboration, M. Aaboud et al., *Combination of the searches for pair-produced vector-like partners of the third-generation quarks at $\sqrt{s} = 13$ TeV with the ATLAS detector*, *Phys. Rev. Lett.* **121** (2018) 211801, [1808.02343].

[141] CMS collaboration, A. M. Sirunyan et al., *Search for pair production of vectorlike quarks in the fully hadronic final state*, *Phys. Rev. D* **100** (2019) 072001, [1906.11903].

[142] N. Arkani-Hamed, A. G. Cohen, E. Katz and A. E. Nelson, *The Littlest Higgs*, *JHEP* **07** (2002) 034, [hep-ph/0206021].

[143] N. Arkani-Hamed, A. G. Cohen, E. Katz, A. E. Nelson, T. Gregoire and J. G. Wacker, *The Minimal moose for a little Higgs*, *JHEP* **08** (2002) 021, [hep-ph/0206020].

[144] T. Han, H. E. Logan, B. McElrath and L.-T. Wang, *Phenomenology of the little Higgs model*, *Phys. Rev. D* **67** (2003) 095004, [hep-ph/0301040].

[145] M. Perelstein, M. E. Peskin and A. Pierce, *Top quarks and electroweak symmetry breaking in little Higgs models*, *Phys. Rev. D* **69** (2004) 075002, [hep-ph/0310039].

[146] M. Perelstein, *Little Higgs models and their phenomenology*, *Prog. Part. Nucl. Phys.* **58** (2007) 247–291, [hep-ph/0512128].

[147] S. Matsumoto, T. Moroi and K. Tobe, *Testing the Littlest Higgs Model with T-parity at the Large Hadron Collider*, *Phys. Rev. D* **78** (2008) 055018, [0806.3837].

[148] R. S. Chivukula, B. A. Dobrescu, H. Georgi and C. T. Hill, *Top Quark Seesaw Theory of Electroweak Symmetry Breaking*, *Phys. Rev. D* **59** (1999) 075003, [hep-ph/9809470].

[149] H. Collins, A. K. Grant and H. Georgi, *The Phenomenology of a top quark seesaw model*, *Phys. Rev. D* **61** (2000) 055002, [hep-ph/9908330].

[150] R. Contino, L. Da Rold and A. Pomarol, *Light custodians in natural composite Higgs models*, *Phys. Rev. D* **75** (2007) 055014, [hep-ph/0612048].

[151] A. Carmona, M. Chala and J. Santiago, *New Higgs Production Mechanism in Composite Higgs Models*, *JHEP* **07** (2012) 049, [1205.2378].

[152] M. Gillioz, R. Grober, C. Grojean, M. Muhlleitner and E. Salvioni, *Higgs Low-Energy Theorem (and its corrections) in Composite Models*, *JHEP* **10** (2012) 004, [1206.7120].

[153] C. Anastasiou, E. Furlan and J. Santiago, *Realistic Composite Higgs Models*, *Phys. Rev. D* **79** (2009) 075003, [0901.2117].

[154] K. Agashe, R. Contino and A. Pomarol, *The Minimal composite Higgs model*, *Nucl. Phys. B* **719** (2005) 165–187, [hep-ph/0412089].

[155] ATLAS collaboration, G. Aad et al., *Constraints on new phenomena via Higgs boson couplings and invisible decays with the ATLAS detector*, *JHEP* **11** (2015) 206, [1509.00672].

[156] P. Maris, C. D. Roberts and P. C. Tandy, *Pion mass and decay constant*, *Phys. Lett. B* **420** (1998) 267–273, [nucl-th/9707003].

[157] G. C. Branco, P. M. Ferreira, L. Lavoura, M. N. Rebelo, M. Sher and J. P. Silva, *Theory and phenomenology of two-Higgs-doublet models*, *Phys. Rept.* **516** (2012) 1–102, [1106.0034].

[158] N. Craig and S. Thomas, *Exclusive Signals of an Extended Higgs Sector*, *JHEP* **11** (2012) 083, [1207.4835].

[159] C.-Y. Chen, S. Dawson and M. Sher, *Heavy Higgs Searches and Constraints on Two Higgs Doublet Models*, *Phys. Rev. D* **88** (2013) 015018, [1305.1624].

[160] F. J. Botella, F. Cornet-Gomez and M. Nebot, *Flavor conservation in two-Higgs-doublet models*, *Phys. Rev. D* **98** (2018) 035046, [1803.08521].

[161] ATLAS collaboration, G. Aad et al., *Search for heavy resonances decaying into a pair of Z bosons in the $\ell^+\ell^-\ell'^+\ell'^-$ and $\ell^+\ell^-\nu\bar{\nu}$ final states using 139*

fb$^{-1}$ *of proton–proton collisions at* $\sqrt{s} = 13$ *TeV with the ATLAS detector*, *Eur. Phys. J. C* **81** (2021) 332, [2009.14791].

[162] CMS collaboration, A. M. Sirunyan et al., *Search for a light charged Higgs boson in the* $H^{\pm} \to cs$ *channel in proton-proton collisions at* $\sqrt{s} = 13$ *TeV*, *Phys. Rev. D* **102** (2020) 072001, [2005.08900].

[163] V. Keus, S. F. King and S. Moretti, *Three-Higgs-doublet models: symmetries, potentials and Higgs boson masses*, *JHEP* **01** (2014) 052, [1310.8253].

[164] N. Darvishi, M. R. Masouminia and A. Pilaftsis, *Maximally Symmetric Three Higgs Doublet Model*, 2106.03159.

[165] K. G. Wilson, *Renormalization group and critical phenomena. i. renormalization group and the kadanoff scaling picture*, *Phys. Rev. B* **4** (1971) 3174–3183.

[166] K. G. Wilson, *Renormalization group and critical phenomena. ii. phase-space cell analysis of critical behavior*, *Phys. Rev. B* **4** (1971) 3184–3205.

[167] W. Buchmuller and D. Wyler, *Effective Lagrangian Analysis of New Interactions and Flavor Conservation*, *Nucl. Phys. B* **268** (1986) 621–653.

[168] H. Georgi, *Effective field theory*, *Ann. Rev. Nucl. Part. Sci.* **43** (1993) 209–252.

[169] D. B. Kaplan, *Five lectures on effective field theory*, nucl-th/0510023.

[170] W. Skiba, *Effective Field Theory and Precision Electroweak Measurements*, in *Theoretical Advanced Study Institute in Elementary Particle Physics: Physics of the Large and the Small*, pp. 5–70, 2011, 1006.2142, DOI.

[171] E. E. Jenkins, A. V. Manohar and M. Trott, *Renormalization Group Evolution of the Standard Model Dimension Six Operators I: Formalism and lambda Dependence*, *JHEP* **10** (2013) 087, [1308.2627].

[172] E. E. Jenkins, A. V. Manohar and M. Trott, *Renormalization Group Evolution of the Standard Model Dimension Six Operators II: Yukawa Dependence*, *JHEP* **01** (2014) 035, [1310.4838].

[173] R. Alonso, E. E. Jenkins, A. V. Manohar and M. Trott, *Renormalization Group Evolution of the Standard Model Dimension Six Operators III: Gauge Coupling Dependence and Phenomenology*, *JHEP* **04** (2014) 159, [1312.2014].

[174] I. W. Stewart, "Effective Field Theory." https://courses.edx.org/c4x/MITx/8.EFTx/asset/notes_EFT.pdf, Lecture notes. Accessed 01 October 2021.

[175] R. Contino, A. Falkowski, F. Goertz, C. Grojean and F. Riva, *On the Validity of the Effective Field Theory Approach to SM Precision Tests*, *JHEP* **07** (2016) 144, [1604.06444].

[176] I. Brivio and M. Trott, *The Standard Model as an Effective Field Theory*, *Phys. Rept.* **793** (2019) 1–98, [1706.08945].

[177] M. J. Kirk, *Charming New Physics in Beautiful Processes?*, Ph.D. thesis, Durham University, 2018.

[178] E. Venturini, *Search for Beyond Standard Model physics at high and low energy colliders*, Ph.D. thesis, SISSA, Trieste, 2019.

[179] T. Cohen, *As Scales Become Separated: Lectures on Effective Field Theory*, *PoS* **TASI2018** (2019) 011, [1903.03622].

[180] A. Biekötter, *Know its limits: A global view on Higgs couplings at the LHC*, Ph.D. thesis, Heidelberg University, 2019.

[181] T. Cohen, N. Craig, X. Lu and D. Sutherland, *Is SMEFT Enough?*, *JHEP* **03** (2021) 237, [2008.08597].

[182] J. M. Cullen, *Precision Higgs Physics in the Standard Model Effective Field Theory*, Ph.D. thesis, Durham University, 2021.

[183] L. Mantani, *Searches for new interactions within the SMEFT framework at present and future colliders*, Ph.D. thesis, Cathol. U. Louvain (main), 2021. 2109.03104.

[184] A. Falkowski, "Lectures on Effective Field Theories." https://indico.in2p3.fr/event/22195/contributions/86017/attachments/59873/81148/eftlectures.pdf, Lecture notes. Accessed 01 October 2021.

[185] J. Y. Reiness, *Pieces of the Higgsaw*, Ph.D. thesis, Durham University, 2020.

[186] T. Appelquist and J. Carazzone, *Infrared singularities and massive fields*, *Phys. Rev. D* **11** (1975) 2856–2861.

[187] E. Fermi, *An attempt of a theory of beta radiation. 1.*, *Z. Phys.* **88** (1934) 161–177.

[188] I. Brivio, T. Corbett, O. J. P. Éboli, M. B. Gavela, J. Gonzalez-Fraile, M. C. Gonzalez-Garcia et al., *Disentangling a dynamical Higgs*, *JHEP* **03** (2014) 024, [1311.1823].

[189] S. Weinberg, *Baryon and Lepton Nonconserving Processes*, *Phys. Rev. Lett.* **43** (1979) 1566–1570.

[190] A. Kobach, *Baryon Number, Lepton Number, and Operator Dimension in the Standard Model*, *Phys. Lett. B* **758** (2016) 455–457, [1604.05726].

[191] B. Grzadkowski, M. Iskrzynski, M. Misiak and J. Rosiek, *Dimension-Six Terms in the Standard Model Lagrangian*, *JHEP* **10** (2010) 085, [1008.4884].

[192] K. Hagiwara, S. Ishihara, R. Szalapski and D. Zeppenfeld, *Low-energy effects of new interactions in the electroweak boson sector*, *Phys. Rev. D* **48** (1993) 2182–2203.

[193] G. F. Giudice, C. Grojean, A. Pomarol and R. Rattazzi, *The Strongly-Interacting Light Higgs*, *JHEP* **06** (2007) 045, [hep-ph/0703164].

[194] R. Contino, M. Ghezzi, C. Grojean, M. Muhlleitner and M. Spira, *Effective Lagrangian for a light Higgs-like scalar*, *JHEP* **07** (2013) 035, [1303.3876].

[195] J. Elias-Miró, C. Grojean, R. S. Gupta and D. Marzocca, *Scaling and tuning of EW and Higgs observables*, *JHEP* **05** (2014) 019, [1312.2928].

[196] D. Liu, A. Pomarol, R. Rattazzi and F. Riva, *Patterns of Strong Coupling for LHC Searches*, *JHEP* **11** (2016) 141, [1603.03064].

[197] L. Lehman, *Extending the Standard Model Effective Field Theory with the Complete Set of Dimension-7 Operators*, *Phys. Rev. D* **90** (2014) 125023, [1410.4193].

[198] Y. Liao and X.-D. Ma, *Renormalization Group Evolution of Dimension-seven Baryon- and Lepton-number-violating Operators*, *JHEP* **11** (2016) 043, [1607.07309].

[199] H.-L. Li, Z. Ren, J. Shu, M.-L. Xiao, J.-H. Yu and Y.-H. Zheng, *Complete set of dimension-eight operators in the standard model effective field theory*, *Phys. Rev. D* **104** (2021) 015026, [2005.00008].

[200] C. W. Murphy, *Dimension-8 operators in the Standard Model Eective Field Theory*, *JHEP* **10** (2020) 174, [2005.00059].

[201] M. Trott, *A methodology for theory uncertainties in the SMEFT*, 2106.13794.

[202] A. Dedes, W. Materkowska, M. Paraskevas, J. Rosiek and K. Suxho, *Feynman rules for the Standard Model Effective Field Theory in $R_\xi$ -gauges*, *JHEP* **06** (2017) 143, [1704.03888].

[203] A. Falkowski, *Higgs Basis: Proposal for an EFT basis choice for LHC HXSWG*, 2015.

[204] R. S. Gupta, A. Pomarol and F. Riva, *BSM Primary Effects*, *Phys. Rev. D* **91** (2015) 035001, [1405.0181].

[205] M. Ghezzi, R. Gomez-Ambrosio, G. Passarino and S. Uccirati, *NLO Higgs effective field theory and κ-framework*, *JHEP* **07** (2015) 175, [1505.03706].

[206] A. V. Manohar, *Introduction to Effective Field Theories*, 1804.05863.

[207] T. Han, *Collider phenomenology: Basic knowledge and techniques*, in *Theoretical Advanced Study Institute in Elementary Particle Physics: Physics in D ≧ 4*, pp. 407–454, 2005, hep-ph/0508097, DOI.

[208] S. Banerjee, *Anomalous Higgs couplings and collider data: some model-independent studies*, Ph.D. thesis, Harish-Chandra Research Institute, 2015.

[209] S. Marzani, G. Soyez and M. Spannowsky, *Looking inside jets: an introduction to jet substructure and boosted-object phenomenology*, vol. 958. Springer, 2019, 10.1007/978-3-030-15709-8.

[210] P. Skands, *Introduction to QCD*, in *Theoretical Advanced Study Institute in Elementary Particle Physics: Searching for New Physics at Small and Large Scales*, pp. 341–420, 2013, 1207.2389, DOI.

[211] PDF4LHC21 COMBINATION GROUP collaboration, T. Cridge, *PDF4LHC21: Update on the benchmarking of the CT, MSHT and NNPDF global PDF fits*, in *28th International Workshop on Deep Inelastic Scattering and Related Subjects*, 2021, 2108.09099.

[212] J. C. Collins and D. E. Soper, *Parton Distribution and Decay Functions*, *Nucl. Phys. B* **194** (1982) 445–492.

[213] Y. L. Dokshitzer, *Calculation of the Structure Functions for Deep Inelastic Scattering and e+ e- Annihilation by Perturbation Theory in Quantum Chromodynamics.*, *Sov. Phys. JETP* **46** (1977) 641–653.

[214] V. N. Gribov and L. N. Lipatov, *Deep inelastic e p scattering in perturbation theory*, *Sov. J. Nucl. Phys.* **15** (1972) 438–450.

[215] G. Altarelli and G. Parisi, *Asymptotic Freedom in Parton Language*, *Nucl. Phys. B* **126** (1977) 298–318.

[216] A. D. Martin, W. J. Stirling, R. S. Thorne and G. Watt, *Parton distributions for the LHC*, *Eur. Phys. J. C* **63** (2009) 189–285, [0901.0002].

[217] R. R. Wilson, *The Tevatron*, *Phys. Today* **30N10** (1977) 23–30.

[218] F. Sauerburger, "LHC cross section plot." https://lhc-xsecs.org/, Accessed 12 September 2021.

[219] CMS collaboration, S. Chatrchyan et al., *The CMS Experiment at the CERN LHC*, *JINST* **3** (2008) S08004.

[220] ALICE collaboration, K. Aamodt et al., *The ALICE experiment at the CERN LHC*, *JINST* **3** (2008) S08002.

[221] ATLAS collaboration, G. Aad et al., *The ATLAS Experiment at the CERN Large Hadron Collider*, *JINST* **3** (2008) S08003.

[222] LHCb collaboration, A. A. Alves, Jr. et al., *The LHCb Detector at the LHC*, *JINST* **3** (2008) S08005.

[223] T. Lenzi and G. D. Lentdecker, *Development and Study of Different Muon Track Reconstruction Algorithms for the Level-1 Trigger for the CMS Muon Upgrade with GEM Detectors*, 2013.

[224] J. S. Schwinger, *Gauge Invariance and Mass*, *Phys. Rev.* **125** (1962) 397–398.

[225] J. S. Schwinger, *Gauge Invariance and Mass. 2.*, *Phys. Rev.* **128** (1962) 2425–2429.

[226] K. G. Wilson, *Confinement of Quarks*, *Phys. Rev. D* **10** (1974) 2445–2459.

[227] CMS collaboration, A. Künsken, *SiPM Operational Experience in Outer HCAL in CMS*, in *2nd Large Hadron Collider Physics Conference*, 2014, 1408.5709.

[228] CMS collaboration, A. M. Sirunyan et al., *Particle-flow reconstruction and global event description with the CMS detector*, *JINST* **12** (2017) P10003, [1706.04965].

[229] CMS collaboration, A. M. Sirunyan et al., *Electron and photon reconstruction and identification with the CMS experiment at the CERN LHC*, *JINST* **16** (2021) P05014, [2012.06888].

[230] CMS collaboration, A. M. Sirunyan et al., *Performance of the CMS muon detector and muon reconstruction with proton-proton collisions at* $\sqrt{s} = 13$ *TeV*, *JINST* **13** (2018) P06015, [1804.04528].

[231] CMS collaboration, J. Strologas, *Performance of Jet reconstruction in CMS at 13 TeV*, *PoS* **ICHEP2016** (2016) 736.

[232] CMS collaboration, A. M. Sirunyan et al., *Performance of missing transverse momentum reconstruction in proton-proton collisions at* $\sqrt{s} = 13$ *TeV using the CMS detector*, *JINST* **14** (2019) P07004, [1903.06078].

[233] C. Englert and M. Spannowsky, *Effective Theories and Measurements at Colliders*, *Phys. Lett. B* **740** (2015) 8–15, [1408.5147].

[234] CMS collaboration, A. M. Sirunyan et al., *Measurement of the differential Drell-Yan cross section in proton-proton collisions at* $\sqrt{\mathrm{s}} = 13$ *TeV*, *JHEP* **12** (2019) 059, [1812.10529].

[235] J. Ocariz, *Probability and Statistics for Particle Physicists*, in *1st Asia-Europe-Pacific School of High-Energy Physics*, pp. 253–280, 2014, 1405.3402, DOI.

[236] J. R. Andersen et al., *Les Houches 2015: Physics at TeV Colliders Standard Model Working Group Report*, in *9th Les Houches Workshop on Physics at TeV Colliders*, 2016, 1605.04692.

[237] N. Berger et al., *Simplified Template Cross Sections - Stage 1.1*, 1906.02754.

[238] ATLAS collaboration, *Methodology for EFT interpretation of Higgs boson Simplified Template Cross-section results in ATLAS*, tech. rep., CERN, Geneva, 2019.

[239] ATLAS AND CMS collaboration, N. Belyaev, *Interpretation of ATLAS and CMS Higgs measurements in STXS and EFT*, *PoS* **LHCP2020** (2021) 137.

[240] G. Panico, F. Riva and A. Wulzer, *Diboson interference resurrection*, *Phys. Lett. B* **776** (2018) 473–480, [1708.07823].

[241] CMS collaboration, A. M. Sirunyan et al., *Measurements of properties of the Higgs boson decaying into the four-lepton final state in pp collisions at* $\sqrt{s} = 13$ *TeV*, *JHEP* **11** (2017) 047, [1706.09936].

[242] ATLAS collaboration, M. Aaboud et al., *Measurement of inclusive and differential cross sections in the* $H \to ZZ^* \to 4\ell$ *decay channel in pp collisions at* $\sqrt{s} = 13$ *TeV with the ATLAS detector*, *JHEP* **10** (2017) 132, [1708.02810].

[243] CMS collaboration, A. M. Sirunyan et al., *Measurement of inclusive and differential Higgs boson production cross sections in the diphoton decay channel in proton-proton collisions at* $\sqrt{s} = 13$ *TeV*, *JHEP* **01** (2019) 183, [1807.03825].

[244] ATLAS collaboration, G. Aad, B. Abbott, D. C. Abbott, A. A. Abud, K. Abeling, D. K. Abhayasinghe et al., *Higgs boson production cross-section measurements and their EFT interpretation in the* $4\ell$ *decay channel at* $\sqrt{s} = 13$ *TeV with the ATLAS detector*, *Eur. Phys. J. C* **80** (2020) 957, [2004.03447].

[245] C. Englert, R. Kogler, H. Schulz and M. Spannowsky, *Higgs coupling measurements at the LHC*, *Eur. Phys. J. C* **76** (2016) 393, [1511.05170].

[246] J. Ellis, C. W. Murphy, V. Sanz and T. You, *Updated Global SMEFT Fit to Higgs, Diboson and Electroweak Data*, *JHEP* **06** (2018) 146, [1803.03252].

[247] CLICdp collaboration, "Physics processes at CLIC." https://clic.cern/physics-processes, Accessed 12 September 2021.

[248] R. Tanaka, *LEP accelerator and detectors*, in *LEP Symposium 2001: Beyond the Electroweak Scale*, 2001.

[249] H. Abramowicz et al., *The International Linear Collider Technical Design Report - Volume 4: Detectors*, 1306.6329.

[250] G. Moortgat-Pick et al., *The Role of polarized positrons and electrons in revealing fundamental interactions at the linear collider*, *Phys. Rept.* **460** (2008) 131–243, [hep-ph/0507011].

[251] H. Baer et al., *The International Linear Collider Technical Design Report - Volume 2: Physics*, 1306.6352.

[252] K. Fujii et al., *The role of positron polarization for the inital* 250 *GeV stage of the International Linear Collider*, 1801.02840.

[253] Linear Collider collaboration, J. List, *Polarised Beams at Future $e^+e^-$ Colliders*, *PoS* **ICHEP2020** (2021) 691, [2012.11267].

[254] K.-i. Hikasa, *Transverse Polarization Effects in $e^+e^-$ Collisions: The Role of Chiral Symmetry*, *Phys. Rev. D* **33** (1986) 3203.

[255] C. Adolphsen et al., *The International Linear Collider Technical Design Report - Volume 3.II: Accelerator Baseline Design*, 1306.6328.

[256] S. Banerjee, R. S. Gupta, O. Ochoa-Valeriano, M. Spannowsky and E. Venturini, *A fully differential SMEFT analysis of the golden channel using the method of moments*, *JHEP* **06** (2021) 031, [2012.11631].

[257] CMS collaboration, *Measurements of properties of the Higgs boson in the four-lepton final state in proton-proton collisions at* $\sqrt{s} = 13$ TeV, Tech. Rep. CMS-PAS-HIG-19-001, CERN, Geneva, 2019.

[258] R. S. Gupta, *Probing Quartic Neutral Gauge Boson Couplings using diffractive photon fusion at the LHC*, *Phys. Rev. D* **85** (2012) 014006, [1111.3354].

[259] R. S. Gupta, H. Rzehak and J. D. Wells, *How well do we need to measure Higgs boson couplings?*, *Phys. Rev. D* **86** (2012) 095001, [1206.3560].

[260] S. Banerjee, S. Mukhopadhyay and B. Mukhopadhyaya, *New Higgs interactions and recent data from the LHC and the Tevatron*, *JHEP* **10** (2012) 062, [1207.3588].

[261] R. S. Gupta, M. Montull and F. Riva, *SUSY Faces its Higgs Couplings*, *JHEP* **04** (2013) 132, [1212.5240].

[262] S. Banerjee, S. Mukhopadhyay and B. Mukhopadhyaya, *Higher dimensional operators and the LHC Higgs data: The role of modified kinematics*, *Phys. Rev. D* **89** (2014) 053010, [1308.4860].

[263] R. S. Gupta, H. Rzehak and J. D. Wells, *How well do we need to measure the Higgs boson mass and self-coupling?*, *Phys. Rev. D* **88** (2013) 055024, [1305.6397].

[264] A. Falkowski and F. Riva, *Model-independent precision constraints on dimension-6 operators*, *JHEP* **02** (2015) 039, [1411.0669].

[265] G. Amar, S. Banerjee, S. von Buddenbrock, A. S. Cornell, T. Mandal, B. Mellado et al., *Exploration of the tensor structure of the Higgs boson coupling to weak bosons in* $e^+e^-$ *collisions*, *JHEP* **02** (2015) 128, [1405.3957].

[266] M. Buschmann, D. Goncalves, S. Kuttimalai, M. Schonherr, F. Krauss and T. Plehn, *Mass Effects in the Higgs-Gluon Coupling: Boosted vs Off-Shell Production*, *JHEP* **02** (2015) 038, [1410.5806].

[267] N. Craig, M. Farina, M. McCullough and M. Perelstein, *Precision Higgsstrahlung as a Probe of New Physics*, *JHEP* **03** (2015) 146, [1411.0676].

[268] J. Ellis, V. Sanz and T. You, *Complete Higgs Sector Constraints on Dimension-6 Operators*, *JHEP* **07** (2014) 036, [1404.3667].

[269] J. Ellis, V. Sanz and T. You, *The Effective Standard Model after LHC Run I*, *JHEP* **03** (2015) 157, [1410.7703].

[270] S. Banerjee, T. Mandal, B. Mellado and B. Mukhopadhyaya, *Cornering dimension-6 HVV interactions at high luminosity LHC: the role of event ratios*, *JHEP* **09** (2015) 057, [1505.00226].

[271] D. Ghosh, R. S. Gupta and G. Perez, *Is the Higgs Mechanism of Fermion Mass Generation a Fact? A Yukawa-less First-Two-Generation Model*, *Phys. Lett. B* **755** (2016) 504–508, [1508.01501].

[272] C. Degrande, B. Fuks, K. Mawatari, K. Mimasu and V. Sanz, *Electroweak Higgs boson production in the standard model effective field theory beyond leading order in QCD*, *Eur. Phys. J. C* **77** (2017) 262, [1609.04833].

[273] J. Cohen, S. Bar-Shalom and G. Eilam, *Contact Interactions in Higgs-Vector Boson Associated Production at the ILC*, *Phys. Rev. D* **94** (2016) 035030, [1602.01698].

[274] S.-F. Ge, H.-J. He and R.-Q. Xiao, *Probing new physics scales from Higgs and electroweak observables at $e^+e^-$ Higgs factory*, *JHEP* **10** (2016) 007, [1603.03385].

[275] A. Biekötter, J. Brehmer and T. Plehn, *Extending the limits of Higgs effective theory*, *Phys. Rev. D* **94** (2016) 055032, [1602.05202].

[276] J. de Blas, M. Ciuchini, E. Franco, S. Mishima, M. Pierini, L. Reina et al., *Electroweak precision observables and Higgs-boson signal strengths in the Standard Model and beyond: present and future*, *JHEP* **12** (2016) 135, [1608.01509].

[277] H. Denizli and A. Senol, *Constraints on Higgs effective couplings in $H\nu\bar{\nu}$ production of CLIC at 380 GeV*, *Adv. High Energy Phys.* **2018** (2018) 1627051, [1707.03890].

[278] A. Azatov, J. Elias-Miro, Y. Reyimuaji and E. Venturini, *Novel measurements of anomalous triple gauge couplings for the LHC*, *JHEP* **10** (2017) 027, [1707.08060].

[279] T. Barklow, K. Fujii, S. Jung, R. Karl, J. List, T. Ogawa et al., *Improved Formalism for Precision Higgs Coupling Fits*, *Phys. Rev. D* **97** (2018) 053003, [1708.08912].

[280] T. Barklow, K. Fujii, S. Jung, M. E. Peskin and J. Tian, *Model-Independent Determination of the Triple Higgs Coupling at e+e- Colliders*, *Phys. Rev. D* **97** (2018) 053004, [1708.09079].

[281] H. Khanpour and M. Mohammadi Najafabadi, *Constraining Higgs boson effective couplings at electron-positron colliders*, *Phys. Rev. D* **95** (2017) 055026, [1702.00951].

[282] C. Englert, R. Kogler, H. Schulz and M. Spannowsky, *Higgs characterisation in the presence of theoretical uncertainties and invisible decays*, *Eur. Phys. J. C* **77** (2017) 789, [1708.06355].

[283] R. Franceschini, G. Panico, A. Pomarol, F. Riva and A. Wulzer, *Electroweak Precision Tests in High-Energy Diboson Processes*, *JHEP* **02** (2018) 111, [1712.01310].

[284] S. Banerjee, C. Englert, R. S. Gupta and M. Spannowsky, *Probing Electroweak Precision Physics via boosted Higgs-strahlung at the LHC*, *Phys. Rev. D* **98** (2018) 095012, [1807.01796].

[285] C. Grojean, M. Montull and M. Riembau, *Diboson at the LHC vs LEP*, *JHEP* **03** (2019) 020, [1810.05149].

[286] A. Biekoetter, T. Corbett and T. Plehn, *The Gauge-Higgs Legacy of the LHC Run II*, *SciPost Phys.* **6** (2019) 064, [1812.07587].

[287] D. Goncalves and J. Nakamura, *Boosting the $H \to$ invisibles searches with $Z$ boson polarization*, *Phys. Rev. D* **99** (2019) 055021, [1809.07327].

[288] R. Gomez-Ambrosio, *Studies of Dimension-Six EFT effects in Vector Boson Scattering*, *Eur. Phys. J. C* **79** (2019) 389, [1809.04189].

[289] F. F. Freitas, C. K. Khosa and V. Sanz, *Exploring the standard model EFT in VH production with machine learning*, *Phys. Rev. D* **100** (2019) 035040, [1902.05803].

[290] S. Banerjee, R. S. Gupta, J. Y. Reiness and M. Spannowsky, *Resolving the tensor structure of the Higgs coupling to $Z$-bosons via Higgs-strahlung*, *Phys. Rev. D* **100** (2019) 115004, [1905.02728].

[291] A. Azatov, D. Barducci and E. Venturini, *Precision diboson measurements at hadron colliders*, *JHEP* **04** (2019) 075, [1901.04821].

[292] S. Banerjee, R. S. Gupta, J. Y. Reiness, S. Seth and M. Spannowsky, *Towards the ultimate differential SMEFT analysis*, *JHEP* **09** (2020) 170, [1912.07628].

[293] A. Biekötter, R. Gomez-Ambrosio, P. Gregg, F. Krauss and M. Schönherr, *Constraining SMEFT operators with associated $h\gamma$ production in weak boson fusion*, *Phys. Lett. B* **814** (2021) 136079, [2003.06379].

[294] K. Rao, S. D. Rindani and P. Sarmah, *Study of anomalous gauge-Higgs couplings using Z boson polarization at LHC*, *Nucl. Phys. B* **964** (2021) 115317, [2009.00980].

[295] J. Y. Araz, S. Banerjee, R. S. Gupta and M. Spannowsky, *Precision SMEFT bounds from the VBF Higgs at high transverse momentum*, *JHEP* **04** (2021) 125, [2011.03555].

[296] I. Dunietz, H. R. Quinn, A. Snyder, W. Toki and H. J. Lipkin, *How to extract CP violating asymmetries from angular correlations*, *Phys. Rev. D* **43** (1991) 2193–2208.

[297] A. S. Dighe, I. Dunietz and R. Fleischer, *Extracting CKM phases and $B_s - \bar{B}_s$ mixing parameters from angular distributions of nonleptonic B decays*, *Eur. Phys. J. C* **6** (1999) 647–662, [hep-ph/9804253].

[298] D. Stolarski and R. Vega-Morales, *Directly Measuring the Tensor Structure of the Scalar Coupling to Gauge Bosons*, *Phys. Rev. D* **86** (2012) 117504, [1208.4840].

[299] Y. Chen, R. Harnik and R. Vega-Morales, *Probing the Higgs Couplings to Photons in $h \to 4\ell$ at the LHC*, *Phys. Rev. Lett.* **113** (2014) 191801, [1404.1336].

[300] Y. Chen, R. Harnik and R. Vega-Morales, *New opportunities in $h \to 4\ell$*, *JHEP* **09** (2015) 185, [1503.05855].

[301] Y. Chen, J. Lykken, M. Spiropulu, D. Stolarski and R. Vega-Morales, *Golden Probe of Electroweak Symmetry Breaking*, *Phys. Rev. Lett.* **117** (2016) 241801, [1608.02159].

[302] J. S. Gainer et al., *Adding pseudo-observables to the four-lepton experimentalist's toolbox*, *JHEP* **10** (2018) 073, [1808.00965].

[303] D. Atwood and A. Soni, *Analysis for magnetic moment and electric dipole moment form-factors of the top quark via e+ e- —> t anti-t*, *Phys. Rev. D* **45** (1992) 2405–2413.

[304] I. Anderson et al., *Constraining Anomalous HVV Interactions at Proton and Lepton Colliders*, *Phys. Rev. D* **89** (2014) 035007, [1309.4819].

[305] A. V. Gritsan, J. Roskes, U. Sarica, M. Schulze, M. Xiao and Y. Zhou, *New features in the JHU generator framework: constraining Higgs boson properties from on-shell and off-shell production*, *Phys. Rev. D* **102** (2020) 056022, [2002.09888].

[306] S. Chen, A. Glioti, G. Panico and A. Wulzer, *Parametrized classifiers for optimal EFT sensitivity*, *JHEP* **05** (2021) 247, [2007.10356].

[307] ATLAS collaboration, G. Aad et al., *Search for the Higgs boson decays $H \to ee$ and $H \to e\mu$ in pp collisions at $\sqrt{s} = 13$ TeV with the ATLAS detector*, *Phys. Lett. B* **801** (2020) 135148, [1909.10235].

[308] CMS collaboration, A. Sirunyan et al., *Measurements of Higgs boson properties in the diphoton decay channel in proton-proton collisions at $\sqrt{s} = 13$ TeV*, *JHEP* **11** (2018) 185, [1804.02716].

[309] CMS collaboration, *Measurements of Higgs boson properties in the diphoton decay channel at $\sqrt{s} = 13$ TeV*, tech. rep., CERN, Geneva, 2020.

[310] ATLAS collaboration, *Projections for measurements of Higgs boson cross sections, branching ratios, coupling parameters and mass with the ATLAS detector at the HL-LHC*, tech. rep., CERN, Geneva, 2018.

[311] A. Pomarol and F. Riva, *Towards the Ultimate SM Fit to Close in on Higgs Physics*, *JHEP* **01** (2014) 151, [1308.2803].

[312] ALEPH, DELPHI, L3, OPAL, SLD, LEP Electroweak Working Group, SLD Electroweak Group, SLD Heavy Flavour Group

collaboration, S. Schael et al., *Precision electroweak measurements on the Z resonance*, *Phys. Rept.* **427** (2006) 257–454, [hep-ex/0509008].

[313] K. Hagiwara, R. D. Peccei, D. Zeppenfeld and K. Hikasa, *Probing the Weak Boson Sector in e+ e- —> W+ W-*, *Nucl. Phys. B* **282** (1987) 253–307.

[314] C. Degrande, J. M. Gerard, C. Grojean, F. Maltoni and G. Servant, *Probing Top-Higgs Non-Standard Interactions at the LHC*, *JHEP* **07** (2012) 036, [1205.1065].

[315] N. Deutschmann, C. Duhr, F. Maltoni and E. Vryonidou, *Gluon-fusion Higgs production in the Standard Model Effective Field Theory*, *JHEP* **12** (2017) 063, [1708.00460].

[316] R. Frederix, S. Frixione, V. Hirschi, F. Maltoni, R. Pittau and P. Torrielli, *Four-lepton production at hadron colliders: aMC@NLO predictions with theoretical uncertainties*, *JHEP* **02** (2012) 099, [1110.4738].

[317] R. M. Godbole, D. J. Miller and M. M. Muhlleitner, *Aspects of CP violation in the HZZ coupling at the LHC*, *JHEP* **12** (2007) 031, [0708.0458].

[318] E. P. Wigner, *Group Theory: And its Application to the Quantum Mechanics of Atomic Spectra*. Pure and applied physics. Elsevier Science, 2012.

[319] F. James, *Statistical methods in experimental physics*. World Scientific Singapore, 2006.

[320] F. Beaujean, M. Chrząszcz, N. Serra and D. van Dyk, *Extracting Angular Observables without a Likelihood and Applications to Rare Decays*, *Phys. Rev. D* **91** (2015) 114012, [1503.04100].

[321] M. Dobbs and J. B. Hansen, *The HepMC C++ Monte Carlo event record for High Energy Physics*, *Comput. Phys. Commun.* **134** (2001) 41–46.

[322] M. Cacciari, G. P. Salam and G. Soyez, *FastJet User Manual*, *Eur. Phys. J. C* **72** (2012) 1896, [1111.6097].

[323] M. Cacciari, G. P. Salam and G. Soyez, *The anti-$k_t$ jet clustering algorithm*, *JHEP* **04** (2008) 063, [0802.1189].

[324] A. Buckley, D. Kar and K. Nordström, *Fast simulation of detector effects in Rivet*, *SciPost Phys.* **8** (2020) 025, [1910.01637].

[325] A. Buckley, J. Butterworth, D. Grellscheid, H. Hoeth, L. Lonnblad, J. Monk et al., *Rivet user manual*, *Comput. Phys. Commun.* **184** (2013) 2803–2819, [1003.0694].

[326] The Particle Data Group collaboration, M. Tanabashi et al., *Review of Particle Physics*, *Phys. Rev. D* **98** (2018) 030001.

[327] S. Banerjee, R. S. Gupta, O. Ochoa-Valeriano and M. Spannowsky, *High energy lepton colliders as the ultimate Higgs microscopes*, *JHEP* **02** (2022) 176, [2109.14634].

[328] M. S. Chanowitz and M. K. Gaillard, *The TeV Physics of Strongly Interacting W's and Z's*, *Nucl. Phys. B* **261** (1985) 379–431.

[329] A. Wulzer, *An Equivalent Gauge and the Equivalence Theorem*, *Nucl. Phys. B* **885** (2014) 97–126, [1309.6055].

[330] N. Craig, J. Gu, Z. Liu and K. Wang, *Beyond Higgs Couplings: Probing the Higgs with Angular Observables at Future $e^+e^-$ Colliders*, *JHEP* **03** (2016) 050, [1512.06877].

[331] J. Yan, S. Watanuki, K. Fujii, A. Ishikawa, D. Jeans, J. Strube et al., *Measurement of the Higgs boson mass and $e^+e^- \to ZH$ cross section using $Z \to \mu^+\mu^-$ and $Z \to e^+e^-$ at the ILC*, *Phys. Rev. D* **94** (2016) 113002, [1604.07524].

[332] J. F. Gunion, T. Han and R. Sobey, *Measuring the coupling of a Higgs boson to Z Z at linear colliders*, *Phys. Lett. B* **429** (1998) 79–86, [hep-ph/9801317].

[333] T. Han and J. Jiang, *CP-violating $ZZh$ coupling at $e^+e^-$ linear colliders*, *Phys. Rev. D* **63** (2001) 096007, [hep-ph/0011271].

[334] T. Han, Z. Liu, Z. Qian and J. Sayre, *Improving Higgs Coupling Measurements Through ZZ Fusion at the ILC*, *Phys. Rev. D* **91** (2015) 113007, [1504.01399].

[335] R. Torre, L. Ricci and A. Wulzer, *On the W&Y interpretation of high-energy Drell-Yan measurements*, *JHEP* **02** (2021) 144, [2008.12978].

[336] G. Panico, L. Ricci and A. Wulzer, *High-energy EFT probes with fully differential Drell-Yan measurements*, *JHEP* **07** (2021) 086, [2103.10532].

[337] ALEPH Collaboration, DELPHI Collaboration, L3 Collaboration, OPAL Collaboration, LEP TGC Working Group collaboration, *A Combination of Preliminary Results on Gauge Boson Couplings Measured by the LEP experiments*, tech. rep., CERN, Geneva, 2003.

[338] G. B. Arfken and H. J. Weber, *Mathematical methods for physicists; 4th ed.* Academic Press, 1995.

[339] M. L. Boas, *Mathematical methods in the physical sciences; 3rd ed.* Wiley, 2006.

[340] C. Degrande, C. Duhr, B. Fuks, D. Grellscheid, O. Mattelaer and T. Reiter, *UFO - The Universal FeynRules Output*, *Comput. Phys. Commun.* **183** (2012) 1201–1214, [1108.2040].

[341] A. Alloul, N. D. Christensen, C. Degrande, C. Duhr and B. Fuks, *FeynRules 2.0 - A complete toolbox for tree-level phenomenology*, *Comput. Phys. Commun.* **185** (2014) 2250–2300, [1310.1921].

[342] J. Alwall, R. Frederix, S. Frixione, V. Hirschi, F. Maltoni, O. Mattelaer et al., *The automated computation of tree-level and next-to-leading order differential*

*cross sections, and their matching to parton shower simulations*, *JHEP* **07** (2014) 079, [1405.0301].

[343] P. Nason, *A New method for combining NLO QCD with shower Monte Carlo algorithms*, *JHEP* **11** (2004) 040, [hep-ph/0409146].

[344] S. Frixione, P. Nason and C. Oleari, *Matching NLO QCD computations with Parton Shower simulations: the POWHEG method*, *JHEP* **11** (2007) 070, [0709.2092].

[345] S. Alioli, P. Nason, C. Oleari and E. Re, *A general framework for implementing NLO calculations in shower Monte Carlo programs: the POWHEG BOX*, *JHEP* **06** (2010) 043, [1002.2581].

[346] NNPDF collaboration, R. D. Ball et al., *Parton distributions from high-precision collider data*, *Eur. Phys. J. C* **77** (2017) 663, [1706.00428].

[347] J. M. Campbell and R. K. Ellis, *MCFM for the Tevatron and the LHC*, *Nucl. Phys. B Proc. Suppl.* **205-206** (2010) 10–15, [1007.3492].

[348] J. Pumplin, D. R. Stump, J. Huston, H. L. Lai, P. M. Nadolsky and W. K. Tung, *New generation of parton distributions with uncertainties from global QCD analysis*, *JHEP* **07** (2002) 012, [hep-ph/0201195].

[349] T. Sjöstrand, S. Ask, J. R. Christiansen, R. Corke, N. Desai, P. Ilten et al., *An introduction to PYTHIA 8.2*, *Comput. Phys. Commun.* **191** (2015) 159–177, [1410.3012].

[350] M. Grazzini, S. Kallweit and D. Rathlev, *ZZ production at the LHC: fiducial cross sections and distributions in NNLO QCD*, *Phys. Lett. B* **750** (2015) 407–410, [1507.06257].

[351] J. M. Campbell and R. K. Ellis, *Next-to-Leading Order Corrections to $W + 2$ jet and $Z + 2$ Jet Production at Hadron Colliders*, *Phys. Rev. D* **65** (2002) 113007, [hep-ph/0202176].

[352] J. de Blas et al., *Higgs Boson Studies at Future Particle Colliders*, *JHEP* **01** (2020) 139, [1905.03764].

[353] G. Durieux, C. Grojean, J. Gu and K. Wang, *The leptonic future of the Higgs*, *JHEP* **09** (2017) 014, [1704.02333].

[354] DELPHES 3 collaboration, J. de Favereau, C. Delaere, P. Demin, A. Giammanco, V. Lemaître, A. Mertens et al., *DELPHES 3, A modular framework for fast simulation of a generic collider experiment*, *JHEP* **02** (2014) 057, [1307.6346].

[355] P. Demin and M. Selvaggi, "Delphes Card ILD." https://github.com/delphes/delphes/blob/master/cards/delphes_card_ILD.tcl, Accessed 1 June 2021.

[356] CLICdp collaboration, D. Arominski et al., *A detector for CLIC: main parameters and performance*, 1812.07337.

[357] E. Leogrande, P. Roloff, U. Schnoor and M. Weber, *A DELPHES card for the CLIC detector*, 1909.12728.

[358] M. E. Peskin and T. Takeuchi, *Estimation of oblique electroweak corrections*, *Phys. Rev. D* **46** (1992) 381–409.

[359] R. Barbieri, A. Pomarol, R. Rattazzi and A. Strumia, *Electroweak symmetry breaking after LEP-1 and LEP-2*, *Nucl. Phys. B* **703** (2004) 127–146, [hep-ph/0405040].